Thèse n° 8280

Helimagnons and Skyrmion Dynamics in $Cu_2OS_eO_3$ and Fe/Gd Multilayers Explored by Brillouin Light Scattering and X-ray Microscopy

Présentée le 26 août 2021

Faculté des sciences et techniques de l’ingénieur
Laboratoire des matériaux magnétiques nanostructurés et magnoniques
Programme doctoral en physique

pour l’obtention du grade de Docteur ès Sciences

par

Ping CHE

Acceptée sur proposition du jury

Prof. O. Yazyev, président du jury
Prof. D. Grundler, directeur de thèse
Prof. G. S. Beach, rapporteur
Prof. S. Demokritov, rapporteur
Prof. J.-Ph. Ansermet, rapporteur

École
polytechnique
fédérale
de Lausanne

2021

To see a world in a grain of sand
And a heaven in a wild flower
Hold infinity in the palm of your hand
And eternity in an hour
— William Blake

观古今于须臾，抚四海于一瞬
陆机

To my mom and my sister

Acknowledgements

Being a scientist was always the dream of the me in childhood. Not until I finished my thesis do I believe that I am really on the way. I would like to express my deep gratitude to the individuals who brought me to the scientific world, guided me as junior researcher and enriched my PhD life. Without them, works presented in this thesis would not have been accomplished. Two pages are not enough to count all my thanks. I will do my best and be grateful for everyone helping my PhD work.

I would first like to thank my thesis director **Prof. Dirk Grundler** for teaching me to think as a researcher, guiding me in my research and study, supporting me in my career and personal life and respecting me as a coworker. It is such a joy to discuss science with him. His brainstorming always inspires me and motivates me for new challenges. Particularly, his responsible attitude and passion on student education impressed me. I learned from him not only how to conduct highly qualified research but also how to bring the knowledge from our research to students in class.

I would like to thank **Prof. Oleg Yazyev**, **Prof. Jean-Philippe Ansermet**, **Prof. Geoffrey S.D. Beach**, **Prof. Sergej Demokritov** for agreeing to be on my PhD defense committee and taking time to go through the thesis. It's a great honor to have a group of top class experts in magnetism as advisers and I am grateful to the inspiring discussions on the defense.

I would also like to show my appreciation to the LMGN buddies. They make the working experience in the lab a great memorable pleasure. To **Korbinian Baumgärtl**, many thanks for the support on BLS measurements, nanofabricaiton, XMCD measurements and the beer suggestions in Berlin, as well as for protecting us as lab's former COSEC. To **Sho Watanabe**, I want to thank him for the help on MFM and VNA setups and all the joy of off-work drinking. Many thanks to **Maria Carmen Giordano** for the support on nanofabrication and for the care as a sister in daily life. Thanks to **Mohammad Hamdi** for the discussion on theory models, simulations and the help on all the IT technical issues. Special thanks to **Andrea Mucchietto** for the support on BLS and MFM setup, simulation works and the discussions in the morning, noon and afternoon coffee breaks. Particularly thanks to him for ensuring the lab and office cleanness during the pandemic period. Lastly, I wish to sincerely thank **Anna Kúkol'ová**, not only for the support in the lab and summer school organization, but also for the accompanying and tolerance in our flat. I would like to thank the former group member **Dr. Kyongmo An** for support on VNA setup and discussion on basic concepts on magnetism. I also want to thank the former group members **Edoardo Catapano** and **Bin Lu** for assistance on BLS and MFM measurement during their master thesis projects. Additionally, I want to thank group member **Le Yu**, **Cagri Ozdilek** and former group member **Prof. Vinayak Bhat**, **Dr. Jian-Rui Soh** for support on daily work in the lab. Last but not least, I would like to express my thanks to **Yuko Kagata** for managing the administrative and financial works for my PhD work.

I would like to acknowledge the Swiss National Science Foundations via grant 171003 for supporting the works in this thesis. We thank HZB for the allocation of neutron/synchrotron radiation beamtime. The Fe/Gd project in this thesis has received funding from the European Union's Horizon 2020 research and innovation programme under grant agreement No 730872.

I want to extend my gratitude to the collaborators. Except for the thanks to the collaboration clarified in the Appendix part, I also want to thank all the members in sinergia network Nanoskyrmionics. They always offer me timely and full support on samples, characterizations and fruitful discussions. At the same time, they helped me develop a balanced PhD life. I would like to express gratitude to **Prof. Anna Fontcuberta i Morral** for the suggestions on my career, discussions and suggestions on the research topics in this thesis. And many thanks to the group members of LMSC for close collaborations. Very special thanks to the staffs from Center of MicroNanoTechnology (CMi), Interdisciplinary Center for Electron Microscopy (CIME) and material science machine shop. I want to thank supports from CMi staff **Julien Dorsaz** on photo-lithography, **Zdenek Benes** for ebeam-lithography and scanning electron microscope, **Joffrey Pernollet** for focus ion beam etching and ion beam etching, **Guy-François Clerc** and **Rémy Juttin** for film growth using thermal evaporation and sputtering, **Patrick Alain Madliger** for sputtering, helium recharge and general usage of clean room, **Corradini Giancarlo** and **Adrien Toros** for wire bonding and dicing. I also want to thank CIME scientist **Marco Cantoni** for scientific discussion on sample fabrication, **Lucie Navrátilová** for focus ion beam etching, and **Danièle Laub** for sample polishing. Thanks to all the other staff and scientist in those institutes for maintaining the setup and offering the daily supports.

Next I would like to thank **Anh Eymann** for the help on administrative works for my PhD project and the support on the summer school organization. And I want to thank my EDPY mentor **Prof. Romuald Houdré** for the help on the balance and smooth going of my thesis.

Sincere thanks to my basketball teammates **Yu Wu** and **Yihui Zuo** and friend **Jianing Li**. You motivated me for healthier life and brought me a lot of happy time with basketball, hiking and delicious food. To my friend and colleague **Dr. Jiaqi Zhou**, thank you for being my fellow on the road of scientific research. I enjoyed our discussion on physics, holidays, cooking, TV shows ...

Finally I want to thank **my family** and **Antoine** for their love and support. I am lucky to have them all in my life and I am fearless and ready for any challenge with their love. Special thanks to the past-away little elf-like cat **Attila** for accompanying me during the work-from-home period.

Lausanne, April 26, 2021 P. C.

Abstract

Spin dynamics in skyrmion hosting materials provide novel functionality in magnonics because of the formation of a novel magnon band structure and the nanoscale sizes of magnetic skyrmions. In this thesis, we explore the spin dynamics in the chiral magnet Cu_2OSeO_3 locally utilizing the scanning micro-focus Brillouin light scattering (BLS) technique at cryogenic temperature. Taking advantage of the high sensitivity and spatial resolution of BLS, we resolved the one-to-one correspondence between different non-collinear phases, such as helical, chiral soliton, conical and skyrmion phases, in a chiral magnet and their collective spin excitations. We show that the continuous-wave laser in BLS enables the stabilization of metastable phases and creation of skyrmion tracks surrounded by the conical phase. The high sensitivity of BLS allows us to deepen the understanding of coexisting phases in the chiral magnet. The results pave the way for the design of further magnonic devices based on chiral magnets. Furthermore, we explore dipolar skyrmions and domain walls in amorphous Fe/Gd multilayers employing scanning transmission x-ray microscopy. We demonstrate the formation of stripe and square lattices of domains by integrating one-dimensional and two-dimensional nanomagnet arrays, respectively. Dynamics of domain walls, multi-domain boundaries and skyrmions were captured with pump-probe spectroscopy. In a skyrmion pair, a magnon wavelength down to 239 nm at 0.33 GHz was observed and compared to the electromagnetic wave whose wavelength is 0.9 m at the same frequency. The extreme wavelength conversion underlines the potential of skyrmion hosting materials concerning miniaturization of information technology and microwave devices.

Résumé

La dynamique du spin dans les matériaux accueillant des Skyrmions offre de nouvelles fonctionnalités en magnonique en raison de la formation de nouvelles bandes d'énergies de magnon et de leur taille nanométrique naturelle. Dans cette thèse, nous explorons la dynamique locale du spin dans l'aimant chiral Cu_2OSeO_3 en utilisant la technique du scanning micro-focus Brillouin light scattering (BLS) à température cryogénique. Profitant de la haute sensibilité et de la résolution spatiale du BLS, nous avons résolu la correspondance d'un pour un entre différentes phases non colinéaires, telles que les phases hélicoïdales, soliton chiral, coniques et les phases de skyrmion, dans l'aimant chiral et leurs excitations de spin collectives. Nous avons montré que le laser continue du BLS aide à stabiliser les phases métastables et à créer des pistes de skyrmion entourées de phases coniques. La grande sensibilité du BLS nous permet d'approfondir la compréhension des phases coexistantes dans l'aimant chiral. Les résultats ouvrent la voie à une conception plus poussée des dispositifs magnoniques basés sur les aimants chiraux. De plus, nous explorons les skyrmions dipolaires et les parois magnétiques dans les multicouches Fe/Gd amorphes en utilisant le STXM (scanning transmission x-ray microscopy). Nous démontrons la formation de réseaux de domaines en bandes et en carrés en intégrant des réseaux nanométriques magnétiques unidimensionnels et bidimensionnels, respectivement. La dynamique des domaines magnétiques, des frontières multi-domaines et des skyrmions a été capturée avec la technique pompe-sonde. Les longueurs d'ondes des magnons observées dans une double paire de skyrmions allaient jusqu'à 239 nm à 0,33 GHz, comparé à 0,9 m pour une onde électromagnétique à la même fréquence. La conversion extrême des longueurs d'onde souligne le potentiel des matériaux accueillant des Skyrmions concernant la miniaturisation des technologies de l'information et des dispositifs à micro-ondes.

Scientific Collaboration

Scientific collaborations have contributed significantly to the works in this thesis. They are acknowledged as the following:

- All the CSO samples investigated in this thesis have been grown by Arnaud Magrez and Helmuth Berger from the Crystal Growth Facility, Institut de Physique, École polytechnique fédérale de Lausanne, Switzerland.

- Fe/Gd multilayers were grown by Prof. Manfred Albrecht and Michael Heigl from Institute of Physics, University of Augsburg, Germany. Superconducting quantum interference measurements were conducted by Michael Heigl.

- Shaping and characterizations on CSO sample B1 and B2 were conducted by Dr. Andrea Bauer and Prof. Christian Pfleiderer from Physik Department E51, Technische Universität München, Germany.

- XRD and TEM characterization on CSO sample B3 were conducted with the help of Thomas Schönenberger from Laboratory for Quantum Magnetism and Anna Kúkol'ová from Laboratory of Nanoscale Magnetic Materials and Magnonics and Laboratory of Semiconductor Materials, École polytechnique fédérale de Lausanne, Switzerland.

- Susceptibility measurement on CSO B3 was conducted by Priya Ranjan Baral from the group Chair of Computational Condensed Matter Physics, Institut de Physique, École polytechnique fédérale de Lausanne, Switzerland.

- All-electrical spin-wave spectroscopy on confined spin waves in CSO sample was conducted with the help of Dr. Ioannis Stasinopoulos from Physik Department E10, Technische Universität München, Germany. Data analysis was helped by master project student Jianing Li from Laboratory of Nanoscale Magnetic Materials and Magnonics, École polytechnique fédérale de Lausanne, Switzerland.

- BLS measurements on CSO sample B2 were assisted by master student Bin Lu from Laboratory of Nanoscale Magnetic Materials and Magnonics, École polytechnique fédérale de Lausanne, Switzerland.

- MFM measurements on Fe/Gd multilayers were assisted by master student Edoardo Catapano from from Laboratory of Nanoscale Magnetic Materials and Magnonics, École polytechnique fédérale de Lausanne, Switzerland.
- STXM measurements were supported by the beam scientists Dr. Joachim Grafe from Max Planck Institute for Intelligent Systems, Stuttgart, Germany, Michael Bechtel and Markus Weigand from Helmholtz-Zentrum Berlin für Materialien und Energie, Berlin, Germany.
- Theoretical supports on BLS measurements were provided by Prof. Markus Garst and Dr. Volodymyr Kravchuk from Karlsruher Institut für Technologie, Germany.
- Theoretical supports on Fe/Gd characterization and parameters calculations are provided by Mohammad Hamdi from Laboratory of Nanoscale Magnetic Materials and Magnonics, École polytechnique fédérale de Lausanne, Switzerland.
- Micromagnetic simulations were helped by Andrea Mucchietto and master student Iseli Gabriel Valentin from Laboratory of Nanoscale Magnetic Materials and Magnonics, École polytechnique fédérale de Lausanne, Switzerland.

The author would like to express her profound gratitude for the supports and collaborations.

List of Tables

List of Figures

Contents

Introduction

Motivation

Integrated micro- and nano-electronics are the key components for computational and communication devices. With the greatly increasing demand of personal and mobile devices as well as the development of modern nano-technologies, basic electronics such as transistors and memories evolved toward miniaturization, faster transmission and higher storage capacity [1–5]. As transistors scale down to below 20 nm, the leakage currents in the channel region between drain and source limit further miniaturization and power consumption bursts [6]. Three dimensional designs of field transistor extended the limit but the limitation still exists [7]. Recent developments in the field of magnonics and skyrmionics have led to novel approaches of beyond-complementary metal– oxide–semiconductors (CMOS) for next generation nano-electronics [8–10].

Magnonics received considerable attention as it promises low-power-consuming information technologies thanks to the spin wave precession with only momentum transmission but no moving charges [11, 12]. Besides, there is a fundamental advantage of magnonic devices coming from the distinct dispersion relations compared with electromagnetic waves [13]. For electromagnetic waves at gigahertz, the wavelength is as long as centimeters and the antennas for telecommunication are macroscopic [14]. Switching to spin waves, they own the wavelength of about micrometers to nanometers at gigahertz (GHz). This property of spin waves brings hope for GHz devices operating on the nanometer scale. Spin wave interference from designed waveguides were proposed as the magnonic circuits [8, 15–18]. Recently an advanced design of a magnon half-adder in 30 nm dimensions functionalized as 7 nm CMOS half-adder was reported to consume power in attojoules [19]. It further highlighted the strength of magnonic devices for low-power consumption. Magnetic textures such as domain walls and stripe-shaped domains were reported as candidates for magnon waveguides for logic devices [20–24]. Magnonic crystals provide novel magnon band structures with bandgaps and minibands [25–27]. They have been constructed with periodic patterns of stripes in a one-dimensional, anti-dots and discs in two-dimensional arrangement on ferromagnets [28–33]. Multifunctional microwave and logic devices can be achieved by reprogramming the magnetic states of magnonic crystals [27]. The observation of spin waves channels created by inhomogeneous fields in the magnonic crystals offers more flexibility for further applications

[30, 34, 35]. With the purpose of reducing the device size, nano-sized magnon waveguides and magnonic crystals are essential, strongly demanding nano-patterning techniques.

Non-collinear spin textures, e.g. skyrmions and helices, have been discovered in noncentrosymmetric chiral magnets with bulk Dzyaloshinskii-Moriya interaction (DMI) [36–44], multilayers with interfacial DMI [45–48], multilayers with perpendicular magnetic anisotropy [49–52], and so on. Lateral size of skyrmions range from several nanometers to hundreds of nanometers. They show the skyrmion Hall effects [53–55] and can be created and manipulated by spin and electric currents [56–59]. Due to these aspects, they draw special attention for storage and logic devices [60–65]. They offers potential for magnonic devices as well. Skyrmions and helices are formed as regular lattices in chiral magnets naturally. Novel magnon band structures are predicted because their textures are identical to magnonic crystals [66, 67]. Bottom-up creation of magnonic crystals can be achieved without challenging nano-fabrication [27]. Variable lattice formats of helices and skyrmion lattices offer more possibilities of band structure formation. Single skyrmions also play a role in spin wave propagation. The scattering of spin waves on skyrmions have been reported to modify the propagation directions and create magnonic frequency comb [68–71]. Currently most of the reports are on theories and micromagnetic simulations, and much less is known about experiments. Not only spin textures, but also the DMI is adjusting the spin waves properties. Both bulk and interfacial DMI introduce shifts in the magnon dispersion and induce non-reciprocity [72–79]. Thus DMI is a tool for controlling spin waves propagation.

So far the spin dynamics in chiral magnets were mostly investigated by all-electrical spin-wave spectroscopy using microwave excitation [80–87] and high-energy neutron scattering [88–90] in bulk chiral magnets. However, complex spin dynamic spectra are always formed in bulk chiral magnets [86] due to the formation of micrometer-size multi-domains and confinement arising from sample boundaries [91, 92]. A scanning technique resolving locally the spin excitations is highly demanded for magnonics research in order to sort out the relations between magnons and magnetic textures. And the one-to-one correspondence between non-collinear phases and their spin dynamics need to be clarified before designing magnonic devices. Based on this need, we extended micro-focus Brillouin light scattering to cryogenic temperatures with a scanning function. We take Cu_2OSeO_3 as a start point for spin dynamics investigations thank to its low damping [93] and extremely rich magnetic phases [39, 94, 95]. We resolved spin dynamics of multiple non-collinear phases including four types of skyrmion lattices.

Materials hosting skyrmions at room temperature with low Gilbert damping are particularly interesting. Multilayers with perpendicular magnetic anisotropy host dipole skyrmions and skyrmion lattices at room temperature, e.g. amorphous Fe/Gd multilayers [49, 51, 52]. The Gilbert damping in this material is of the order of 0.01 [51] and promising. Therefore we choose amorphous Fe/Gd multilayers for spin dynamics exploration on skyrmions and domain walls at room temperature. Using the scanning transmission x-ray microscopy at Bessy II, Berlin, we observed several spin waves modes in domain walls and skyrmion dynamics with a spatial resolution of about 20 nm. Spin waves are found to propagate in complex patterns along micrometer long domain walls and in individual skyrmions.

Thesis Outline

This thesis is organized as follows: In chapter 1, we introduce theoretical aspects of ferromagnetism, chiral magnetism, skyrmion hosting materials and magnetization dynamic of both collinear and non-collinear states. In chapter 2, we describe the experimental methods and setups used in this thesis, including the all-electrical spin-wave spectroscopy, Brillouin light scattering, scanning transmission x-ray microscopy and the protocol of controlling magnetic fields versus temperature histories. In chapter 3, we present the bulk sample preparation and nano fabrication with detailed process flows. In chapter 4, we report the Brillouin light scattering revealing spin dynamics and multi-phases in bulk shape Cu_2OSeO_3 at cryogenic temperatures. In chapter 5, we investigate the spin waves excited in well-ordered stripe domain lattices, boundaries of multi-domains and dipole skyrmions in Fe/Gd multilayers utilizing scanning transmission x-ray microscopy and pump-probe technique. In chapter 6, we conclude the thesis and give a outlook.

1 Theory Background

In this chapter, we summarize the theoretical background of static and dynamic magnetism in ferro- (ferri-) and chiral magnets. In section 1.1, we introduce the magnetism in solids, energy terms in the magnetic systems and the static magnetic states in materials including ferromagnets (collinear states) and chiral magnets (non-collinear states). In section 1.2, we outline the skyrmion hosting materials with respect to different stabilization mechanisms. In section 1.3.1, we introduce the spin dynamics including ferromagnetic resonances of uniform spin procession and spin waves with finite wavevectors. In section 1.3.2, we discuss the spin dynamics of non-collinear magnetic states. In section 1.3.3, we compare the dispersion relations in materials with and without Dzyaloshinskii-Moriya interaction.

1.1 Magnetism

1.1.1 Ferromagnetism

The magnetization of a defined volume ΔV is defined as [96]

$$\boldsymbol{M} = \frac{\sum_{\Delta V} \mathfrak{M}}{\Delta V} \tag{1.1}$$

$\sum_{\Delta V} \mathfrak{M}$ is vector sum of the magnetic moments in the volume ΔV.

The relation between the magnetization and the applied field is defined as susceptibility tensor $\hat{\chi}$

$$\boldsymbol{M} = \hat{\chi}\,\boldsymbol{H} \tag{1.2}$$

It is simplified to the scalar quantity χ in isotropic materials [97]. The value of χ can be used to classify the magnetic materials. For instance, when $\chi >> 0$, the material is a ferromagnet or a ferrimagnet (e.g. iron Fe or magnetite Fe_3O_4); when $\chi \approx 0$, the material is an antiferromagnet (e.g. hematite Fe_2O_3); when $\chi > 0$, the material is a paramagnet (e.g. aluminum); when $\chi < 0$, the material is a diamagnet (e.g. carbon).

The total magnetic flux density consists of both the magnetization and the applied field

$$
\begin{aligned}
\boldsymbol{B} &= \mu_0(\boldsymbol{M}+\boldsymbol{H}) \\
\boldsymbol{B} &= \mu_0(\chi+1)\boldsymbol{H}
\end{aligned}
\tag{1.3}
$$

where $\mu_0 = 4\pi \times 10^{-7}$ H/m is the vacuum permeability. $\mu = \mu_0(\chi+1)$ is the magnetic permeability of a material.

The ground magnetic states in a material are decided by the effective field, which is a sum of all effective fields from different interactions:

$$\boldsymbol{H}_{\text{eff}} = \boldsymbol{H}_{\text{ex}} + \boldsymbol{H}_{\text{DM}} + \boldsymbol{H}_{\text{Z}} + \boldsymbol{H}_{\text{ani}} + \boldsymbol{H}_{\text{dem}} + \dots \tag{1.4}$$

including the $\boldsymbol{H}_{\text{ex}}$ from symmetric exchange interaction, $\boldsymbol{H}_{\text{DM}}$ from Dzyaloshinskii-Moriya interaction (asymmetric exchange interactions), $\boldsymbol{H}_{\text{Z}}$ from Zeeman interaction, $\boldsymbol{H}_{\text{ani}}$ from magnetocrystalline anisotropy, $\boldsymbol{H}_{\text{dem}}$ from shape anisotropy, and so on. This field is relevant for magnetization dynamics discussed in section 1.3. It is defined as the minimization of total energy in the system

$$\boldsymbol{H}_{\text{eff}} = -\frac{1}{\mu_0}\frac{\partial \boldsymbol{E}_{\text{tot}}}{\partial \boldsymbol{M}} \tag{1.5}$$

The total energy $\boldsymbol{E}_{\text{tot}}$ is taking into account all the energy terms in the system

$$E_{\text{tot}} = E_{\text{ex}} + E_{\text{DM}} + E_{\text{Z}} + E_{\text{ani}} + E_{\text{dem}} + \dots \tag{1.6}$$

In the following, we discuss the energy terms in charge of the magnetic states investigated in this thesis.

Exchange interaction

The exchange interaction energy between two spins $\boldsymbol{S}_i$ and $\boldsymbol{S}_j$ is decided by

$$E_{\text{ex}} = -2J_{ij}\boldsymbol{S}_i\boldsymbol{S}_j \tag{1.7}$$

where J_{ij} is the exchange integral. $\boldsymbol{S}_i$ and $\boldsymbol{S}_j$ are spin angular momenta. When $J_{\text{ex}} > 0$, the two spins prefer to be parallel. When $J_{\text{ex}} < 0$, the two spins prefer to be anti-parallel. When considering a lattice of spins, the total exchange energy is

$$E_{\text{ex}} = -2\sum_{i>j} J_{ij}\cdot\boldsymbol{S}_i\boldsymbol{S}_j \tag{1.8}$$

Dzyaloshinskii-Moriya interaction

Dzyaloshinskii-Moriya Interaction (DMI) is an asymmetric exchange interaction firstly proposed in the Refs. [98, 99]. The Hamiltonian is describes as [61]

$$\mathfrak{H}_{\mathrm{DM}} = \boldsymbol{D}_{ij} \cdot (\boldsymbol{S}_i \times \boldsymbol{S}_j) \tag{1.9}$$

$\boldsymbol{D}_{ij}$ is the DMI vectors. The energy corresponding to DMI is [61]

$$E_{\mathrm{DM}} = \int \mathrm{d}V D\boldsymbol{M}(\boldsymbol{r}) \cdot (\nabla \times \boldsymbol{M}(\boldsymbol{r})) \tag{1.10}$$

From the Hamiltonian and the energy term, the system favors the neighboring spins to be perpendicular to each other. It obstructs the spins to be aligned (parallel or anti-parallel). Combined with the symmetric exchange interactions, the spins are canted, and DMI assists the formation of chiral spin textures.

Zeeman interaction

Zeeman energy prefers to align the magnetization along the applied field [100]:

$$E_{\mathrm{Z}} = -\mu_0 \int \boldsymbol{M}\boldsymbol{H} \tag{1.11}$$

Magnetocrystalline anisotropy

Magnetocrystalline anisotropy is intrinsic to the crystals and it mainly originates from the spin-orbit coupling. When the applied field attempts to align the spins of the electrons, the orbits need to arrange accordingly. At the same time, the orbits are fixed to the crystal lattice. Thus the anisotropy energy is needed to align the sample's spins away from the so-called easy axis, which is named also as crystal anisotropy energy.

The relevant energy terms for a cubic crystal are expressed as [101]

$$E_{\mathrm{ani}}^{\mathrm{cubic}} = K_0 + K_1(\alpha_1^2\alpha_2^2 + \alpha_2^2\alpha_3^2 + \alpha_3^2\alpha_1^2) + K_2(\alpha_1^2\alpha_2^2\alpha_3^2) + \ldots \tag{1.12}$$

Here, α_1, α_2 and α_3 are the cosines of the angles between $\boldsymbol{M}$ and the crystal axes. K_0, K_1 and K_2 are the anisotropy constants corresponding to the material. Those constants could not be calculated from models and their values need to be measured experimentally. K_0 is not related to the angles and K_2 is often small. So generally they are neglected. K_1 is important because its sign determines if the anisotropy energy will be added to or reduced from the total energy. When $K_1 > 0$, the easy axis is $\langle 100 \rangle$. When $K_1 < 0$, the easy axis is $\langle 111 \rangle$.

For an uniaxial or easy-plane anisotropy, the anisotropy energy is describe as [101]

$$E_{\text{ani}}^{\text{uniaxial}} = K_0 + K_1 \sin^2\theta + K_2 \sin^4\theta + \ldots \tag{1.13}$$

Here, θ is the angle of the applied field with respect to the anisotropy axis, e.g. the c-axis. When $K_1 > 0$ and $K_2 > 0$, this axis is an easy axis and the material owns uniaxial anisotropy. When $K_1 < 0$ and $K_2 < 0$, c-axis is the hard axis and the plane perpendicular to the c-axis is the easy plane. If K_1 and K_2 have different signs, then their values need to be compared to determine the type of anisotropy.

Demagnetization effect

The demagnetization field is defined as

$$\boldsymbol{H}_{\text{dem}} = \overleftrightarrow{N}\boldsymbol{M} \tag{1.14}$$

Here, $\overleftrightarrow{N}$ is the demagnetization tensor to describe the shape anisotropy [96]:

$$\overleftrightarrow{N} = \begin{vmatrix} N_{11} & N_{12} & N_{13} \\ N_{12} & N_{22} & N_{23} \\ N_{13} & N_{23} & N_{33} \end{vmatrix}. \tag{1.15}$$

For ellipsoidal shape magnets (including infinitely thin plates and infinitely large thin cylinders), the tensor $\overleftrightarrow{N}$ becomes diagonal and it traces amount to $N_x + N_y + N_z = 1$. The energy term determined by the demagnetization effect is defined as [102]

$$E_{\text{dem}} = -\frac{\mu_0}{2}\int_{\text{V}} \boldsymbol{M}\boldsymbol{H}_{\text{dem}} \mathrm{d}V. \tag{1.16}$$

It reflects the long-range dipole-dipole interaction.

1.1.2 Chiral Magnetism

Chirality is one type of the asymmetric properties of materials, structures and spin textures. Spin textures are chiral when they are not identical with their mirrored textures. In the following, we outline the chiral spin textures in the chiral magnets with bulk DMI. They are illustrated in Fig. 1.1. The left-handed (LH) and right-handed (RH) textures do not satisfy any mirror symmetry. Thus they are chiral.

There are three types of one-dimensional non-collinear states reported in chiral magnets [95, 103]: helical, chiral soliton (CSL) and conical phases. Spins rotate with respect to the pitch vectors $\boldsymbol{q}$ in those states. In the helical phase at $H = 0$, there are three pitch vectors $\boldsymbol{q}$ following the easy axes instead of the applied magnetic field. When the applied field is perpendicular to $\boldsymbol{q}$, the helical state can be modified into CSL where the region of the spins parallel to the applied field enlarges. As the applied field increases, the pitch vector $\boldsymbol{q}$ gets aligned with the applied field direction and spins start to tilt to the field directions as well. This is the conical phase. When temperature T is increased to right below T_C, Bloch-type skyrmions are stabilized in chiral magnets via thermal fluctuation [36]. Their textures change with chirality as well and their planes are perpendicular to the magnetic field. In chiral magnets, the very first experimentally discovered skyrmion lattices (SkL) was a hexagonal lattices [36] shown in Fig. 1.1 (e). Under this circumstance, there are three pitch vectors $\boldsymbol{q}_1$, $\boldsymbol{q}_2$, and $\boldsymbol{q}_3$ in the SkL plane.

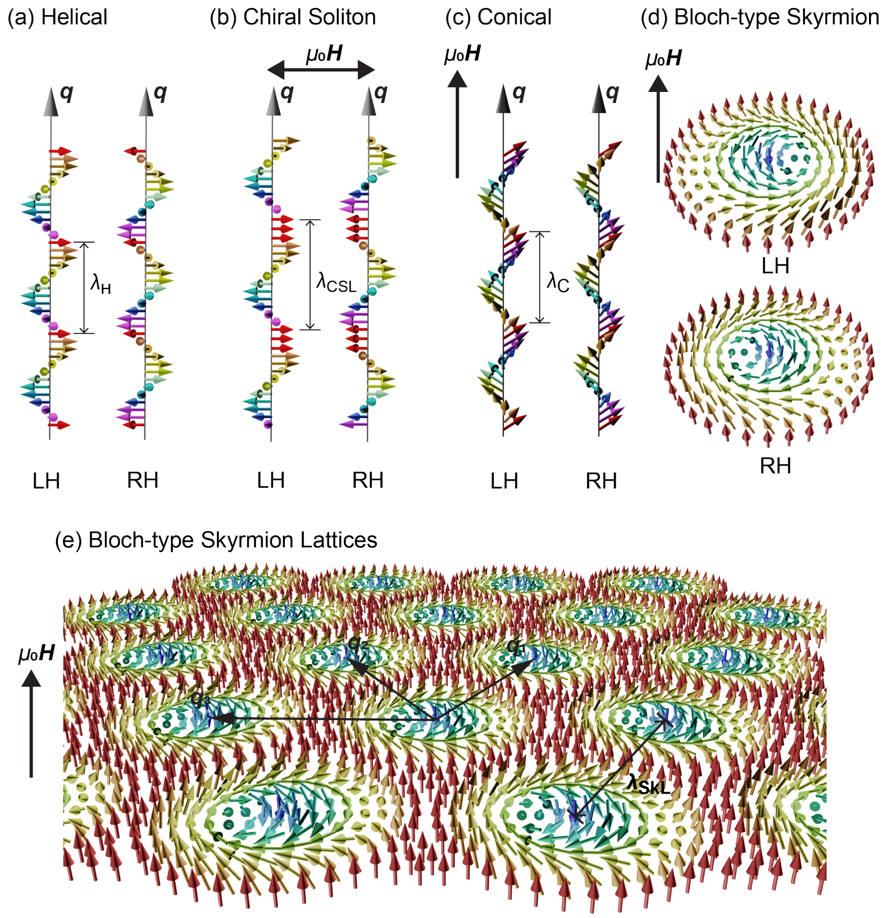

Figure 1.1 – **Illustration of the non-collinear states with different chiralities.** (a) Helical phase. (b) Chiral soliton phase. (c) Conical phase. (d) Single Bloch-type skyrmions. (e) Bloch-type skyrmion lattice. LH represents the left-handed chirality. RH represents the right handed one. $\boldsymbol{q}$, $\boldsymbol{q}_1$, $\boldsymbol{q}_2$, and $\boldsymbol{q}_3$ represent pitch vectors. $\mu_0\boldsymbol{H}$ indicates the applied field.

There are parameters describing the topological properties of skyrmions, such as helicity and skyrmion number. Helicity constant γ_{sk} is related to the chirality, e.g. γ_{sk} is $\pm\frac{\pi}{2}$ for Bloch-type skyrmions with left-handed or right-handed chirality [104]. And the swirling structures are characterized by the skyrmion number $w = \deg f$. It indicates the number of times spins are wrapped onto the topologically distinct mapping f. It is also called the winding number. The spin textures with different w are topologically inequivalent and can not be transformed into each other. The value w for spins on an one-dimensional chiral chain is expressed as soliton winding number [105]:

$$w = \frac{1}{2\pi}\int_{-\infty}^{\infty} dx \partial_x \Theta \tag{1.17}$$

where Θ is the angle of the spins with respect to the chosen coordinates. For the spherical spins with two dimensions, w is expressed as the two-dimensional skyrmion winding number [105, 106]:

$$w = \frac{1}{4\pi}\int\int dxdy \boldsymbol{m}_{\text{sk}}(\partial_x \boldsymbol{m}_{\text{sk}} \times \partial_y \boldsymbol{m}_{\text{sk}}) \tag{1.18}$$

where $\boldsymbol{m}_{\text{sk}} = \frac{\boldsymbol{M}}{M_0}$ is the unit vector of magnetization in a single skyrmion. w = 1 for a single skyrmion structure and w = -1 for a single anti-skyrmion structure.

1.2 Skyrmion Hosting Materials

Since the first experimental observation of magnetic skyrmions [36], skyrmion hosting materials have received considerable critical attention especially the non-trivial non-collinear phases [66]. It has been noted that skyrmions, particularly skyrmion lattices play a pivotal role in miniaturized magnonic devices with low-power consumption thanks to their novel magnonic properties [80, 107–110]. Simultaneously skyrmion-based storage logic devices come into sight because the spin textures are in nano-dimension, and they can have high stability energy barrier and mobility with low threshold current [45, 61, 65, 111–118]. Recently researchers suggested that skyrmions have the potential for neuromorphic computing as they can be well modulated by currents and fields [119, 120]. Thus it is essential to look for the skyrmion hosting materials exhibiting novel magnonic and transport properties. In this thesis we focus on the chiral magnet Cu_2OSeO_3 (CSO) to understand the magnonic properties of multiple non-collinear phases. Here the phases are formed at $T < T_C$ = 57 K. We extend the exploration to Fe/Gd multilayers with perpendicular magnetic anisotropy (PMA) hosting dipole skyrmions at room temperature.

1.2.1 Bulk Magnets

In the non-centrosymmetric lattice of chiral magnets where the inversion symmetry is broken, bulk DMI arise from spin-orbit coupling. Asymmetric exchange interaction DMI, coexisting simultaneously with symmetric exchange interaction, dipole interaction and Zeeman interaction, energetically stabilizes non-collinear spin textures in chiral magnets, e.g. skyrmions and spin spirals at intermediate field values as illustrated in Fig. 1.1. We choose CSO to explore spin dynamics because it has a low damping and rich non-collinear phases [39, 81, 94, 95, 121]. CSO is a insulating chiral magnet with cubic anisotropy hosting bulk DMI [39, 122]. Damping

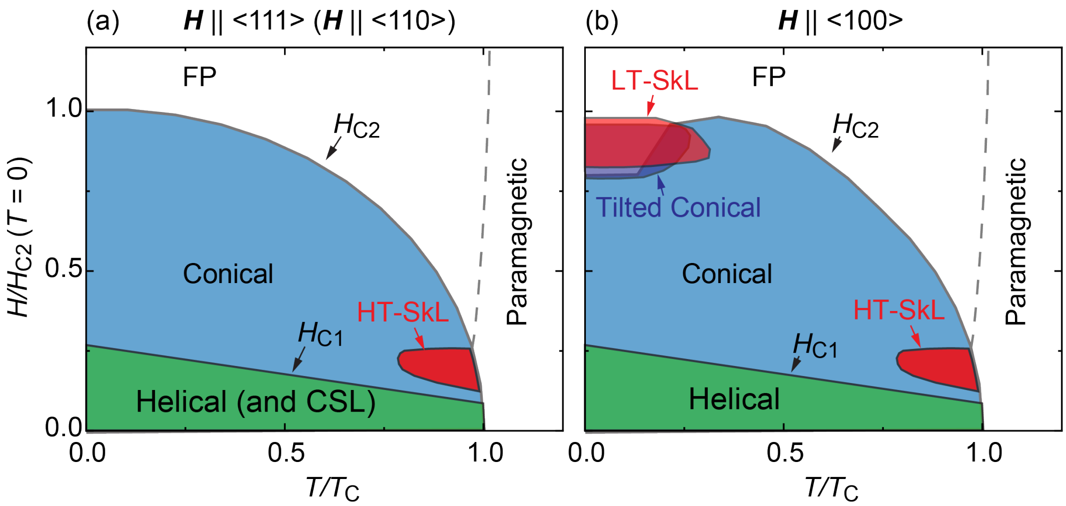

Figure 1.2 – **Schematic phase diagrams of chiral magnet Cu_2OSeO_3 when field along different crystallographic orientations.** (a) Schematic phase diagrams when $\boldsymbol{H} \parallel \langle 111 \rangle$ ($\boldsymbol{H} \parallel \langle 110 \rangle$). (b) Schematic phase diagrams when $\boldsymbol{H} \parallel \langle 100 \rangle$. Both diagrams consider the situation when magnetic field is scanned from 0 mT up after cooling down at 0 mT

parameter α was reported to be the lowest in the so far discovered skyrmion hosting materials with $\alpha = 1 \times 10^{-4}$ at $T = 5$ K [81]. Phases will be introduced in the following with respect to different crystallographic orientations.

The magnetic phase diagrams of chiral magnet CSO are sketched in Fig. 1.2. When the magnetic field was applied along crystallographic orientation $\langle 111 \rangle$ (Fig. 1.2 (a)), the helical phase stabilizes near zero field and it transforms into a conical phase when the applied field increases. The transition field is called first critical field labeled as H_{C1}. Stronger fields bring the system to the second critical field H_{C2} where the magnetic states transit from conical state to field polarized (FP) state. In the FP state, CSO is equivalent to a ferrimagnet. Below T_C, there appears the so called 'A-phase' which was proved to be the hexagonal SkL from the neutron scattering in Ref. [36]. The formation of high temperature SkL (HT-SkL) near T_C is dominated by bulk DMI and it is thermally stabilized. This phase diagram is not only for CSO along $\langle 111 \rangle$, but also typical in other chiral magnets such MnSi, FeGe, and so on [36, 38, 104].

Different from other crystallographic orientations, when the field was applied along $\langle 110 \rangle$, a double-transition process from helical to conical phase was suggested by a theory model [121]. There are three pitch vectors in helical phase when field is applied along $\langle 110 \rangle$: $\boldsymbol{q}_1$ along $\langle 100 \rangle$, $\boldsymbol{q}_2$ along $\langle 010 \rangle$ and $\boldsymbol{q}_3$ along $\langle 001 \rangle$. Before $\boldsymbol{q}_1$ and $\boldsymbol{q}_2$ reorient to the applied field direction, they are firstly tilted towards direction of the applied field in $\langle 001 \rangle$-$\langle 010 \rangle$ plane. The energy minimum falls in between 0 and 45 degree instead of staying at 0 degree along the easy axes $\langle 100 \rangle$ and $\langle 010 \rangle$. With the increasing field, the energy minimum moves to a higher angles before a sudden transition to conical phase arrives. But $\boldsymbol{q}_3$ is meta-stable along $\langle 001 \rangle$ and does not tilt before abrupt transition to conical phase.

CSL structure was firstly discovered in monoaxial chiral magnet $CrNb_3S_6$ [123–127] as a result of easy axis anisotropy, DMI and Zeeman interaction. In this material, when the applied field was tilted from the monoaxial axis, tilted-CSL phases exist up to 90 degree of field tilt [128]. Lattice constant of CSL were reported to be modified by the field strength. When the magnetic field was applied along crystallographic orientation ⟨110⟩ in strained CSO lamella, it was found that tensile strain provoked the CSL with a modulation vector along the strain direction [95]. CSL coexisted with the helical phase (as shown in Fig. 1.2 (a)). At small field values, applied field is unable to modify the lattice constant of CSL. Recent study also prove the existence of CSL in FeGd lamella with tensile strain when an external field was applied perpendicular to the tensile axis[103]. In FeGe it was reported that even a tiny magnetic field adjusted the lattice constant of CSL.

Meanwhile new skyrmion phases and tilted conical phases were found when $\boldsymbol{H} \parallel \langle 100 \rangle$ [94, 121, 129, 130]. ⟨100⟩ is one of the easy axes of cubic anisotropic CSO. These two new phases were stabilized by cubic anisotropy at low temperature (e.g. around 5 K to 20 K depending on the temperature versus field histories). A phase diagram with low-temperature SkL (LT-SkL) phases and tilted conical phases is shown in Fig. 1.2 (b). The phase diagram demonstrate the phase change when field is scanned from 0 mT up. It was reported that the LT-SkL phase usually transits from the tilted conical phase instead of from conical phase directly. They both exist near H_{C2}. Because of the presence of those new phases, H_{C2} is first increasing with temperature at low temperature, which is different with other crystallographic orientations. When the temperature is above about 20 K, H_{C2} decreases with increasing temperature.

Cooling down the chiral magnets through the HT-SkL phase with fast cooling rate is known as a method to quench the meta-stable skyrmion phase down to low temperature [131–134] and extend the phase boundary of HT-SkL phases to relatively low temperature. The square lattice of SkL was found to evolve from the meta-stable hexagonal lattice in MnSi and a thin slice of Cu_2OSeO_3 fabricated by focus ion beam etching [132, 134]. The fast cooling method always works in thin-plate or lamella shape CSO samples [95, 134, 135]. However it is not clear yet if it has the same effect on bulk samples with different crystallographic orientations. The results varied in different reports [94, 130, 131, 136].

Multiple techniques were reported for investigating the phase diagram of chiral magnets such as ac-susceptibility [36, 39–41, 137], transverse field (TF) muon-spin rotation (μ+SR) [43], magnetic diffraction techniques like small-angle neutron scattering (SANS) [36, 41, 44, 94, 121, 138], resonant elastic X-ray scattering (REXS) [91], real-space imaging by Lorentz transmission electron microscopy (LTEM) [37–39, 41, 44, 124, 137, 139] and magnetic force microscopy (MFM) [42, 91]. Microwave excited spin dynamics in chiral magnet were determined by magnetic phases and vice verse. They can reveal the phase transitions consistent with the techniques mentioned above [80–87, 140]. However, micrometer-sized multi-domains are often formed in the bulk chiral magnets [91, 92] and they experience different local effective fields. Together with the contributions from sample boundaries, complex spin dynamic spectra are formed [86]. A scanning technique resolving locally the spin excitations is highly demanded for magnonics research in order to sort out the relations between magnons and magnetic textures. Furthermore, this technique is helpful for exploring hidden phases in bulk samples especially for those who contribute weakly to the magnetic diffraction techniques and collective spin excitations.

1.2.2 Multilayers

Inversion symmetry is broken in magnetic multilayers when the magnetic layers are adjacent to normal metals with different spin-orbit couplings. Interfacial DMI arises at the interfaces [45–48]. It supports the formation of isolated N*é*el-type skyrmions as illustrated in Fig. 1.3. Due to the multilayers extremely thin thickness and strong spin-orbit couplings, the losses for magnetization dynamics are expected to be high. So it is detrimental for investigations on spin dynamic properties in multilayers with interfacial DMI. Recent reports on metal/thulium iron garnet $Tm_3Fe_5O_{12}$ structure and ultra-thin yttrium iron garnet $Y_3Fe_5O_{12}$ (YIG) with interfacial DMI created new attentions [141–144]. Especially in the 7-nm thick YIG, spin wave propagation was addressed up to 2 um length [144]. However there is not yet a direct evidence on skyrmion observations in those materials.

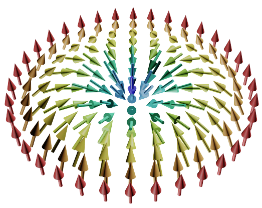

Figure 1.3 – **N*é*el type skyrmion.**

We searched for a room-temperature skyrmion hosting multilayered material with low Gilbert damping. Amorphous Fe/Gd multilayers attracted our interest because of the lack of magnetocrystalline anisotropy and the low damping in the system [50]. At room temperature stripe-shape domains, dipole skyrmions and dipole skyrmion lattices are formed thanks to the perpendicular magnetic anisotropy (PMA) and the dipole-dipole interaction [49, 50, 52]. We simulate the magnetic phases with micromagnetic simulations using Mumax3 [145]. Parameters are referred to the pioneering publication [50]. The magnetization figures are plotted in Fig. 1.4. Phase images are arranged in the order of out-of-plane magnetic field scanning up from 0 mT. The ground state at zero field consists of stripe-shape domains as shown in (a). They gradually evolve into the mixed states of stripe-shape domains, type I bubbles and type-II bubbles. The texture marked by the dashed circle is a type-II bubble [146] which hosts a skyrmion number of 0. It is topologically trivial. It was firstly recognized as a biskyrmion (a bound state of two skyrmions) but was proved to be a type-II bubble later [49]. In the following, we call this type of texture as bubble. The texture marked by the solid circle is a type-I bubble and also called dipole skyrmion whose skyrmion number is +1. In the following we call this texture as dipole skyrmion. When the field strength increases, the stripe domains break into the skyrmions from the tail and into chains of bubbles from the body. The bubbles will further transform into skyrmions when the field further increases. Hexagonal lattices of dipole skyrmions are reached. The Fe/Gd multilayers get fully saturated at nearly 200 mT to 400 mT depending on the thickness, repetition of the multilayers and the induced PMA strength.

Skyrmion configurations in Fe/Gd multilayers are not identical to either Bloch- or Néel-type skyrmions but more similar to a mixed states [50, 52]. We plot the spin configuration of the top surface, middle layer and bottom surface of the skyrmions in Fig. 1.4 (b). Both the top and bottom surfaces are comparable to Néel-type skyrmion and the middle is comparable to a Bloch-type skyrmion.

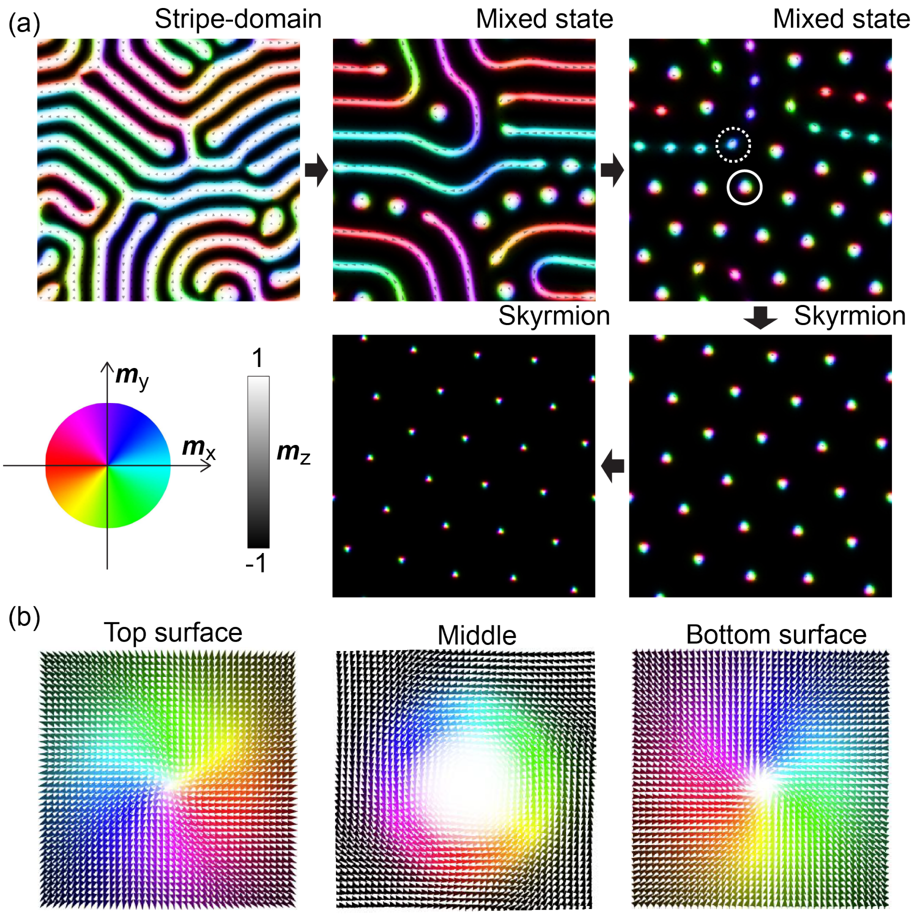

Figure 1.4 – **Phase evolution in Fe/Gd multilayers from micromagentic simulation.** (a) The phase evolution from stripe-domain to skyrmion states with increasing applied field. (b) Illustration of dipole skyrmions in Fe/Gd multilayers with PMA. Black arrows represent spin directions. For both (a) and (b), the hue, saturation and value color circle represents in-plane magnetization. Black and white color bar represents out-of-plane magnetization.

1.2.3 Other Materials

Besides CSO, Bloch-type skyrmions were reported to be hosted by non-centrosymmetric bulk magnets such as MnSi [36, 40, 132, 138], FeGe [38, 147, 148], FeCoSi [37] and Co-Zn-Mn alloys [44]. They are stabilized all by bulk DMI. At the same time, skyrmions and magnetic bubbles in centrosymmetric bulk mangets where DMI was absent were observed. For instance, Bloch-type SkL were found in centrosymmetric magnets such as Gd_2PdSi_3 and $Gd_3Ru_4Al_{12}$ because of Ruderman-Kittel-Kasuya-Yosida (RKKY) interaction [149, 150]. Four-spin exchange interactions can also dominate the Bloch-type SkL formation and it was found in the itinerant magnet $Y_3Co_8Sn_4$ [151]. Anti-skyrmions have the opposite skyrmion number -1 and have been discovered in Heusler materials [152, 153], $MnSc_2S_4$ (fractional antiferromagnetic skyrmion lattice) [154], and Ir-doped Fe/Gd multilayers [155].

1.3 Magnetization Dynamics

1.3.1 Equation of Motion

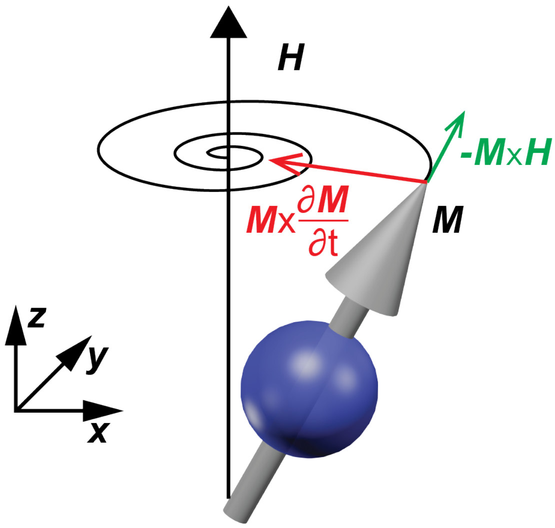

Figure 1.5 – **Illustration of the magnetization precession.**

The equation of motion describing magnetization dynamics was proposed by Landau and Lifshitz [156]:

$$\frac{\partial \boldsymbol{M}}{\partial t} = -\gamma \boldsymbol{M} \times \mu_0 \boldsymbol{H}. \tag{1.19}$$

γ is the gyromagnetic ratio. This expression for the precession of the magnetization vector $\boldsymbol{M}$ does not involve magnetic losses. One important property of Eq. (1.19) is that the magnitude of $\boldsymbol{M}$ is conserved [96]:

$$\frac{\partial \boldsymbol{M}^2}{\partial t} = 0. \tag{1.20}$$

When dissipation is considered, the equation of motion is modified into the well-known Landau-Lifshitz-Gilbert (LLG) equation [157]:

$$\frac{\partial \boldsymbol{M}}{\partial t} = -\gamma \boldsymbol{M} \times \mu_0 \boldsymbol{H} + \frac{\alpha}{M} \boldsymbol{M} \times \frac{\partial \boldsymbol{M}}{\partial t}. \tag{1.21}$$

Here α is the Gilbert damping coefficient. Considering the static and dynamic components, the magnetization is rewritten as

$$\boldsymbol{M} = \boldsymbol{M}_0 + \boldsymbol{m} \tag{1.22}$$

and the effective field as

$$\boldsymbol{H} = \boldsymbol{H}_0 + \boldsymbol{h}, \tag{1.23}$$

where $\boldsymbol{m}$ and $\boldsymbol{h}$ are the dynamic components. The illustration of the precession is sketched in Fig. 1.5. Equation (1.21) can be linearized as

$$i\omega \boldsymbol{m} = -(\gamma \boldsymbol{m} \times \mu_0 \boldsymbol{H}_0 + \gamma \boldsymbol{M}_0 \times \boldsymbol{h}) + \frac{i\alpha\omega}{M_0} \boldsymbol{m} \times \boldsymbol{M}_0 \tag{1.24}$$

when $|\boldsymbol{m}| << |\boldsymbol{M}|$ and $|\boldsymbol{h}| << |\boldsymbol{H}|$. Three-dimensional vectors of dynamic components are

$$\begin{aligned} \boldsymbol{m} &= m_x \boldsymbol{x} + m_y \boldsymbol{y} + m_z \boldsymbol{z}, \\ \boldsymbol{h} &= h_x \boldsymbol{x} + h_y \boldsymbol{y} + h_z \boldsymbol{z}, \end{aligned} \tag{1.25}$$

and $m_z = 0$, $h_z = 0$. So Eq. (1.25) is equivalent to [96]:

$$\begin{aligned} i\omega m_x + (\omega_H + i\frac{M_0}{M}\alpha\omega) m_y &= \gamma M_0 \mu_0 h_y, \\ i\omega m_y + (\omega_H + i\frac{M_0}{M}\alpha\omega) m_x &= \gamma M_0 \mu_0 h_x, \end{aligned} \tag{1.26}$$

where $\omega_H = \gamma \mu_0 H_0$. The high-frequency magnetic susceptibility describing the time-dependent relations is written in a non-symmetric second-rank tensor firstly presented as Polder tensor $\overleftrightarrow{\chi}$ [158]

$$\overleftrightarrow{\chi} = \begin{vmatrix} \chi & i\chi_a & 0 \\ -i\chi_a & \chi & 0 \\ 0 & 0 & \chi_\parallel \end{vmatrix} \tag{1.27}$$

where $\chi_\parallel$ is either zero or a very small non-resonant value when the ferromagnets are saturated [96]. In the case of the LLG equation, the solution of the linearized equations Eq. (1.26) is the

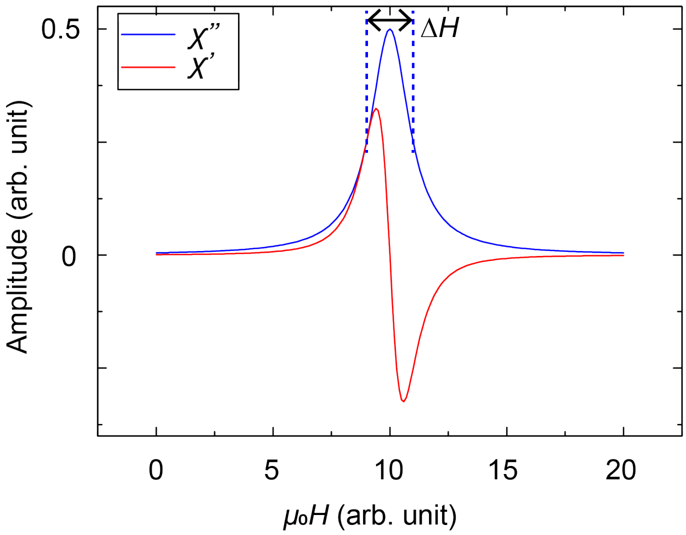

Figure 1.6 – **Real and imaginary parts of the magnetic susceptibility tensor.**

tensor $\overleftrightarrow{\chi}$ projected onto coordinate axes as $\boldsymbol{m} = \overleftrightarrow{\chi}\,\boldsymbol{h}$ and

$$\begin{aligned}
\chi' &= \frac{\gamma M_0 \omega_H [\omega_H^2 - (1-\alpha^2)\omega^2]}{[\omega_H^2 - (1+\alpha^2)\omega^2] + 4\alpha^2\omega^2\omega_H^2},\\
\chi'' &= \frac{\alpha\gamma M_0 \omega [\omega_H^2 + (1+\alpha^2)\omega^2]}{[\omega_H^2 - (1+\alpha^2)\omega^2] + 4\alpha^2\omega^2\omega_H^2},\\
\chi'_a &= \frac{\gamma M_0 \omega [\omega_H^2 - (1+\alpha^2)\omega^2]}{[\omega_H^2 - (1+\alpha^2)\omega^2] + 4\alpha^2\omega^2\omega_H^2}, and\\
\chi''_a &= 2\alpha\gamma M_0 \omega^2 \omega_H,
\end{aligned} \tag{1.28}$$

The real and imaginary parts are sketched in Fig. 1.6. The imaginary part can be normalized into a Lorentzian peak shape. For the eigenmodes of oscillation we take the damping $\alpha = 0$ [96]. For an isotropic ferromagnet, the resonance is at

$$\omega_r = \sqrt{\omega_H(\omega_H + \omega_M)} \tag{1.29}$$

with $\omega_M = \gamma\mu_0 M_0$.

Width of the Lorentz resonance curve is defined as intervals between ω or H_0 [96]

$$\begin{aligned}
\Delta\omega &= 2\alpha\omega, \text{and,}\\
\mu_0 \Delta H &= \frac{2\alpha\omega}{\gamma}
\end{aligned} \tag{1.30}$$

In the real experiments, extra broadening of the peak may influence the linewidth but their dependence on ω are still related only to the effective damping parameter. It can be estimated using [159]:

$$\delta f = \frac{\gamma}{2\pi}\mu_0 \Delta H + 2\alpha_{\mathrm{eff}} f. \tag{1.31}$$

Here, $f = 2\pi\omega$.

1.3.2 Ferromagnetic Resonances

Ferromagnets are usually anisotropic due to e.g. shape and magnetocrystalline anisotropy. The resonance frequency fro uniform precession, i.e. ferromagnetic resonance (FMR) is given by the Kittel formula [160]

$$\omega_r = \sqrt{[\omega_H + (N_x - N_z)\omega_M][\omega_H + (N_y - N_z)\omega_M]} \tag{1.32}$$

For example, in an infinitely large cylinder where the field is applied along $\boldsymbol{z}$ and the cylinder, the magnetization is aligned along the cylinder as well. Here $N_x = N_y = \frac{1}{2}$ and $N_z = 0$. The ferromagnetic resonance formula is simplified to be $\omega_r = \omega_H + \frac{\omega_M}{2}$.

The magnetocrystalline anisotropy will be accounted by an effective anisotropy field $\boldsymbol{H}_a$. In the saturated state of a ferromagnet with cubic anisotropy when $\boldsymbol{M}$ is well aligned with $\boldsymbol{H}$ the effective fields are [97]

$$\begin{aligned}
|\boldsymbol{H}^{\langle 100\rangle}| &= H_0 + \frac{2K_{C1}}{M_0}, \\
|\boldsymbol{H}^{\langle 110\rangle}| &= \sqrt{(H_0 - \frac{2K_{C1}}{M_0})(H_0 + \frac{K_{C1}}{M_0} + \frac{K_{C2}}{2M_0})}, \; and \\
|\boldsymbol{H}^{\langle 111\rangle}| &= H_0 - \frac{4K_{C1}}{3M_0} - \frac{4K_{C2}}{9M_0},
\end{aligned} \tag{1.33}$$

where K_{C1} and K_{C2} are the first and second order of cubic anisotropy. $\boldsymbol{M}$ is aligned well with $\boldsymbol{H}$ if $\boldsymbol{H}$ is parallel to easy or hard axes.

In the thin film with PMA, Kittel formula is in the format of [161]:

$$\omega = \gamma(\mu_0 H + \mu_0 M_{\mathrm{eff}}). \tag{1.34}$$

Here $\mu_0 M_{\mathrm{eff}} = \mu_0 M_{\mathrm{S}} - 2K_{\mathrm{U}}/M_{\mathrm{S}}$ is the effective magnetization consisting of both shape anisotropy and perpendicular magnetic anisotropy.

1.3.3 Spin Waves

Dispersion relations

For FMR, spins are oscillating with the same phase. For spin waves, spins are oscillating with a regular phase difference as shown in Fig. 1.7 (b). Wavelength λ is defined as the 2π phase difference, and the wavevector is $k = 2\pi/\lambda$. The quantum of a spin wave is called magnon.

In an unbounded ferromagnet, where the wavevector of a spin wave k and the static magnetization $\boldsymbol{M}_0$ are given as shown in Fig. 1.8, the dispersion relation of bulk spin waves [96, 162]

$$\omega = \sqrt{(\omega_H + A\omega_M k^2)(\omega_H + A\omega_M k^2 + \omega_M \sin^2\theta_k)} \tag{1.35}$$

where A is the exchange constant.

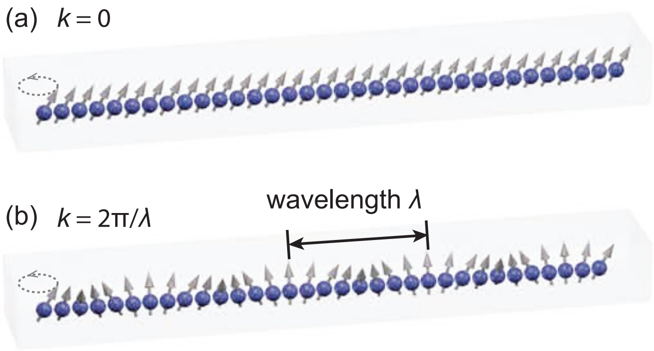

Figure 1.7 – **Schematic diagram of spin oscillation with/without phase difference.** (a) FMR. (b) Spin waves with finite wavevector k.

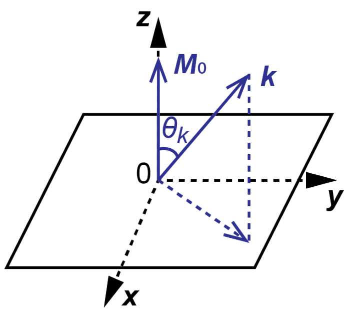

Figure 1.8 – **Geometry of the spin wavevector in an unbounded ferromagnet.**

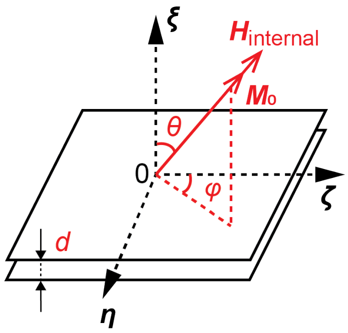

Figure 1.9 – **Geometry of a bounded thin film.**

When considering both the dipole and exchange interactions in the mixed exchange boundary conditions (surface spin pinning conditions) of a thin film (Fig. 1.9), wavevector of the spin waves are defined by $k^2 = k_\xi^2 + \kappa_n^2$. k_ξ is the out-of-plane component of the wavevectors and κ_n is the in-plane component. The dispersion relations reads [13]

$$\omega_n = \sqrt{(\omega_H + A\omega_M k^2)(\omega_H + A\omega_M k^2 + \omega_M F_{nn})}, \tag{1.36}$$

with

$$F_{nn} = P_{nn} + \sin_2\theta(1 - P_{nn}(1+\cos^2\phi) + \omega_M \frac{P_{nn}(1 - P_{nn}\sin^2\phi)}{\omega_H + A\omega_M k_n^2}) \tag{1.37}$$

and

$$\begin{aligned} P_{nn} &= \frac{k_\xi d}{2} \text{ when } n = 0 \\ P_{nn} &= \frac{(k_\xi d)^2}{n^2\pi^2} \text{ when } n > 0 \text{ and } n \text{ is an integer.} \end{aligned} \tag{1.38}$$

d is the thickness of the film.

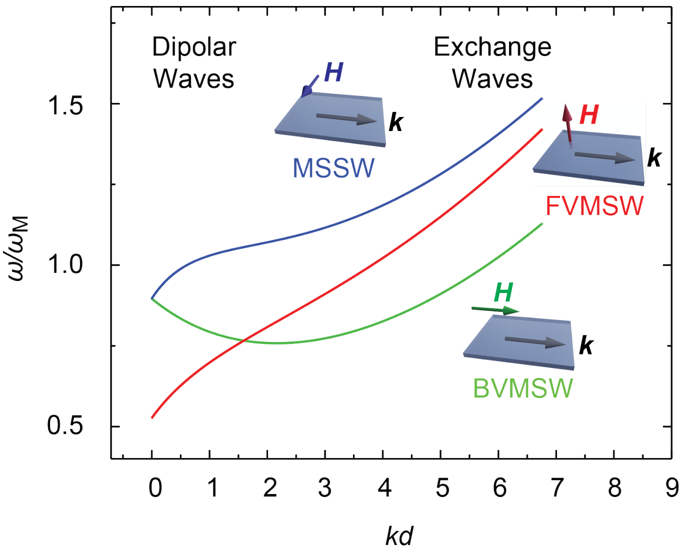

Figure 1.10 – **Dispersion relations of spin waves in thin films.** They are calculated using the parameters of yttrium ion garnet from Ref. [163]. Parameters are listed in Appendix 1.1.1.

There are three modes of spin waves in thin films depending on the relative direction between the effective magnetic field and the spin wave wavevector (Fig. 1.10): the magnetostatic surface spin wave (MSSW), backward volume magnetostatic spin wave (BVMSW) and forward volume magnetostatic spin wave (FVMSW). When k is small, the anisotropic dipole-dipole interaction dominates. When k is large, the isotropic exchange interaction dominates.

By integrating nanoscale magnetic arrays on ferromagnetic thin films, short-waved spin waves can be excited via the magnonic grating coupler (GC) effect [164–167]. Microwave antennas placed or fabricated on top of ferromagnetic thin films are often used for spin wave excitation. When the radio-frequency currents injected in the antenna induce a dynamic field $\boldsymbol{h}_{\rm rf}$, there is the torque applied on the magnetization $\tau = \boldsymbol{M} \times \mu_0 \boldsymbol{h}_{\rm rf}$ to excite spin precessions. If $\boldsymbol{h}_{\rm rf}$ is inhomogeneous, its distribution contributes to define the excited spin-wave wavevector k_1. When a periodic magnetic array is embedded underneath the microwave antennas, the spin wave excitation field is modified periodically according to the array structure because of the stray fields. Hence it can modify the spin-wave wavevector by adding the reciprocal lattice vectors on k_1. So far, it has been reported that a spin wave of wavelength down to 50 nm was excited by a one-dimensional GC on yttrium ion garnet thin films [166].

Spin waves in magnets with bulk Dzyaloshinskii-Moriya interaction

As a consequence of the asymmetric exchange interaction, DMI introduces non-reciprocity in the spin wave dispersion relations. Interfacial DMI modifies the MSSW [74–77] and bulk DMI modifies the BVMSW in both non-collinear and collinear states [72, 73, 78, 79, 90, 168, 169]. Therefore magnets with DMI can serve as non-reciprocal microwave devices [78]. Here we focus on the BVMSW mode in chiral magnets with bulk DMI. The dispersion relation of BVMSW mode reads (1.36) is

$$f = \frac{1}{2\pi}\sqrt{(\omega_H + A\omega_M k^2)[\omega_H + A\omega_{\rm M} k^2 + \omega_M(1 - \frac{kd}{2})]} \tag{1.39}$$

Here, k is the wavevector of spin waves. A is the exchange constant. d is the thickness of the sample. BVMSW modes with and without DMI in FP states are sketched depicted in Fig. 1.11. When considering only the exchange interactions, the dispersion relation is shifted with respect to $k = 0$. When considering both the exchange and dipole interactions, the dispersion relation looks different as sketched in Fig. 1.11 (b). The frequency difference between the conventional BVMSW and DMI modified BVMSW dispersion relations is expressed as [73]

$$\Delta f = \frac{4\gamma M_S k D}{2\pi} \tag{1.40}$$

where D is the DMI constant in the unit of length.

In the non-collinear states, two spin dynamics modes of helical and conical phase, and three spin dynamics modes of SkL were prominent in many experiments [66, 82–87, 93, 140, 170]. These mainly observed branches are sketched in Fig. 1.12 stimulated by Refs. [66, 170]. It is notable that there is an abrupt jump of the frequency when entering and leaving the SkL phase. This jump is attributed to a reorientation of pitch vectors $\boldsymbol{q}$ (compare with Fig. 1.2) and a modified effective field $\boldsymbol{H}_{\rm eff}$. When the system transforms from conical phase to FP phase, there is no frequency jump because the pitch vector $\boldsymbol{q}$ is already aligned with the applied field and the spin orientation changes adiabatically. Still, the mode branches behave non-monotonically at $H_{\rm C2}$. We will consider frequency jumps and non-monotonic variations of resonance frequencies as relevant signatures to identify phase transitions via spin dynamics experiments.

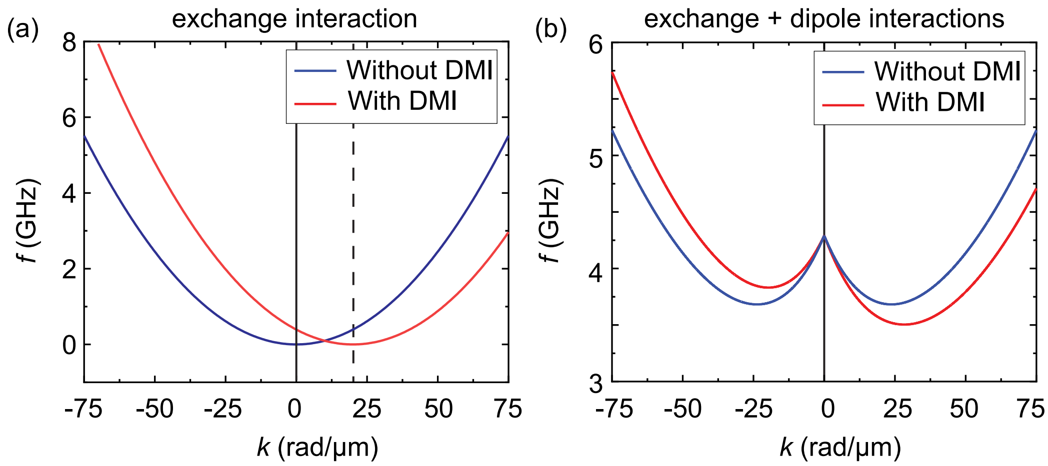

Figure 1.11 – **Dispersion relations of BVMSW spin waves with bulk DMI.** (a) With only exchange interaction considered. (b) With both exchange and dipole interactions considered.

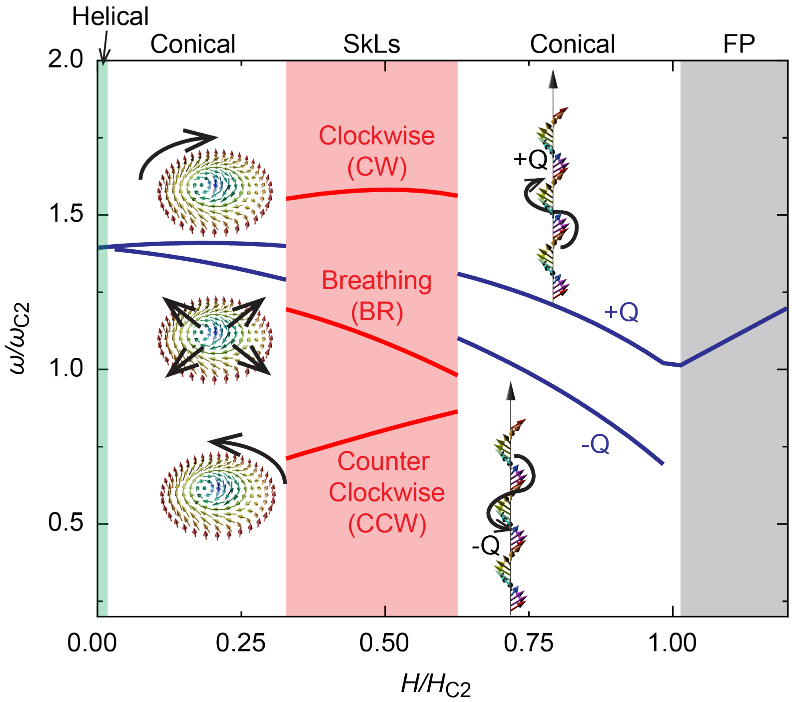

Figure 1.12 – **Sketch of the spin waves spectra of chiral magnets assuming uniform excitation fields.** Insets illustrate the spin precessional motion for +Q, -Q and skyrmion lattice modes. Note that we do not depict any higher order modes in this sketch or modes excited by non-uniform fields.

In the helical and conical states, the two modes +Q and -Q are often observed. In case of the

+Q mode, the spins oscillate with a phase difference and form a spin wave winding along $\boldsymbol{q}$ up. In the case of the -Q mode, the phase of the spin wave evolves in the opposite direction as illustrated inset the Fig. 1.12. In the skyrmion phase, three prominent modes have been identified as counter clockwise (CCW), clockwise (CW) and breathing (BR) modes [82]. They have been excited with radio-frequency magnetic fields and special selection rules of the excitation field $\boldsymbol{h}_{\mathrm{rf}}$ with respect to the static field $\boldsymbol{H}_0$ have been [82, 83]. When $\boldsymbol{h}_{\mathrm{rf}} \perp \boldsymbol{H}_0$, $\boldsymbol{h}_{\mathrm{rf}}$ is in-plane of the skyrmions and excites the CCW and CW modes. When $\boldsymbol{h}_{\mathrm{rf}} \parallel \boldsymbol{H}_0$, $\boldsymbol{h}_{\mathrm{rf}}$ is perpendicular to the plane of skyrmions and excites only the BR mode. When both parallel and perpendicular components are present, all three modes are excited.

In chiral magnets, non-collinear states are formed usually as lattices below T_{C}. The resonance modes mentioned above were excited in the lattices and they are the fundamental modes relevant for helical, conical and SkL states. Higher order modes were investigated in CSO [86]. Here, the 2nd and 3rd order of confined modes in helical and conical phase were reported and occurred at high frequencies up to 20 GHz. The fundamental modes in CSO reside between about 1 and 5 GHz [83].

Spin dynamics of CSL has been reported in monoaxial chiral magnet $CrNb_3S_6$ both theoretically and experimentally [171–173]. Two type of resonance mode were excited: a Pincus mode and a Kittel mode [173]. The Pincus mode originates from the surface spins and the Kittel mode lays on the interior spins inside CSL. By changing the angles between h_{rf} and c-axis, different modes are excited. In sample with pinning surface, e.g. thin lamella, Pincus mode are always excited despite the h_{rf} direction. $h_{\mathrm{rf}} \perp c$-axis is in charge of the Kittel mode. Their simplified dispersion relations at zero applied field are expressed as [173]

$$\omega_{\mathrm{Kittel(CSL)}} = \sqrt{k^2[k^2 - q_s^2 + 2q_s\frac{D}{A}]}, \tag{1.41}$$

$$\begin{aligned} \omega_{\mathrm{Pincus}} =& \sqrt{k\tan(\frac{kd}{2})(1+\frac{Dq_s}{A}) - \frac{k^2}{2} - \frac{H_S\cos\phi_0 d}{2}} \\ &\times \sqrt{k\tan(\frac{kd}{2}) - \frac{k^2}{2} + \frac{q_s^2}{2} - \frac{Dq_s}{A} - \frac{H_S\cos\phi_0 d}{2}}. \end{aligned} \tag{1.42}$$

in which k is the spin wavevector, d is the sample thickness which is equivalent to the total length of CSL structures, D and A are DMI and exchange constants, H_s is the pinning field strength on the surfaces, ϕ_0 is the angle between spin orientations on the surface and the applied field direction. q_s is vector determined by the lattice length of CSL L_{CSL} as indicated in Fig. 1.1 (b). It is defined as $q_s = \frac{2\pi}{L_{\mathrm{CSL}}}$. When considering the applied magnetic fields, the frequency versus field relation are in dome shape for Pincus mode. For Kittel mode, frequency decrease with increasing field strength in almost linear manner [173]. There is not yet any report on CSL dynamics in skyrmion hosting chiral magnets.

Spin waves in multilayers with perpendicular magnetic anisotropy

In the following we outline collective spin excitations reported for Fe/Gd multilayers [50]. They were explored by means of micromagnetic simulations. Four modes have been observed in the dipole skyrmion lattice phase. The spin-precessional motion of the skyrmions is complex and varies from the top to the bottom surface of the multilayers. The four different dynamic patterns are sketched in Fig. 1.13 which depend on frequencies and dynamic field directions. The external field $\boldsymbol{H}_z$ is applied out-of-plane. When the dynamic excitation field $\boldsymbol{h}_{\mathrm{rf}}$ is perpendicular to $\boldsymbol{H}_z$, the three dynamic modes occur between about 1.3 GHz and 2.6 GHz near $\mu_0 H_z$ = 200 mT (they vary with magnetic field and material parameters such as PMA strength). When $\boldsymbol{h}_{\mathrm{rf}} \perp \boldsymbol{H}_z$, from low to high frequency three modes are described as follows

(i) at f = 1.3 GHz: BR mode from top surface to bottom surface, through the middle layers. Their breathing axes are sketched by red arrows. In top surface, the BR axis follow the $\boldsymbol{h}_{\mathrm{rf}}$ direction. In the middle layer and bottom surface, BR axes have a tilt angle of 135° compared to the top surface motion. BR motion in top surface is in anti-phase with BR motions in middle layer and bottom surface.

(ii) at f = 1.8 GHz: CW mode + BR mode. The top surface and the middle layer are in BR mode following the axes along $\boldsymbol{h}_{\mathrm{rf}}$ direction. They are in phase. The bottom surface is in CW motion.

(iii) at f = 2.6 GHz CW mode + BR mode with tilt. The top surface is in BR mode a bit tilted from $\boldsymbol{h}_{\mathrm{rf}}$ direction. The middle layer is in BR mode following $\boldsymbol{h}_{\mathrm{rf}}$ direction and in phase with top surface motion. The bottom surface is in CW motion.

When the chirality of skyrmion changes, the top and bottom surface exchange their motions and the middle layer keeps the same.

When $\boldsymbol{h}_{\mathrm{rf}}$ is parallel to $\boldsymbol{H}_z$, only one mode were found near 2.6 GHz. It is at the same frequency with mode (iii) of $\boldsymbol{h}_{\mathrm{rf}} \perp \boldsymbol{H}_z$. This time, there are BR modes with perpendicular axes on all surfaces and layers. They are not perfectly in phase and same in BR direction. In order to separate motions at different time, we use solid arrows for the motion in half π phase and dashed arrows for motions in the other half π phase.

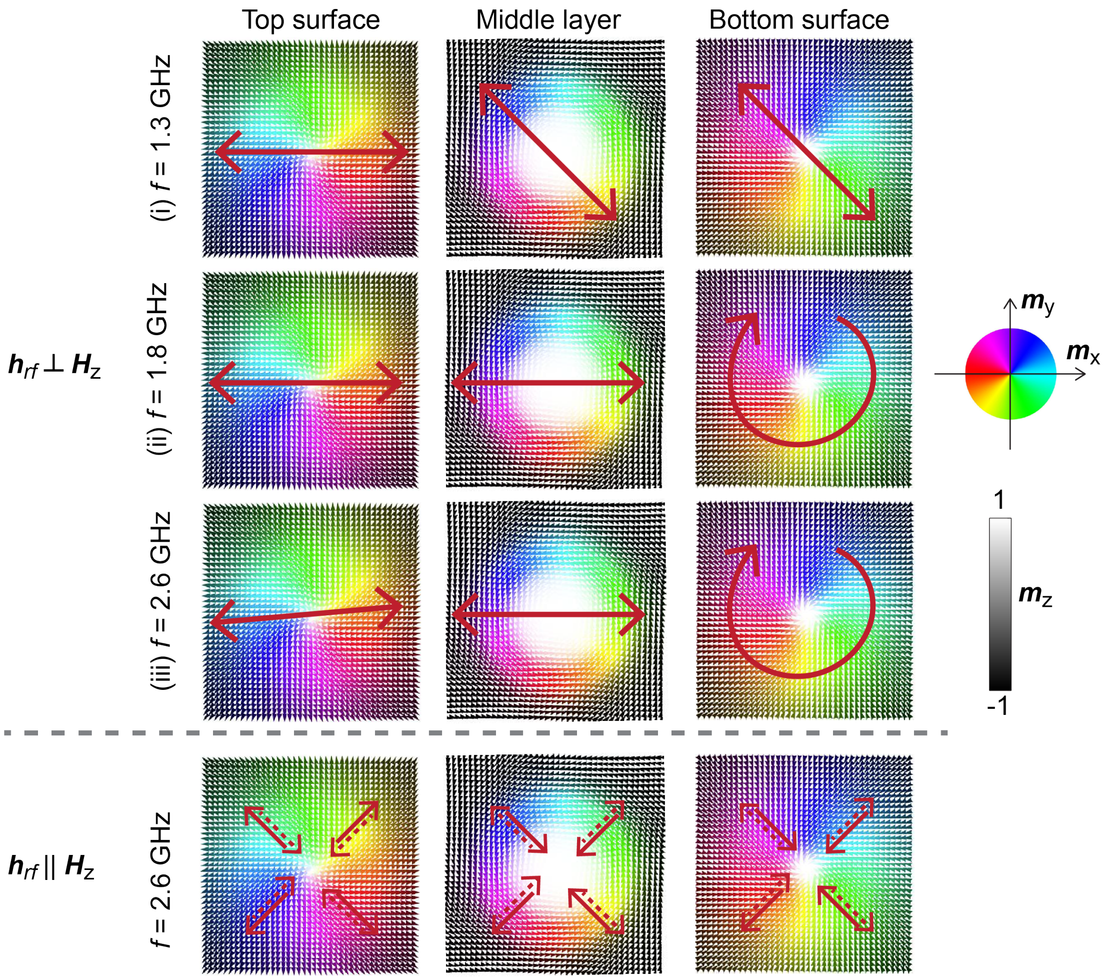

Figure 1.13 – **Sketch of the dynamic motions of dipole skyrmions in Fe/Gd multilayers.** They are the dynamic motions near $\mu_0 H_z = 200$ mT. Red arrows indicate the motions of different position in the layer at different frequencies. The hue, saturation and value color circle represents in-plane magnetization. Black and white color bar represents out-of-plane magnetization.

2 Experimental Setup and Methods

In this chapter we introduce the working principles and parameters of the experimental setups and methods. It is organized in 4 sections. In section 2.1, the all-electrical spin-wave spectroscopy is introduced and it is used for the measurements in section 4.1, 5.1.2, 5.3 and 5.4. In section 2.2, the Brillouin light scattering technique and the integrated cryostat are introduced, which are used for the measurements in section 4.2 and 4.3. In section 2.3, scanning transmission X-ray microscopy 'MAXYMUS' at Bessy II beamline is outlined for the measurements presented in section 5.2, 5.3 and 5.4. In the last section of this chapter 2.4, the magnetic field versus temperature histories are described which are used to control the magnetic states in CSO reported in section 4.2 and 4.3.

2.1 All-Electrical Spin-Wave Spectroscopy

The setup for all-electrical spin-wave spectroscopy consists of a vector network analyzer (VNA), microwave cables and connectors (or microwave probes), coplanar waveguides (CPW) (Fig. 2.1), magnetic field coils and computer-controlled power supply. The 4-port VNA is utilized as both microwave signal generator and detector by using different ports. The magnetic field is controlled by dc-currents in coils with yokes or by permanent magnets.

In Fig. 2.1, we sketch how a radio-frequency (rf) current coming from port1 of the VNA is injected into a CPW in through-configuration. The microwave voltage signals in the CPW are detected in the opposite side by port 2. The dynamic magnetic field $\mathbf{h}_{\mathrm{rf}}$ (purple arrows) excite spins in the sample placed on top of the CPW. They absorb the rf energy when the spin-precession motion is in resonance. So the transmitted microwave signal is reduced. Corresponding spectra are collected at port2. At the same time, the spin resonance generates a reflection signal back to the port1. The VNA can collect both the transmission and reflection signals in the format of S-parameters S_{21} and S_{11} respectively. Port1 and port2 can be receiver and generator or vice versa. In order to measure microwave signals with high precision, impedance matching need to be taken into account. In the following, impedance matching, S-parameters and the design of CPWs will be discussed.

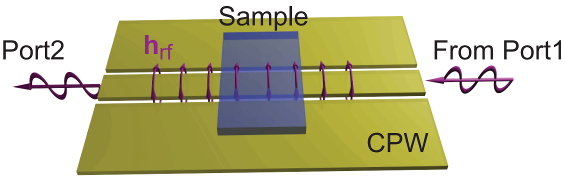

Figure 2.1 – **Coplanar waveguide with sample for all-electrical spin-wave spectroscopy.**

2.1.1 Impedance Matching

In all-electrical spin-wave spectroscopy, it is essential to avoid unintentional back-reflection of microwave power. Firstly when considering the direct current circuit, a simplified model of a power transfer circuit from a source (S) to the load (L) is shown in Fig. 2.2 (a). Here a source providing the voltage V_S has the resistance R_S. There is a load resistor R_L connected to the source. Voltage on the load is

$$V_L = \frac{R_L V_S}{R_L + R_S} \tag{2.1}$$

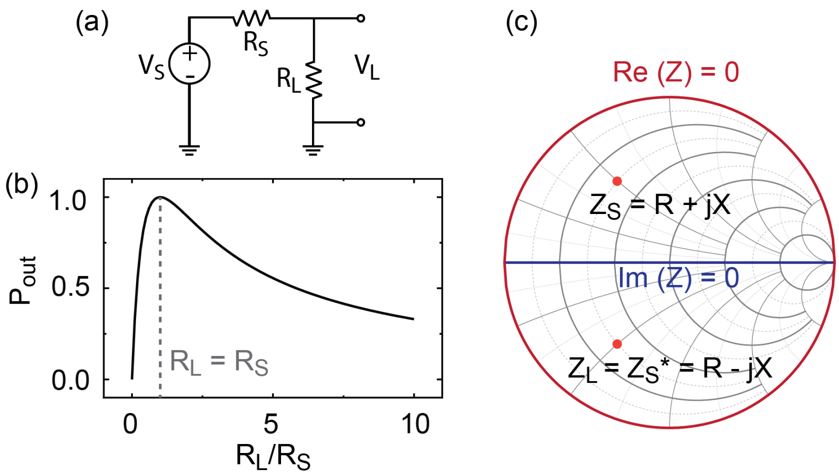

Figure 2.2 – **Power transfer and impedance matching.** (a) Direct current circuit diagram modeling power transfer from the source to a load. (b) Normalized output power on the load with respect to the ratio between R_L and R_S in direct current current. (c) Smith chart showing the conjugate matching of complex impedance in alternative current circuit. It is a winding format showing the real part and imaginary part of the impedance. Blue line represents zero imaginary part. Red circle represents zero real part.

The output power, which is the power on the load can be calculated

$$\begin{aligned} P_{\text{out}} &= \frac{V_1^2}{R_L} \\ P_{\text{out}} &= \frac{R_L V_S^2}{(R_S + R_L)^2} \end{aligned} \tag{2.2}$$

The maximum output power need to satisfy

$$\frac{dP_{\text{out}}}{dR_L} = 0 \tag{2.3}$$

whose solution is

$$R_L = R_S \tag{2.4}$$

The normalized P_{out} with respect to R_L/R_S is plotted in Fig. 2.2 (b). In the maximum when $R_L/R_S = 1$, 50 % of the power is transferred to the load.

When we consider the alternative current circuit, capacitance and inductance need to be considered via complex impedance $\widetilde{Z}$. The complex impedance of the source is $\widetilde{Z}_S = R + jX$. In order to achieve the highest power transfer, impedance matching is required as a conjugate matching (Fig. 2.2 (c)) so that

$$\widetilde{Z}_L = \widetilde{Z}_S^* = R - jX \tag{2.5}$$

For measurements conducted with VNA, calibrations are demanded to remove the systematic errors coming from the analyzer itself, cable and connector mismatch errors and the differences in cable lengths. Standard electrical components are provided from company to measure the error terms. Those terms are removed (to a large extent) from the data by specific calibration routines.

2.1.2 S-Parameters

Spin waves were detected in the format of S-parameters by the VNA. When considering a device under test (DUT) between port1 and port2, there are 4 S-parameters to be measured (Fig. 2.3) including the forward S-parameters

$$\begin{aligned} S_{11} &= \frac{\text{Reflected}}{\text{Incident}} = \frac{b_1}{a_1} \\ S_{21} &= \frac{\text{Transmitted}}{\text{Incident}} = \frac{b_2}{a_1} \end{aligned} \tag{2.6}$$

Here, a_i and b_i represent the emitted and received wave, respectively, at post i. The reverse S-parameters read

$$\begin{aligned} S_{22} &= \frac{\text{Reflected}}{\text{Incident}} = \frac{b_2}{a_2} \\ S_{12} &= \frac{\text{Transmitted}}{\text{Incident}} = \frac{b_1}{a_2} \end{aligned} \tag{2.7}$$

In our all-electrical spin-wave spectroscopy setup, the magnetic sample together with the CPW (like Fig. 2.1) is the DUT. Thus the S-parameters reflect the dynamic properties of the magnetic sample. Depending on the design of the CPW, different collective spin excitations are addressed (e.g. uniform precession versus spin waves with finite wavevector k).

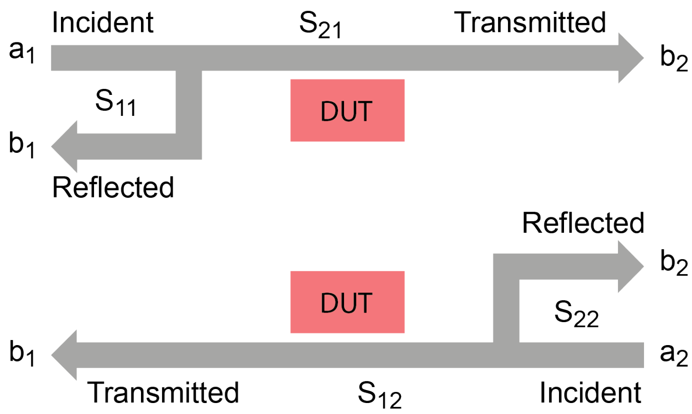

Figure 2.3 – **S parameters of VNA measurements.**

2.1.3 Coplanar Waveguides

In this thesis, we use the CPW named as 'through (thru) configuration'. Its diagram is plotted in Fig. 2.4. The CPW consists of one signal line in center and two ground lines aside. The signal line is used for carrying the rf current and the ground lines are used for shielding currents. The rf currents exist in the ground lines because of induction or the shortening between the signal line and ground lines. On the top and bottom surfaces of the CPWs, the radio-frequency magnetic field components $\boldsymbol{h}_{\mathrm{rf}}$ are parallel to the CPW surface plane. In the gaps of the CPW leads, $\boldsymbol{h}_{\mathrm{rf}}$ components are perpendicular to the CPW plane.

In the thru-configuration, there is only one CPW with all continuous lines (Fig. 2.4). We use this design for flip chip measurements. By changing the placement of the samples (on the signal line or across the gaps), $\boldsymbol{h}_{\mathrm{rf}}$ applied on the sample is different. It can also be fabricated directly on the magnetic materials. The reflected parameters S_{11} and S_{22} contain peaks at the magnetic resonance frequency. The transmitted parameters S_{21} and S_{12} contain dips at the same frequency where peaks appear in S_{11} and S_{22}. When the size of the CPW is comparable to or smaller than the magnetic samples, the excitation is non-uniform and inhomogeneous

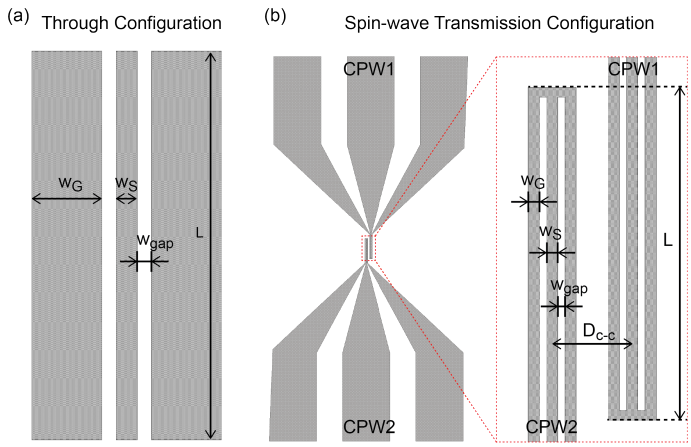

Figure 2.4 – **Design of CPWs.** The sketch of the (a) through (Thru) configuration CPW and (b) spin wave (SW) transmission configuration.

Table 2.1 – Table of parameters of CPWs design.

Labels	w_G (μm)	w_S (μm)	w_{gap} (μm)	L (μm)	Material
1.Thru	5000	1000	1000	16000	Cu
2.Thru	3000	1000	1000	5000	Ti (10 nm) / Au (150 nm)
3.Thru	295	20	12.38	7000	Ti (10 nm) / Au (150 nm)
4.Thru	2.1	1.7	1.6	120	Ti (10 nm) / Al (120 nm) /Cu (10 nm)
5.SW Trans.	2.1	1.7	1.6	80	Ti (10 nm) / Cu (120 nm) /Al (10 nm)

broadening can occur due to the accompanying wavevector distribution. When the size of the CPW is much smaller than the magnetic samples, the transferred wavevector k can be specified, by calculating the Fourier transform of the $\boldsymbol{h}_{\text{rf}}$ spatial distribution.

In the transmission configuration, there is a pair of CPWs: CPW1 and CPW2. They are connected to port1 and port2 respectively. They can be fabricated directly on the sample or on a substrate where a lamella can be flipped on them. The working principle are different from the through configuration. Here the reflected parameters S_{11} and S_{22} show the magnetic resonance excited near the CPWs. But the transmitted parameters S_{21} and S_{12} are no longer identical to reflected parameters. They represent the propagating spin waves from CPW1 to CPW2 or vice versa. The propagation only happens in the region between the micro-structured CPWs so they offer the dynamic properties of the magnetic materials between those two CPWs, e.g. the dispersion relations, group velocities and decay lengths. In this scenario, magnetic samples are often in larger dimension than CPWs so the spin wavevector k are defined from CPW. For all the CPWs designed and used in this thesis, their parameters are listed in Table. 2.1, such as the width of the signal line, ground lines and the gaps, etc.

2.2 Brillouin Light Scattering

2.2.1 Inelastic Brillouin Light Scattering

Brillouin light scattering (BLS) is an inelastic scattering when the incident photons and scattered photons do not have the same energy and momentum [174–176]. Scattering happens between the photon and quasi-particles in a media, such as phonons, polaritons and magnons. As shown in Fig. 2.5 (a), the energy difference of the incident light ω_{L} and the scattered light ω_{S} refer to the energy of the created quasi-particles ω_{Q} or annihilated quasi-particles. These energy differences are named as Stokes shift and anti-Stokes shift. At the same time, the momentum difference between $\hbar\boldsymbol{k}_{\mathrm{L}}$ and $\hbar\boldsymbol{k}_{\mathrm{S}}$ refers to the created quasi-particles momentum $\hbar\boldsymbol{k}_{\mathrm{Q}}$ (Fig. 2.5 (b)). During the scattering process, not only the creation of the quasi-particles but also the annihilation happens. So the conservation laws are

$$\hbar\omega_{\mathrm{L}} = \hbar\omega_{\mathrm{S}} \pm \hbar\omega_{\mathrm{Q}} \tag{2.8}$$

$$\hbar\boldsymbol{k}_{\mathrm{L}} = \hbar\boldsymbol{k}_{\mathrm{S}} \pm \hbar\boldsymbol{k}_{\mathrm{Q}} \tag{2.9}$$

The energy loss of the incident light donates to the Stoke peaks in the BLS spectrum and the energy gain donates to the anti-Stoke peaks in Fig. 2.5 (c).

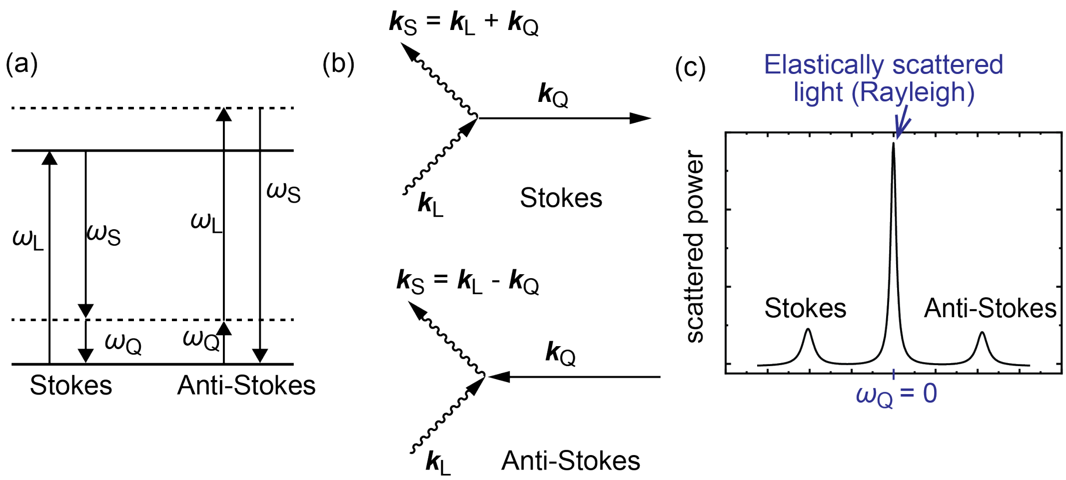

Figure 2.5 – **Schematic diagram of inelastic scattering and Brillouin scattering.** (a) and (b) Energy and momentum conservation of inelastic scattering between the incident light and quasi-particles. (c) The frequency spectrum of the Brillouin scattering.

This technique has been used to study both the thermal surface and bulk magnons [177, 178]. Here the BLS laser interacts with thermally excited spin fluctuations. When the medium is magnetic and scattering happens between photons and magnons, we can extract the frequency (energy) and the wavevector (momentum) of the magnons from BLS spectroscopy. The polarization of the scattered photons is rotated by 90 degree compared with the incident photon. The classical picture is that the magnons introduce a dynamic perturbation on the dielectric permittivity due to magneto-optical effect [179, 180]. The BLS signal intensity is proportional to the magneto-optical constant and the square of the dynamic magnetization amplitude locally at the scattering location.

The wavevector of magnons can be decomposed according to $\boldsymbol{k}_\mathrm{m} = \boldsymbol{k}_\parallel + \boldsymbol{k}_\perp$ where $\boldsymbol{k}_{||}$ is the magnon wavevector parallel to the sample surface and $\boldsymbol{k}_\perp$ is the one perpendicular to the sample surface. In thin films or the bulk samples in which the incident laser could not penetrate too much (penetration depth is much smaller than the laser wavelength), the translational invariance is broken on the perpendicular axis and the momentum conservation only holds for the in-plane component $\boldsymbol{k}_\parallel$ [179]. By changing the laser incident angle θ with respect to the normal axis, on thin films $\boldsymbol{k}_\parallel$ varies as $\boldsymbol{k}_\parallel = 2\boldsymbol{k}_\mathrm{L}\sin(\theta) = 2\frac{2\pi}{\lambda_\mathrm{L}}\sin\theta$. The wavevector $\boldsymbol{k}_\mathrm{m}$-dependent BLS measurements are based on this angle dependence [181]. In bulk samples where the light penetrates deep, both $\boldsymbol{k}_\parallel$ and $\boldsymbol{k}_\perp$ need to be considered [162]. Additional to the surface magnon, the bulk magnon is relevant and the dispersion relation Eq. 1.35 has been introduced in Section 1.3.3.

2.2.2 Cryogenic Micro-Focused Brillouin Light Scattering Setup

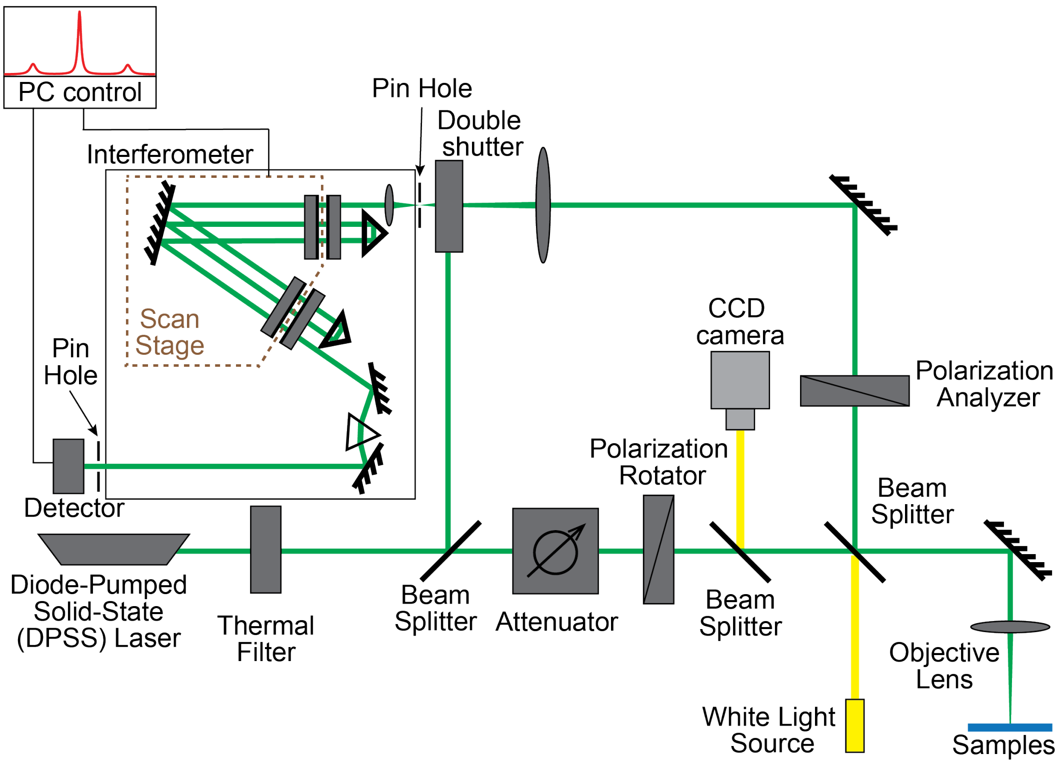

Figure 2.6 – **Schematic diagram of Brillouin light scattering.**

The micro-focused BLS setup is sketched in Fig. 2.6 [175, 180]. We use a monochromatic continuous-wave solid-state laser with a wavelength of $\lambda_\mathrm{L} = 532$ nm. It goes through a thermal filter to reduce side peaks. The following beam splitter allows to generate a reference light beam for the operation and calibration of the interfere work. The straight path of the laser is focused on the sample surface after going through an attenuator. By tuning the attenuator, we control the laser power incident onto the surface. The cross-polarized configuration is used to improve the signal-to-noise ratio and suppress the phonon peaks. Both the reference and scattered light beams are collected and processed in a six-pass Fabry–Perot interferometer TFP-2 (JRS Scientific Instruments). The pin holes work as the spatial filters. White light is also projected onto the sample through an objective lens by where the laser is focused with a view field of 50 μm × 50 μm. We use a Mitutoyo M Plan Apo SL 100x objective lens with NA = 0.55 (numerical aperture) and WD = 13 mm (working distance). The optical images are taken by a CCD camera so we can locate laser positions during the measurements. Combined with the piezoelectric stages underneath the sample, a scanning function is achieved to explore micro- and nanostructures.

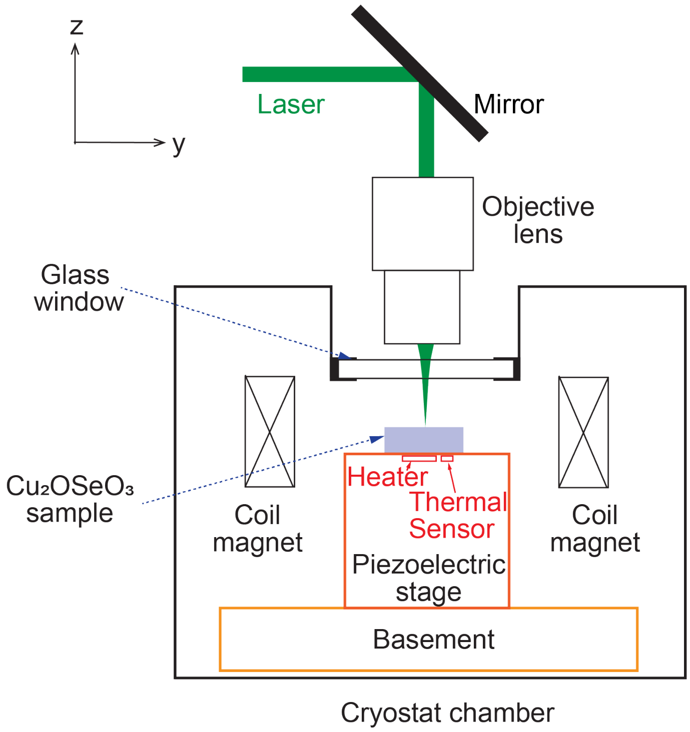

Figure 2.7 – **Schematic diagram of the cryostat installed on the BLS setup in incorporating a piezoelectric scanning stage.**

A cryostat with a closed-loop helium circle was integrated with the BLS setup for exploring spin dynamics at cryogenic temperatures (Fig. 2.7). The basement is cooled by the compressed helium gas down to about 4.5 K. It further cools down the whole chamber as a cold finger. Both the basement and the holder stage are made of Cu to guarantee good thermal conductivity. The sample is placed on top of the holder stage consisting of a three-axis piezo-positioner and the temperature controlling chip carrier. The controlling unit contains a thermal sensor and a heater. They are directly buried underneath the sample so the fast control of the sample temperature can be achieved by varying a proportional–integral–derivative controller. In this thesis we use the set nominal temperatures for all the discussions. Green laser is incident normal to the top surface of the sample and focused through a window. One pair of coil magnets were installed inside the cryostat chamber. They offer a bipolar magnetic field up to ± 0.5 T in the plane of the chip carrier.

2.2.3 Short-Waved Thermal Magnon Excitation in Brillouin Light Scattering in Cu_2OSeO_3

In the following, we illustrate the bulk magnon excitation in bulk shaped materials using BLS. We compare the BLS excited bulk magnon in a bulk shape Cu_2OSeO_3 (CSO) sample with the all-electrical spin-wave spectroscopy data in saturated states. This work was conducted together with the master thesis student Bin Lu in our lab.

Concerning the thermal magnon excitation in thin films by BLS, magnons have only the in-plane wavevectors following the momentum conservation law. In bulk samples, not only the in-plane but also the out-of-plane wavevectors are considered [162]. Especially for CSO, the green laser can penetrate through samples with millimeter thickness. Thus the out-of-plane wavevectors play an important role. In our setup, we use the objective lens with NA = 0.55 so the laser was focused within the range from -33° to 33° on the sample surface (Fig. 2.8).

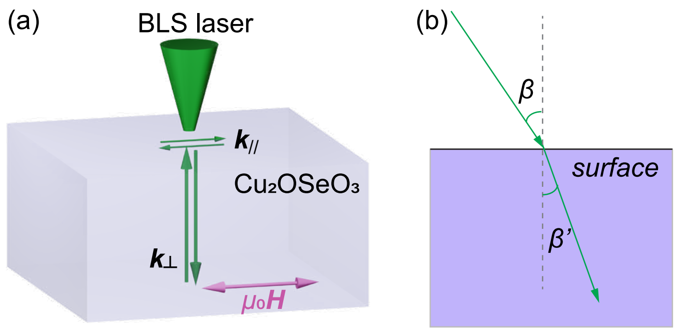

Figure 2.8 – **Configuration of bulk magnon excitation in BLS.** (a) Laser focusing on the CSO sample surface leading to different incident angles. (b) Sketch of the light refraction and scattering.

Bulk magnons excited in CSO sample have both in-plane wavevectors $\boldsymbol{k}_\parallel$ and out-of-plane wavevectors $\boldsymbol{k}_\perp$: $\boldsymbol{k}^2 = \boldsymbol{k}_\parallel^2 + \boldsymbol{k}_\perp^2$ [182]. From Snell's law we get

$$\frac{\sin\beta}{\sin\beta'} = \frac{n_{\mathrm{CSO}}}{n_{\mathrm{air}}} \tag{2.10}$$

Here, β is the angle of incidence and β' is the angle of refraction. $n_{\mathrm{air}} = 1$ and n_{CSO} are the refractive indexes of the air and CSO material, respectively. Considering the conventional momentum conservation, the wavelength and wavevector of magnons in CSO are defined as

$$\lambda = \frac{\lambda_L}{n_{\mathrm{CSO}}}$$
$$k = \frac{2\pi n_{\mathrm{CSO}}}{\lambda_L} \tag{2.11}$$

The objective lens mostly collect the back-scattered components, then $k = \sqrt{k_{\parallel} + k_{\perp}} = 2\frac{2\pi n_{\mathrm{CSO}}}{\lambda_L}$ along the refractive angle β'.

We conducted both all-electrical spin-wave spectroscopy and BLS spectroscopy on bulk CSO sample to compare the spin waves excitation. CSO sample B2 (in Table. 3.1) was fixed on the CPW (No.2 in Table. 2.1) in a way that the longer axis (500 μm) is perpendicular to the CPW lines. It was placed in the center of a 1-mm-wide signal line. So the excitation field $\boldsymbol{h}_{\mathrm{rf}}$ is mainly along the longer axis of CSO sample. The magnetic field $\boldsymbol{H}$ was applied along the CPW lines so $\boldsymbol{H} \perp \boldsymbol{h}_{\mathrm{rf}}$. The CSO sample was cooled down with zero field and we swept the magnetic field up. When the VNA measurements were conducted, the BLS laser was not focused on the sample. When the BLS data was collected, the microwave current was turned off. The extracted resonance frequencies at T = 20 K are shown in Fig. 2.9 as red squares (BLS) and blue squares (VNA).

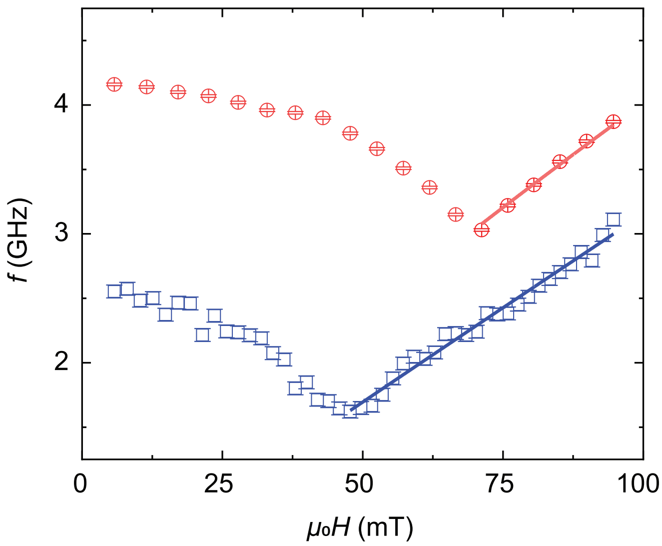

Figure 2.9 – **Resonance frequencies measured on bulk CSO at 20 K.** Red circles are the fitted resonance peaks from thermally excited BLS spectra using a Lorentz function. Blue squares are the fitted resonance peaks from all-electrical spin-wave spectroscopy using a Lorentz function. Error bars come from the fitting. The red line is fitted using the bulk magnon dispersion relation. The blue line is fitted using the Kittel formula.

In VNA measurement, the ferromagnetic resonance (FMR) was excited. The resonance is expected to follow the Kittel formula Eq. (1.32). The effective magnetization $\mu_0 M_{\mathrm{eff}}$ = 130 mT and exchange constant $A = 3.25 \times 10^{-17}$ T m^2 were obtained from the fitting of FMR data. Thermal magnons excited and collected by BLS are bulk magnons following the bulk magnon dispersion relation Eq. (1.35). Using the parameters from FMR fitting for VNA data, the wavevector k of thermal magnons is fitted to be $k = 35.8\ (\pm\ 0.4) \times 10^7$ rad/μm. It corresponds to a wavelength of $\lambda = 176$ nm. There is only one resonance mode observed in the BLS spectra so we mostly consider only the main mode $k_\perp = 2\frac{2\pi n_{\mathrm{CSO}}}{\lambda_L}$. Thus we obtained the refractive index of CSO as $n_{\mathrm{CSO}} = 1.52 \pm 0.02$.

2.3 Scanning Transmission X-ray Microscopy

2.3.1 X-ray Magnetic Circular Dichroism

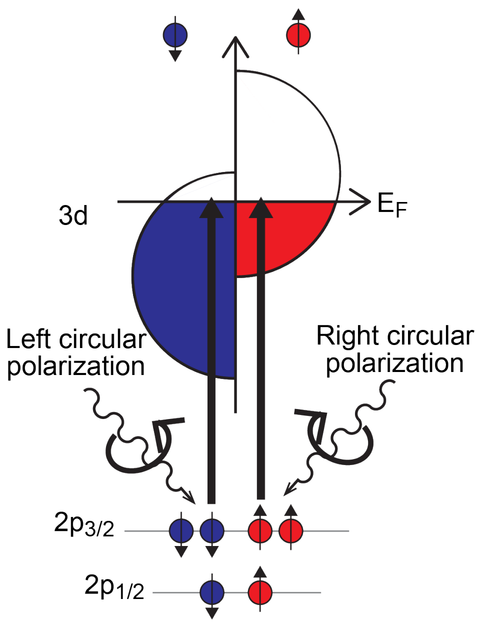

Figure 2.10 – **Diagram of X-ray magnetic circular dichroism.**

X-ray magnetic circular dichroism (XMCD) uses circularly polarized X-rays to probe the magnetization in ferromagnets and ferrimagnets [183, 184]. The diagram is illustrated in Fig. 2.10 [175, 185, 186] using the example of core-level excitation of electrons into the 3d states of a ferromagnet such as iron or cobalt. When the photon is right (left) circularly polarized it carries the angular momentum $\hbar$ (-$\hbar$). And when it is left circularly polarized, it carries the angular momentum -$\hbar$. It is partly transferred to the spin of the photonelectron through spin-orbit coupling. Spins are hence created by oppositely circularly polarized photons. In the absorption process, spin flip is forbidden. Thus the electrons with spin-up and spin-down in the p shell will be excited only to d holes of spin-up and spin-down, respectively. The d shell states experience an imbalance due to the exchange splitting. The imbalanced valence shell can detect the spin of the excited photoelectron. By this mean, XMCD detects the local magnetization. Here the spin-up and spin-down are defined by the photon angular momentum so it will be parallel or antiparallel to the X-ray propagation direction. Depending on the sign of the spin-orbit coupling of different p shells (e.g. $2p_{3/2}$ compared with $2p_{1/2}$), the transition intensities have opposite signs. XMCD detects the component of magnetization $\boldsymbol{M}$ projected on the x-ray propagation direction.

2.3.2 Configuration for Fe/Gd Experiments

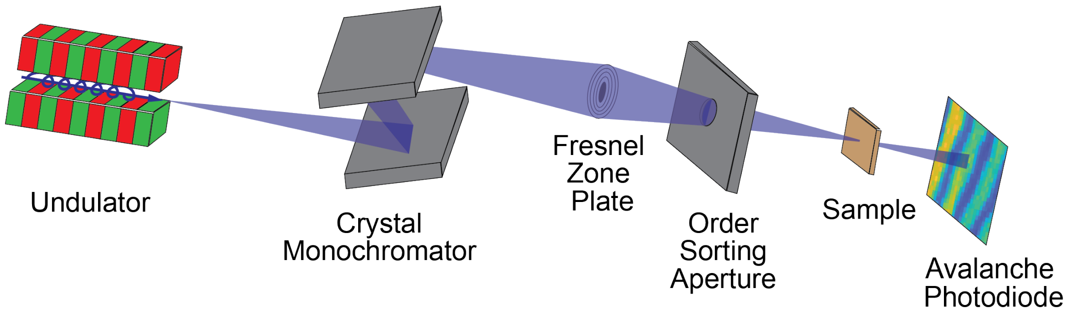

Figure 2.11 – **Simplified schematic diagram of scanning transmission X-ray microscopy.**

We conducted dynamic XMCD measurements using the scanning transmission x-ray microscopy (STMX) at MAXYMUS station, Bessy II, Berlin [187] supported by the local beamline scientists and our group member Andrea Mucchietto and Korbinian Baumgärtl. A simplified schematic diagram of the beam station is plotted in Fig. 2.11. It uses soft X-rays. The undulator covers the range from 130 eV to 2000 eV. A monochromatic beam get focused through the Fresnel zone plate. The order sorting aperture ensures to select the wanted focusing order. X-ray is focused on the sample to image the magnetization of a local region. By scanning the sample position, we are able to obtain a magnetic contrast image of the scanned region. The spatial resolution is about 25 nm. To image the dynamic motion of magnetic textures, we use the pump-probe function of MAXYMUS thanks to the time structure of the synchrotron radiation. Continuous microwave currents with fixed frequency are injected into the CPW integrated on the sample for exciting the dynamic motion. Magnetization were measured by X-ray beam pulse. Several magnetization images are taken by STMX in one periodicity of the microwave excitation (13 or 23 times in our experiments). By this means the time-dependent motions of the magnetic textures are constructed. The time resolution is about 100 ps in the multi-bunch mode.

The simplified schematic diagram of the Fe/Gd sample installed in the STXM setup is shown in Fig. 2.12. We tilted the sample to $\psi = 30$ degree with respect to the incident X-ray. So we recorded the magnetization vectors projected onto the $\boldsymbol{x}$-$\boldsymbol{y}$ plane. When counting the dimensions of the domains in the projected images, there is no modification along the $\boldsymbol{y}$ axis but a compression of $\frac{\sqrt{3}}{2}$:1 along the $\boldsymbol{x}$ axis. An external magnetic field $\boldsymbol{H}_{\perp}$ was applied perpendicular to the Fe/Gd multilayers by moving and rotating the two pairs of permanent magnets. Before the sample was placed into the X-ray chamber, we magnetized it along $\boldsymbol{y}$ axis with a permanent magnet at about 200 mT. After being introduced into the chamber, we demagnetize the sample with an oscillating $H_{\perp}$ from $\pm$ 240 mT to 0 mT before conducting measurements. All the measurements were conducted at the Gd M5 edge with 1187.6 eV. We use linearly polarized x-rays so the transmission intensities exhibit spin directions: region of less transmission is spin-up and region of more transmission is spin-down. In the region with CPWs made of Ti/Al/Cu (No. 4 in Table 2.1), magnetic contrast were modified because the Ti/Al/Cu layers of CPW reduced the X-ray transmission. In the data analysis sections in Chapter 5, we plot the the static transmission signals normalized to the highest and lowest values. Dynamic STXM images are normalized to the static transmission signals.

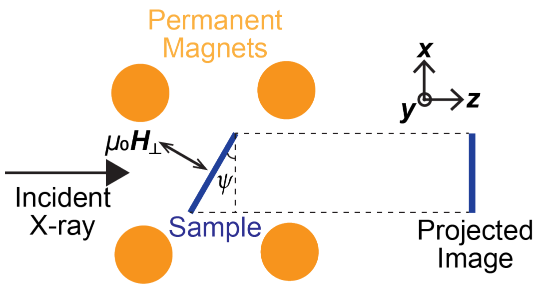

Figure 2.12 – **Simplified top view of 30 degree configuration in STXM.** The Fe/Gd sample was tilted by an angle ψ = 30 degree.

2.4 Magnetic Field versus Temperature Histories

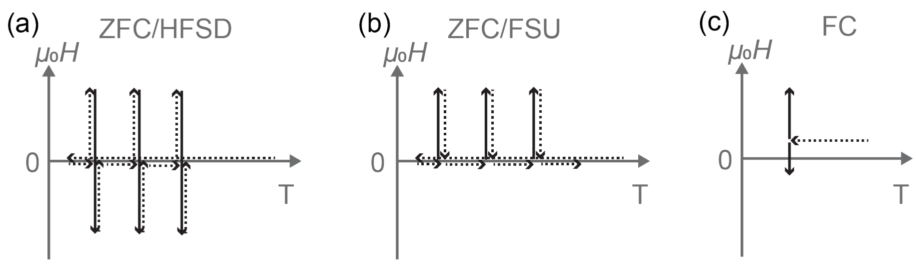

Figure 2.13 – **Magnetic field versus temperature histories.**

Three typical temperature versus magnetic field histories were exploited in the chiral magnet experiments (Fig. 2.13): zero-field cooling (ZFC) and field scan-up (FSU); zero-field cooling and high field scan down (HFSD); and field cooling (FC). Here the term 'zero field' indicates the magnetic field generated by the same current in the magnet coils as calibrated as zero field at room temperature. Within the protocol of ZFC/FSU after zero-field cooling, the absolute value of H was increased starting from 0 mT. It includes scanning to a negative field of reverse direction. Within the protocol of ZFC/HFSD, after zero-field cooling, the magnetic field was first increased to 140 mT and saturated the sample. Then we swept down the field to the opposite direction through 0 mT. Within the protocol of FC, the cooling down was performed with a certain field applied, e.g. 16 mT, and the field was either (i) scanned up or (ii) scanned down from the cool-down field as a starting point. In between each two scans (i) and (ii), the sample was heated up to 100 K for 10 minutes and cooled down again. Spectra were collected after the temperature had been stabilized for at least 10 minutes.

3 Sample Preparation

In this chapter we describe the bulk sample preparation procedures and nanofabrication techniques in two sections. In section 3.1, all the bulk samples explored in this thesis will be listed and the treatment will be outlined. In section 3.2, thin-film techniques are going to be specified. We will present a detailed process flow for the integration of coplanar waveguides (CPW) and nanomagnet arrays.

3.1 Bulk Sample Preparation

Table 3.1 – Table of bulk CSO samples.

Sample Name	Dimensions (μm^3)	Crystallographic orientations
B1	1000 × 290 × 290	$\langle 100\rangle \times \langle 010\rangle \times \langle 001\rangle$
B2	400-600 (irregular) × 290 × 290	$\langle 100\rangle \times \langle 010\rangle \times \langle 001\rangle$
B3	2000 × 1500 × 500	$\langle 001\rangle \times \langle 110\rangle \times \langle \bar{1}10\rangle$

We investigated three bulk (B) Cu_2OSeO_3 (CSO) samples in all-electrical spin wave spectroscopy and temperature and field dependent Brillouin light scattering (BLS) experiments. They are named as B1, B2 and B3 (Table 3.1). All of them are single crystals grown by chemical vapor deposition in the Crystal Growth Facility at EPFL. For samples B1 and B2, the crystallographic orientation characterization and upper surface polishing were performed at Technische Universität München, Germany, by the group of Prof. Christian Pfleiderer. For sample B3, the crystallographic orientations were characterized by X-ray diffraction on the bulk sample and double-checked with transmission electron microscopy (TEM) diffraction patterns on a thin lamella made out of the bulk sample. The upper surface was also polished for BLS experiments.

3.2 Nano-fabrication Techniques

For thin film and lamella processing, a variety of fabrication techniques was utilized in the Center of MicroNanotechnology (CMI) and Interdisciplinary Centre for Electron Microscopy (CIME). Photo-lithography was exploited for patterning structures with critical dimensions larger than 2 μm. For smaller structures, electron-beam (ebeam) lithography was employed. Two types of patterning were explored: the first type was based on positive resists and lift-off processing; the second type was based on the negative resists and etching techniques. Thin films were grown by thermal evaporation, ebeam evaporation and sputtering, depending on the material, film quality and available targets in different growth chambers. Concerning etching techniques, ion beam etching (IBE) was mostly applied. To etch lamella, we use the focused ion beam (FIB) technique combined with scanning electron microscopy (SEM).

We used FIB in CIME especially for insulating samples. We made use of the carbon deposition in the FIB chamber at CIME for conducting surfaces and protection, which had less influence on spin wave experiments.

3.2.1 Fe/Gd Multilayers on Membranes with Nanomagnet Arrays

Table 3.2 – Table of periodicites and sizes of nano arrays on Fe/Gd samples.

Sample Type	Dimension	Width of the Co stripe w (nm) or Diameter of the Co disc d (nm)	Periodicity p (nm)
Type 1	1D	150	300
	1D	175	350
	1D	200	400
	1D	225	450
	1D	250	500
Type 2	2D	175	350
	2D	200	400
	2D	225	450

To explore the magnetic phases and spin dynamics of non-collinear states with high time and spatial resolution, Fe/Gd multilayers on X-ray transparent membranes were needed. In order to obtain well-ordered spin textures and excite short-waved spin waves, one-dimensional (1D) and two-dimensional (2D) nanomagnet arrays were integrated on continuous Fe/Gd multilayers. The SEM image of a 2 mm × 2 mm fabricated sample chip is shown in Fig. 3.1 (a). The yellow frame marks the edge of the integrated CPW. The CPW on top of the 1D nanomagnet array is depicted in Fig. 3.1 (b). The widths of the ground lines, gaps and signal line were designed to be 2.1 μm, 1.6 μm and 1.7 μm, respectively. Two types of sample chips were designed: one with five 1D arrays and the other one with three 2D arrays. The arrays differed concerning periodicity and nanomagnet sizes, as listed in Table. 3.2. The thickness of the Co is 20 nm for all structures. SEM images of the nanomagnet arrays right after lift-off processing are shown in Fig. 3.1 (c) and (d).

Fe/Gd multilayers were grown on Si_3N_4 membranes in the group of Prof. Manfred Albrecht at University of Augsburg, Germany. Photo-lithography, ebeam-lithography, thermal and ebeam evaporation as well as lift-off techniques were utilized at CMi of EPFL for fabricating markers, nanomagnet arrays and CPWs. The detailed process flow is described in the following (Fig.3.2).

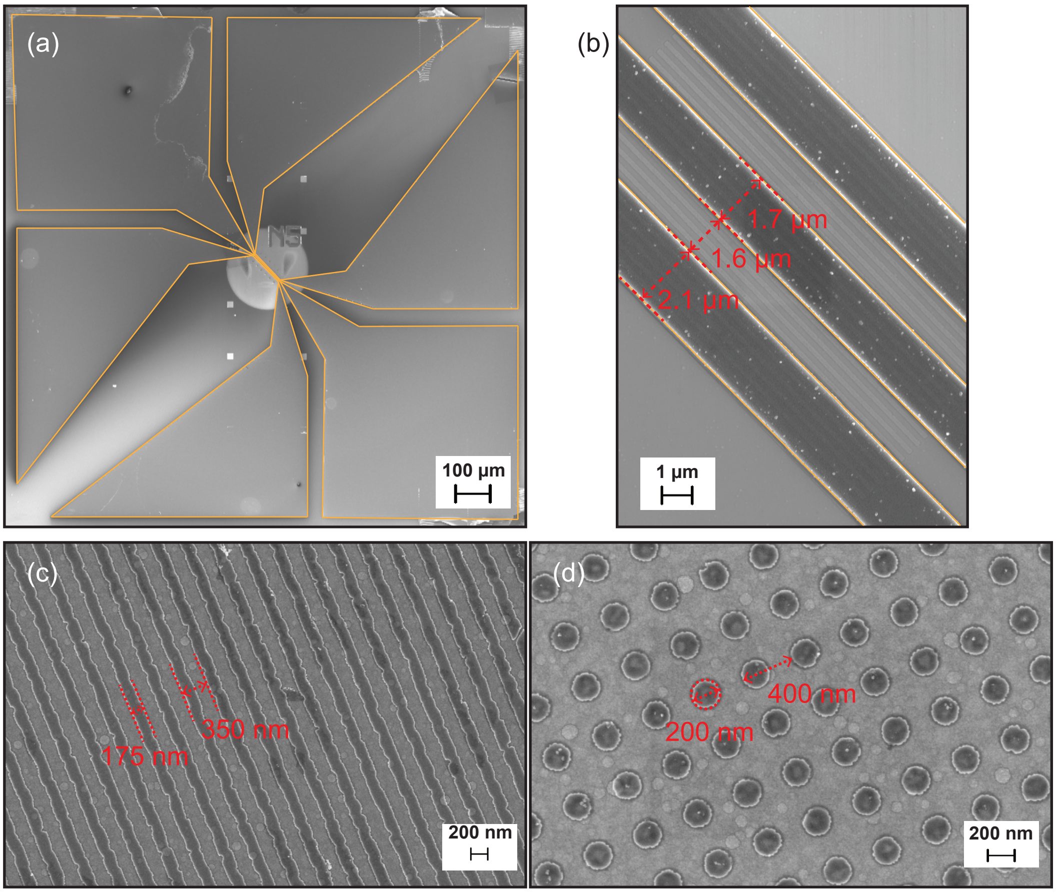

Figure 3.1 – **SEM images of a Fe/Gd samples multilayer on a membrane with nanomagnet arrays.** (a) SEM image of the Fe/Gd sample. The yellow frame mark the edges of the CPWs. (b) Detailed SEM image of CPW lines on top of 1D nanomagnet array being in the center of a 100-nm-thick Si_3N_4 membrane. Yellow frames mark the edges of the CPW lines. (c) and (d) SEM images of 1D and 2D Co nanomagnet arrays.

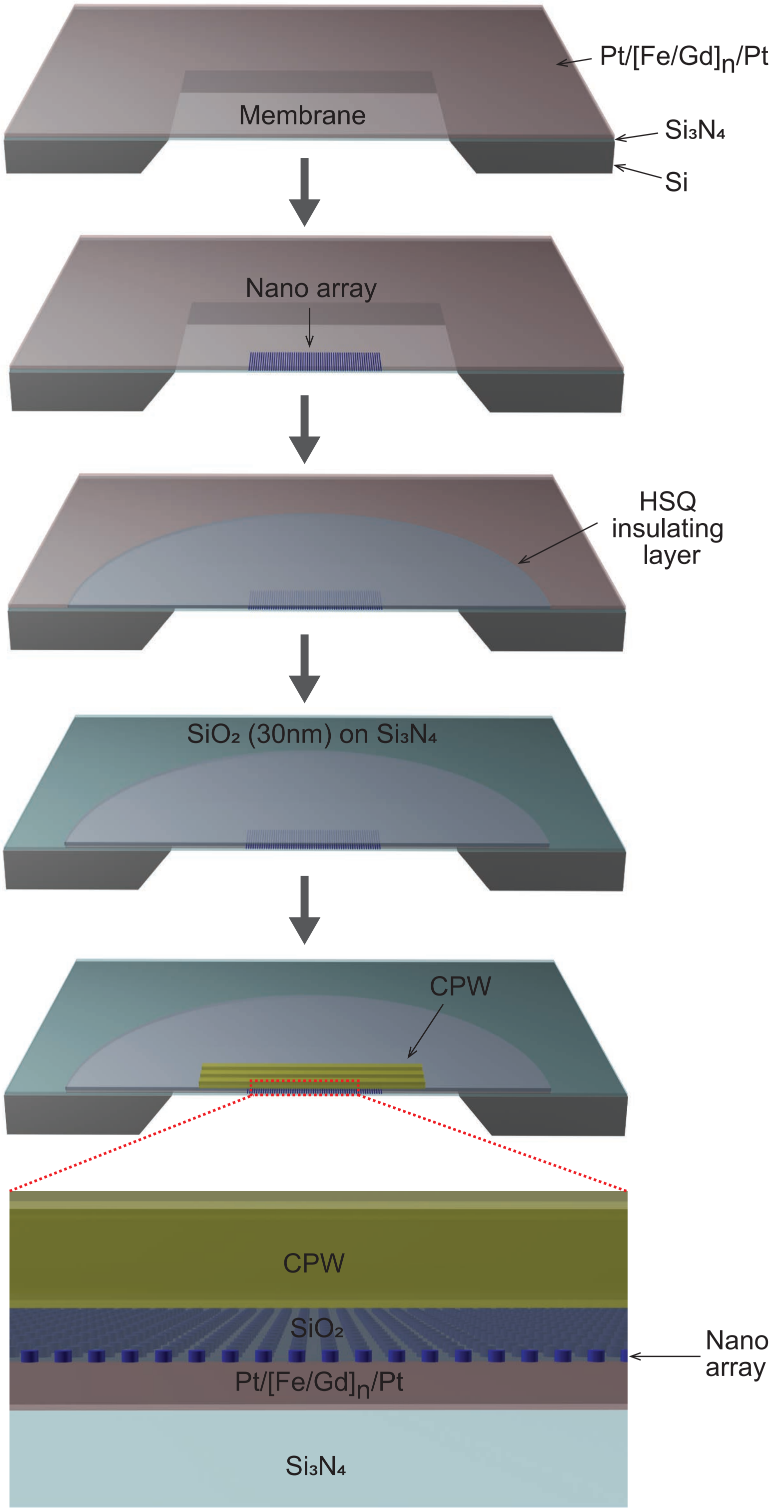

Figure 3.2 – **Process flow for fabricating nanomagnet arrays on Fe/Gd multilayers grown on a 100-nm-thick membrane.**

I. Marker fabrication by photo lithography: The sample was firstly cleaned by IPA and deionized (DI) water, pre-baked at 100°C for 120 s. A 0.48-μm-thick layer of photo resist LOR 5A was coated by 4000 rpm. It was then baked at 190°C for 250 s. Then a 1.1-μm-thick layer of photo resist AZ 1512 HS was coated by 6000 rpm and baked at 100°C for 90 s. Then we use the 405-nm-laser writing setup Heidelberg Instruments MLA150 with dose 48 mJ/cm^2 and defocus 0. The resists were then developed in AZ® 726 MIF in the wet bench for about 45 s. 10-nm-thick Ti and 120-nm-thick Au were grown on top by ebeam-evaporation using Alliance-Concept EVA 760 machine. The whole chip was placed into Remover 1165 for 2 days for lift-off processing at room temperature. IPA and DI water were used for the final cleaning of the sample.

II. Electron-beam-lithography of 1D and 2D nano-grating arrays: First, the sample was cleaned by acetone and IPA, and then baked at 180°C for 300 s. Then the double layer of 180-nm-thick ebeam resists EL6 and 100-nm-thick 495 A2 were spin coated with the spinning speed of 2500 rpm and 1700 rpm respectively. After the coating of each layer, the sample was baked at 180°C for 300 s. It is noticed that a direct fix of the membrane sample on the vacuum chuck brought no visible damage on the membrane windows. The EBPG5000ES system was utilized for performing the ebeam exposure with 100 keV electron source. Manual alignment was applied. A dose of 600 μC/cm^2 was used for exposure of 1D arrays and 500 μC/cm^2 for 2D arrays. The currents amounted to 200 pA in both exposures. The written pattern was immediately developed by MiBK:IPA 1:3 solution for 60 s after moving out of the vacuum environment of the ebeam chamber and cleaned by being placed in IPA for 1 min. After being dried by nitrogen gas, a 20-nm-thick Co layer was evaporated using the Alliance-Concept EVA 760 machine. Remover 1165 was then used for lift-off processing after evaporation. IPA and DI water were used for the final cleaning of the sample.

III. Protection HSQ layer: After cleaning, we coated a 90 nm-thick layer of HSQ 002 (negative ebeam resist) with a spinning speed of 2000 rpm. No baking was needed in this step. HSQ was exposed with an ebeam dose of 3000 μC/cm^2 using a 100 nA ebeam current. To create the mesa with a diameter of 140 μm, no proximity effect correction was applied (intentionally) so the thickness of HSQ at the edges of the pattern changed adiabatically. There were no sharp edges. After exposure, the sample was immediately placed into the CD26 solution with 1.5 % NaCl for development for 1 minute and then washed by flowing DI water.

IV. Removal of metal layer and integration of insulating layer: The sample was fixed on a wafer by Kapton tape and placed in the chamber of the Veeco Nexus IBE350 machine for etching of the metal layer in the region not covered by HSQ pattern. The recipe "Medium-IBE" was used and 3 etching steps of 60 s + 10 s + 10 s were performed. After each step, the sample was taken out of the chamber for checking the resist and color change. After the etching, a 30-nm-thick SiO_2 layer was grown on the whole sample by the Oxford plasmalab system 100

PECVD.

V. Ebeam-lithography of CPWs: For the fabrication of CPWs, similar procedures were conducted as in step II. This time, a double layer of ebeam resists consisting of 320-nm-thick EL9 and 100-nm-thick 495 A2, were spin coated with the spinning speed of 4000 rpm and 1700 rpm, respectively. After the coating of each layer, the sample was baked at 180°C for 300 s. A dose of 1200 μC/cm^2 was used for writing CPWs with a 100 nA beam current. After being dried by nitrogen gas, 10 nm of Ti, 120 nm of Al and 10 nm of Cu were thermally evaporated using the Leybold Optics LAB 600H machine. Remover 1165 was then used for lift-off processing after evaporation which lasted for 2-3 days. IPA and DI water were used for the final cleaning of the sample.

Another process flow on the flipped CSO lamella on CPW with grating couplers is described in the Appendix.

4 Helimagnons and Spin Dynamics of Skyrmion Lattices in the Bulk Chiral Magnet Cu_2OSeO_3 at Cryogenic Temperatures

In this chapter, we introduce the helimagnons and spin dynamics of skyrmion lattices in bulk chiral magnet Cu_2OSeO_3 (CSO) utilizing both the all-electrical spin-wave microscopy and cryogenic BLS. Here we report the properties of spin waves in different phases and the discovery of a stabilization mechanism of new phases in CSO. In section 4.1, we discuss the confined spin waves in field polarized states excited by microwave currents and studied by micromagnetic simulation. In section 4.2, we report the chiral soliton phase observed in CSO by BLS, its spin dynamic and anisotropic properties. In section 4.3, we focus on the spin dynamics of high temperature skyrmion phases and new phases at low temperature including the low temperature skyrmion phases and tilted conical phase. In the last section of this chapter, section 4.4, we report the metastable phases in CSO and their dynamic properties. We discover a new mechanism of stabilizing the metastable skyrmion phases and brushing the skyrmions using a continuous-wave laser.

4.1 Confined Spin Waves in Field Polarized States Revealed by Broadband Spin-Wave Spectroscopy

In ferromagnets without bulk DMI, the conventional confined spin waves exhibit symmetric dispersion relations. In case of confinement, standing spin waves were formed with fixed nodes and anti-nodes. Intensities of the spin wave resonance vary systematically with the order of confinement [188–196]. In chiral magnets with bulk DMI, the dispersion relation of the $\boldsymbol{k} \parallel \boldsymbol{M}$ spin waves is asymmetric so that the spin waves propagating along opposite directions at the same frequency own different k. The discrepancy in k does not allow for the conventional standing spin waves. Numerical methods showed involved spin waves phase profiles in nanoscale magnets with DMI [197–199]. In thin films of the chiral magnet FeGe,

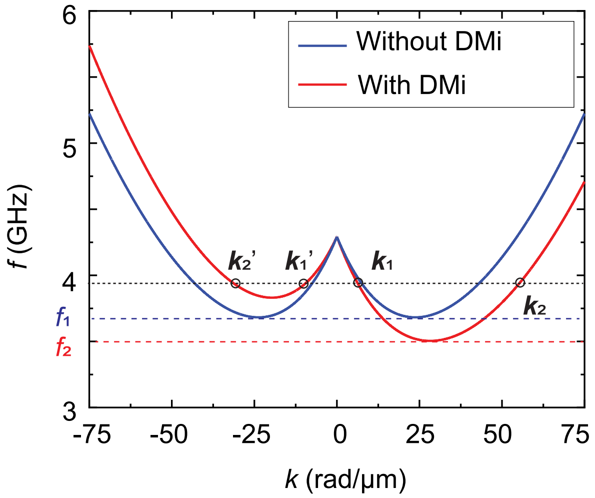

Figure 4.1 – **Sketch of the dispersion relation of the $\boldsymbol{k} \parallel \boldsymbol{M}$ mode with and without bulk DMI.**

an oscillating factor $\exp(-iQz)$ explained a frequency shift of the ferromagnetic resonance (FMR) at $k = 0$ and perpendicular standing spin waves (PSSW) with finite k, where Q is the pitch vector in a chiral magnet [200] and z is the spatial direction. Standing spin waves were assumed in bulk CSO [86, 87] but their characteristics remained unexplored.

Here we report on confined spin waves observed in the bulk chiral magnet CSO probed by broadband microwave spectroscopy and micromagnetic simulation. We excited spin waves by a dynamic field across the whole sample and numerous resonance peaks with systematically varying intensities appeared in the field polarized phase. We attributed those series of peaks to confined $\boldsymbol{k} \parallel \boldsymbol{M}$ modes and additional $\boldsymbol{k} \perp \boldsymbol{M}$ modes. We performed micromagnetic simulations on a micron-sized sample exhibiting the same form factor, i.e., the same shape anisotropy (demagnetization effect). When considering a non-zero DMI, we observed both the odd and even order numbers n of confined volume modes at low frequency consistent with the experimental observation. Moreover, short-waved magnons down to a wavelength of about 40 nm appeared at frequencies at which the discretized volume modes existed. These modes depended characteristically on the DMI strength. The origin of the short-waved magnons in the exchange regime is attributed to the interplay of symmetric and asymmetric exchange interactions. They appear for both uniform and non-uniform excitation scenarios. Our results suggest DMI to be a strong tool to excite exchange-dominated spin waves without challenging nanofabrication.

4.1.1 Dispersion Relation Modified by Bulk DMI

The effective field term generated by bulk DMI only enters the dispersion relation of the $\boldsymbol{k} \parallel \boldsymbol{M}$ spin waves and has no influence on the $\boldsymbol{k} \perp \boldsymbol{M}$ spin waves or surface spin wave mode.

Dispersion relations of the $\boldsymbol{k} \parallel \boldsymbol{M}$ spin waves with and without the bulk DMI are sketched in Fig. 4.1 [13, 73]. With bulk DMI $D > 0$, the dispersion relation is asymmetric with respect to k = 0 rad/μm: the branch with positive k owns lower frequency than the system of no DMI and the branch with negative k owns higher frequency. Here the asymmetry due to DMI is exaggerated to make the difference in dispersion relations visible. When the bulk DMI is absent, the wavevectors own the same modulus of different sign so a standing spin wave with vector $|k_0|$ = $(|k_+| + |k_-|)/2$ can form with fixed nodes and antinodes. In a one-dimensional case, $|k_0|$ is specified as $|k_0| = n\pi/L$ where n is related to the number of nodes 0, 1, ... and L is the length (or width) of the sample [188]. If no specific surface asymmetry plays a role, broadband spin wave spectroscopy can barely detect the odd modes (odd n) because the antinodes with π phase shift induce counter-acting voltage signals in the signal line of the coplanar waveguides (CPW) which cancel each other. When bulk DMI is present, the dispersion relation is no longer symmetric so at each frequency $|k_1| \neq |k_1^{'}|$ and $|k_2| \neq |k_2^{'}|$. Traveling waves with fixed nodes are expected to form [198] but the amplitudes of spin waves at π phase shift are no longer symmetric. In this scenario, the voltage signals induced by the odd modes are no longer canceled and induce a net voltage in the CPW. Considering our experimental data, we estimate $|k_0| = (|k_1| + |k_1^{'}|)/2$ instead of $|k_1|$ and $|k_1^{'}|$ separately, because the excitation took place at each fixed frequency and multiple k ($|k_1|$ and $|k_1^{'}|$) were excited at the same time. In the micromagnetic simulation, we evaluate the integrated Fourier transform of the spin wave amplitudes so the working principle is consistent with CPW detection. With the help of the phase profile, $|k_0|$ is accurately calculated from fitting.

4.1.2 Broadband Spin Wave Spectroscopy on Bulk Cu_2OSeO_3 in Field Polarized State

The broadband microwave measurements were conducted on the bar-shape CSO sample named B1 in Table. 3.1. It was placed on the commercial CPW No.1 in Table. 2.1. The CSO sample was positioned at the center of the CPW in a way that the longer axis of the sample was parallel to the signal line, as shown in Fig. 4.2. Because the width of the signal line was 1 mm and more than three times wider compared to the sample width 0.29 mm, the in-plane component of $\mathbf{h}_{\mathrm{rf}}$ was assumed to be uniform with respect to $\mathbf{x}$ and $\mathbf{y}$ (it varied as a function of $\mathbf{z}$). Measurements were conducted at two cryogenic temperatures: 5 K and 20 K. Magnetic fields were applied by superconducting magnets. A residual magnetic field of 36 mT along $\mathbf{z}$ was present due to technical reasons when the sample was cooled down. The reported field values $\mu_0 H$ do not consider this background field, but describe the additional field applied via a current in the superconducting coil. A radio-frequency current I_{rf} was injected into the CPW by a VNA and induced a dynamic magnetic field $\mathbf{h}_{\mathrm{rf}}$ (purple circular arrows). At T = 5 K, $\mu_0 H$ = 150 mT was first applied along $+\mathbf{y}$ to saturate the CSO and then reduced in a step-wise manner. The same saturation process was conducted when we changed the applied field direction to $\mu_0 H \parallel \mathbf{x}$ and $\mu_0 H \parallel \mathbf{z}$ for different measurements. The sample was then heated to 20 K to perform the same series of measurements with the different field directions.

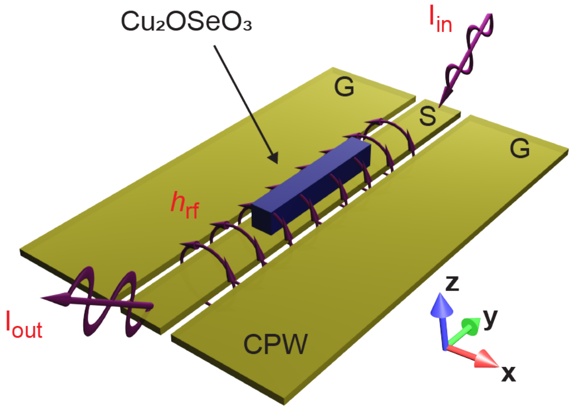

Figure 4.2 – **Schematic diagram of bulk CSO sample placed on CPW.**

Field dependent spectra taken at T = 5 K are shown in Fig. 4.3 (a) for $\mu_0 H \parallel \mathbf{x}$. A change in slope df/dH of resonance frequencies f was seen at $\mu_0 H_{C2}$ = 52 mT marked by a black dashed line. For $\mu_0 H > \mu_0 H_{C2}$, resonance frequencies f increased almost linearly with H indicating the field polarized (FP) phase. For $\mu_0 H < \mu_0 H_{C2}$, the slope df/dH indicated an unsaturated state, such as the conical phase in CSO [170]. In the following we focus on the numerous resonances detected for $\mu_0 H > \mu_0 H_{C2}$. Lineplots at fields $\mu_0 H$ = 100 mT and $\mu_0 H$ = 96 mT are shown in Fig. 4.3 (b). 14 peaks was observed (marked by arrows). Color-coded map of spin waves spectra at T = 20 K and the line plot at $\mu_0 H$ = 112 mT and $\mu_0 H$ = 108 mT are shown in Fig. 4.3 (c) and (d). We find $\mu_0 H_{C2}$ = 56 mT at 20 K. This value is slightly higher than at T = 5 K which is consistent with the phase diagram modification along the easy axis (as introduced in Fig. 1.2 (b)). Above $\mu_0 H_{C2}$, 5 peaks (marked by arrows) was clearly visible. Fewer resonance are seen which is an evidence of higher damping, consistent with earlier reports on temperature-dependent damping [81, 169]. For the mode with highest intensity, it requires a higher applied field of 112 mT at T = 20 K to achieve the same frequency compared with T = 5 K (100 mT), resulting from the temperature-dependent saturation magnetization [81].

We have categorized the resonances marked by blue arrows depending on their systematic peak-to-peak intensity variation. Solid arrows mark $\boldsymbol{k} \parallel \boldsymbol{M}$ modes owing the wavevector k_y. Dashed arrows mark the additional $\boldsymbol{k} \perp \boldsymbol{M}$ modes on top of $\boldsymbol{k} \parallel \boldsymbol{M}$ modes whose wavevectors read $k^2 = {k_y}^2 + {k_\perp}^2$ with $k_\perp$ perpendicular to $\boldsymbol{y}$. Each sequence of peaks was ranked with order numbers 1, 2, ..., with intensity I varying from high to low. The intensities I of resonances marked by solid arrows are summarized in Fig. 4.4 (a) in a double-logarithmic manner. The linear variation suggests that I is inversely proportional to the order number which is a sign of discrete spin waves with different numbers of nodes [195]. $\boldsymbol{k} \parallel \boldsymbol{M}$ spin waves are confined along $\mathbf{y}$. We attribute wavevectors to the discrete modes of Fig. 4.3 (b) and (d) according to $k_y = (\pi n_y)/\Delta y$ where n_y = 0, 1, ... and Δy = 1 mm is the length of the bar-shape sample. Figure 4.4 (b) now shows the resonance frequencies identified in Fig. 4.3 (b) and (d) as a function of

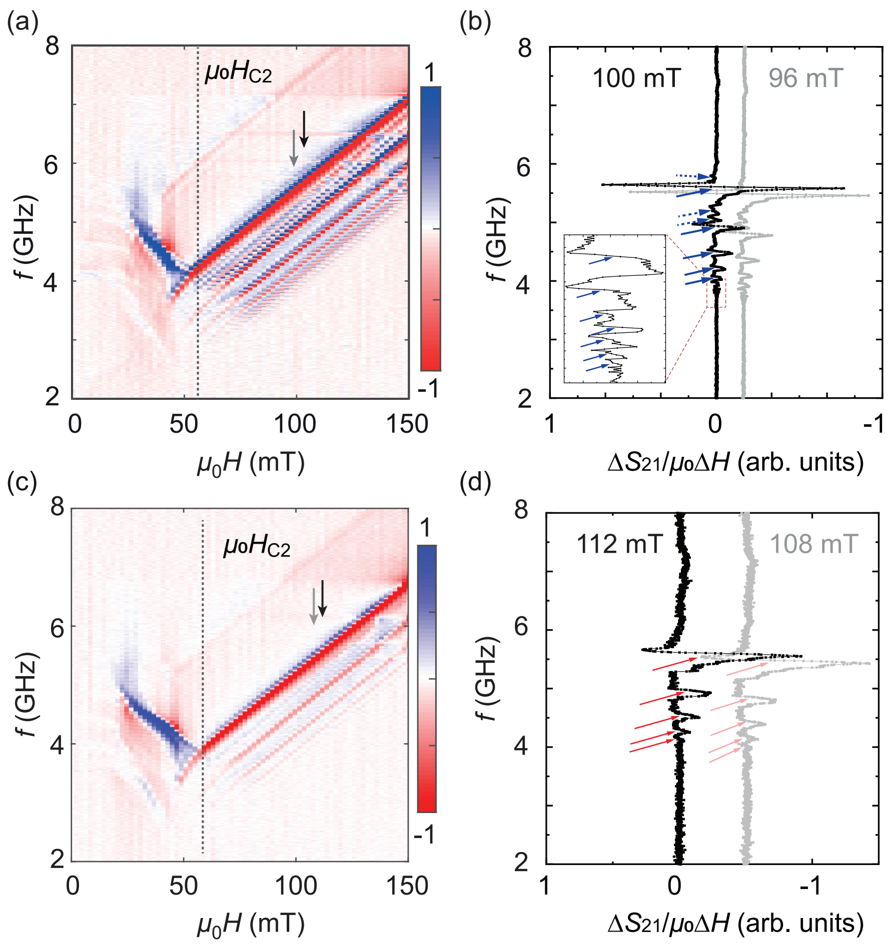

Figure 4.3 – **Broadband spin wave spectra of bulk CSO sample.** (a) Color-coded maps of broadband spin wave spectra taken as a function of applied field $\mu_0 H$ along **y** at 5 K. Color scale bar represents $\Delta S_{12}/\mu_0\Delta H(\times 10^{-3}\ \mathrm{T}^{-1})$. Black and gray arrows indicate where the lineplots in (b) were taken. (b) Lineplots of spectra $\Delta S_{12}/\mu_0\Delta H$ at 5 K and $\mu_0 H = 100$ mT (black) and 96 mT (gray) indicated by arrows in (a). Solid blue arrows mark the frequencies which we attribute to discrete $\boldsymbol{k} \parallel \boldsymbol{M}$ modes and dashed blue arrows mark the frequencies that we categorize in terms of discrete $\boldsymbol{k} \perp \boldsymbol{M}$ modes. (c) Color-coded maps of broadband spin wave spectra taken as a function of applied field $\mu_0 H$ along **y** at 20 K. (d) Lineplots of spectra $\Delta S_{12}/\mu_0\Delta H$ at 20 K and $\mu_0 H = 112$ mT (black) and 108 mT (gray) indicated by arrows in (a). Solid red (and light red) arrows mark the frequencies which we attribute to discrete $\boldsymbol{k} \parallel \boldsymbol{M}$ modes.

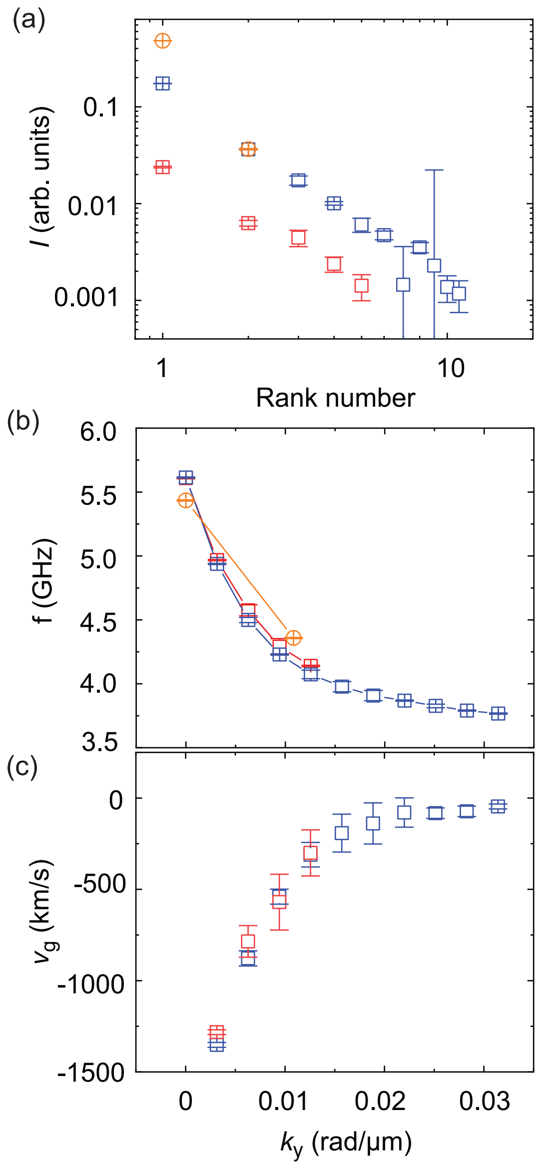

Figure 4.4 – **Intensity, dispersion relation and group velocities extracted from confined $\boldsymbol{k} \parallel \boldsymbol{M}$ modes experimentally.** (a) Peak-to-peak intensity of resonances in a double-logarithmic plot corresponding to the confined $\boldsymbol{k} \parallel \boldsymbol{M}$ mode sequences. Error bars represent the noise level in the spectra and the deviation in reading out the peaks. (b) Dispersion relation of spin waves extracted experimentally. Error bars reflect the frequency resolution of the VNA and the deviation in reading out the peaks. (c) Group velocities calculated as $2\pi\Delta f/\Delta k_y$ from (b). Error bars originate from the frequency domain in (b). In (a) (b) and (c), blue squares and red squares were extracted from solid arrows in Fig. 4.3 (b) and (d) with $\mu_0 H \parallel \mathbf{y}$ at $T = 5$ K and $T = 20$ K, respectively. Yellow circles were extracted from data taken at $\mu_0 H = 150$ mT at $T = 5$ K when $\mu_0 H \parallel \mathbf{z}$ (Fig. 4.5 (a)).

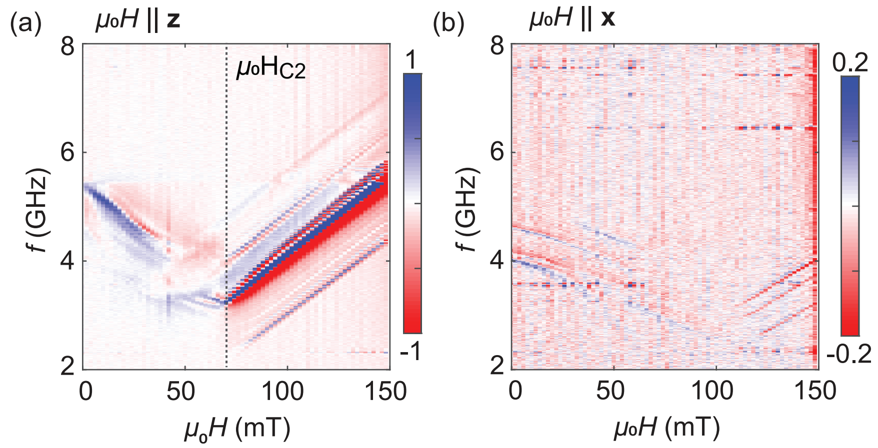

Figure 4.5 – **Broadband spin wave spectra of variable field directions.** (a) and (b) Color-coded maps of broadband spin waves spectra taken as a function of applied field $\mu_0 H \parallel \mathbf{z}$ and $\mu_0 H \parallel \mathbf{x}$ at $T = 5$ K. Color scale bars represent $\Delta S_{12}/\mu_0 \Delta H \times 10^{-3}\ \mathrm{T}^{-1}$).

values k_y (blue squares). The frequencies follow $f(k)$ expected for $\boldsymbol{k} \parallel \boldsymbol{M}$ modes. The group velocity was calculated from (b) as $v_g = 2\pi\Delta f/\Delta k_y$ and shown in Fig. 4.4 (c). The sequence of peaks marked by dashed arrows (Fig. 4.3 (b)) are attributed to conventional standing spin waves because the bulk DMI does not modify $\boldsymbol{k} \perp \boldsymbol{M}$ modes. The confined modes along $\mathbf{z}$ and $\mathbf{x}$ are degenerate because the dimensions of the bulk CSO: $\Delta z = \Delta x = 0.29$ mm.

The colored-coded maps of the broadband spin wave spectra with other field directions are plotted in Fig. 4.5. When the field was applied along $\mathbf{z}$, only one order of confined $\boldsymbol{k} \parallel \boldsymbol{M}$ mode can be clearly resolved at low frequency. This is because the wave vector determined by the dimension $\Delta z = 0.29$ mm is large and may approach the bottom of the $\boldsymbol{k} \parallel \boldsymbol{M}$ spin-wave brunch. The observed frequency of 4.3 GHz at 150 mT is consistent with the dispersion relation of Fig. 4.4 (b) as $k = 0.01$ rad/μm. In Fig. 4.5 (a), confined $\boldsymbol{k} \perp \boldsymbol{M}$ modes are seen up to high frequency. When the field was applied along $\mathbf{x}$ (Fig. 4.5 (b)), $\mathbf{h}_{\mathrm{rf}}$ is parallel with the magnetization and the torque $\tau = \boldsymbol{h}_{\mathrm{rf}} \times \boldsymbol{M}$ for excitation is nearly zero. There are still three modes seen in the FP state beyond 120 mT. Considering the relatively strong signal strength they might originate from the region in the CSO for which the magnetization is not fully aligned with $\boldsymbol{H} \parallel \boldsymbol{h}_{\mathrm{rf}}$. We speculate that some of these resonances correspond to edge modes in region where due to the demagnetization effect $\boldsymbol{M}$ deviates from $\boldsymbol{H}$ and τ is clearly non-zero. It can be also confirmed from the intensities of these two lower-laying peaks in frequency as they are identical instead of following the inverse scaling with order number as reported for confined spin waves. In other configurations such as $\mu_0 H \parallel \mathbf{y}$ and $\mu_0 H \parallel \mathbf{z}$, the excitation of edge modes also exists but can not be identified clearly because the density of magnons is much smaller than the ones of the confined modes. We note that the micromagnetic simulation presented in the following also provide spectra which contain edge mode resonances.

4.1.3 Micromagnetic Simulations on Confined Spin Waves in Chiral Magnets

In order to further understand the role of DMI for the confined spin waves, we conducted spin dynamics simulations using the micromagnetic program Mumax3 [145]. A bar-shaped sample with $0.128 \times 2.048 \times 0.128\ \mu m^3$ with no periodic boundary condition (PBC) was considered. The cell sizes were 4 nm along **y** and 8 nm along **x** and **z** to resolve quantized spin waves. Here we used $1 \leq ix \leq 16$, $1 \leq iy \leq 512$ and $1 \leq iz \leq 16$ to identify the cell number along **x**, **y** and **z** directions respectively. Parameters such as exchange stiffness $A = 7 \times 10^{-13}$ J/m, DMI constant $D = 7.4 \times 10^{-5}$ J/m^2, saturation magnetization $M_{sat} = 1.03 \times 10^5$, 1st order cubic anisotropy constant $K_{C1} = 6 \times 10^2$ J/m^3 and Gilbert damping constant $\alpha = 5 \times 10^{-4}$ were taken from Refs. [81, 122, 201]. The static magnetic field $\mu_0 H$ was varied from 160 mT to 80 mT along **y** with 0.5 degree tilting angle with respect to **x** to avoid numerical errors in simulation. The dynamic magnetic field $\mu_0 h$ in the form of a sinc function for broadband excitation was applied along **x** and 0.5 degree tilted away from **z**. The integrated Fourier transform (FFT) amplitude of magnetization component m_z among all the cells is plotted in Fig. 4.6. We find one mode of largest intensity. On the low-frequency side of this most prominent peak, multiple resonances peaks are seen. This is consistent with the observation in the experiment (Fig. 4.3 (a) and (c)). It is noted that when the PBC was applied along **y**, there were no multiple peaks at lower frequency in the simulation. Therefore, the resonance peaks at lower frequency show the discrete spin waves confined by the sample boundaries. The peaks at 3.2 GHz and 4.0 GHz (at $\mu_0 H = 160$ mT) reflect two edge modes as discussed in the previous section.

The bulk DMI constant was varied from 0 to 10 ($\times 10^{-5}$ J m^{-2}) in Fig. 4.7. Here the applied field was fixed at 160 mT. Multiple peaks with decreasing amplitudes towards lower frequency are present for all the different D constants, proving the formation of discrete spin wave modes due to boundary conditions in all configurations. When $D = 0$, confined spin waves reside between 4.4 GHz and 7.3 GHz and the highest intensity peak appears at 6.5 GHz. When D increases up to 10×10^{-5} J m^{-2}, the peak with the highest intensity moves to a higher frequency of 6.8 GHz and more resonance peaks appear within a larger frequency range extending from 2.3 GHz to 7.7 GHz. As shown in Fig. 4.1 (a), when the bulk DMI is present, the dispersion relation of $\boldsymbol{k} \parallel \boldsymbol{M}$ spin waves is asymmetric and the asymmetry can be enhanced by increasing D. The lowest frequency f_2 possible to be excited is lower than for the symmetric dispersion relation f_1 ($D = 0$), which would explain the larger frequency regime in which discrete spin wave modes occur for $D \neq 0$. On the other hand, the asymmetry results in the visibility of both the even and odd modes in the integrated FFT amplitudes in our simulation. So compared with the spectrum of $D = 0$ whose resonances correspond to the confined order 1, 3, 5, ..., the spectrum of $D = 10 \times 10^{-5}$ J m^{-2} contains additionally the evenly numbered mode. Thus all the confined orders of 1, 2, 3, ... modes appear and the number of resonance peaks increase.

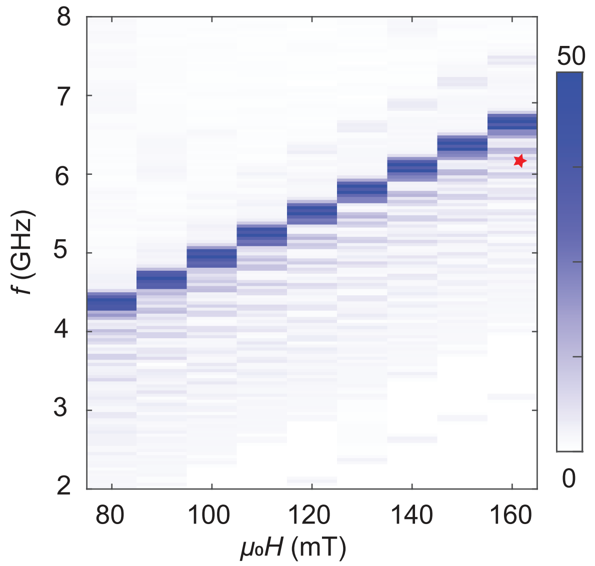

Figure 4.6 – **Color-coded maps of spin waves spectra from micromagnetic simulation** The spectra were taken from layer iz = 6 in **z** direction. Color scale bar represents the amplitude of Fourier transform of m_z.

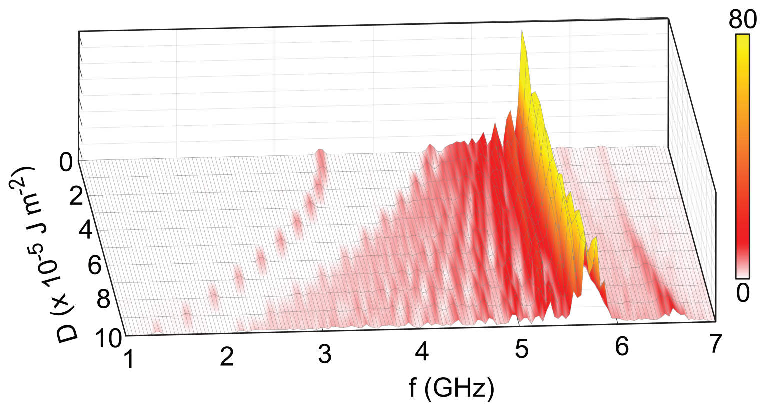

Figure 4.7 – **Spectra of quantized spin waves when DMI constant changes.** The color bar represents the z axis which is the integrated Fourier transform (FFT) amplitude of magnetization component m_z.

To compare the confined spin waves in the sample with and without DMI, we plot the amplitude A and phase Φ maps, as well as the line plots in Fig. 4.8 (a) and (c). Figure 4.8 (a) was taken at the resonance peak marked by the red star in Fig. 4.6. For comparison, a simulation with all the other parameters identical but DMI strength $D = 0$ was plotted in Fig. 4.8 (b) and (d). The color maps display the wave distribution in the x-y plane with iz = 6. In the system without DMI, the standing spin waves were formed by only odd-numbered modes giving non-zero FFT intensities. At $f = 6.2$ GHz, the 5th confined order mode is seen. At D

$= 7.4 \times 10^{-5}$ J m^{-2} the same order of confinement appears at 6 GHz. We marked the peaks in Fig. 4.8 (c) and (d) by light red and blue arrows for eye-guiding. They are categorized as different orders of confined $\boldsymbol{k} \parallel \boldsymbol{M}$ modes. Grey arrows mark the edge modes originating from the regions near the edges where the magnetization is not uniform.

In the spin wave amplitude A and phase Φ maps inside the chiral magnet (layer iz = 6) at $f = 6$ GHz when $D = 7.4 \times 10^{-5}$ J m^{-2}, a signal modulation with a wavelength of around 50 nm appears (Fig. 4.8). Especially in the Φ map, a confined long-waved spin wave (marked by dashed red arrows) and a short-waved mode (marked by solid red arrows) are present. Examples of the phase line plots of ix = 6 and iz = 6 at $f = 6$ GHz at 160 mT are plotted in Fig. 4.9. They display the coexistence of two waves with different wavelengths. We name them as long-waved spin waves (LWSWs) and short-waved spin waves (SWSWs) , respectively.

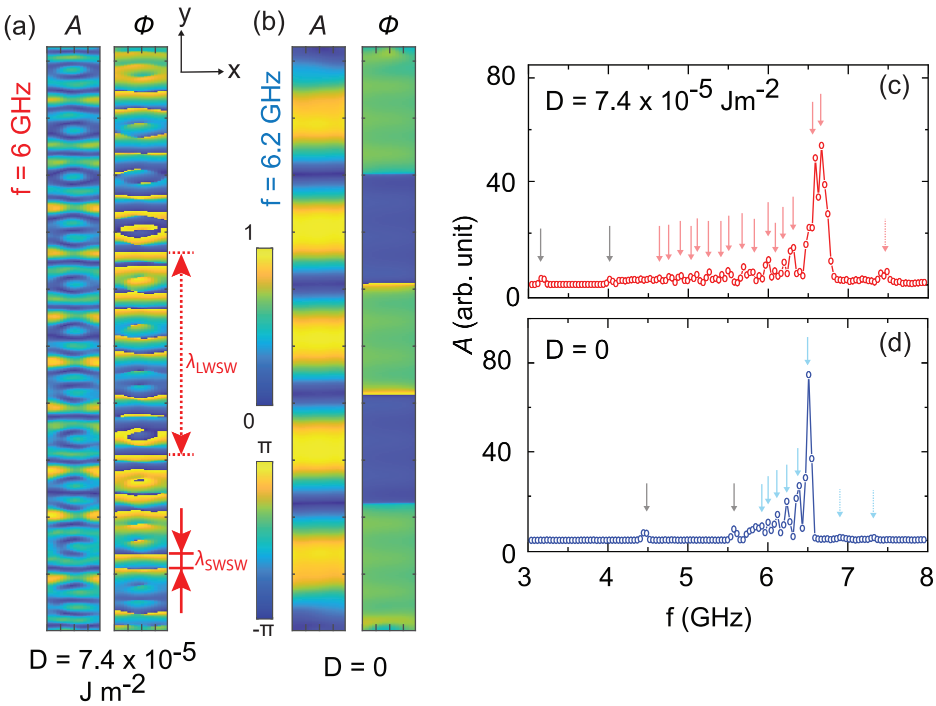

Figure 4.8 – **Confined spin waves with and without DMI.** Color coded maps of amplitude A and phase Φ in the x-y plane of z layer iz = 6, with (a) D = 7.4×10^{-5} J m^{-2} and (b) D = 0. The color scale of amplitude maps are normalized so that blue represents 0 and yellow represents 1. In the phase maps, blue and yellow color represents -π and π, respectively. Lineplots of FFT amplitude A at layer ix = 6 from micromagnetic simulation at $\mu_0 H = 160$ mT of (c) D = 7.4×10^{-5} J m^{-2} and (d) D = 0. The gray arrows highlight edge modes. The red ones are even and odd numbers for confined modes. The light blue arrows refer to odd-numbered orders.

The resonance frequencies of both LWSWs and SWSWs are plotted in Fig. 4.10. An exchange-dominated spin wave with λ down to 47.2 ($\pm$ 0.05) nm is found ($k = 133$ rad/μm). When the DMI constant increased up to $D = 10 \times 10^{-5}$ J m^{-2}, the spin wave wavevectors of SWSWs

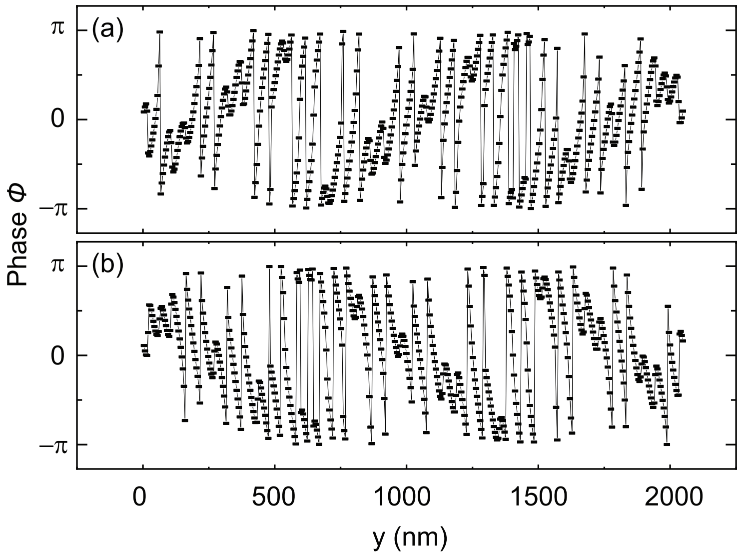

Figure 4.9 – **Lineplot of phase profile with opposite DMI.** Line plots of phase at f = 6.004 GHz with (a) $D = 7.4 \times 10^{-5}$ J m^{-2} and (b) $D = -7.4 \times 10^{-5}$ J m^{-2}.

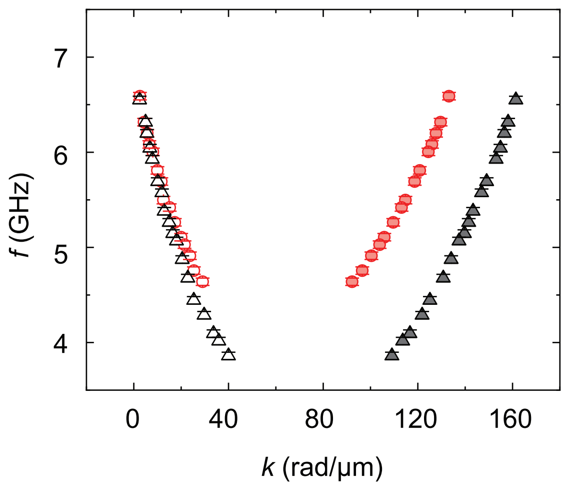

Figure 4.10 – **Dispersion relation of resonance extracted from the micromagnetic simulation.** Red squares are taken from $\mu_0 H$ = 160 mT with $D = 7.4 \times 10^{-5}$ J m^{-2}. Black triangles are taken from $\mu_0 H$ = 160 mT with $D = 10 \times 10^{-5}$ J m^{-2}. Hollow triangles are LWSW and corresponds to the dashed red markers in (b). Filled triangles are SWSW and corresponds to the solid red markers in (b).

increase as indicated in Fig. 4.10. The shortest excited wave is extracted to be λ = 38.9 ($\pm$ 0.04) nm (k = 162 rad/μm). At the same time, the wavelengths of the LWSWs remain similar to the small D case. The small deviation is because of the enhancement of the asymmetry of the $\boldsymbol{k} \parallel \boldsymbol{M}$ mode dispersion relation. The sign of DMI does not play a role in the wavevector definition but it changes the sign of phase velocity of both LWSWs and SWSWs (Fig. 4.9). We attribute the coexistence of multiple wavevector excitations at each frequency to the exchange interactions. The asymmetric DMI, together with the symmetric exchange interaction, create the periodic modulation of exchange interactions for spins in chiral magnets and the period is controlled by the strength of DMI constant D and exchange stiffness A.

4.1.4 Conclusion

In summary, we reported confined spin waves formed by the sample boundaries in a bar-shaped bulk CSO sample explored by both broadband spin wave spectroscopy and micromagnetic simulations. In the simulations extremely short-waved spin waves were predicted beyond the experimentally observed dipole-dominated $\boldsymbol{k} \parallel \boldsymbol{M}$ modes. They were attributed to the DMI induced asymmetry of the dispersion relation and the periodic modulation of exchange interaction in chiral magnets. It has been proved that the wavelength and phase velocity strongly depend on the DMI strength. By increasing the DMI strength, a shorter wavelength can be achieved. Shorter exchange-dominated spin waves maybe further reached by using materials with smaller pitch vectors such as MnSi [66]. Our findings provide an alternative route for exchange-dominated spin wave excitation without the need of nanofabrication.

4.2 Helimagnons in the Chiral Soliton Phase of the Bulk Chiral Magnet Cu_2OSeO_3 Resolved by Brillouin Light Scattering

In this section, we focus on the spin dynamics of non-collinear chiral soliton (CSL), helical and conical phases resolved by BLS. Thanks to the high sensitivity of the BLS technique, we resolved the temperature- and field-dependent magnetic phase diagrams by virtue of clearly distinguishable thermal magnon spectra of CSL, helical, conical and FP states. Two modes were interpreted as CSL features. We further tuned the applied field directions and temperature to explore the stabilization mechanism and anisotropic properties of CSL in bulk CSO. It has been found that the CSL formation does not require the applied field $\mu_0\boldsymbol{H}$ to be perpendicular to the easy anisotropy axis but a projected field component was sufficient. Our results manifest that cryogenic BLS is an efficient tool to study locally spin excitations and to search for new phases in chiral magnets.

4.2.1 Magnon Modes in the Chiral Soliton Phase When Field Applied Along ⟨110⟩

BLS measurements were conducted on the bulk sample B3 in Table. 3.1. The sample sketch is shown in Fig. 4.11. It was placed in the crystat chamber of Fig. 2.7 on top of the sample holder and we focused the incident laser on the top polished surface. The sample was fixed by cryogenic glue directly on the Cu holder to guarantee thermal anchoring. The external magnetic field $\mu_0 H$ was applied in the **x**-**y** plane. By rotating the sample, we varied the angle θ of $\mu_0\boldsymbol{H}$ with respect to the crystallographic direction ⟨110⟩.

When the magnetic field $\mu_0 H$ was applied along ⟨110⟩ direction ($\theta = 0°$), we observed the transition behaviors among the known helical, conical and FP states by means of the thermal magnon spectra. The typical BLS spectra of ZFC/HFSD (refer to Chapter 2.4) at $T = 18$ K are shown in a color-coded graph in Fig. 4.12. The CSO sample was firstly saturated at 140 mT. H was then scanned to the negative field values. Selected lineplots of spectra for each phase are plotted in Fig. 4.13. When the applied field is above $\mu_0 H_{C2} = 74$ mT or below $\mu_0 H_{C2}' = -84$ mT, CSO is in the FP state. At $\mu_0 H = 100$ mT and $\mu_0 H = -100$ mT, the lineplots show only one peak in each spectrum which is consistent with the discussion in Fig. 2.9 and section 2.2.3. In between $\mu_0 H_{C1}$ and $\mu_0 H_{C2}$ (in between $\mu_0 H_{C1}'$ and $\mu_0 H_{C2}'$), the resonance frequency of the most prominent branch decreases when $\mu_0|H|$ increases. This field regime corresponds to the conical phase along ⟨110⟩ direction. We observe that at $\mu_0 H = 50$ mT and $\mu_0 H = -50$ mT, there are two peaks with different intensity in the lineplots. They are the +Q and -Q modes of the conical phase. Field dependencies of those two peaks are not fully identical because of the dynamic demagnetization effect in slice-shaped CSO sample [66].

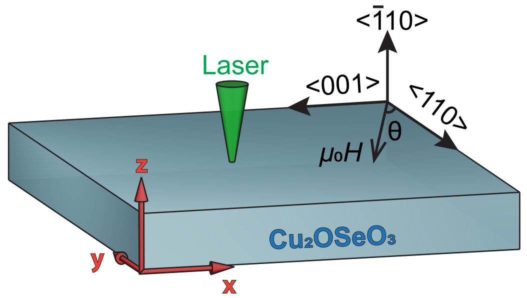

Figure 4.11 – **Schematic diagram of bulk-shape Cu_2OSeO_3 sample B3.**

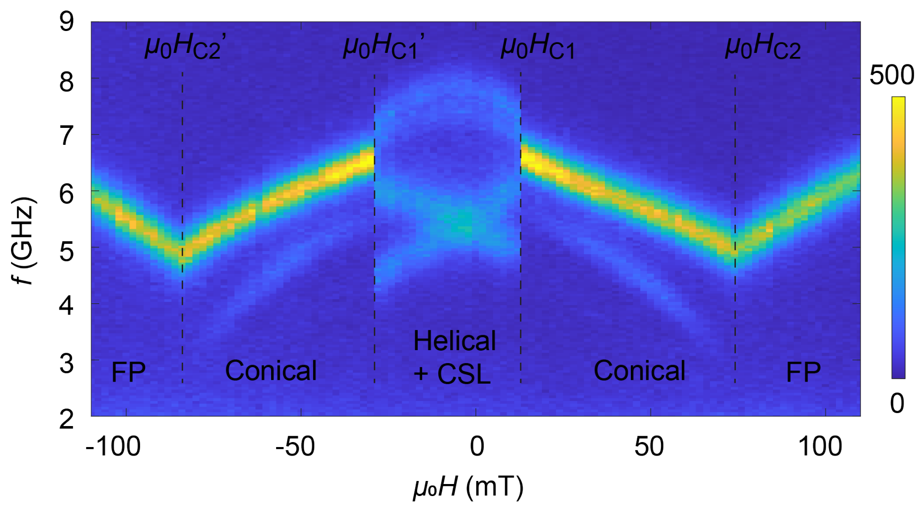

Figure 4.12 – **Typical BLS spectra obtained when field applied along ⟨110⟩ at T = 18 K.** The color bars represent the BLS intensity.

The discontinuous resonance frequency variations at $\mu_0 H_{C1}$ = 12 mT and $\mu_0 H_{C1}$' = -30 mT indicate a reorientation of the pitch vectors from the applied field direction to an easy axis direction and vice versa. The sample transits between conical and helical phases. At $\mu_0 H$ = 10 mT and $\mu_0 H$ = -10 mT, there are four resonances (see e.g. P_1, P_2, -Q and +Q in Fig. 4.13). Near 7.5 GHz there are the +Q and -Q modes of the helical phase and the other two peaks near 5.5 GHz are novel compared with the earlier reported spectra in Ref. [83, 85, 86, 93, 170] (introduced in Fig. 1.12 and section 1.3.3). They are interpreted as the CSL domains coexisting with the helical domains according to the magnetic field range and the crystallographic orientation of the magnetic field [95]. For the convenience of following discussion, we label these novel two peaks as P_1 and P_2 (P_1' and P_2'). Near 0 mT field, the P_1 and P_2 (P_1' and P_2') peaks merge into one peak labeled as P_0. When the magnetic field $\mu_0 H$ was scanned in the reversed direction from negative to positive fields after saturation at -140 mT, a hysteresis behavior was seen in the CSL, conical and helical (Fig. 4.14). Note that the appearance of mode P_0 near $\mu_0 H$ = 0 mT is also hysteretic.

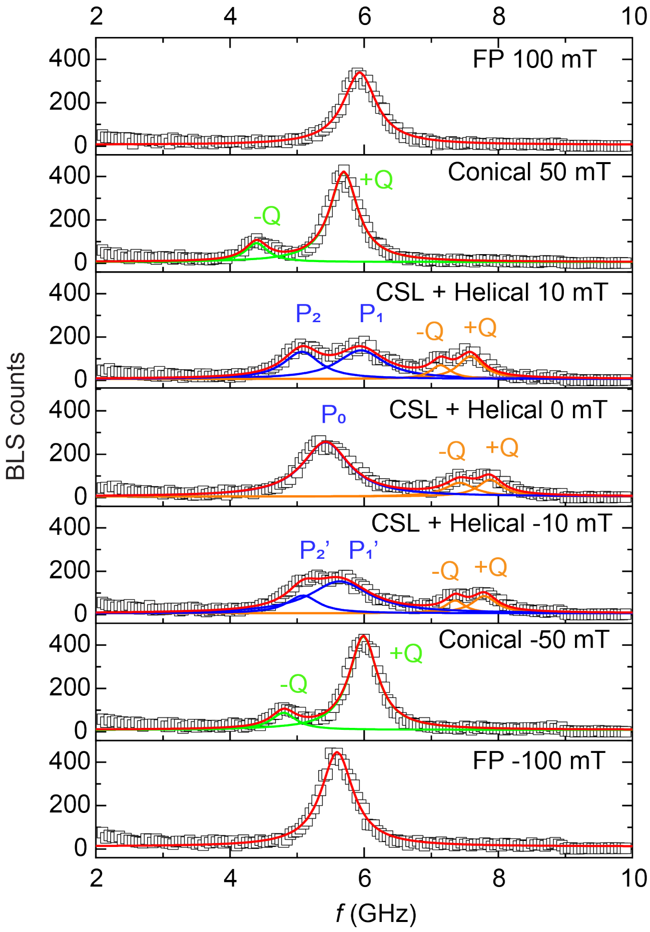

Figure 4.13 – **Lineplots of different phases when field applied along ⟨110⟩ at T = 18 K.** Solid lines are the fitted curves using Lorentz peak function. Red lines are the summed fitted curves. Green lines represent the +Q and -Q modes of conical phase. Orange lines represent the +Q and -Q modes of helical phase. Blue lines represent the modes of CSL phase.

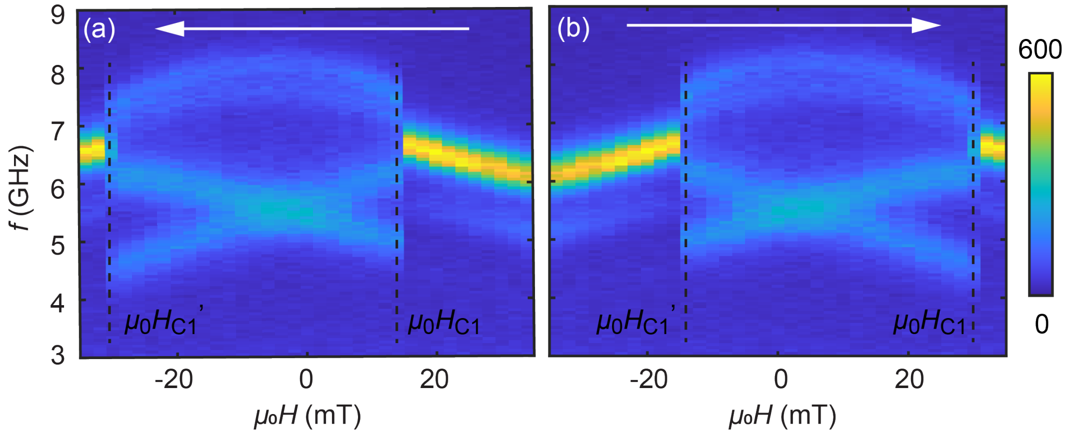

Figure 4.14 – **Field hysteresis behavior of the chiral soliton phase.** (a) Spectra of field scanning from positive to negative values at $T = 12$ K. (b) Spectra of field scanning from negative to positive values. White arrows indicate the field scan directions at $T = 12$ K. The color bars represent the BLS intensity.

4.2.2 Temperature Dependence of Chiral Soliton Lattice Resonances

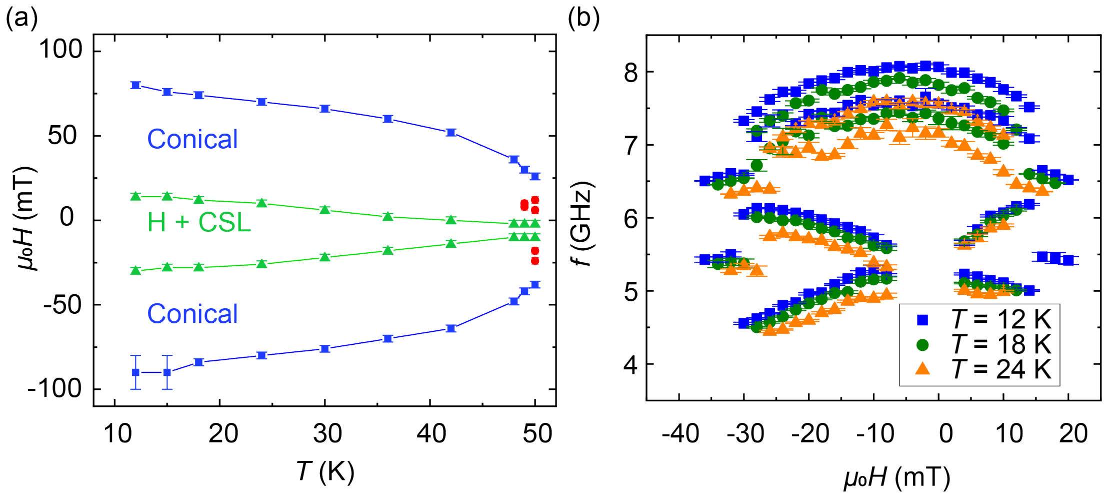

Figure 4.15 – **Phase diagram of bulk Cu_2OSeO_3 and temperature-dependent CSL resonances resolved by BLS when field applied along ⟨110⟩.** (a) Phase diagram resolved from the temperature- and field-dependent BLS spectra. Error bars indicate the field scan steps. (b) Resonance peaks fitted of different temperatures using Lorentz peak function. The resonance frequencies were extracted. Error bars come from the fits.

Temperature dependent spectra of ZFC/HFSD were taken from $T = 12$ K to $T = 51$ K in the central region of the CSO sample. The extra two peaks P_1 and P_2 existed up to $T = 51$ K as plotted in the phase diagram in Fig. 4.15. Above $T = 51$ K, the resonance peaks of non-collinear phases are below 1.4 GHz and they are unable to be separated from the BLS reference peak.

When the temperature exceeded 55 K, the peak intensity of the FP states was below the noise level. We hence allocate 55 K to be the temperature at which the CSO sample entered the paramagnetic phase. Compared with the reported Curie temperature $T_C \sim 59$ K [39, 104, 202], we estimated the temperature at the laser focused location to be about 4 K above the nominal temperature set by the PID system as introduced in section 2.2.2.

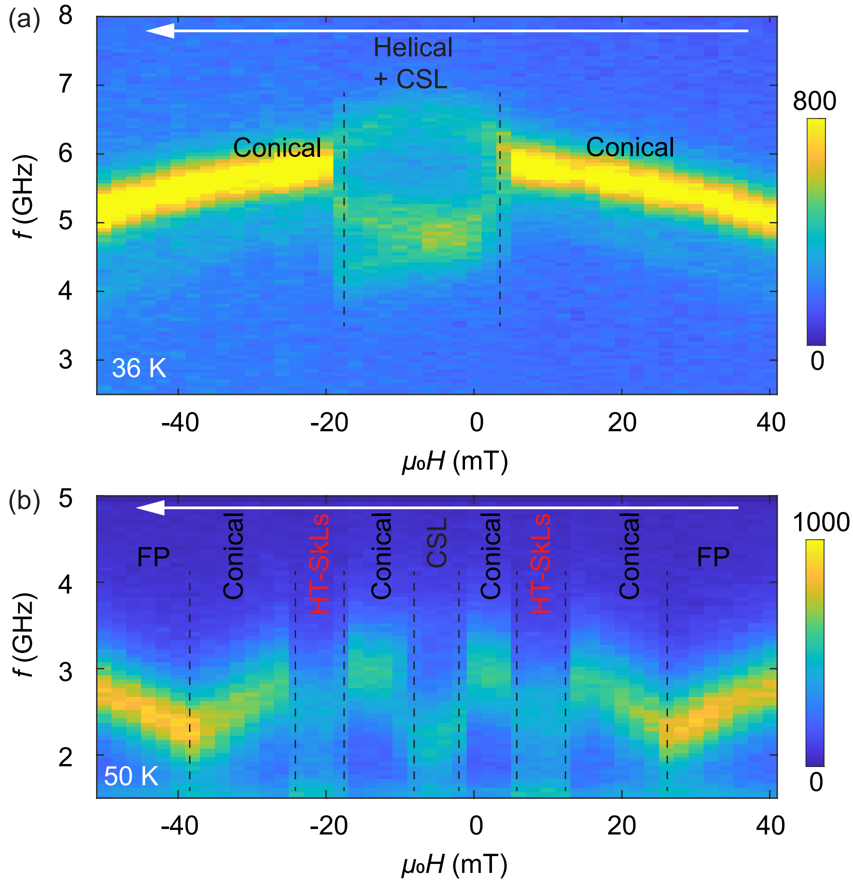

Figure 4.16 – **BLS spectra of field applied along ⟨110⟩ at T = 36 K and T = 50 K with ZFC/HFSD.** BLS spectra of ZFC/HFSD at (a) T = 36 K and (b) T = 50 K. White arrows indicate the field scan directions. HT-SkL represents the high-temperature lattices phase. The color bars represent the BLS intensity.

The fitted resonance peaks of multiple temperatures T = 12 K, 18 K and 24 K are summarized in Fig. 4.15 (b) for $\mu_0 H$ < -6 mT and $\mu_0 H$ > 2 mT. The absolute values of transition field $\mu_0 H_{C1}$ and $\mu_0 H_{C2}$ decreased when the temperature increased. The resonance frequency of both helical and CSL phases decreased with temperature increasing. We interpret the reason to be the decrease of the magnetic moment at higher temperature [203]. The frequency variation with changing magnetic fields $\mathrm{d}f/\mu_0\mathrm{d}H$ (if assume to be linear in this field range) of CSL resonances show two pair of similarity among themselves, e.g. at T = 12 K:

$$\begin{aligned}
\frac{\mathrm{d}f_{P1}}{\mu_0 \mathrm{d}H} &= (0.039 \pm 0.008)\ \mathrm{GHz/mT}\,,\\
\frac{\mathrm{d}f_{P2}}{\mu_0 \mathrm{d}H} &= (-0.022 \pm 0.004)\ \mathrm{GHz/mT}\,,\\
\frac{\mathrm{d}f'_{P1}}{\mu_0 \mathrm{d}H} &= (0.034 \pm 0.002)\ \mathrm{GHz/mT}\,,\\
\frac{\mathrm{d}f'_{P2}}{\mu_0 \mathrm{d}H} &= (-0.024 \pm 0.002)\ \mathrm{GHz/mT}\,,
\end{aligned} \tag{4.1}$$

These variation are similar at different temperatures. The agreements between P_1 and P_2' peaks and between P_2 and P_1' peaks suggest that the CSL resonances consist of two crossing branches. Those variation were hysteretic as discussed before for Fig. 4.14. The 4-peak characteristic of CSL resonances started to vanish at T = 30 K and less peaks were seen at temperature $T \geq 30$ K. We display in Fig. 4.16 the BLS spectra on CSL phase at T = 36 K and T = 50 K. At T = 36 K, resonance P_2 was invisible and resonance P_1 started to disappear. When reaching T = 50 K, only resonance peak P_2' can be still resolved. High-temperature SkL (HT-SkL) phase was seen in the spectra here.

4.2.3 Anisotropic Properties of Chiral Soliton Phases

BLS spectra at T = 12 K of both ZFC/FSU and ZFC/HFSD are plotted in Fig. 4.17 when the field $\boldsymbol{H}$ was rotated from $\theta = 0$ degree (along $\langle 110 \rangle$) to $\theta = 45$ degree and $\theta = 90$ degree (along easy axis $\langle 001 \rangle$). CSL resonance peaks appeared both in the configuration of $\theta = 0$ degree and $\theta = 45$ degree, but not in the configuration of $\theta = 90$ degree. The intensities of CSL resonance compared with helical and conical resonances change with field history. In order to compare the frequency and intensity differences of CSL phase under different angle θ and field histories, we show the lineplots at $\mu_0 H = 0$ mT of both HFSD and FSU at two field angles in Fig. 4.18. We define $\xi = \frac{\text{Magnons numbers from } P_0}{\text{Magnons numbers from } \pm Q}$ to represent the volume ratio of CSL domain and helical domain. The magnons numbers were calculated by reading out the area of fitting with Lorentz peak function. Here we use phase volume to describe the number of volume of each phases under the laser focus spot. The fact that $\xi < 1$ at $\theta = 45$ degree HFSD suggest that helical phase had a higher phase volume there (Fig. 4.17 (d)). CSO preferred to be transformed to helical

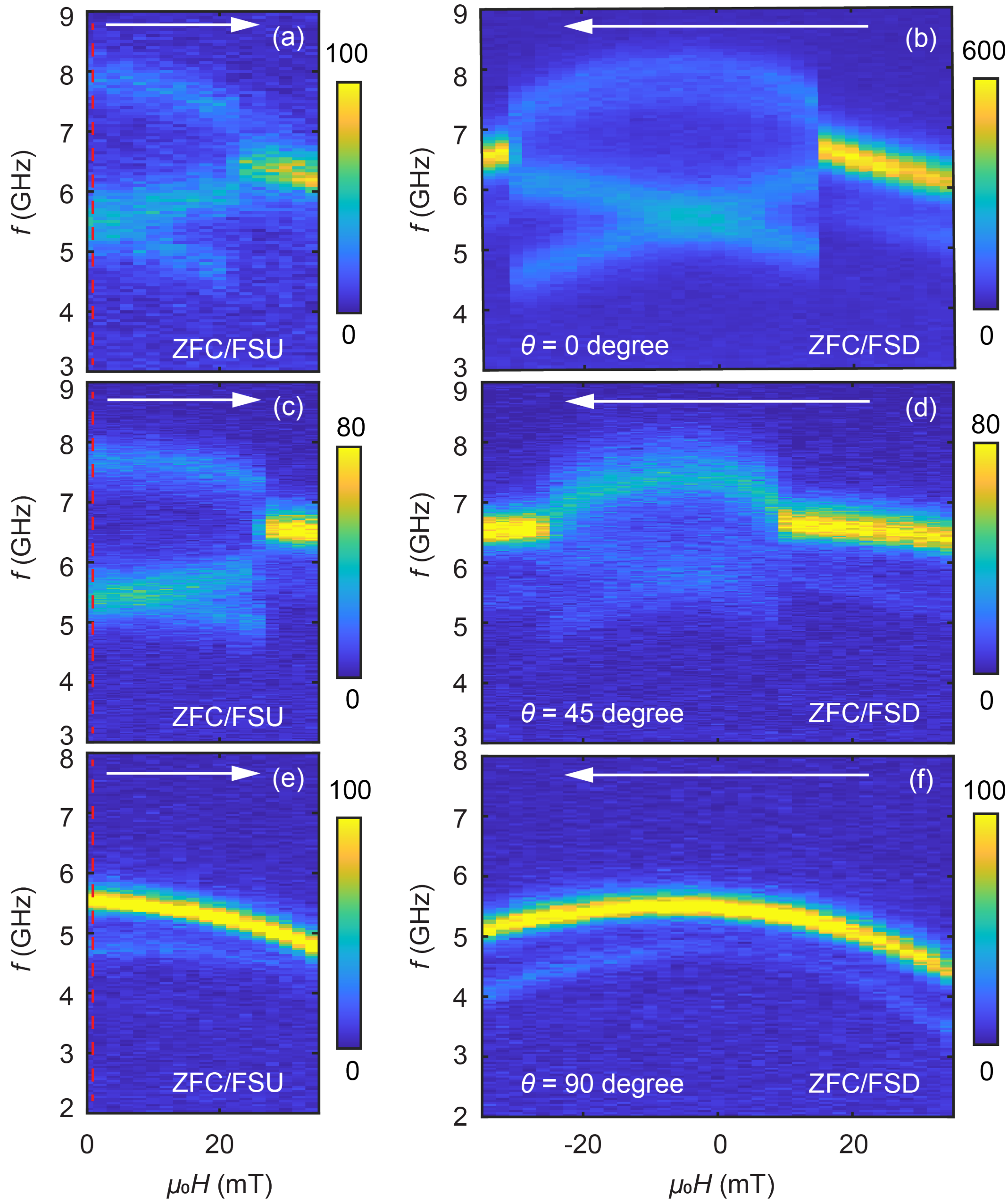

Figure 4.17 – **Anisotropic characteristics of chiral soliton lattices phase at T = 12 K.** Thermal magnon spectra mapped by Brillouin light scattering with three different magnetic field directions (a), (b) $\theta = 0$ degree, (c), (d) $\theta = 45$ degree and (e), (f) $\theta = 90$ degree. Two temperature versus magnetic field histories of ZFC/HFSD and ZFC/FSU are shown here, respectively. Red dashed lines mark the position we compare the resonances in Fig. 4.19. The color bars represent the BLS intensity. In between the measurements, we have changed detector in the BLS setup so there is difference in the intensity of the resonance peaks with the same data collecting duration.

phase than CSL phase. All the other three configurations own the $\xi > 1$ and are comparable to each other (Fig. 4.18 (a), (b), and (c)). It suggest that the phase volume of CSL was higher than helical phase in all these configurations. This offers us the possibility to control the CSL domains formation by changing the field history.

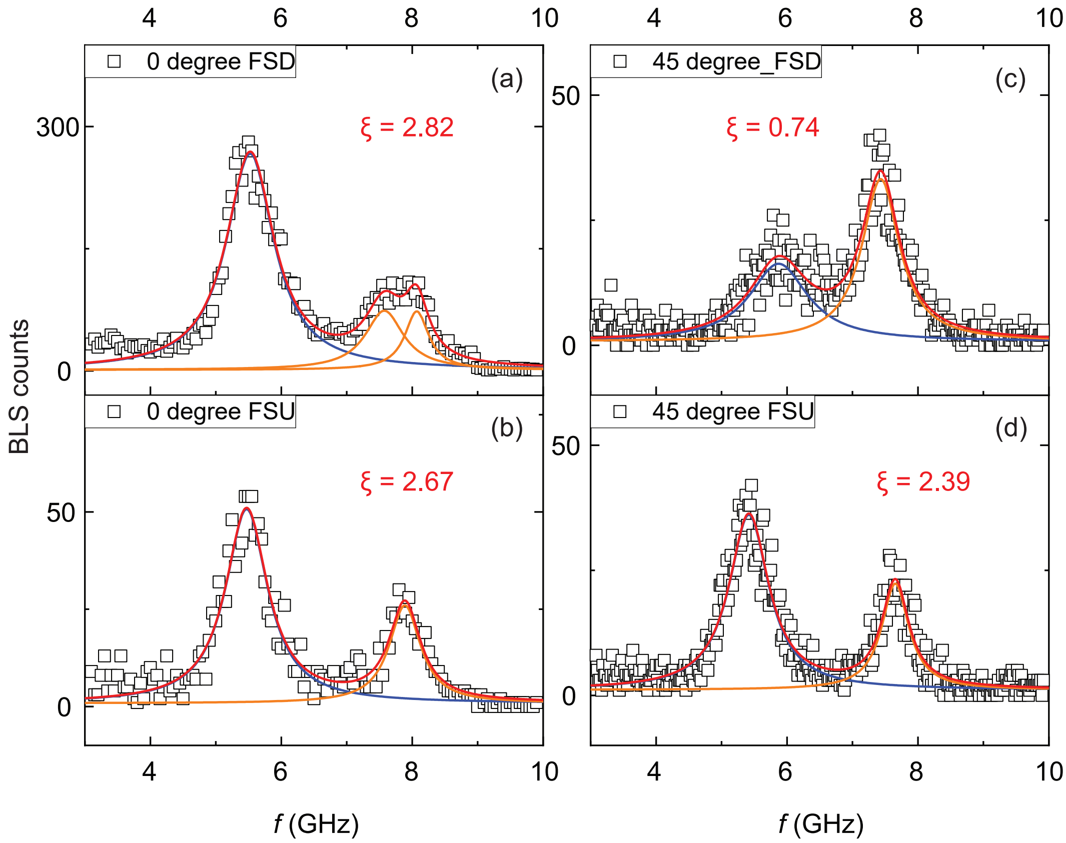

Figure 4.18 – **Line plots of HFSD and FSU when θ = 0 degree and θ = 45 degree.** ξ is defined as the ratio between the magnon numbers from peak P_0 of CSL phase and the magnon numbers from peaks +Q and -Q of helical phase. We calculate it by counting the ratio of fitted areas for the corresponding peaks.

We plot the spectra at 0 mT directly after ZFC in Fig. 4.19 (a) as indicated by the red dashed lines in Fig. 4.17. If two spectra share the same resonance frequency, then the origin of this resonance is identical. We have observed that the CSL resonance peak P_0 was near 5.5 GHz at θ = 0 degree and θ = 45 degree. It is notable that the +Q mode peak of helical phase at θ = 90 degree exhibits the same frequency. Thus we expect that the zero-field states of the CSL phase at θ = 0 degree and θ = 45 degree agree with the zero-field state of the helical phase at θ = 90 degree. When the field was applied along θ = 90 degree (along ⟨001⟩, Fig. 4.17 (e)), there is no frequency discontinuity for the helimagnon modes +Q and -Q when the helical phase transforms into the conical phase. This is a sign that the pitch vector does not undergo a reorientation. So we can attribute the state at θ = 90 degree at $\mu_0 H$ = 0 mT to a helical state with $\boldsymbol{q}_3$ along easy axis ⟨001⟩. Therefore, we deduce that the CSL phase at θ = 0 degree and θ = 45 degree share the state along the same axis of ⟨001⟩ and develop into a CSL when an external field is applied. At the same time, there is still the helical phase resonance peak at around 7.5 GHz. So the complete zero-field state at θ = 0 degree and θ = 45 degree consists of multi-domains including CSL along $\boldsymbol{q}_3$ and helical states along $\boldsymbol{q}_1$ and $\boldsymbol{q}_2$. The schematic diagram of the CSL is shown in Fig. 4.19 (b). We use L_{CSL} as the lattice constant of CSL and L_{H} for helical lattice.

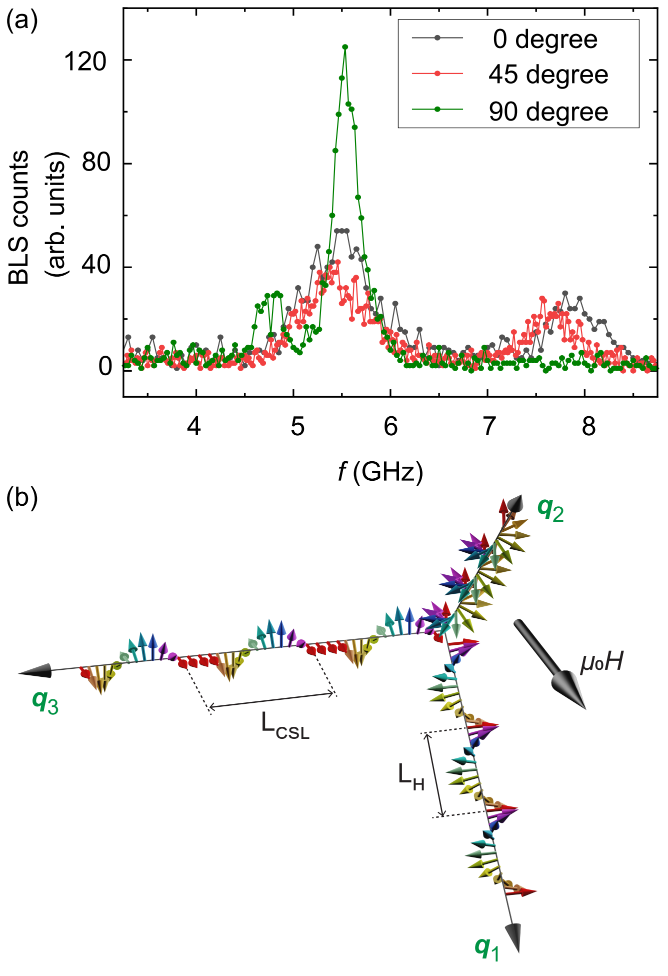

Figure 4.19 – **Resonances at $\mu_0 H$ = 0 mT indicating CSL axis.** (a) BLS spectra at $\mu_0 H$= 0 mT at T = 12 K with three different angles θ between applied field and ⟨110⟩. (b) Schematic diagram of CSL when θ = 90 degree. L_{CSL} (L_{H}) is the length of one unit of CSL (helical) states.

4.2.4 Discussion

In the following, we discuss the possible source of the CSL resonances and the stabilization processes of CSL phase at different field angles θ in our sample.

As stated in section 1.3.2, two type of modes were discovered in CSL phase in monoaxial chiral magnet $CrNb_3S_6$: Pincus mode from the surface spins and Kittel mode from the interior spins. In our experiment, bulk magnon was excited so we expect to see only Kittel mode from the interior spins in CSO. We attribute P_1 and P_1' to regions with local uniform magnetization. P_2 and P_2' modes are related to the soliton region, for which a breathing mode was expected. The local uniform region where spin precession contributed to P_1 when $H > 0$ mT will be tuned to soliton region contributing to P_2' when the magnetic field reversed to $H <$. Same process happened for the other regions concerning P_2 and P_1' in the reverse manner. Compared with the theoretical model of CSL dynamics in $CrNb_3S_6$ [173], two additional resonances P_1 and P_1' are only observed in our spectra on CSO sample. A possible explanation is the CSL structure may be different in monoaxial chiral magnet and cubic anisotropic chiral magnet.

Considering both the frequency of CSL resonances and lattice structure were determined by the local effective field, so we assume a dependence of L_{CSL} versus magnetic field from our observations on the field dependencies of the CSL modes. This does not agree well with the CSL observation in 200-nm-thick CSO lamella [95]. The shape of CSO sample and strain in the lamella are inferred to influence the lattice modification.

At $\theta = 0$ degree, our observation agrees with the double-transition process as stated in section 1.2.1 referring to Ref. [121]: $\boldsymbol{q}_3$ stayed metastable under magnetic field and the lattice structure was modified; $\boldsymbol{q}_1$ and $\boldsymbol{q}_2$ tilted toward the field direction and they hosted helical phase before H_{C1}. In the angular-dependent spectra, CSL exists on $\boldsymbol{q}_3$ in both $\theta = 0$ degree and $\theta = 45$ degree configurations, we conclude that CSL emerges not only when $\mu_0 H$ is perpendicular to one easy axis, but also when there is a projection of the field perpendicular to the easy axes. Compared with Fig. $\theta = 0$ degree, spectra at $\theta = 45$ degree shows a smaller frequency difference between P_1 and P_2 (Fig. 4.17 (a) and (c)). The field dependence suggested that the projection of $\mu_0\boldsymbol{H}$ is less efficient in modifying the lattice parameter L_{CSL}. Unlike the monoaxial chiral magnet, in CSO, there are three easy axes instead of only one c-axis. So the tilted magnetic field can not tilt the CSL at $\theta = 90$ degree in CSO.

In summary, we resolved the spin dynamics of CSL formed along the easy axis $\langle 001 \rangle$ in a bulk CSO sample when the magnetic field was applied along $\langle 110 \rangle$ axis. It consists of the resonances from both the uniform magnetized region and the soliton region. By tuning the field history, CSL dynamics emerged when the magnetic field was 45 degree tilted away. It disappeared when the magnetic field was applied along easy axes. The perpendicular projection of the field on easy axis helped to stabilize the CSL phase. From the dynamic behaviors, we conclude that the magnetic field modified the lattice constant of CSL. And the lattice modification was less efficient when the field was tilted. Our observation prove the existence of CSL in cubic anisotropic chiral magnet without tensile strain and provide the method to control the CSL domains formation by changing the field angle and history.

4.3 Skyrmion Lattices and Tilted Conical Phases in Bulk Cu_2OSeO_3 Revealed by Brillouin Light Scattering

In this section, we report the spin dynamics from multiple skyrmion phases observed in a bulk CSO sample when the field applied along the easy axis ⟨001⟩ and ⟨110⟩. By comparing the thermal magnon frequency and field dependence of different phases, we identify the high temperature hexagonal skyrmion lattices (HT-h-SkL) and low temperature hexagonal skyrmion lattices (LT-h-SkL) phases. We observed the nonreciprocal behavior of resonance mode in conical phase which is consistent with the theoretical model on dispersion relations of -Q mode and the unpublished macro-BLS result [182]. If not commented, the spectra were collected from Anti-Stokes side of BLS.

4.3.1 Spin Dynamics of High-Temperature Skyrmion Lattices Phase

The spectra of CSO at two temperatures and two field histories are compared in Fig. 4.20. According to Fig. 1.12 in introduction Chapter 1.3.3, we category them with different phases as FP, conical, helical and HT-SkL phase. It can be clearly seen that at T = 50 K the sample enters a specific phase between $\mu_0 H$ = 10 mT and 16 mT (Fig. 4.20 (b)) compared to T = 49 K (Fig. 4.20 (a)) when the field was scanned up from 0 mT. The additional low frequency branch near 2 GHz is a clear signature of a SkL phase, here the HT-h-SkL. Similar difference in the spectra were noticed in (c) and (d) for HFSD after saturation. To further look into the details, we plot the lineplots at different fields (phases) at T = 50 K in Fig. 4.21 and fit them with the Lorentz peak function. Some modes are only fitted partially because the resonance frequency is too close to the BLS limitation. There is only one resonance peak in the lineplot of the FP phase and conical phase (+Q mode). The frequency variation between conical and FP phase is continuous. The tilted conical phase does not appear. At 0 mT in Fig. 4.21 (a) for FSU and -4 mT in (b) for HFSD (an example from the low field range), we observe double peaks. They are absent when we reach lower temperature. We ascribe those double peaks to helical resonance originating from multiple pitch vectors along different easy axes with a small magnetic field.

In the spectra of HT-h-SkL phase, we observe two resonance modes. To see the clear frequency variation, we plot the extracted frequencies from Fig. 4.21 (b) and (d) in Fig. 4.22) near the transition field H_{C2} . In shaded regions between 10 mT to 16 mT in (a) and between 6 mT to 12 mT in (b), the mode at about 1.5 GHz follow the expected frequency tendency ($\Delta f/\Delta H >$ 0) of CCW mode and mode at about 2.2 GHz follow the slope $\Delta f/\Delta H < 0$ as BR mode of SkL [82, 83, 170, 202]. We observed the characteristic HT-h-SkLs modes also when the field was applied along ⟨110⟩ (extracted resonance frequencies in Fig. 4.22). In Fig. 4.22 (a) the shaded region varies in FSU field history to 6 mT to 14 mT. CCW mode data was not collected due to technical reason.

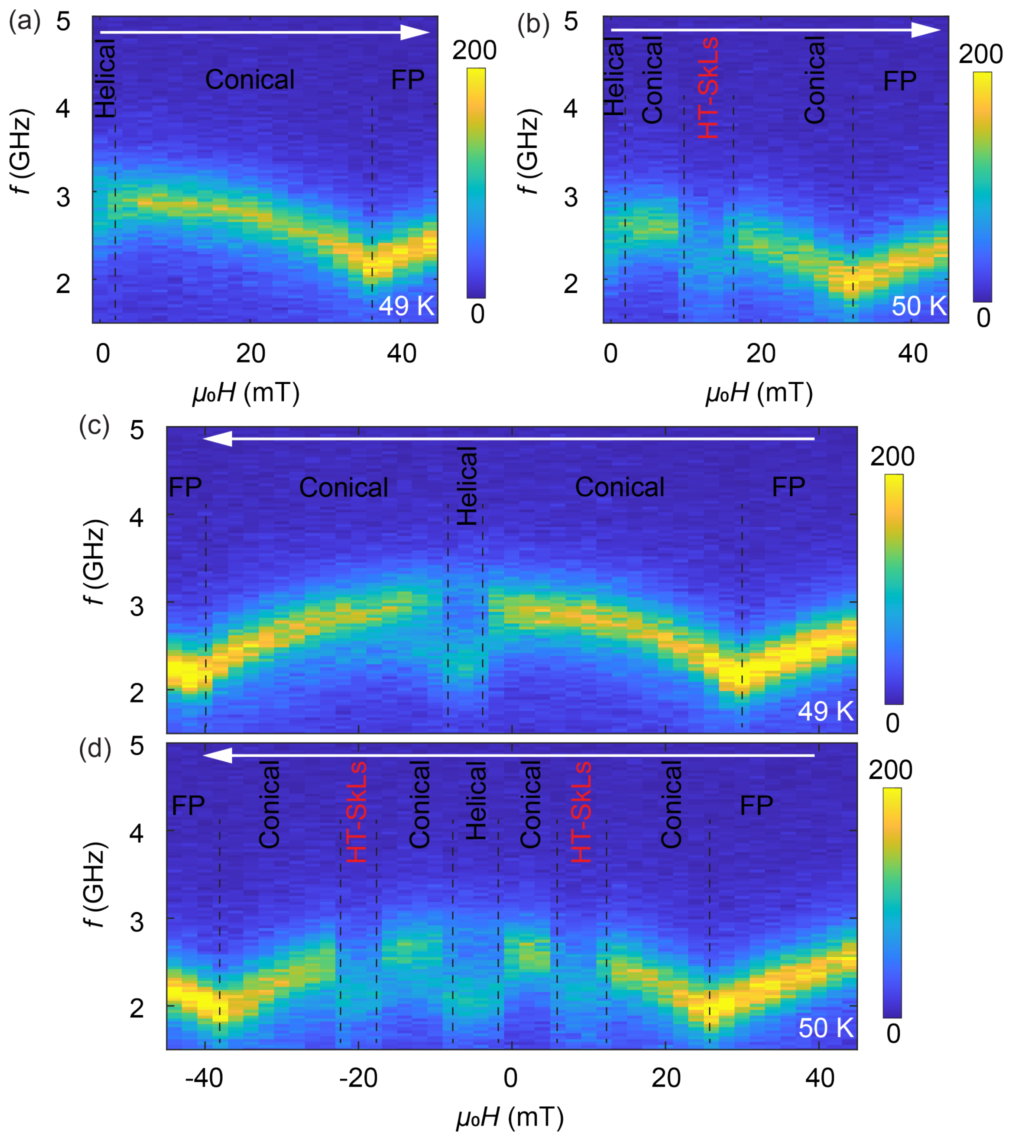

Figure 4.20 – **BLS spectra with a field applied along ⟨001⟩ at T = 49 K and T = 50 K with ZFC/FSU and ZFC/HFSD.** (a) and (b) BLS spectra of ZFC/FSU at T = 49 K and T = 50 K. (c) and (d) BLS spectra of ZFC/HFSD at T = 49 K and T = 50 K.

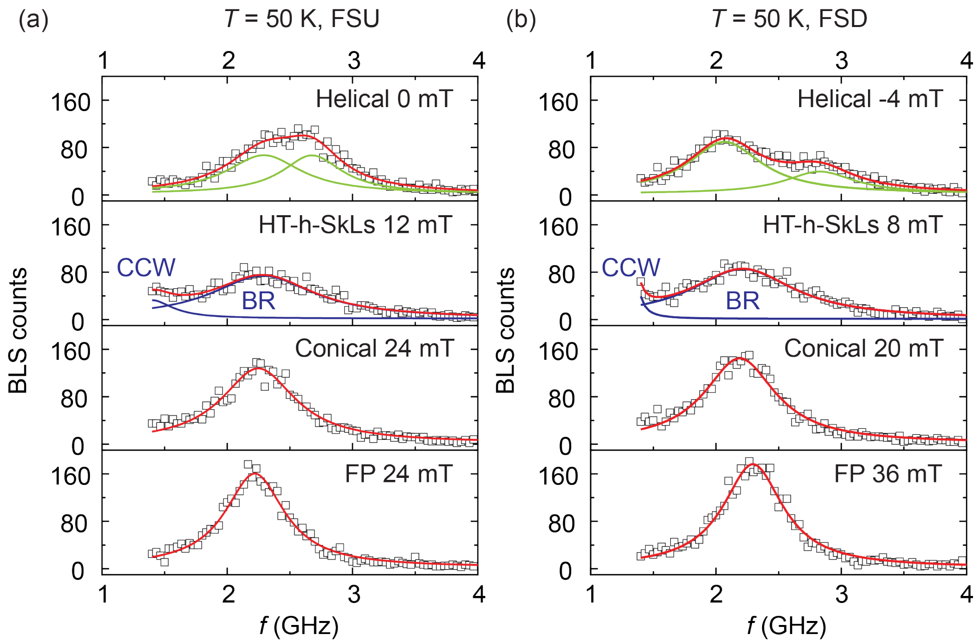

Figure 4.21 – **Lineplots of BLS spectra with the field applied along ⟨001⟩ performing T = 50 K with ZFC/FSU and ZFC/HFSD.** (a) Lineplots at T = 50 K for ZFC/FSU (hollow squares). (b) Lineplots at T = 50 K for ZFC/HFSD (hollow squares). Solid lines are the fittings with Lorentz peak function.

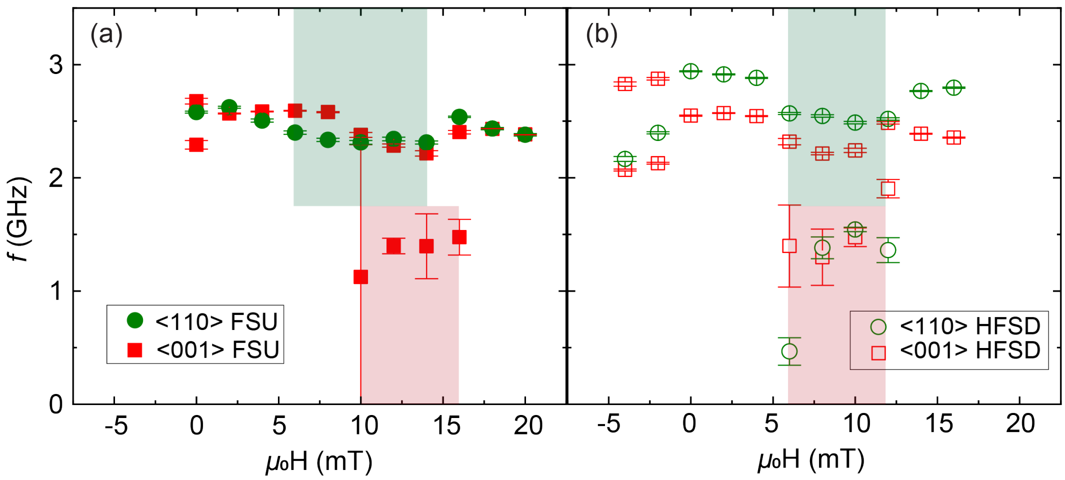

Figure 4.22 – **Extracted resonance frequencies versus magnetic field near the HT-h-SkLs pocket.** The solid and hollow squares and circles are fitted resonance frequencies versus magnetic fields with Lorentz peak function. Error bars come from the fitting. The light red and green shaded regions indicate the field region covered by the HT-h-SkL phase.

4.3.2 Spin Dynamics of Tilted Conical Phases at Low temperature

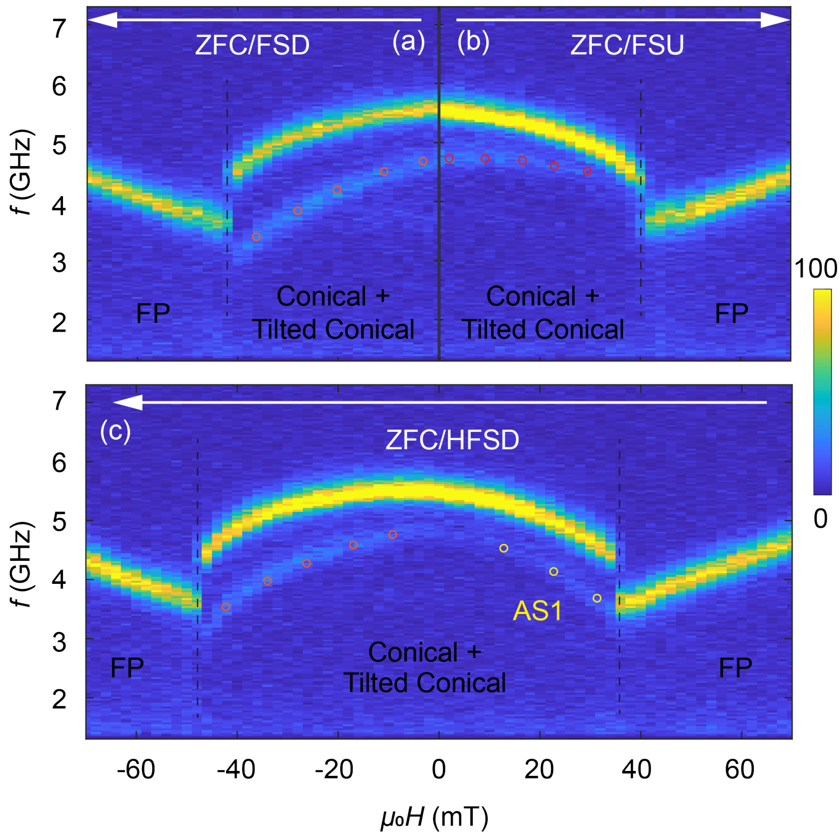

Figure 4.23 – **BLS spectra obtained when field applied along ⟨001⟩ at T = 12 K with ZFC/FSU and ZFC/HFSD.** (a) BLS spectra of field scanned from 0 mT to negative fields after ZFC. (b) BLS spectra of field scanned from 0 mT to positive fields after ZFC. (c) BLS spectra of ZFC/HFSD from 70 mT to -70 mT after saturation at 140 mT. White arrows indicate the field scan directions. Orange and red symbols indicate the -Q modes of conical phase. Yellow circles indicate the AS1 mode.

In Fig. 4.23 we show spectra that we obtained after the CSO sample had been cooled down with zero field applied. We increased the field values in positive (a) and negative direction (b). The field $\boldsymbol{H}$ was collinear with ⟨001⟩. We compare these data with spectra that we took after first saturating the CSO sample at 140 mT and then decreasing H as shown in Fig. 4.23 (c). Before each of these measurements, we heated up the sample to T = 100 K with zero field for at least 10 minutes. The spectra were taken with the laser focused in the center of the sample (at least 100 μm away from the sample edge). In all spectra, there is a frequency jump between the modes detected in the conical and FP phase. This feature indicated the formation of the tilted conical phase whose pitch vectors are not aligned with the external field but tilted toward to crystallographic orientation ⟨110⟩. The frequency jump reflects the pitch vector reorientation from the tilted direction to the applied field direction. Comparing the spectra of Fig. 4.23 (a) and (b), there are two branches in each spectra in conical and tilted conical phase. According to Ref. [66], these branches reflect the +Q and -Q modes of the tilted conical phase. The branches with the higher intensity agree with the features of +Q mode. The weaker branches, categorized as -Q mode, clearly lack mirror symmetry with respect to $H = 0$ (marked by orange and red open circles).

Asymmetries are also observed in Fig. 4.23 (c). The weaker mode is not continuous near 0 mT and is separated into two parts marked by orange and yellow circles, respectively. The orange-circled mode agrees with the -Q mode in Fig. 4.23 (a) and a mode resolved by macro-BLS in Ref. [182]. The yellow-circled mode has not been observed in Ref. [182] and we label it as AS1 ('AS' represents Anti-Stokes for BLS). When we reversed the field sweep direction where we saturated the sample at -140 mT and increased the magnetic field to positive values (data not shown), the -Q and AS1 modes were not hysteretic. The asymmetry was identical to Fig. 4.23 (c) with respect to $H = 0$. We conclude that the -Q mode of (tilted) conical phase has asymmetric dichroism for $\boldsymbol{H} \parallel \langle 001 \rangle$ but no magnetic hysteresis. The -Q and AS1 modes became symmetric with respect to $H = 0$ at a high temperature of 30 K when the tilted conical phase disappeared and only the conical phase existed. So the asymmetry may be only related to the tilted conical phase.

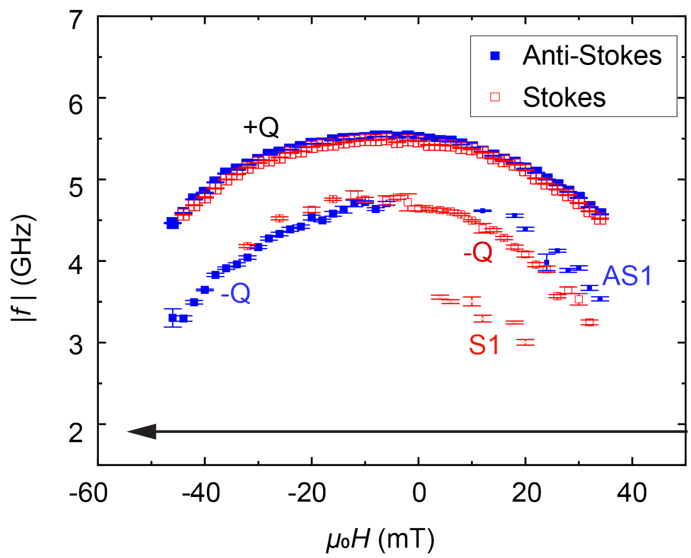

Figure 4.24 – **Extracted frequencies of resonances in the tilted conical phase extracted from Anti-Stokes and Stokes signals in BLS when field was applied along ⟨001⟩ at T = 12 K. We followed the protocol of ZFC/HFSD.** Blue solid squares are extracted frequencies from the Anti-Stokes side. Red hollow squares are extracted from the Stokes side. The black arrow indicates the field scan direction. The size of red and blue squares illustrates the intensities.

We compare the extracted resonance frequencies in tilted conical phase at the Anti-Stokes (positive frequency) and Stokes (negative frequency) sides in Fig. 4.24. We conducted the same measurements as in Fig. 4.23 (c) and collected both Anti-Stokes and Stokes signals. The +Q modes have the same tendency but a slight frequency difference averaged to be 0.04 GHz which is on the order of our experimental frequency resolution (0.33 GHz). The -Q modes (medium sized squares in Fig. 4.24) have mirrored characteristics. The data on the Anti-Stokes and Stokes sides reflect $-k$ and $+k$ magnons, respectively, and suggest that the asymmetric dichroism may be related to the polarization of the resonance modes. An additional mode near 3 GHz was observed with weak intensity in the Stokes spectra. It is labeled as S1 ('S' represents for Stokes). According to its low frequency, it may be a resonance related to the LT-h-SkL phase [87] which will be reported in the next section.

4.3.3 Spin Dynamics of Low-Temperature Skyrmion Lattices

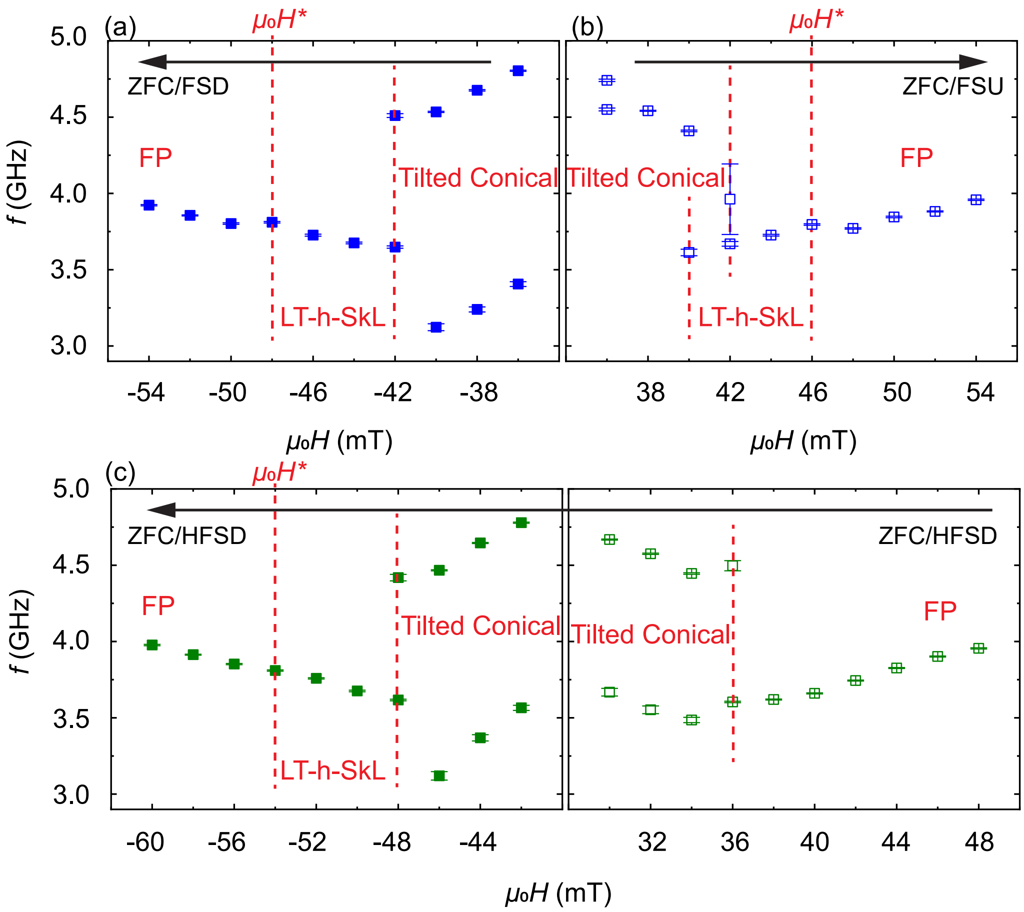

Figure 4.25 – **Extracted frequencies of resonances near transition field $\mu_0 H_{C2}$.** (a) Extracted frequencies of resonances from Fig. 4.23 (a) near H_{C2}. (b) Extracted frequencies of resonances from Fig. 4.23 (b) near H_{C2}. (c) Extracted frequencies of resonances from Fig. 4.23 (c) near H_{C2} on both field sides. Black arrows indicate the field sweep directions. Red dashed lines mark the phase transitions.

Figure 4.25 shows the extracted resonance frequencies f near H_{C2} and in the FP state from Fig. 4.20. A detailed inspection of the branches (compare open symbols) suggests changes in slope

$\Delta f/\Delta H$ at the field position H^* marked in the figure by long red dashed line. For these fields, CSO enters the FP state coming from the tilted conical state. Below H^* we attribute the branch to the CCW of the LT-h-SkL according to its field-dependent frequency variation and the field range [87]. This discontinuity is not clear for ZFC/HFSD at positive field near 36 mT which means LT-h-SkL does not appear in this case. The only difference with the other three cases is that CSO enters the tilted conical phase from the FP state. It evidences that the LT-h-SkL phase only can occur from the tilted conical phase, not directly from FP phase. This is consistent with the reports on the low temperature phase [94, 121]. When the field was swept down from FP to tilted conical phase (in the scenario of right panel in Fig. 4.25 (c)), LT-h-SkL was expected below $\mu_0 H$ = 36 mT. The slope $\Delta f/\Delta H < 0$ of mode S1 discussed in last section (Fig. 4.24) and their frequencies at about 3 GHz agrees with the signature of BR mode of LT-h-SkL phase [87].

4.3.4 Discussion

Comparing the BLS spectra with reported CPW-based spectroscopy results [82, 83, 170, 202], we notice agreements on spectra in HT-h-SkL, LT-h-SkL phases and differences in excitation configurations of those modes. Additional asymmetries in resonances of tilted conical phases were observed by comparing the Stokes and Anti-Stokes spectra. In the following, we will outline the comparison between the BLS spectra and CPW-based spectroscopy and discuss the asymmetric feature.

In the HT-h-SkL phase, both BR mode and CCW mode were excited at the same time (Fig. 4.20) different from previous CPW-based spectroscopy [81]. Due to the asymmetric dichroism of CW and CCW modes, the CW mode of the SkL and the -Q mode of the conical phase were predicted to obey a low intensity [85, 194]. This may be the reason that the CW mode and -Q mode are not resolved in the BLS spectra near T_C. The results on LT-h-SkL agree well with the explored phase diagram [94, 121] and the dynamic behaviors except for mode S1.

Asymmetric dynamic behaviors were observed for the S1 mode (suspected BR mode) in the LT-h-SkL phase, and the -Q and AS1 modes in the tilted conical phase. Lately the exploration of the conical phases with $\boldsymbol{H} \parallel \langle 001 \rangle$ using macro-BLS and the corresponding theoretical model showed a similar asymmetric behavior of the -Q mode which was due to the combined influence of Dzyaloshinskii-Moriya and dipolar interactions [182]. It explains the lack of both mirror symmetry and hysteresis of the -Q mode in our study. AS1 and S1 modes were not resolved in the reported macro-BLS experiments. A possible explanation can be that the domain formation is different in each sample considering conical, tilted conical, LT-h-SkL and their mixed states.

4.4 Stabilizing and Extending Metastable Skyrmion Lattices in Bulk Cu_2OSeO_3 Using Continuous-Wave Laser in Brillouin Light Scattering

In this section, we discuss metastable states under fast field cooling (FC) operation. When fast cooled down in a finite field H_{FC} corresponding to the HT-SkL pocket with the green laser on, the CSO enters metastable hexagonal skyrmion lattices (MT-h-SkL) locally. We find that the MT-h-SkL transforms into the newly discovered phase which we attribute to square skyrmion lattices (MT-s-SkL) or low temperature elongated hexagonal skyrmion lattices (LT-eh-SkL) when the magnetic field is decreased. Most crucially, we discover that the focused continuous-wave green laser of BLS extends the metastable SKL phase into the region of conical phase and create a track of SkL in CSO when the laser is moved in micrometer wide step. Our findings propose that the chiral magnets are promising for magnonic devices thanks to the rich magnon spectra originating from the multiple phases. The discovery of the phase control and the SkL track writing using a continues-wave laser pave the way for skyrmion-based memory devices and switches.

4.4.1 Stabilization of Metastable Skyrmion Lattices

The metastable skyrmion phases were stabilized by three control parameters in our experiment: cooling field $\mu_0 H_{FC}$, cooling rate and the presence of BLS green laser.

We cooled down the CSO sample in different cooling fields H_{FC} applied along $\langle 001 \rangle$ direction from 100 K to the target temperature of $T = 12$ K (Fig. 4.26) with the cooling rate 25 K/min. Each spectrum was taken at the ground state (with the cooling field still on) after the temperature stabilized for at least 10 minutes. When the sample was cooled with $\mu_0 H_{FC} = 0$ mT or 20 mT, only the $\pm$Q modes of conical phase were present. When cooled at $\mu_0 H_{FC} = 10$ mT, two further broad peaks were noticed below 2 GHz and near 4 GHz. For $\mu_0 H_{FC} = 13$ mT and 16 mT, these modes were more prominent and an additional mode at 4.8 GHz showed up. These peaks are related to the metastable hexagonal SkL (MT-h-SkL) because they only appeared when H_{FC} resided in the HT-h-SkL pocket. In Fig. 4.20 (b), the HT-h-SkL pocket exists from 10 mT to 16 mT (with $\pm$2 mT error bar from the field scan step). This field range is consistent with the cooling fields $\mu_0 H_{FC} = 10$ mT, 13 mT and 16 mT highlighting the additional peaks inferred as MT-h-SkL resonance modes. We label these modes by CCW, BR and CW. At $\mu_0 H_{FC} = 10$ mT, the +Q mode is still very strong and MT-h-SkL's modes are much weak. This result may be explained by the multiple domains in the sample when cooled down. The multi-domains scenario might also explain the remaining +Q peak for spectra with $\mu_0 H_{FC} = 13$ mT and 16 mT.

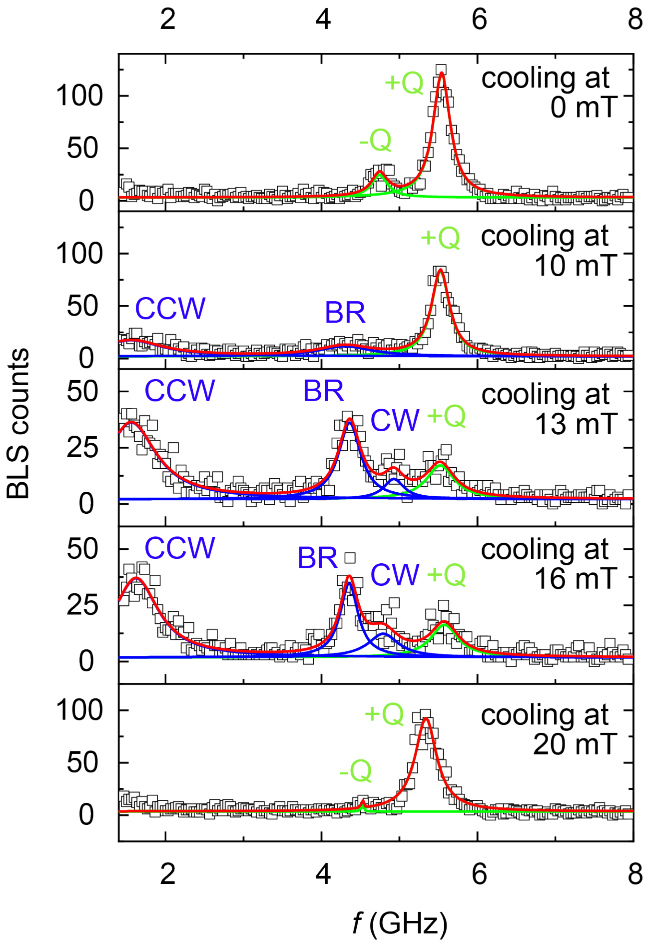

Figure 4.26 – **BLS lineplots of the ground states after field cooling down with different fields.** Hollow squares are the BLS data. The solid lines are the fitted peaks with Lorentz function. Light green lines represent the ±Q mode of (tilted) conical phase. Blue lines represent the SkL resonance modes. Red lines are the cumulative lines of all fitted curves in one spectrum.

Secondly, the cooling rate is decisive. We have conducted FC measurements with controlled cooling rates (Fig. 4.27). We use the excitation of the CCW and BR mode as a probe of the MT-h-SkL phase. Consistent with the literature [132], there is a cooling rate threshold of 6 K/min to generate an SkL at low temperature. Only when the system was cooled no slower than 6 K/min, the MT-h-SkL phase stabilized. We have noticed a new phase showing a dynamic resonance at about 4 GHz appeared between 0 mT to -20 mT together with MT-h-SkL phase. It is labeled as phase X. It will be discussed at the end of this section.

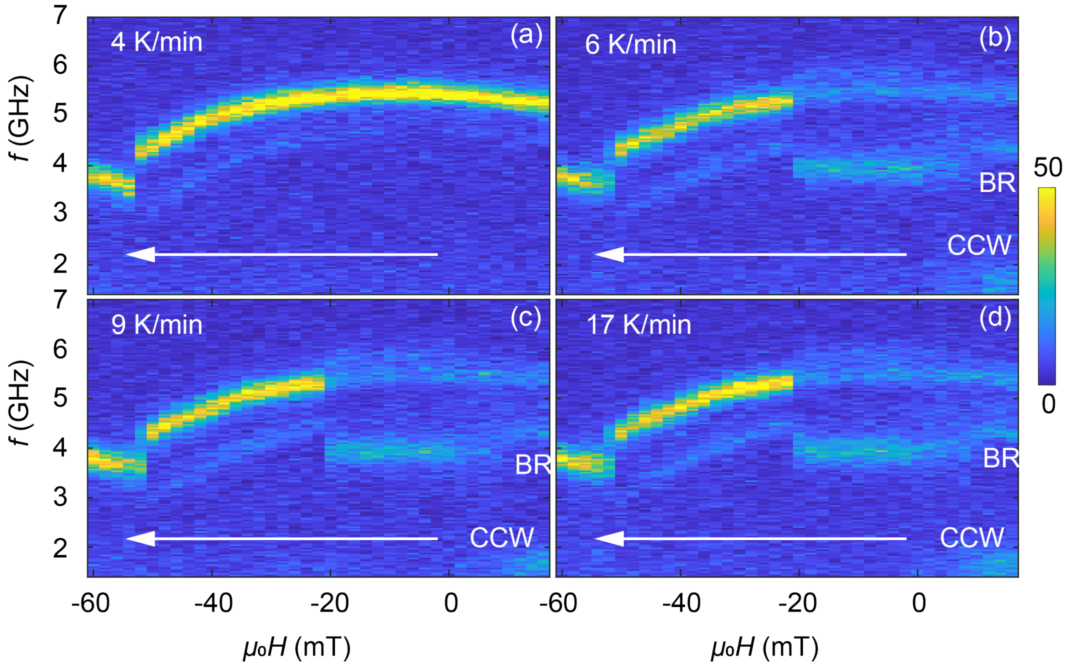

Figure 4.27 – **BLS spectra at T = 12 K with $\mu_0 H_{FC}$ = 16 mT and variable cooling rates.** The cooling rates are (a) 4 K/min, (b) 6 K/min, (c) 9 K/min and (d) 17 K/min. White arrows indicate the field scan directions.

For our experiment also laser illumination turned out to be essential. We conducted the AC susceptibility measurements on a CSO sample that was cut from the same big single crystal. The data are plotted in Fig. 4.28 (a) and (b). The skyrmion phase was observed at T = 57 K between 11 mT and 20 mT with ZFC/FSU. We further cooled down the sample with $\mu_0 H_{FC}$ = 15 mT with a cooling rate of 15 K/min to T = 15 K. When we scanned from the 15 mT to -80 mT, no evidence of the MT-h-SkL phase or phase X was seen. Near the phase transition at -52 mT, we see an enhanced susceptibility in conical phase when the spins were more and more aligned with teh external field and entered to FP state. The lack of both MT-h-SkL and phase X is consistent with our BLS data: $\mu_0 H_{FC}$ and cooling rate were not enough to stabilize the MT-h-SkL phase.

We fixed the laser power at 11 mW and cooled down the sample to T = 12 K with $\mu_0 H_{FC}$ = 16 mT and cooling rate 25 K/min. During this process, we kept the laser always on the sample at position A. There is clear CCW and BR mode and the peak X1 for phase X in the BLS spectra in Fig. 4.28. However, when we moved the laser to position B 300 μm away from position A, there was no evidence of resonances attributed to MT-h-SkL or phase X. Here the piezostage took about 1 second to move from A to B. We collected also the signals after focusing the laser for 10 minutes at B. No new signals were noticed. We further tested at other positions and found out that signs of metastable phases were still clear in a circle with a diameter of 50 μm centered around position A. The signals became weaker for larger separations and vanished in the noise level after 200 μm distance. Based on these observation, we conclude that the continuous-wave green laser is essential for forming the MT-h-SkL phase. Once formed, the phase was however hard to be erased. We tested demagnetizing the whole samples with fast oscillating fields and raising the temperature up to 300 K. After all the operations, the MT-h-SkL phase was found at position A even when cooled without laser. All those procedures were conducted in the vacuum chamber without ventilation.

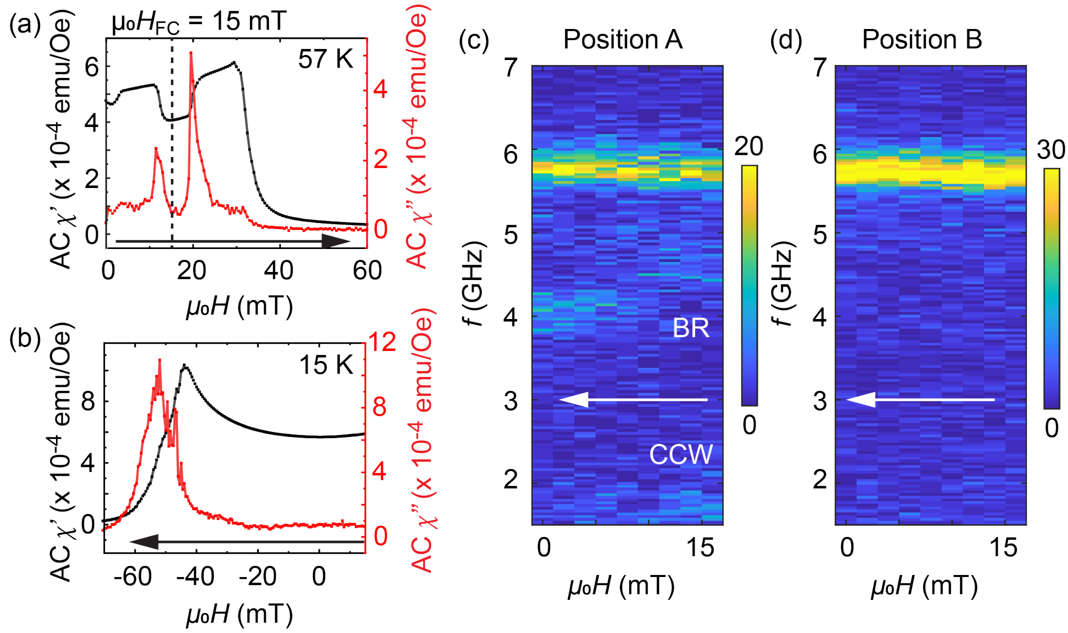

Figure 4.28 – **Metastable phases with/without laser on.** (a) AC susceptibility data collected at 57 K with ZFC/FSU. (b) AC susceptibility data collected at 15 K with FC with $\mu_0 H_{FC}$ = 15 mT and cooling rate 15 K/min. Black arrows indicate the field scan directions. (c) and (d) BLS spectra taken at location A and location B at 12 K with FC with $\mu_0 H_{FC}$ = 16 mT and cooling rate 25 K/min. White arrows indicate the field scan directions.

In relevant BLS spectra when MT-h-SkL is present we discovered peculiar dynamic behavior near 0 mT when the field was scanned from $\mu_0 H_{FC}$ to negative field values. We show relevant lineplots for $\mu_0 H_{FC}$ = 16 mT at T = 12 K. They are plotted in Fig. 4.29. We observe the three SkL modes and the +Q mode of conical phase at 16 mT. When sweeping the field to smaller value, a strong peak at 4 GHz appears which we label as Peak X1. Considering the branch variation depicted in Fig. 4.29 a new phase seems to exist near H = 0 mT and we label the resonances at 5.6 and 6 GHZ with X2 and X3, respectively. The peak near 3 GHz is from the setup instead of the CSO sample so it is not counted. From the phase diagram there are two possible sources of those resonances: the metastable square skyrmion lattice (MT-s-SkL) [134] or the low temperature elongated hexagonal SkL (LT-eh-SkL) [87]. In particular peak X1 shows almost no field dependency. This is similar to the dynamic modes of the LT-eh-SkL shown in the supplementary Fig. S4 of Ref. [87]. Phase X vanishes at $\mu_0 H$ = -22 mT when the ±Q modes of conical phase reappear. When further decreasing the magnetic field, phase transition appears. There is the narrow field range near H_{C2} where the resonances attributed to the LT-h-SkL phase are observed. Only BR and CCW modes can be identified. For $\mu_0 H <$ -50 mT, the CSO sample enters FP state.

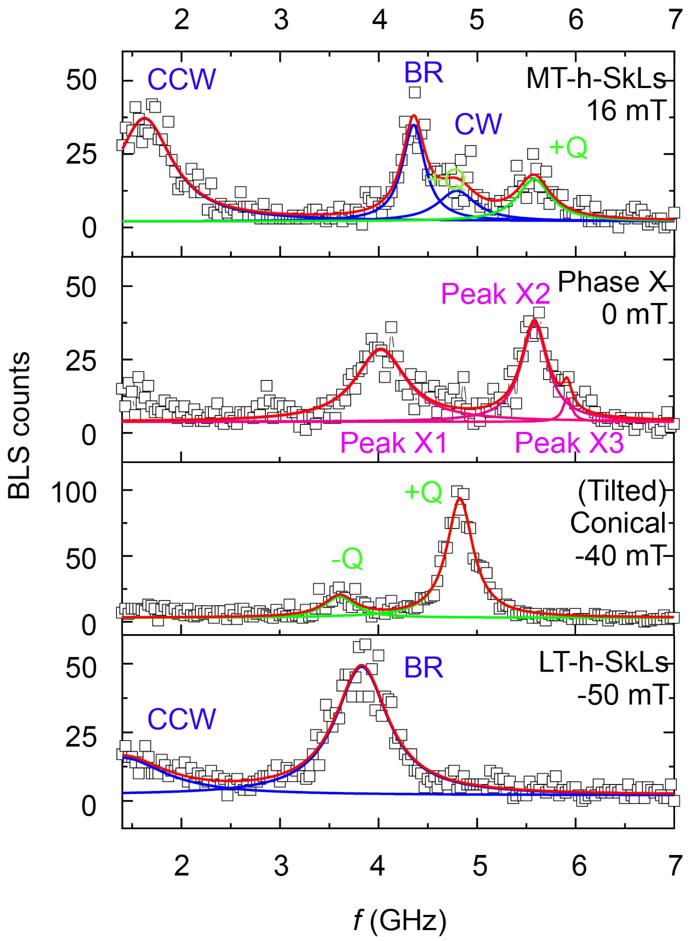

Figure 4.29 – **BLS lineplots of the different applied fields with $\mu_0 H_{FC}$ = 16 mT.**

Discussion on continuous-wave laser effect

According to the previous reports [135], MT-h-SkL phase was quenched in bulk shape CSO sample with big difference on crystallographic orientations. It is relatively hard for ⟨001⟩. Strain in a lamella-shaped sample or electrical fields were reported to stabilize the metastable states in CSO [95, 131, 135]. In our case, there are three possible mechanisms: strain, temperature gradient or an additional effect from the continuous-wave laser.

Firstly strain might originate from magnetostriction effect [204]. During fast cooling down, the temperature at the laser position is about 4 K higher than in the surrounding region. The laser region enters the magnetic state earlier and differently orientated domains can form with domain walls defined by the laser. Depending on the strength of the magnetostriction effect, local strain might emerge in the cooling process and introduce structural modification which survives the demagnetizing or warm-up process.

Second possible reason to be considered is the temperature gradient. It can create a torque described as thermal spin transfer (TST) torque [205]

$$\tau_{\mathrm{TST}} \propto |\frac{1}{M_S}\frac{dM_s}{dT}|\vec{\nabla}T \tag{4.2}$$

This may be helpful for inducing the SkL phase at low temperature. But it is unclear how to keep the metastable state at position A when increasing T to 300 K.

Thirdly, CSO is a insulator with bandgap of about 2.25 (2.45 eV) at 250 K (10 K) in CSO [206], comparable to the energy of the green laser we use for BLS (2.3 eV). During cool down, the laser can excite interband transitions. The excited electrons may be trapped in defects. So local electrical fields can be created and kept in vacuum. However, in order to make use of the magnetoelectric properties of CSO the electrical fields need to be applied on the polar axes which are active when the magnetic field is applied along ⟨110⟩ or ⟨111⟩ [84, 207]. In our case, the field was applied along symmetry axis ⟨001⟩ so there is no polar axis able to interact with an electrical field in this configuration. There maybe other effects related to the electrical field to be relevant here.

Further studies are needed, still as we show in the last section-the effect can be used to extensively generate extended domains of the metastable X-phase.

4.4.2 "Brushing" the Novel Phase X Using a Continuous-Wave Laser

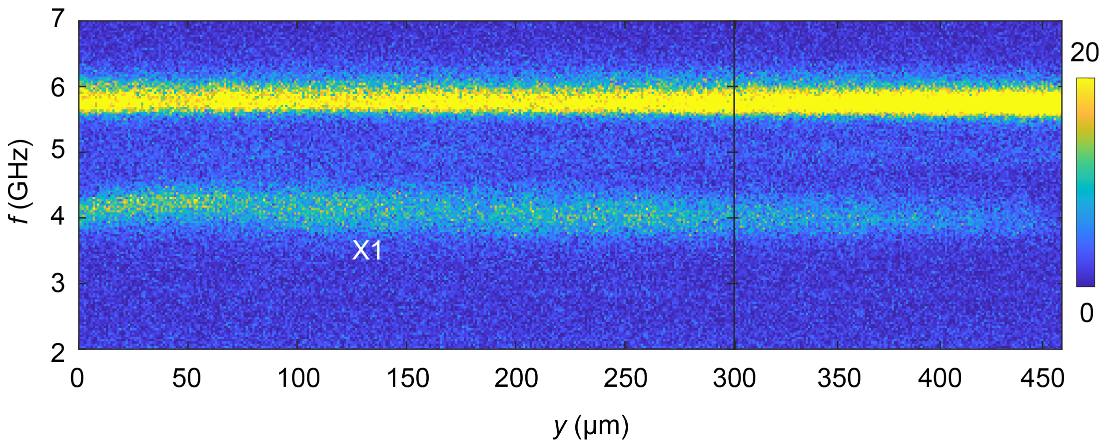

Figure 4.30 – **BLS spectra of brushing the skyrmion phases.** At $y = 0$, the sample was cooled with $\mu_0 H_{\mathrm{FC}} = 16$ mT and field was swept to $\mu_0 H = 0$ mT. The field was fixed at 0 mT and the laser spot was moved along y direction in steps of 1 μm.

The 11 mW continuous-wave green laser used in BLS is key for stabilizing the metastable states. We now show how it is used to expand ("brush") the phase X into regions of the conical phase. First, the metastable phase was formed underneath the laser spot after cooling with $\mu_0 H_{FC}$ = 16 mT. And phase X was appeared after we swept the field to $\mu_0 H$ = 0 mT. Second, we conducted BLS measurements with the laser moving away from position A in steps of 1 μm. At each position we measured the BLS spectrum. BLS spectra are plotted in Fig. 4.30. The resonances of phase X are at 4 GHz and 6 GHz. They existed up to y = 450 μm. When the laser approached 460 μm, the -Q modes of conical phase gradually appeared at about 5 GHz.

Hear flow has been reported to drive and tailor the skyrmion trajectories acting like an electrical current [208]. Very recent report on the observation of skyrmion lattice movement in CSO lamella driven by heat flow amount to about 11 mK/mm [209] provide a possible explanation on our founds. In the CSO sample with laser on, we estimate the in-plane temperature gradient to be in the range of Kelvin per millimeter. Refer to the explored skyrmion lattice movement velocities in Ref. [209], we expect the movement velocity higher than 0.15 mm/s. However when we measured the phase at position B after cooling down at position A and laser moving to position B (300 μm away from position A) for 10 minutes, there was no sign of phase change from conical phase to phase X. With movement velocity of 0.15 mm/s, skyrmion lattice should take only 2 second to reach position B from position A which is in contrast with our observation. So we expect extra effects in the "brushing" process working together with the heat flow.

From this observation, we conclude that the continuous-wave green laser helped us to brush the phase X into the region of conical phase. The intentional "writing" of a metastable phase is encouraging in designing devices based on non-collinear spin structures for both magnonics and spintronics.

4.4.3 Dynamic Behaviors of Metastable Phases

We plot the spectra and resonance frequencies extracted from the field dependent data in Fig. 4.31. For this dataset, the sample had been cooled to T = 18 K in $\mu_0 H_{FC}$ = 16 mT and then H was either increased (white right arrow) or decreased (white left arrows) in separate cooling cycles. We mark the regions from I to VI considering frequency jumps and non-monotonic variations of resonance frequencies as relevant signatures for phase transitions. From the reported BLS spectra in last section, the introduction on Fig. 1.12 in Chapter 1.3.3 and phase diagram of FC reported in Ref. [94], we category region I and VI as FP state, II as LT-h-SkL phase, III as conical phase (change to tilted conical phase near -44 mT), IV as the novel phase X, and V as the MT-h-SkL phase. In this section, we will focus on the unconventional dynamic features compared with reported VNA spectra [83, 87, 169, 170] and offer a new view from BLS data.

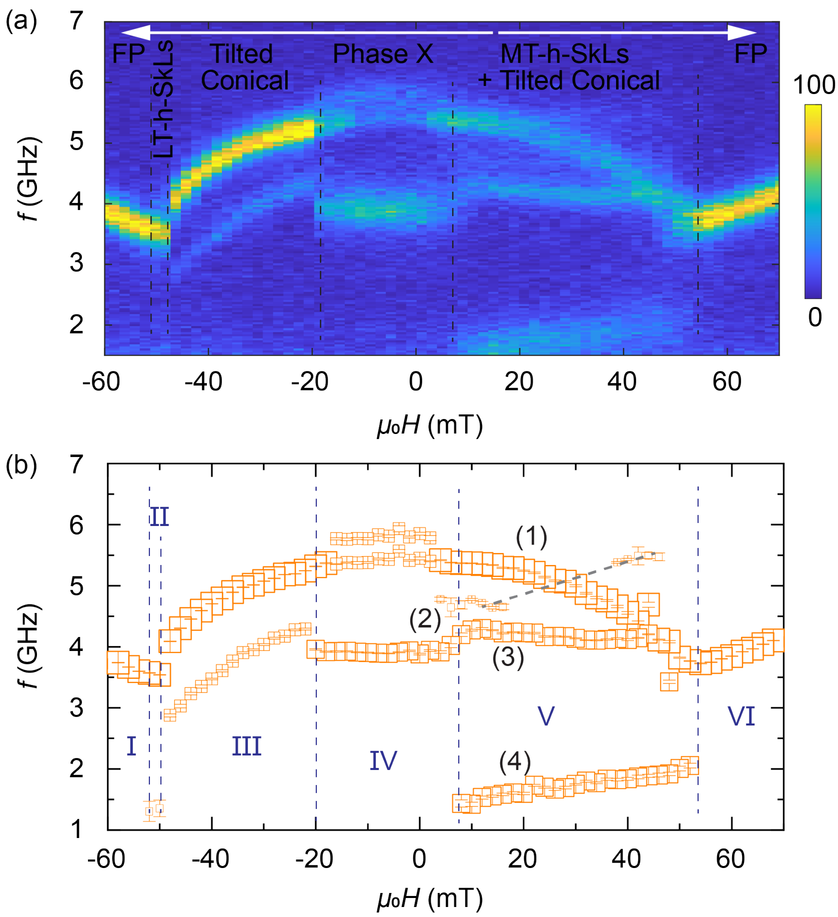

Figure 4.31 – **BLS spectra with *H* along ⟨001⟩ at T = 18 K with $\mu_0 H_{FC}$ = 16 mT.** (a) BLS spectra. (b) Extracted frequency from fitting. The size of orange squares illustrates the intensities. The vertical blue dashed lines indicate transition fields extracted from frequency jumps and non-monotonic variations of resonance frequencies. Gray dashed line illustrates the expected behavior of +Q modes.

CCW mode of MT-h-SkL phase

From 6 mT to 48 mT (region V), there are four modes labeled as (1) to (4). For mode (3), the frequency decreases with increasing field. This agrees with the characteristic of a BR mode. Mode (4) between 1.5 GHz to 2.1 GHz is at extremely low frequency compared with the other three modes. Such low frequency is usually attributed to the CCW mode of SkL. The slope $\Delta f / \Delta H$ agrees with the CCW mode [194]. Meanwhile BLS provides different excitation mechanism of magnons so more SkL resonance modes maybe seen [66]. From microwave excitation, only three CCW, CW and BR modes are known. However the frequency of mode (3) is too low compared to the BR mode (directly agreed with previous report) and reported frequency of CCW mode in MT-h-SkL phase [169]. We compare the frequency difference between mode (3) (BR mode) and mode (4) (suspected CCW mode) and notice the big difference with Ref. [169] which is the only report on complete spin dynamic mode in MT-h-SkL phase using all-electrical spin-wave spectroscopy. There maybe two possibilities [182]: cubic anisotropy lowers the CCW frequency at low temperature; or mode (3) is a phonon-like dynamic mode invisible for previously used microwave excitation and detection. Our data and the estimated data from Ref. [169] could provide the understanding of MT-h-SkL dynamics from complementary perspectives.

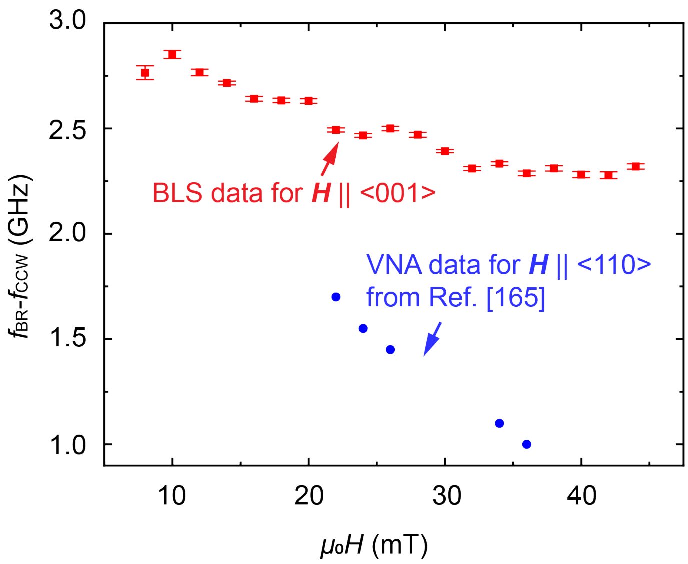

Figure 4.32 – **Frequency difference of BR and CCW mode of MT-h-SkL phase.** Red squares are extracted from our BLS measurements for $\boldsymbol{H} \parallel \langle 001 \rangle$. Blue circles are estimated from Fig. 3 in Ref. [169].

Interactional dynamics of CW modes of MT-h-SkL and +Q mode of conical phase

In Fig. 4.23, the crossing behavior is visible between mode (1) and mode (2). Mode (1) is very strong and continuous following the behavior of +Q mode of conical phase ($\Delta f/\Delta H < 0$) as plotted in Fig. 1.12. Mode (2) is weak. The extracted frequencies seem to follow the CW mode of SkL indicated by the gray dashed line ($\Delta f/\Delta H > 0$).

We plot another FC measurements at T = 18 K with $\mu_0 H_{FC}$ = 16 mT in Fig. 4.33. The only difference is the laser spot positions on the sample during two cooling process. All the other parameters are identical. In Fig. 4.33 mode (1) in region V evolves from +Q mode of conical phase at 16 mT. However the mode stays at a high frequency and its slope is not $\Delta f/\Delta H < 0$ as indicated by the dashed line. This curve with $\Delta f/\Delta H < 0$ illustrates the behavior expected for a +Q mode. Mode (2) starts at the CW mode of the SkL phase but it does not follow the expected frequency tendency ($\Delta f/\Delta H > 0$). For these branches we assume an avoided crossing [210–214] occurs due to a strong coupling between the CW and +Q mode. The gap is (0.58 ± 0.08) GHz. The anticrossing observed here is different to the one between the breathing mode and a dark higher-order clockwise gyration mode reported in Ref. [87]. There the LT-h-SkL phase resulted from the hybridization with a dark octupole gyration mode mediated by the magnetocrystalline anisotropies. The anticrossing in Fig. 4.33 is attributed to the modes of two different neighboring domains.

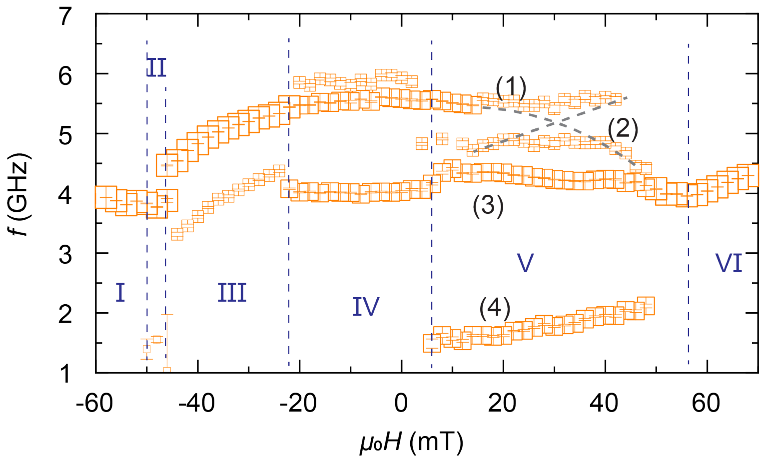

Figure 4.33 – **BLS spectra with Anticrossing feature with H along ⟨001⟩ at T = 18 K with $\mu_0 H_{FC}$ = 16 mT.** Extracted frequency from fitting. The size of orange squares illustrates the intensities. The vertical blue dashed lines indicate transition fields extracted from frequency jumps and non-monotonic variations of resonance frequencies. Gray dashed curves illustrate the expected behavior of +Q and CW modes.

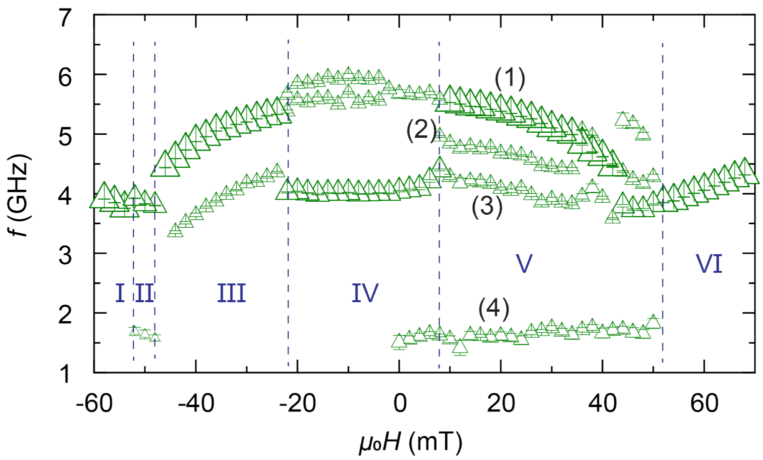

Figure 4.34 – **BLS spectra with H along ⟨001⟩ at T = 12 K with $\mu_0 H_{FC}$ = 10 mT.** Extracted frequency from fitting. The size of green squares illustrates the intensities. The vertical blue dashed lines indicate transition fields extracted from frequency jumps and non-monotonic variations of resonance frequencies.

Anticrossing were observed up to T = 30 K. In all 9 sets of data we collected for FC with $\mu_0 H_{FC}$ = 13 mT or 16 mT, the anticrossing feature appeared 7 times and the crossing feature only appeared 2 times. We deduce the appearance of the anticrossing is related to the laser probing locations with respect to the boundaries of multi-domains.

BLS spectra with $\mu_0 H_{FC}$ = 10 mT show the a different interactional behavior between mode (1) and mode (2). Mode (1) follows the +Q mode of conical phase clearly (refer to Fig. 1.12). The slope of mode (2) is modified to $\Delta f / \Delta H < 0$ which is in contrary to the conventional behavior of CW mode of MT-h-SkL ($\Delta f / \Delta H > 0$). Multi-domains with conical phase as majority domain is expected in this case highlighted by the strong +Q peak and weak SkL peaks in Fig. 4.26. Instead of being related to the laser probing position, it is more likely to be induced by the different domain compositions: conical domain as majority and MT-h-SkL domain as minority.

Non-reciprocity Resolved From Stokes and Anti-Stokes BLS Spectra

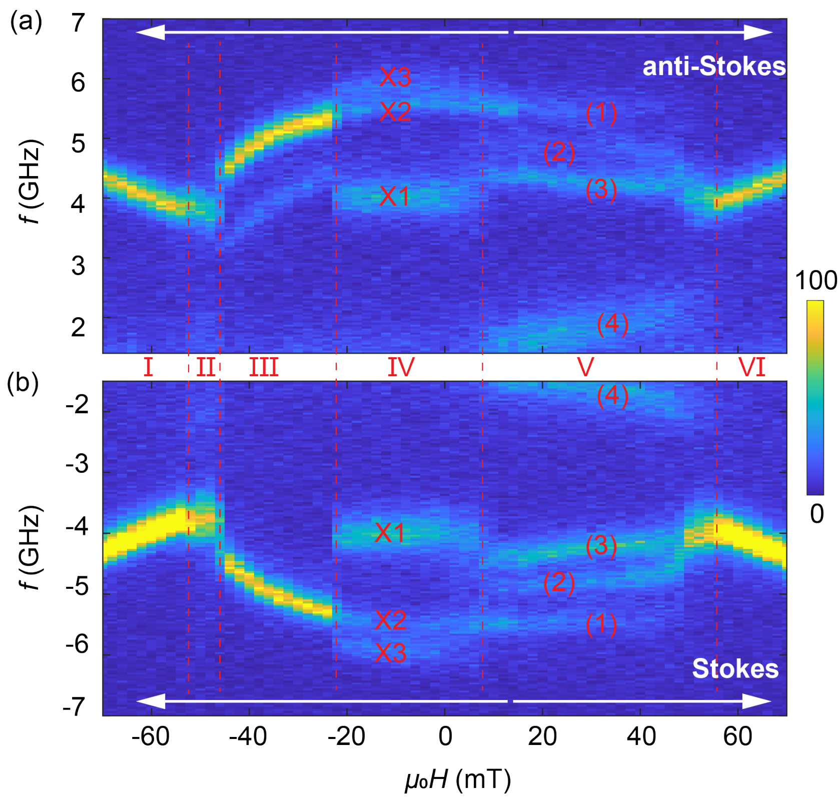

Figure 4.35 – **Stokes and Anti-Stokes BLS spectra obtained when field applied along ⟨001⟩ at T = 12 K with $\mu_0 H_{FC}$ = 16 mT.** (a) Anti-Stokes and (b) Stokes BLS signals of FC with 16 mT applied while cooling down.

We now investigate the non-reciprocity of the dynamic modes discussed above by comparing the Stokes (negative frequency) and Anti-Stokes (positive frequency) peaks. Both frequency sides of the FC measurements with $\mu_0 H_{FC}$ = 16 mT at T = 12 K are plotted in Fig. 4.35. The spectra can be subdivided into region I to VI. We note significant asymmetries in region III, IV and V. In region III, the non-reciprocity of -Q mode in tilted conical phase has been discussed in section 4.2.2. Region IV and V show significant difference in frequencies of mode X3 and mode (4) (CCW mode of MT-h-SkL).

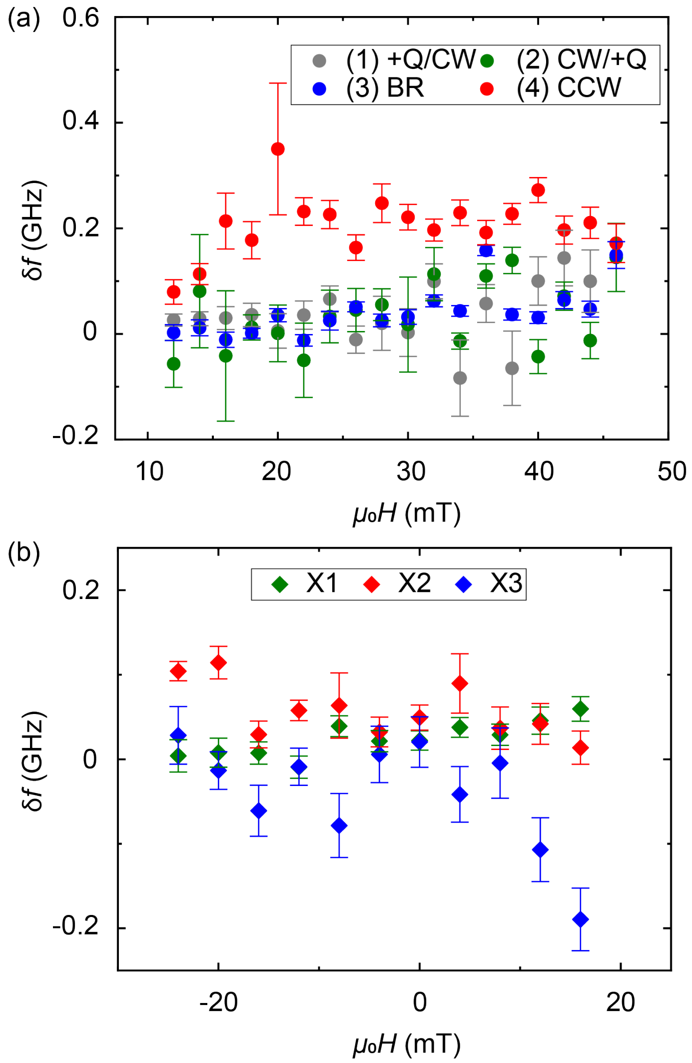

Figure 4.36 – **Frequency shifts between Anti-Stokes and Stokes signals of MT-h-SkL phase and phase X.** Frequency shifts between Anti-Stokes and Stokes signals of (a) MT-h-SkL phase and (b) phase X calculated from δf = $f_{\text{Anti-Stokes}}$ - f_{Stokes}. Error bars are calculated from Lorentz peak fitting.

In order to compare the asymmetries quantitatively, we plot the frequency shifts between Stokes and Anti-Stokes spectra in MT-h-SkL phase and phase X (Fig. 4.36) as δf = $f_{\text{Anti-Stokes}}$ - f_{Stokes}. In Fig. 4.36 (a), 4 modes in MT-h-SkL phase are compared. Anti-Stokes (-$\boldsymbol{k}$) peaks of mode (4) (CCW mode) are at higher frequency than Stoke peaks (+$\boldsymbol{k}$) and the frequency shift amount to about 0.2 GHz. δf shows a rough tendency of increasing with magnetic field. The frequency of other three modes are tiny but the increase tendencies of δf with magnetic field are also noticed. In phase X (Fig. 4.36 (b)), mode X3 exhibits a clear higher frequency in Stokes peaks (+$\boldsymbol{k}$) and the frequency shift increased with higher magnetic field. Mode X2 shows tiny but opposite frequency shifts that Anti-Stokes peaks (-$\boldsymbol{k}$) have a slight higher frequency. No clear frequency shift is found in mode X1 peaks.

Except for frequencies, asymmetries in peak intensities are seen in region I, IV, V and VI (Fig. 4.35). We show the typical lineplots of different phases in Fig. A.3 with peak fitting. Linewidths (FWHM) and areas of the peak from fitted data are summarized in Table. A.1, A.2 and A.3. Both Stokes peaks are stronger than Anti-Stokes ones in region I and VI reveals that the creation of magnons is more efficient than annihilation of magnons at low temperature T = 12 K in the FP state. The areas underneath the peaks show a ratio of about 2. Similar features are observed also in region IV (phase X) and V (MT-h-SkL phase) but with different ratio: 1.3 for peak X1 at $\mu_0 H$ = 0 mT; 1.4 for +Q mode, 1.3 for CW mode, and 1.6 for BR mode at $\mu_0 H$ = 16 mT. It should be related to the different magneto-optic constants for Anti-Stokes and Stokes processes [182].

Our results on asymmetries on both frequency and intensity of MT-h-SkL phase and phase X (suspected LT-eh-SkL) owns nonreciprocal dispersion relations In MT-h-SkL phase, frequency shifts induced by bulk DMI on CCW mode (when $\boldsymbol{k} \parallel \boldsymbol{H}$) was reported to be 0.07 - 0.08 GHz. From our BLS data, phase shift of about two to three times larger at 0.2 GHz were extracted when $\boldsymbol{k} \perp \boldsymbol{H}$. The nonreciprocal dispersion relation in conical phase were found in a similar configuration [182] which results from a combination of dipole and Dzyaloshinskii-Moriya interactions. Hence we deduce that the same mechanism can induce nonreciprocity in SkL modes as we observed. The large frequency shift of 0.2 GHz recommend the chiral magnet as a candidate of magnon diode in MT-h-SkL phase.

Temperature dependency of spin dynamics in the metastable skyrmion lattice phase

The frequencies of MT-h-SkL resonances were extracted at multiple temperatures from T = 12 K to T = 42 K (Fig. 4.37). The three modes varied differently with T. CCW modes remained below 2.1 GHz and their frequencies decreased only slightly with the increasing temperature. Between 2 GHz to 4.5 GHz, the resonances of BR modes were observed and decreased significantly with increasing temperature. For instance, the frequency difference between 42 K and 30 K amounted to about 0.7 GHz and about 0.3 GHz between 30 K to 18 K. The CW modes were extracted near 40 mT from 12 K to 30 K showing a similar tendency as the BR modes. Above 30 K, the CW mode was not resolved.

According to the literature [87, 203], there are two main parameters modifying the frequencies when the temperature varies: saturation magnetization and cubic anisotropy. The variation of saturation magnetization with respect to temperatures agree with the frequency variation we observed on BR and CW modes [203]. Concern the cubic anisotropy, it has been theoretically calculated that the frequency of SKL at low temperature in CSO is lower when the K_U is higher [87]. However the exploration on temperature dependent cubic anisotropy strength were not yet reported in chiral magnet CSO. The different frequency variation with temperature among CCW, BR and CW mode implies that their dispersion relations are influenced differently from saturation magnetization and cubic anisotropy.

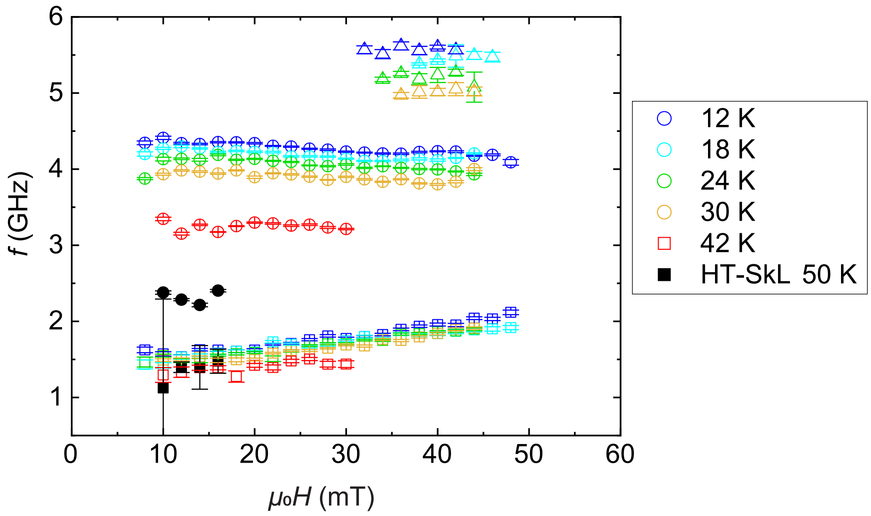

Figure 4.37 – **Resonance frequencies of MT- and HT-h-SkL at different temperatures.** Resonance frequencies were extracted from the fitting using Lorentz functions. Colors represent different temperatures. Triangles indicate the CW modes. Circles indicate the BR modes. Squares indicate the CCW mode. The filled black circles and squares are extracted from the HT-h-SkL phase representing the BR and CCW mode, respectively.

4.4.4 Discussion

In the following, we discuss the possible reasons for the interactional dynamics between CW mode in MT-h-SkL phase and +Q mode in conical phase (crossing and anticrossing).

Domain formations revealed by dynamic behaviors of CW mode and +Q mode

Anticrossing and crossing behaviors between CW mode in MT-h-SKL phase (mode (2)) and +Q mode in conical phase (mode (1)) in region V were both observed. Anticrossing which reflects strong couplings between SkL domain and conical domain was more often seen with about 78% among our experiments. The important parameter here is the laser probing location on the CSO sample. We propose a d_D-multi-domain model as an explanation in which the domains owning a dimension (diameter or length) d_D comparable with our laser spot (Fig. 4.38). When we focus the laser spot at position 1, +Q mode of conical phase dominates and owns a stronger intensity. Because there is scattering of the laser inside the CSO samples, so we can still collect SkL modes but not hybridized with +Q mode of conical phase. When we focus the laser spot at position 2, domain boundaries dominate the dynamic behavior and couplings between two phase emerge at the boundaries. As anticrossing is statistically preferred, we assume that the size of the domains d_D should be comparable with the laser spot size so boundaries are often spotted by the laser. In our experiment, the laser amount to about 5-8 μm depending on the temperature. Hence we conclude the domain size d_D should be in the same order. The SkL domain sizes of about 20 μm at T = 57 K was reported in CSO using the technique of resonant magnetic x-ray diffraction [215]. Our result is not far from the reported value and it holds until T = 30 K. The difference suggests that the domain size may have temperature dependency.

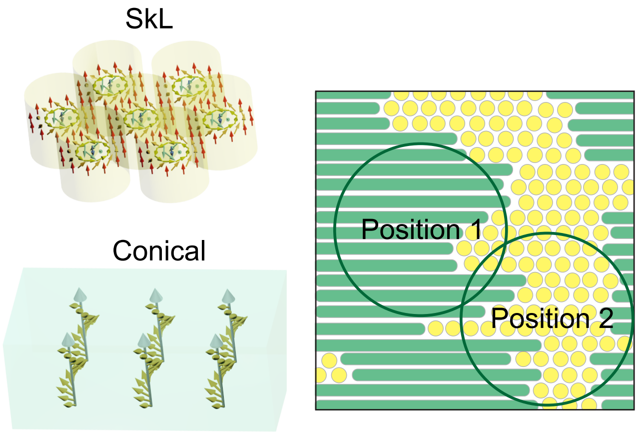

Figure 4.38 – **Sketch of BLS laser probing positions with respected to the multi-domains.** Yellow circles represent skyrmion tubes. Green stripe represent conical lattice. Dark green circles indicate the BLS laser spot at position 1 and position 2.

5 Spin Dynamics in Fe/Gd Multilayers with Perpendicular Magnetic Anisotropy at Room Temperature

In this chapter, we report the spin dynamics of dipole skyrmions, domains and domain walls in Fe/Gd multilayers with nano grating elements utilizing scanning transmission X-ray microscopy (STXM). It will be organized in 4 sections. In section 5.1, the magnetic characterizations with magnetic force microscopy (MFM) and all-electrical spin-wave spectroscopy are presented. In section 5.2, we report magnetic states after integrating nanomagnet arrays utilizing STXM. In section 5.3 and 5.4, we investigate the spin dynamics of dipole skyrmions and domains in Fe/Gd multilayers with nanomagnet arrays utilizing the time-resolved STXM. In section 5.5, we report the magnonic grating coupler (GC) effect observed in Fe/Gd multilayers with one-dimensional Co nanomagnet arrays.

5.1 Magnetic Characterization of Bare Fe/Gd Multilayers

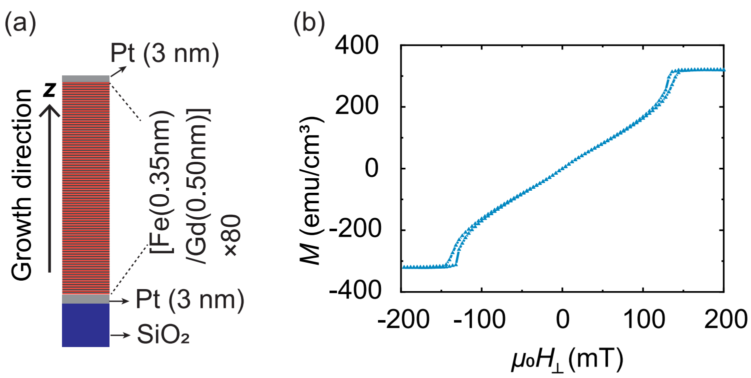

Figure 5.1 – **Magnetic hysteresis of Fe/Gd multilayers with out-of-plane field.** (a) View of cross-section of the Fe/Gd sample. (b) Hysteresis loop with out-of-plane field $H_{\perp}$.

The amorphous Fe/Gd multilayers (Fig. 5.1 (a)) were studied by magnetization measurements (Fig. 5.1 (b)), magnetic force microscopy (MFM) and ferromagnetic resonance (FMR) using all-electrical spin-wave spectroscopy. We analyzed material parameters, such as the perpendicular magnetic anisotropy (PMA), saturation magnetization, exchange constant, and damping parameters.

5.1.1 Phase Diagram of bare Fe/Gd multilayers

The Fe/Gd multilayers were grown in a ultra high vacuum (UHV) environment under 3.5 μbar argon pressure at room temperature by DC-magnetron sputtering. The substrate is a Si (100) chip coated with 100-nm-thick SiO_2 layer. Ultra-thin Gd and Fe layers are grown alternatively for multiple times, e.g. 0.5 nm-chick Gd and 0.35 nm-thick Fe for 80 times as sketched in Fig. 5.1 (a). The hysteresis loop (Fig. 5.1 (b)) detected by a superconducting quantum interference device (SQUID) provided the out-of-plane saturation magnetization. $\mu_0 M_S = 0.4$ ($\pm$ 0.001) T was extracted at $\mu_0|H_\perp| > 150$ mT. Both the multilayers growth and the SQUID characterization were conducted by Michael Heigl and Prof. Manfred Albrecht from Institute of Physics, University of Augsburg, Germany.

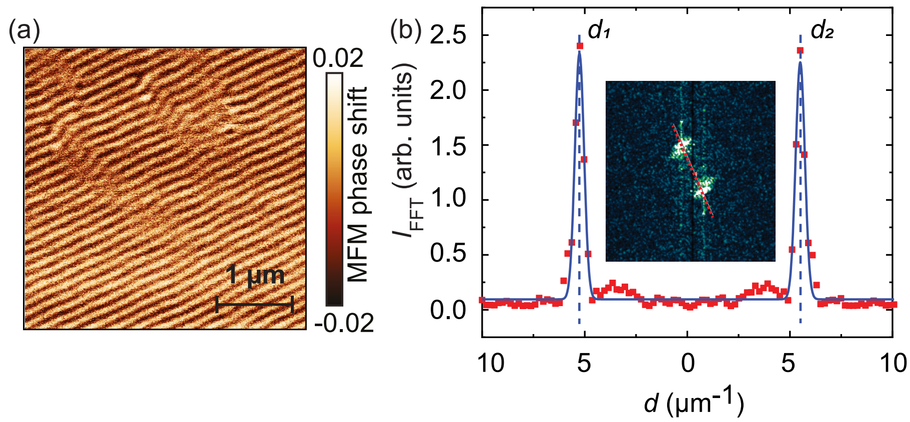

Figure 5.2 – **Stripe domains at $\mu_0 H_\perp$ = 0 mT.** (a) MFM image at $\mu_0 H_\perp = 0$ mT. Color bar represents the MFM phase shift. And it indicates the direction of the magnetization in the sample. (b) Fourier transformation (FFT) of MFM image of (a). The inset graph show the FFT intensity. A linescan (the red squares) was extracted at the position marked by the red dashed line. The blue line is a fitting using Gaussian function. Positions of two peaks d_1 and d_2 reflect the inverse of the periodicity of domain structures.

The magnetic configuration was characterized by MFM. The measurements were conducted together with the master thesis student Edoardo Catapano in our lab. A low-moment tip was utilized to reduce the stray-field effect on magnetic states. The state at $\mu_0 H_\perp = 0$ mT is shown in Fig. 5.2 (a) and stripe domains are clearly seen. Fourier transformation of the image is shown in Fig. 5.2 (b). Two peaks were fitted and extracted by Gaussian function at d_1 and d_2, which indicate the domain periodicity as $p = \frac{2}{|d_2|+d|_1|} = 185.8$ ($\pm$ 0.1) nm. The average domain width is calculated to be half $L = \frac{p}{2} = 93$ nm. The value results from the interplay of magnetostatic energy E_m and domain wall energy E_dw give by [216]:

$$E_\mathrm{m} = \frac{16\, M_\mathrm{S}{}^2 L}{\pi^2\, t} \sum_{n>0,\mathrm{odd}}^{\infty} \frac{1-\exp(-k_n\, t)}{n^3} \quad \text{and} \quad k_\mathrm{n} = \frac{n\pi}{L} \tag{5.1}$$

$$E_\mathrm{dw} = \frac{\sqrt{A K_\mathrm{U}}}{L} \tag{5.2}$$

The minimum energy corresponding to $L = 93$ nm requires $AK_\mathrm{U} = 0.29\ \mathrm{erg}^2/\mathrm{cm}^4$.

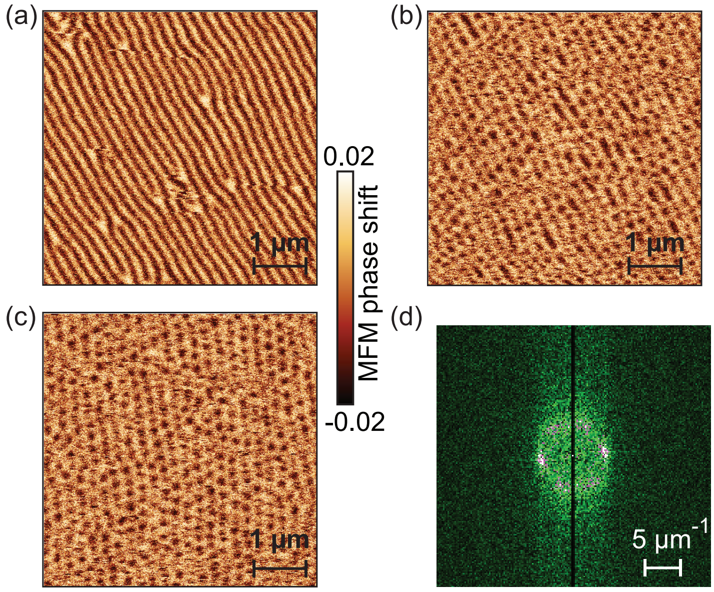

Figure 5.3 – **MFM images of Fe/Gd multilayers.** MFM images with out-of-plane fields of (a) 40 mT, (b) 75 mT, and (c) 85 mT. Color bar represents the MFM phase shift and reflects the magnetization direction. (d) 2D FFT image of MFM image (c).

The stripe-domain configuration was tuned by applying magnetic field $H_\perp$ perpendicular to the sample surface. In our MFM setup, $H_\perp$ was applied by permanent magnets. With increasing $H_\perp$, Zeeman energy needs to be taken into account. The periodicity of stripe domains increased (Fig. 5.3 (a)). Then domains started to collapse into type-II bubbles and dipole skyrmions (Fig. 5.3 (b)). At $\mu_0 H_\perp = 85$ mT, stripe-domain vanished and hexagonal lattices of dipole skyrmions started to form (Fig. 5.3 (c)). Figure 5.3 (d) is the two-dimensional Fourier transformation of (c) revealing a diffraction pattern of a hexagonal lattice reflecting a lattice constant of 226 nm ± 2 nm. When comparing the domain stripes at 40 mT with 0 mT, the direction of the domain structures changed suggesting a tiny in-plane component of the permanent magnets re-aligning the direction of the domain stripes.

5.1.2 Ferromagnetic Resonance of Fe/Gd multilayers

To examine FMR in the multilayers system, we put a triangular shape sample (5.4 (a)) face down on a coplanar waveguide (CPW) (No. 3 in Table. 2.1). The longer axis of the sample was about 1 cm-long and larger than the width of the CPW such that both in-plane and out-of-plane components of $\boldsymbol{h}_{\mathrm{rf}}$ played a role for excitation. External magnetic field $H_{\perp}$ was applied perpendicular to the sample surface. Considering the size of the sample is quite large compared with the magnetic yokes. So the applied field near the edge may contain an in-plane component. Magnetic resonance spectra of transmission signal ΔS_{21} with magnetic field sweeping from -450 mT to 450 mT are plotted in Fig. 5.4 (b).

Below -131 mT and above 147 mT, resonance frequencies increased with magnetic field strength, implying the saturated state of Fe/Gd multilayers. In this state, two main modes A and B were observed with distinct frequency difference. Mode B vanished when $\mu_0 H_{\perp}$ approached -400 mT and 400 mT. The extension lines of mode B intersect with field axis at about -100 and 130 mT. Hence mode B are likely to be related to the in-plane components of the applied field. Resonance mode A following the field dependency suggested by the Kittel formula for a PMA sample in out-of-plane field $H_{\perp}$ [161]. They were analyzed for the anisotropy strength, saturation magnetization and Gilbert damping parameters. The resonance peaks were fitted by Lorentz peak function and the field dependent resonance frequencies are plotted in Fig. 5.5 (a). Error bars of f came from the standard error of Lorentz fitting. Experimental data was fitted using Kittel formula Eq. (1.34) introduced in Chapter 1. $\mu_0 M_{\mathrm{eff}} = \mu_0 M_{\mathrm{S}}$ - $2K_{\mathrm{U}}/M_{\mathrm{S}} = (-14 \pm 10)$ mT was extracted from the fitting. Combined with the hysteresis measurement and domain size characterization, the anisotropy strength and exchange constant can be calculated K_{U} = 66.2 kJ/m^3 and $A = 6.1 \times 10^{-12}$ J/m. They are comparable with reported values [51]. The full width of half maximum (FWHM) δf of the fitted peaks are shown in Fig.5.5 (b) with standard errors from Lorentz peak function fittings. To extract the damping parameter α, frequency dependent δf was fitted linearly by the equation Eq. 1.31. The damping parameter was $\alpha = 0.009 \pm 0.001$. It is smaller compared with interfacial DMI systems hosting skyrmions and consistent with the value reported from similar multilayers [50].

In the unsaturated state, five resonance modes are present. Three modes are highlighted by red circles. At positive $H_{\perp}$ they connect to mode A. Two modes are connected to mode B (highlighted by green circles). We focus on the modes marked by red circles between about $\mu_0 H_{\perp}$ = 88 mT and the saturation field of 147 mT. In this regime skyrmion lattice should exist combining the MFM measurements. The behavior of these modes is consistent with the dynamic simulations of dipole skyrmion lattices in Ref. [50] and description is in Chapter 1.3.3 and Fig. 1.13. The mode with the highest frequency near 5 GHz may be excited by both contributions of $\boldsymbol{h}_{\mathrm{rf}} \perp \boldsymbol{H}_{\perp}$ and $\boldsymbol{h}_{\mathrm{rf}} \parallel \boldsymbol{H}_{\perp}$.

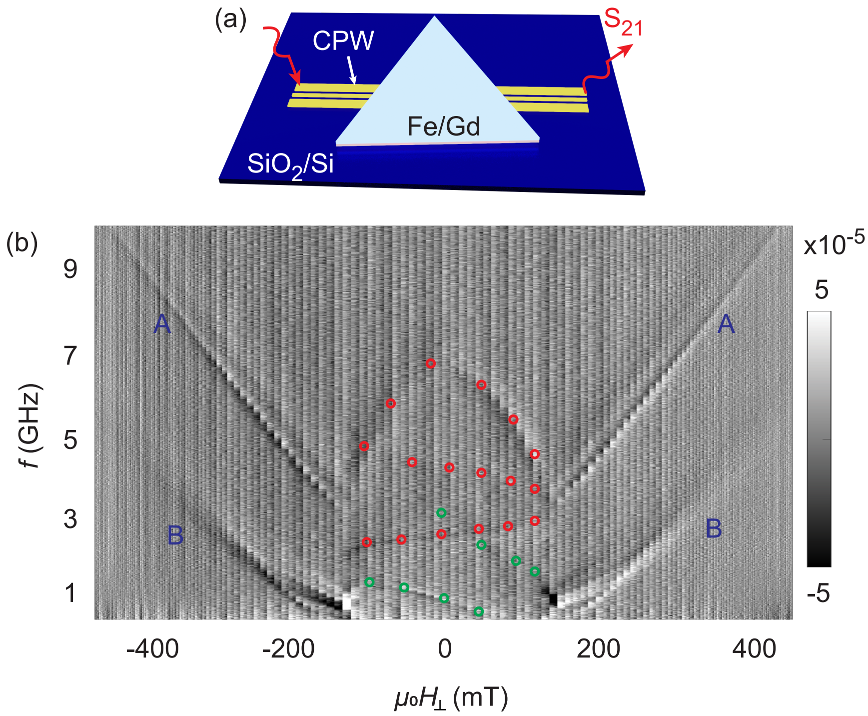

Figure 5.4 – **Spectra of flip chip measurements on Fe/Gd multilayers.**(a) Schematic diagram of flip-chip measurement of the Fe/Gd chip. Red arrays indicate the directions of the microwave current flows. (b) Magnetic resonance spectra of transmission signal S_{21} with magnetic field sweeping from -450 mT to 450 mT.

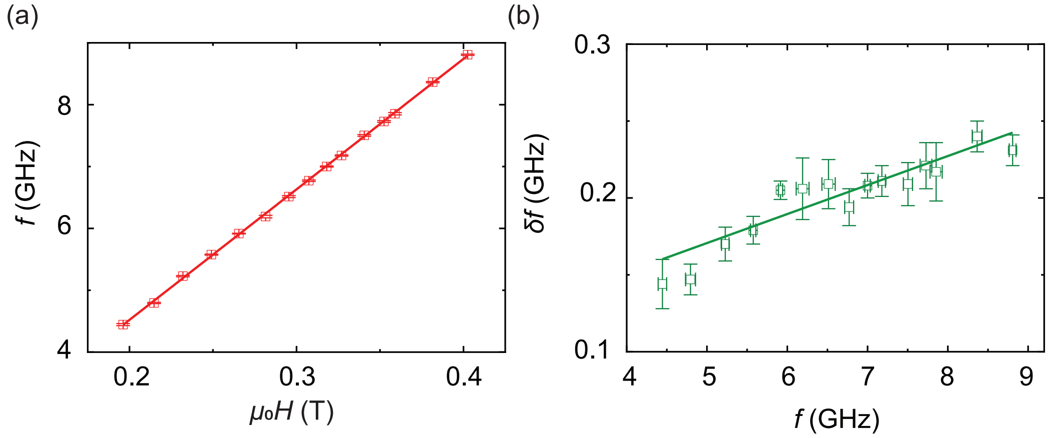

Figure 5.5 – **Dynamic parameters of FMR in Fe/Gd chip.** (a) Field dependent resonance frequencies (red circles). Red line is the fitted curve of Kittel formula Eq. (1.34). Error bars in both (a) and (b) indicate the standard error in fitting resonance peaks with Lorentz peak function.

5.2 Phase Modification in Fe/Gd Multilayers by Nano Arrays Resolved by Scanning Transmission X-ray Microscopy

In this section, we report the magnetic phases in Fe/Gd multilayers grown on the Si_3N_4 membranes with integrated nanomagnet arrays utilizing the STXM. Cobalt nano-structures fabricated on Fe/Gd multilayers are described in Section 3.2.1. We compare the magnetic states in different regions underneath and next to the Co nanomagnets. We show that the arrays force the stabilization of domain and skyrmion lattices. In order to understand the states, we conducted micromagnetic simulations to specify the effects of exchange and dipolar interactions. Our observation offers a methodology to control the distribution of domains and skyrmions for designing storage and magnonic devices.

5.2.1 Phase of Bare Fe/Gd Multilayers

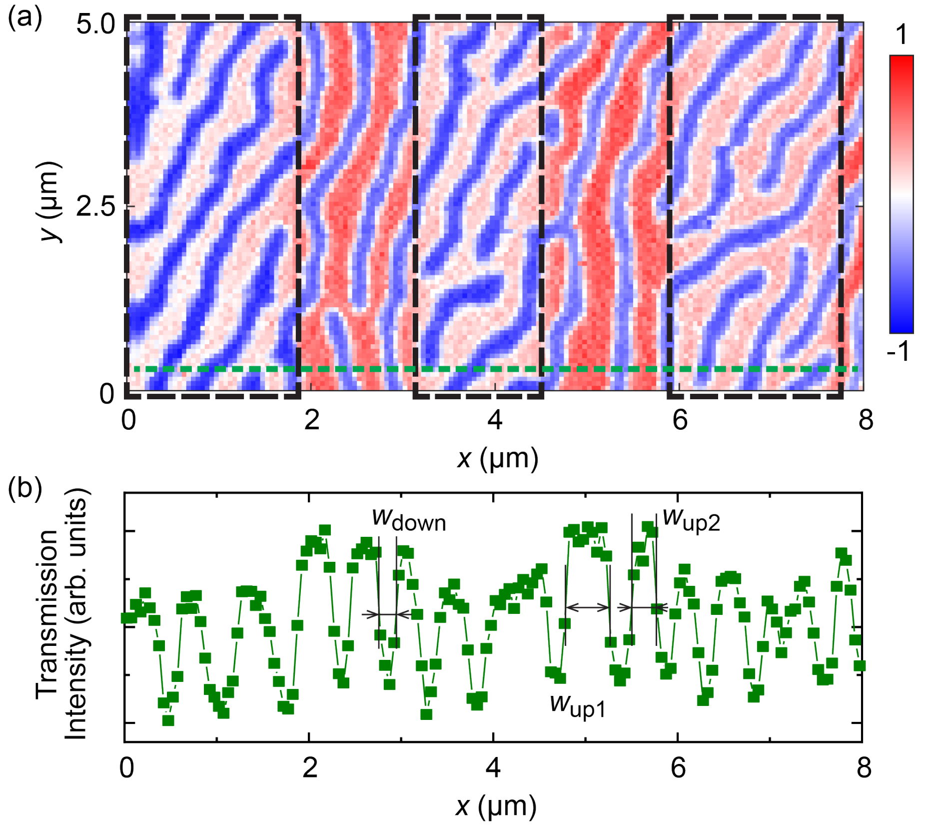

Figure 5.6 – **Static STXM image and line cut of domains in bare Fe/Gd multilayers.** (a) Static STXM image. Color bar represents normalized X-ray transmission intensity. The boxes highlight the position of the integrated CPW. Here, the absorption of X-ray is larger compared to neighboring regions. (b) Line cut was taken at $y = 0.3$ μm in (a) at the position marked by green dashed line.

The schematic diagram of the setup and experiment configuration are introduced in Fig. 2.11 and Fig. 2.12. The X-ray resolved magnetization map of Fe/Gd without nanomagnets is shown in Fig. 5.6 (a) in where stripe domains are observed. Dashed black frames mark the position of CPW lines. Unlike Fig. 5.2 (a), stripe domains are not well aligned with periodicity of p = 185 nm. Their widths vary. We look into a line profile (5.6 (b)) of the magnetization map at the dashed green line in 5.6 (a). From $x = 2$ μm to 3 μm and from $x = 5$ μm to 6 μm, the width of the domains are extracted by counting the widths at the half maximum of transmission signals locally. Considering the projection of 30 degree, width of spin down domains amounts to $w_{\mathrm{down}} = (231 \pm 58)$ nm. Width of spin up domains varies from position to position. We extracted the width from two of them to be $w_{\mathrm{up1}} = (528 \pm 58)$ nm and $w_{\mathrm{up2}} = (318 \pm 58)$ nm.

We noticed that the skyrmion lattice was not stabilized spontaneously and domains collapsed into individual skyrmions. Instead of get saturated at $\mu_0 \boldsymbol{H}_\perp = 132$ mT, region without nano arrays get fully saturated at $\mu_0 \boldsymbol{H}_\perp = 22$ mT. The discrepancies of domain structure, effective saturation field and skyrmion formation process before and after nanofabrication are attributed to a modification of material parameters due to e.g. baking processes when coating photoresists. Considering Ref. [51], a lower PMA value K_{U} agrees with our observation (when we assume the exchange parameter A to stay constant).

5.2.2 Modified Magnetic Phases by One- and Two-Dimensional Nanomagnet Arrays

Different domain structures were observed in the region with 1D nanomagnet arrays (Fig. 5.7). Three periodicities $p = 300$ nm, $p = 350$ nm and $p = 450$ nm are compared (from top to bottom). 1D arrays of $p = 350$ nm formed the most regular domain lattices (Fig. 5.7 (b)). Out of the yellow frames (no nanomagnet), the domains resemble Fig. 5.6. Line cut of domain lattice marked by green dashed line in Fig. 5.7 (b) is plotted (Fig. 5.8). In the region with Co nanomagnet arrays, the periodicity of the domains (D) are perfectly formed as (300 ± 50) nm. After the correction of projection, $p_{\mathrm{D}} = (346.5 \pm 57.8)$ nm, which is consistent with the design of Co arrays. Magnetization points to downwards underneath the grating elements. It is notable that the transmission signals out of the yellow frame have higher intensity than inside. In side the yellow region, transmission signal intensity is higher in the area uncovered by CPWs.

1D arrays with $p = 300$ nm formed complex domain structures (Fig. 5.7 (a)). Spin-up domains and spin-down domains are similar in this case. Two typical width of domains are extracted as $w_{\mathrm{wide}} = (303 \pm 29)$ nm and $w_{\mathrm{narrow}} = (144 \pm 29)$ nm. They are related to the periodicity of the Co nanomagnet array (300 nm) and the widths of the 1D Co stripe and gaps (150 nm). From another perspective, we categorized the magnetization map as multi-domains consisting of domain stripes as wide as $w_{\mathrm{wide}} = (303 \pm 29)$ nm with specific domain boundaries. The boundaries will be discussed in details in section 5.4.

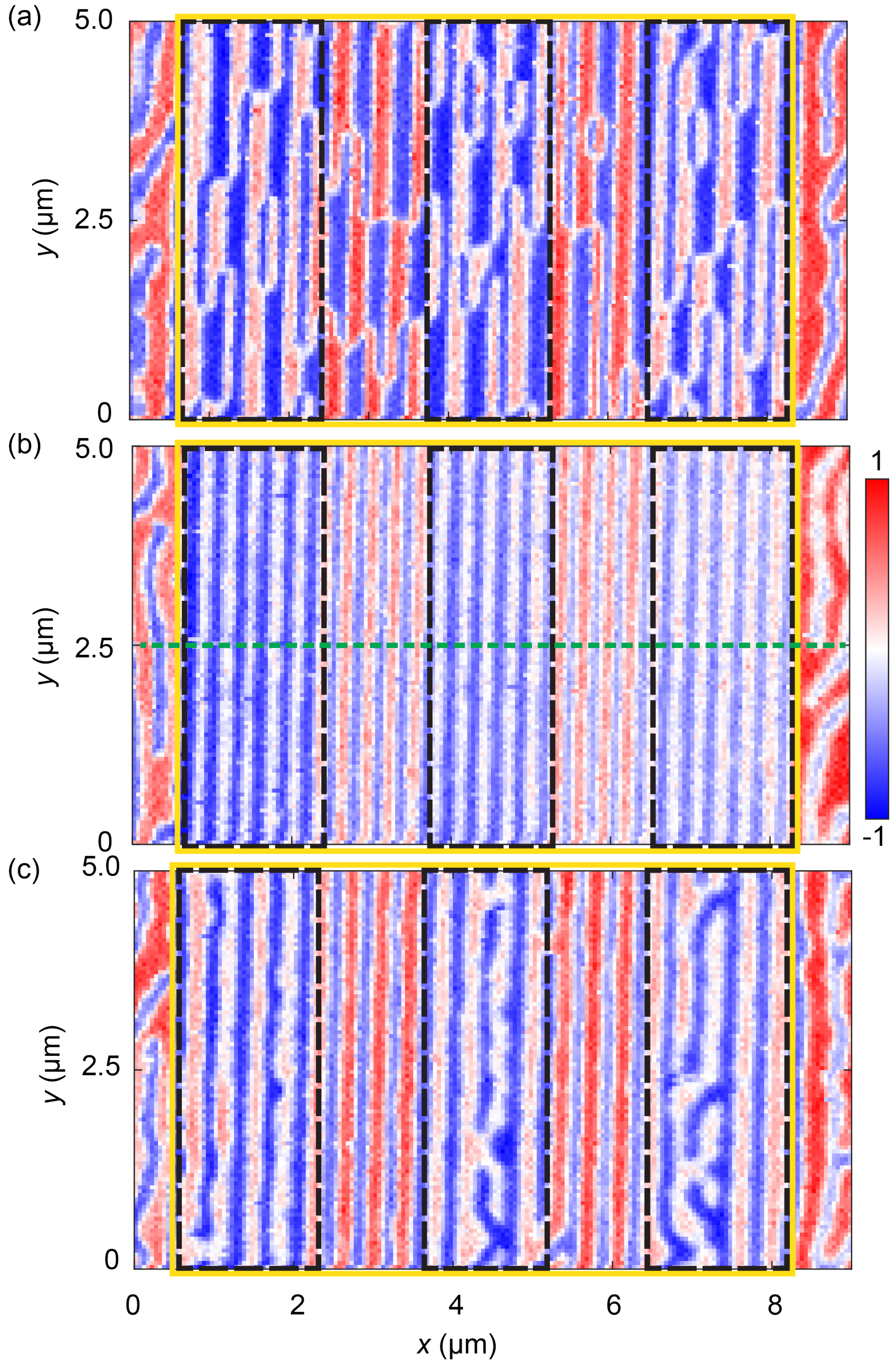

Figure 5.7 – **Static STXM images of domains modified by 1D nanomagnet arrays at $\mu_0 H_\perp$ = 0 mT.** Domains underneath 1D nanomagnet arrays of periodicity (a) p = 300 nm, (b) p = 350 nm, and (c) p = 450 nm. The olor bar represents normalized X-ray transmission intensity. Dashed black frames indicate the regions of the CPW lines. Yellow frames indicate the region of nanomagnet arrays.

1D arrays with p = 450 nm induced regular domain lattices partially (Fig. 5.7 (c)), similar to other arrays with p = 400 nm and p = 500 nm (data not shown). Lattices were formed only in the regions without CPW lines and the domain periodicities agreed with nanomagnet arrays. In the regions underneath CPWs, domain stripes merged. During the wire bonding or microwave circuit test, the regions underneath CPW lines may be heated up and material properties varied a bit.

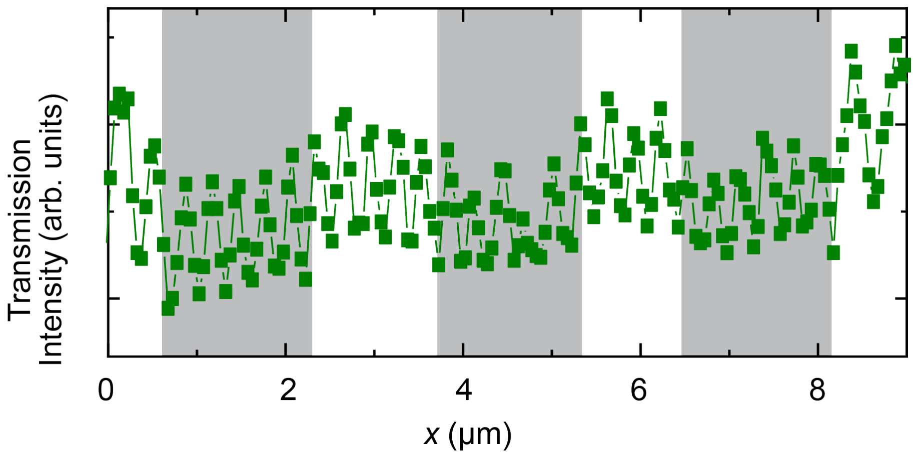

Figure 5.8 – **Line cut of transmission intensity modified by 1D nano arrays with p = 350 nm.** Line cut was taken at y = 2.5 μm in Fig. 5.7 (b) at the position marked by green dashed line. Gray boxes mark the region of CPW lines.

Not only the 1D Co stripe arrays but also the 2D Co nanodisc arrays modified the magnetic phase in Fe/Gd multilayers, particularly the square lattice array with periodicity p = 400 nm. Field dependent magnetization maps in the region with 2D nano arrays are plotted in Fig. 5.9. At $\mu_0 H_\perp$ = 0 mT, stripe domains were observed. Outside the 2D array region, domains were identical to the bare film of Fig. 5.6. In the 2D array region, domains followed mostly a horizontal or vertical direction in the Fig. 5.9 (a) and (b). As the magnetic field increased, upwoard magnetization was recorded at the position of Co discs. At $\mu_0 H_\perp$ = 20 mT, square lattices of upward Fe/Gd magnetization were created locally following the designed lattice constant p_D = 400 nm.

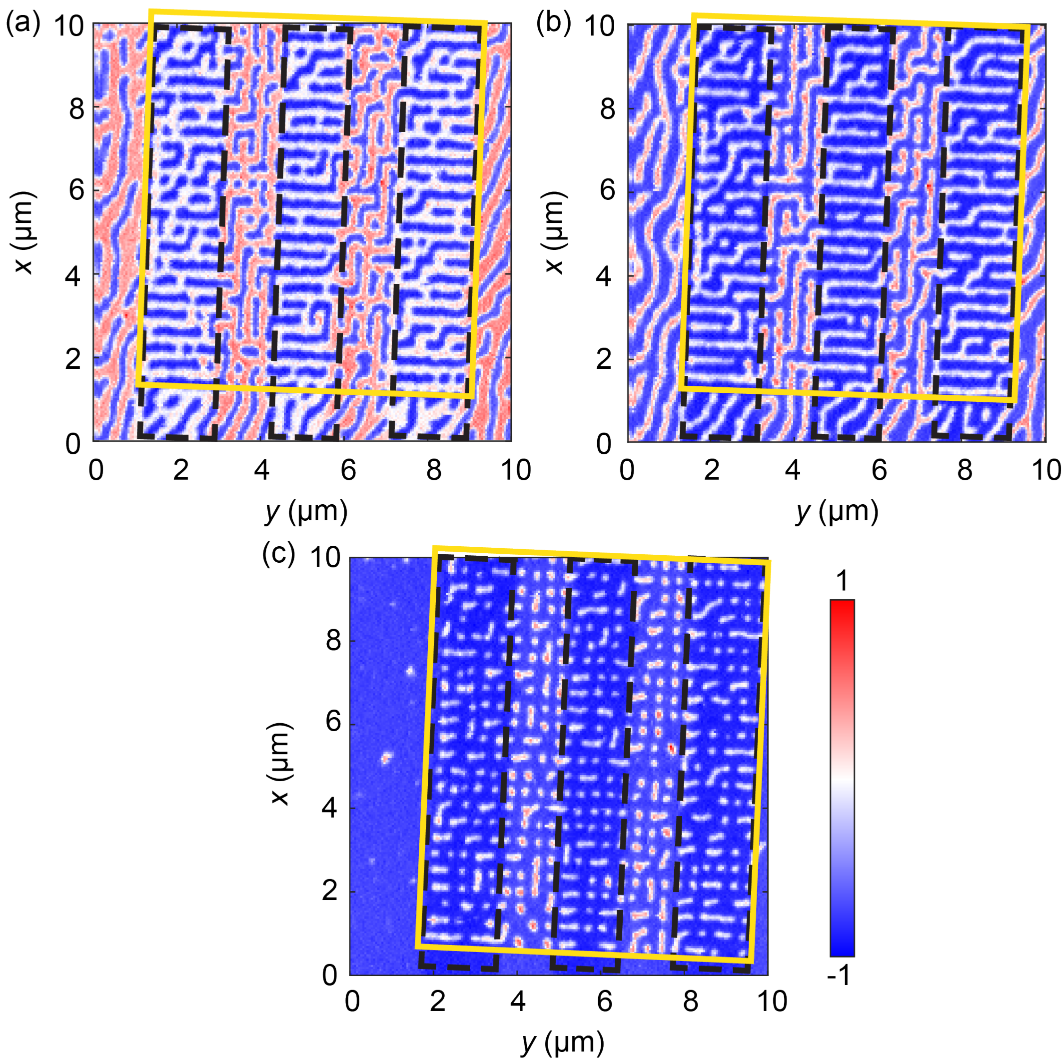

Figure 5.9 – **Static STXM image of domains modified by two-dimensional Co nanomagnet arrays.** Domains modified by two-dimensional nanomagnet arrays with periodicity $p = 400$ nm at (a) $\mu_0 H_\perp = 0$ mT, (b) $\mu_0 H_\perp = 10$ mT, and (c) $\mu_0 H_\perp = 20$ mT. The color bar represents the normalized X-ray transmission intensity. Dashed black frames indicate the regions of CPW lines. Yellow frames indicate the regions of nanomagnet arrays.

5.2.3 Micromagnetic Simulation on Fe/Gd Multilayers with Co Stripes and Discs

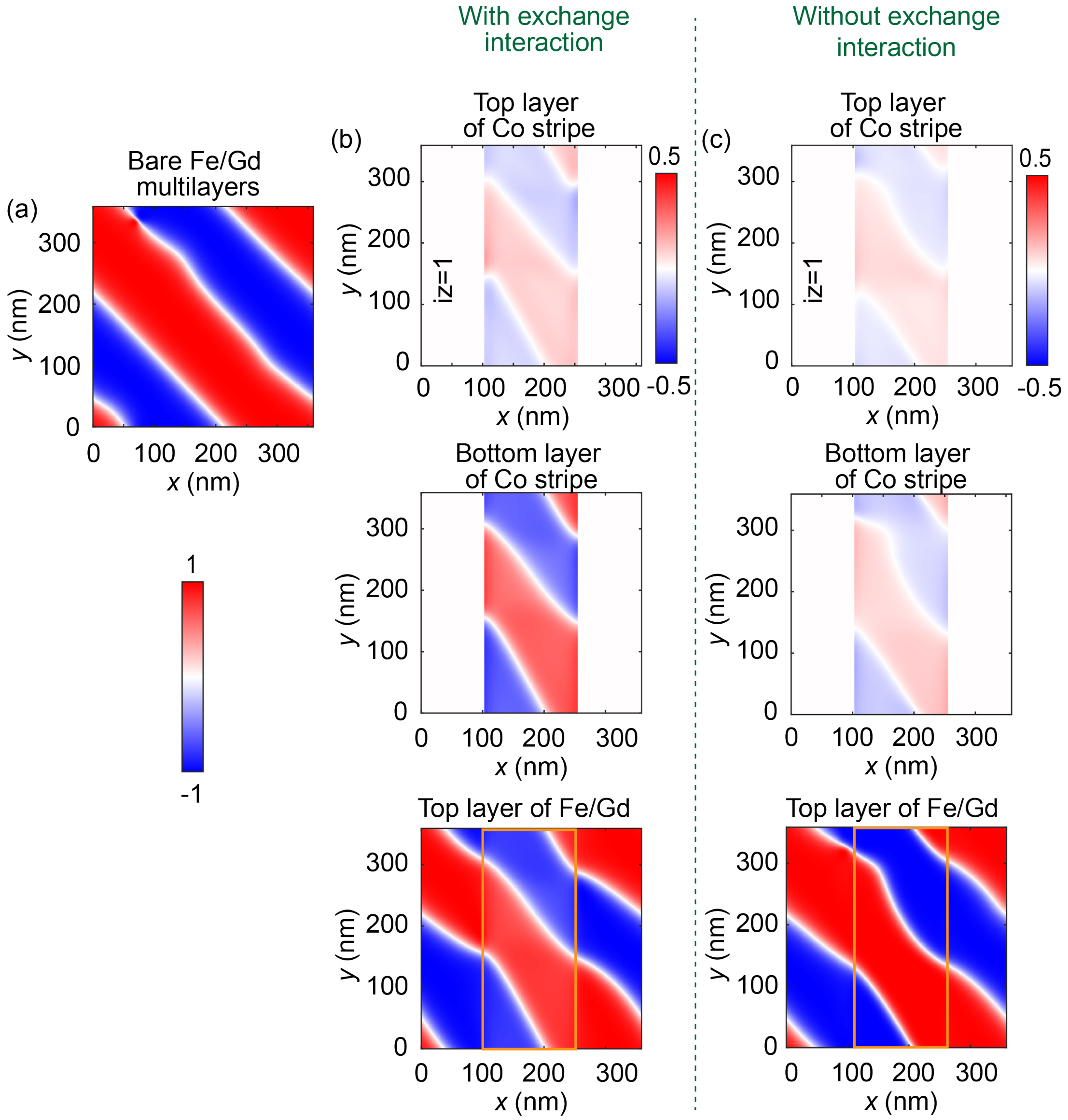

Figure 5.10 – **Simulated magnetic states in bare Fe/Gd multilayers and with Co stripe at $\mu_0 H_\perp$ = 10 mT.** (a) Bare Fe/Gd multilayers. (b) Fe/Gd multilayers with Co stripe with interfacial exchange interaction. (c) Fe/Gd multilayers with Co stripe without exchange interaction. The color bar represents normalized magnetization $\boldsymbol{m}_z$ along $\boldsymbol{z}$.

To investigate the competing between Co nanomagnets and the Fe/Gd multilayers, three sets of micromagnetic simulations were carried out using Mumax3 code [145]. Fe/Gd multilayers with an area of 358.4 nm × 358.4 × 80 nm with periodic boundary condition (PBC) = (20,20,0) were simulated. Cell sizes were 1.4 nm along $\boldsymbol{x}$ and $\boldsymbol{y}$, 2 nm along $\boldsymbol{z}$. All of them are smaller than half of the exchange lengths of Fe/Gd and Co. The model contains ix × iy × iz = 256 × 256

× 40 cells. We utilized the parameters extracted from the sample characterization in section 5.1 such as exchange constant $A = 6 \times 10^{-12}$ J/m, saturation magnetization $M_{\mathrm{sat}} = 320$ kA/m, PMA value $K_U = 6.6 \times 10^4$ J/m^3 and Gilbert damping constant $\alpha = 0.01$. The magnetization component m_z shows the stripe-shape domains in bare Fe/Gd multilayers in the simulation for $\mu_0 H_\perp = 10$ mT (Fig. 5.10 (a)). This image was taken at the top surface iz = 1 of the sample.

In simulation set 1, we constructed a 20-nm-thick, 120-nm-wide Co stripe on top of the Fe/Gd sample through $\boldsymbol{y}$ direction. The same cell size and (PBC) were used. Parameters of Co were set as exchange constant $A = 1.4 \times 10^{-11}$ J/m, saturation magnetization $M_{\mathrm{sat}} = 1400$ kA/m and Gilbert damping constant $\alpha = 0.5$ according to Refs. [217, 218]. The initial state of the Co stripe was defined as magnetization along $\boldsymbol{y}$. We made use of the 'ex_scaleExchange' function to control the exchange interaction between Co and Fe/Gd [145]. m_z are compared in Fig. 5.10 (b) to (c). They are taken from the top layer and bottom layer of Co stripe, and top layer of Fe/Gd material.

In the case of normal exchange interactions (scale 1 defined by function ex_scaleExchange), Co stripe did not vary the state of Fe/Gd significantly (Fig. 5.10 (b)). Domains are smaller in the region adjacent to the Co stripe. Tiny deviations of domain walls in Fe/Gd sample were noticed at the location of the edges of Co stripes. On contrary, the magnetic configuration in the Co stripe was modified through all layers. Co stripe did not keep a uniform magnetization along $\boldsymbol{y}$ as initially set. Stripe domains generated in the Co stripe. Without interfacial exchange interaction, a similar magnetic configuration was found in bottom layer of Co stripe with smaller intensity (Fig. 5.10 (c)). Still the domain structures are through all layers. In Fe/Gd, stripe-shape domains are almost identical with or without exchange interaction. The tiny modification of the domain wall at the Co stripe edge disappeared in the case without exchange interactions. We conclude that exchange interaction do not play a decisive role for the phases observed in our STXM experiments. Meanwhile, domains were printed in Co stripe even without exchange interaction. On the other hand, stripe domains are smaller in the region covered by the Co stripe which may be caused by domains printing back from Co to Fe/Gd. This indicates the dipole interaction was dominating this process. However when without exchange interactions, the print of domains in Co stripe was weaker. It suggests that even though exchange interaction is not deciding the phase modification but it enhances the process.

In simulation set 2, we looked into a larger region with complete Co stripe on Fe/Gd multilayers at $\mu_0 H_\perp = 10$ mT (Fig. 5.11). We increased the size of the area to 224 nm × 1433.6 × 80 nm with periodic boundary condition (PBC) = (20,0,0) using ix × iy × iz = 160 × 1024 × 40 cells. Co stripe was defined as 112 nm wide, 980 nm long and 20 nm thick. All the other parameters remain the same as the previous simulation. When considering normal exchange interaction, in Fe/Gd, stripe domains in Fe/Gd started to follow the Co stripes (Fig.5.11 (a)). At about $y = 460$ nm domain walls deviated towards the direction of Co $+\boldsymbol{x}$ edge. In the other region underneath Co stripe, domains were mostly parallel to the Co stripe. Near the $+\boldsymbol{y}$ edge of Co stripe spins pointed downwards, and near the $-\boldsymbol{y}$ edge spins pointed upwards. Inside the domain wall underneath Co stripe, the spins are pointing along $-\boldsymbol{y}$. They followed the stray field direction generated by the Co stripe. In Co stripe, the phases change from $\boldsymbol{M} \parallel +\boldsymbol{y}$ to partially tilted to in-plane following the domain structures in Fe/Gd. In the case without interfacial exchange interaction (Fig.5.11 (b)), similar domains were observed as in (a). The domains were nicely aligned following Co stripe. No deviation appeared. Unlike the simulation containing only a short part of the Co stripe (simulation set 1 in Fig. 5.10 (b) and (c)), domains followed the Co stripes this time. The difference is mainly the presence of the stripe edges. Thus we propose that the stray fields generated by a Co stripe are the key for the formation of well-aligned domains.

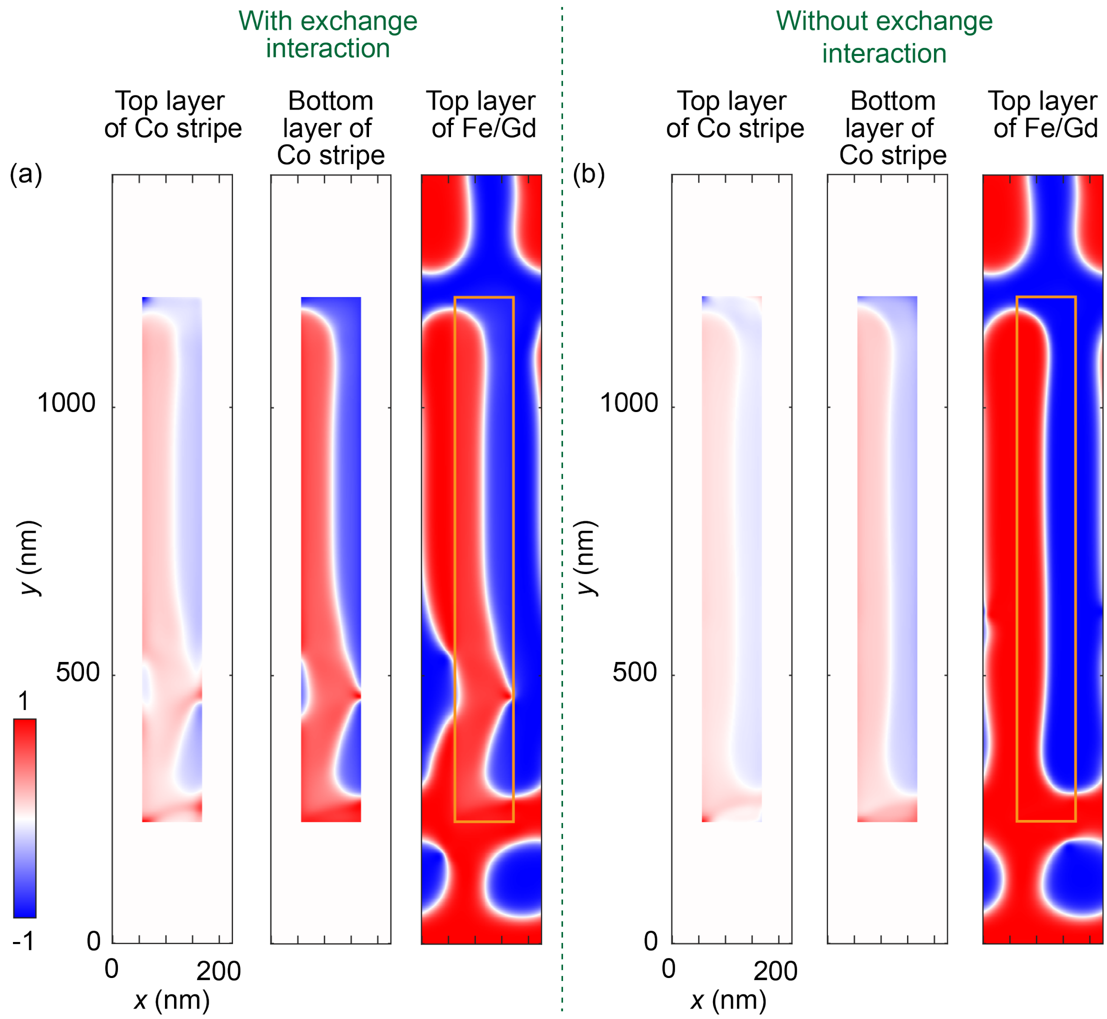

Figure 5.11 – **Simulated magnetic states in Fe/Gd multilayers with complete Co stripe at $\mu_0 H_\perp$ = 10 mT.** (a) Fe/Gd multilayers with complete Co stripe with interfacial exchange interaction. (c) Fe/Gd multilayers with complete Co stripe without exchange interaction. The color bar represents normalized magnetization $\boldsymbol{m}_z$ along $\boldsymbol{z}$.

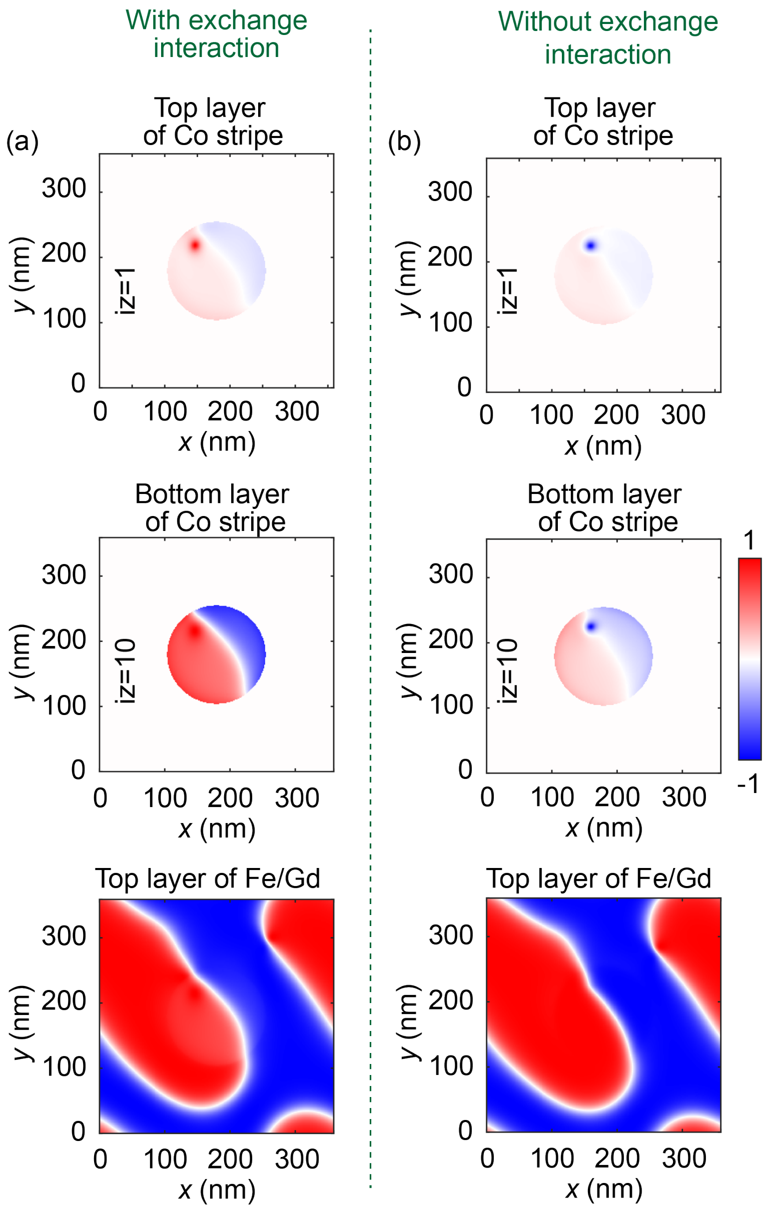

Figure 5.12 – **Simulated magnetic states in bare Fe/Gd multilayers and with Co stripe.** (a) Fe/Gd multilayers with Co disc with interfacial exchange interaction. (b) Fe/Gd multilayers with Co disc without exchange interaction. Color bar represents normalized magnetization $\boldsymbol{m}_z$ along $\boldsymbol{z}$.

Simulation set 3 switched from Co stripe to Co disc with a diameter of 150 nm and thickness of 20 nm. All the other parameters are the same as set 1. The magnetic phases in both Co disc and Fe/Gd multilayers are plotted in Fig. 5.12. Compared with the bare Fe/Gd multilayers (Fig. 5.10 (a)), phases were modified from stripe domains to 2D domain lattices when Co disc were present in Fe/Gd. In Co disc, the ground state should be vortex counting the shape and external field ($\mu_0 H_\perp$ = 10 mT). Here the spins configuration were modified. Spins started to tilt to out-of-plane direction following the stray field from Fe/Gd. And the vortex core in Co disc were weaken on the bottom surface near Fe/Gd. When interfacial exchange interaction were shut down, spins in Co disc still tilted but the core had less change. Phases in Fe/Gd (Fig. 5.12 (b)) remained very much similar to Fig. 5.12 (a). Based on these observations, we deduce that the dipolar interaction has a strong influence on the phases in both Fe/Gd multilayers and Co disc. Exchange interaction between two materials help enhance the spin tilting in Co disc and weaken the magnetization of vortex core.

5.2.4 Discussion

In the following we discuss aspects of dipolar interaction in our samples. In our STXM data, the Co stripes aligned induced preferred direction of stripe domains in Fe/Gd multilayers. We sketch the Co stripes on top of the STXM picture in Fig. 5.13. Black arrows indicate the assumed magnetization directions in the Co stripes after pre-alignment described in section 2.3.2. We infer that they should generate stray field lines going into the Fe/Gd multilayers at their edges. Indeed near these edges the Fe/Gd multilayers shown downward magnetization, consistent with the stray field directions of Co stripes. This agrees with the micromagnetic simulation of Fig. 5.11. Those edge regions may work as the starting points of domain nucleation. We checked the other side of the stripes and their region showed upward magnetization following the complementary stray field. We hence suggest that the stray field of Co nanostructures allowed us to modify the domain configuration in Fe/Gd multilayers. There is still a difference on domain wall positions between our STXM data (Fig. 5.13) and simulation (Fig.5.11). It should be related to the dimension of Co stripes in our simulation limited by the computing ability. This also agrees with our observation of domain structures with different periodicity p of 1D nanomagnets arrays (Fig. 5.7).

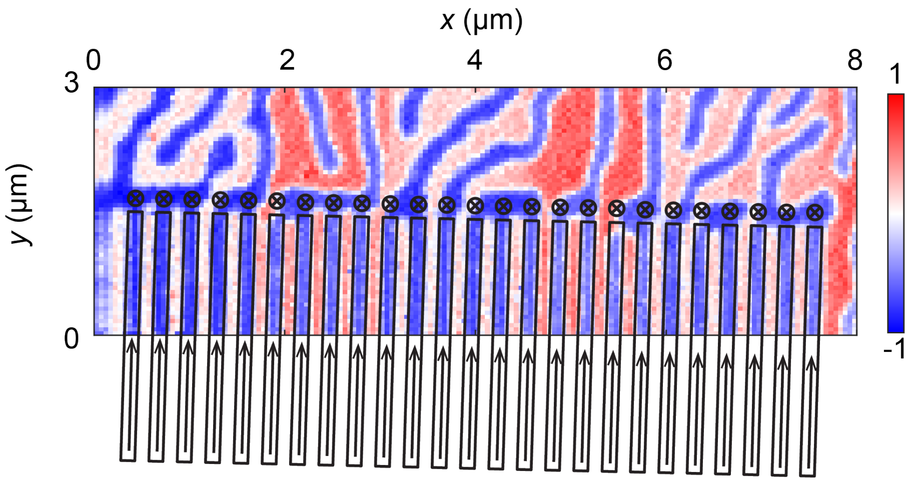

Figure 5.13 – **Dipole field at the edge of 1D Co stripes.** Static STXM map at the edge of 1D nano arrays of p = 350 nm and the sketch of the dipole fields.

In case of the Co nanodiscs, we speculate that a vortex state was formed in discs and the vortex core provided relevant stray fields. It was noticed that at $\mu_0 H_\perp = 0$ mT in Fig. 5.9, magnetization were mostly pointing upwards underneath Co disc arrays. If following the ground states of vortex in Co disc, only half of region were expected to own magnetization upward. This fact suggest that vortex core were strongly modified by the stray field from Fe/Gd.

Based on our findings, the design of variable skyrmion or domain lattices becomes possible by tailored shapes of grating elements with different stray-field patterns.

5.3 Spin Dynamics of Domain Walls in Fe/Gd Multilayers

We investigated the spin dynamics below 1 GHz in domain walls and multi-domain phases modified by 1D nanomagnet arrays as shown in Fig. 5.7 (b) and (a). Continuous-wave radio-frequency current I_{rf} was injected into the signal line of the integrated CPW to excite spin waves. It generated the dynamic magnetic field $\boldsymbol{h}_{rf}$ around the signal line. X-ray beam pulses were utilized to collect the dynamic transmission signals in 13 channels in the time domain. We averaged 13 signals and subtracted the average value from the transmission signals to extract the dynamic signals. They were further normalized by the average value.

5.3.1 Spin Dynamics of Well-Aligned Domain Walls

The normalized static and dynamic transmission signals at f = 0.31 GHz are plotted in Fig. 5.14 (a) and (b). The Co stripe grating an Fe/Gd had a period of p = 350 nm. Dynamic signals were pronounced underneath the signal line indicating that the in-plane component of $\boldsymbol{h}_{rf}$ dominated the excitation. Spin waves with finite wavevector were excited, e.g. in the region

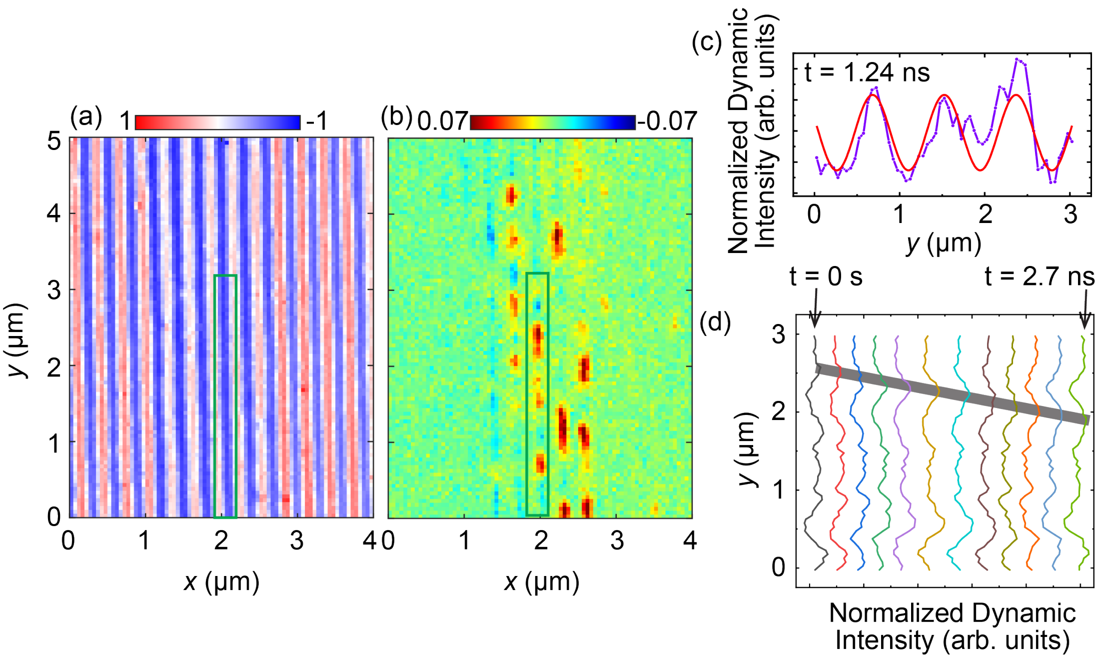

Figure 5.14 – **STXM images of domain walls excited locally at f = 0.31 GHz.** (a) Static STXM image of domains formed by the 1D Co nanomagnet array with p = 350 nm. The color bar represents the normalized transmission intensity. (b) Snapshot of dynamic STXM image of domains excited at f = 0.31 GHz underneath the signal line of CPW. The color bar represents the normalized dynamic components. (c) Normalized dynamic magnetization intensities at t = 2 ns averaged for 5 cells along x in the region marked by the green box. (d) Time-dependent average dynamic magnetization intensities in the region marked by green box.

marked by green box in Fig. 5.14 (b). The line cut at $t = 1.24$ ns (Fig. 5.14 (c)) are fitted with a sine wave form. We extracted wavelength of $\lambda = 814$ nm. In Fig. 5.14 (d), we show the signal evolution from $t = 0$ s to $t = 2.7$ ns. Considering the wave propagation along $\boldsymbol{y}$ as highlighted by the gray line, we calculate the phase velocity to be $v_g = 0.24$ km/s.

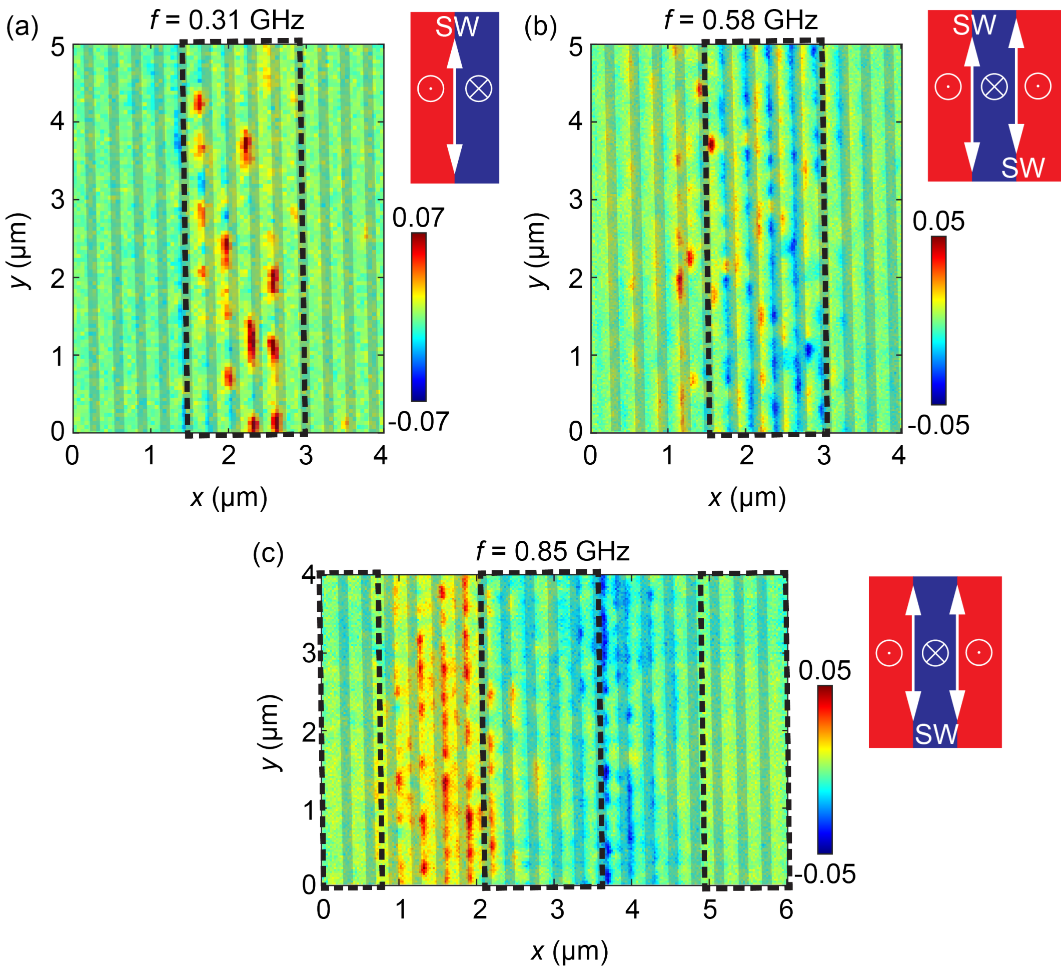

Figure 5.15 – **Dynamic STXM images at three different excitation frequencies.** Dynamic STXM images of domain walls excited at (a) $f = 0.31$ GHz, (b) $f = 0.58$ GHz and (c) $f = 0.85$ GHz. Gray stripes indicate the positions of domains with downward magnetization (downward domains). Dashed black boxes indicate CPW lines.The color bars represent the dynamic transmission signals normalized to the static signal.

The snapshots of spin waves and their schematic propagation direction are plotted in Fig. 5.15. At $f = 0.31$ GHz, spin waves were observed only in the domain walls on the left side of downward domains. At $f = 0.46$ GHz, spin waves at the right edge of downwards domains were visible (data not shown). At $f = 0.58$ GHz, spin waves were clearly visible at both edges. They propagated along both directions in the regions without defects. Spin waves propagated in both domain walls on the left and right of the downward domains. At $f = 0.85$ GHz, spin waves were excited in the gap between the CPW signal and ground lines (Fig. 5.15 (c)). Spin waves of $\lambda = 409$ nm were excited at both edges of downward domains. It evidenced that at $f = 0.31$ GHz, there is selection rules of spin waves propagation that may be decided by the chirality of the domain walls.

5.3.2 Spin Dynamics of Domain Walls Located at Multi-Domain Boundaries

Multi-domains of quasi-periodic stripe domains were formed by 1D Co arrays with $p = 300$ nm as highlighted by black lines in the static transmission map Fig. 5.16. In the following we call these region separated by the black line super-domains. Note that the black lines follow domain walls. They separate five regions where domains are specifically arranged, as indicated in Fig. 5.16 (b). From the line cuts taken at positions A to E in Fig. 5.16 (c) and (d). We calculate domain wall width in the boundaries to be $w^b_{\mathrm{DW}} = 182$ nm considering the 30 degree STXM configuration. We read the size from the positions with abrupt change in $\mathrm{d}I/\mathrm{d}x$ and $\mathrm{d}I/\mathrm{d}y$. Domain walls inside the domains have $w_{\mathrm{DW}} = 177$ nm. The width do not differ significantly from each other.

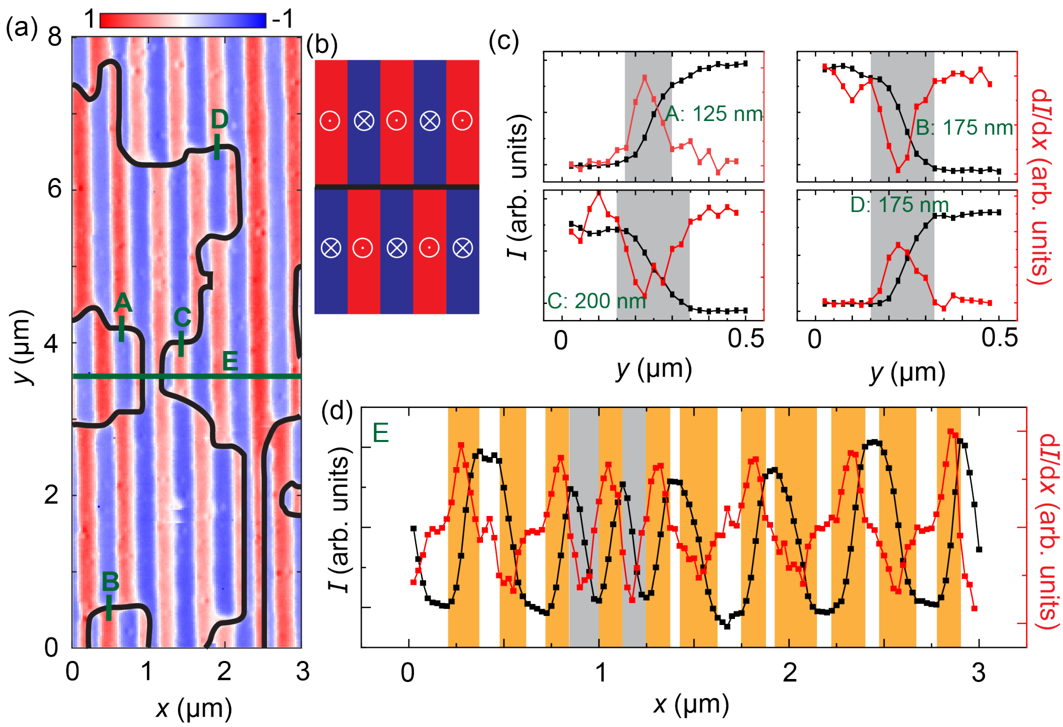

Figure 5.16 – **Domain walls inside and in between super-domains.** (a) Static STXM image of domains formed by 1D Co nanomagnet arrays with $p = 300$ nm. Black lines mark the boundaries between regularly arranged group of stripe domains. (b) Sketch of a super-domain boundary. (c) and (d) Transmission intensities of domain walls marked by green lines in (a). Gray frames mark the size of domain walls inside the multi-domains. Yellow frames mark the size of the domain walls between stripe domains. Those regions are located according to abrupt changes in $\mathrm{d}I/\mathrm{d}x$ and $\mathrm{d}I/\mathrm{d}y$.

At f = 0.38 GHz, a special resonance mode was observed (Fig. 5.17 (a)) following the long black line of Fig. 5.16 (a), i.e. the boundary between our provisionally defined super-domains. When frequency increased, resonances were excited in domain walls both at the boundaries and inside the super-domains, e.g. at f = 0.58 GHz in Fig. 5.17 (b). For the boundary modes, there are two type of resonances: standing waves and propagating waves. In the boundaries along x direction, standing spin waves were preferably seen. In the boundaries along y direction, spin waves propagated as indicated by gray arrows in Fig. 5.17 (a). Their propagation followed the same scenario as sketched in well-aligned domain walls in Fig. 5.15 (b). Spin waves propagated also along curved segments of the boundaries between the super-domains.

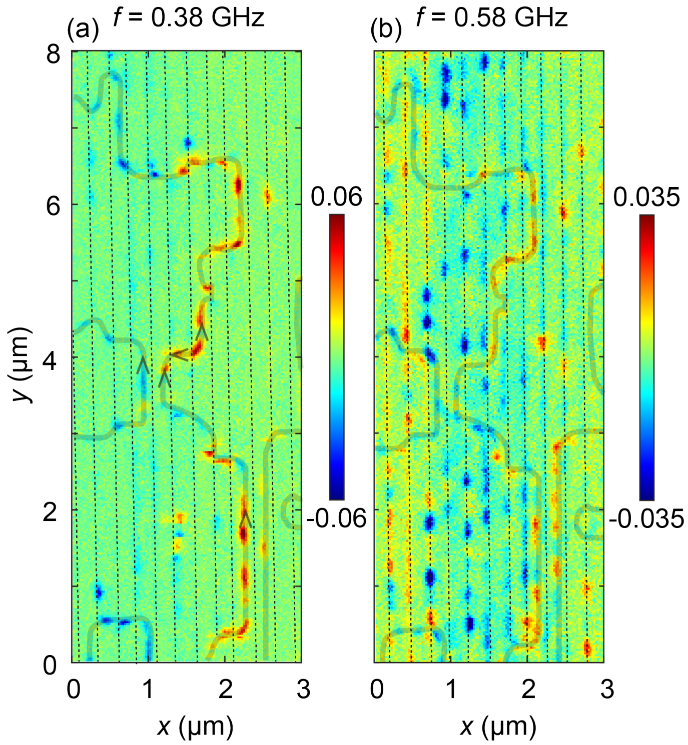

Figure 5.17 – **Dynamic STXM images of domain walls inside and between super-domains.** (a) Domain wall resonance along the boundaries (gray solid lines) of super-domains at f = 0.38 GHz. Black dashed lines mark the positions of regular domain walls. Arrow heads indicate propagation direction of excited spin waves. (b) Domain walls resonance at f = 0.58 GHz.

5.3.3 Discussion

Comparing the spin wave excitation at different frequencies by in-plane $\boldsymbol{h}_{\mathrm{rf}}$ in well-aligned domain walls, wavelengths varied from λ = 814 nm at f = 0.31 GHz to λ = 388 nm at f = 0.65 GHz. We extracted the dispersion relation from the STXM measurements (Fig. 5.18) and plot together with the data points from out-of-plane $\boldsymbol{h}_{\mathrm{rf}}$ and super-domain boundaries. Dispersion relations of spin waves in a Bloch-type domain wall read [219]

$$f = \frac{\gamma}{2\pi}\sqrt{\frac{2Ak^2}{M_S}(\frac{2Ak^2}{M_S}+\frac{2}{M_S}\frac{\mu_0 N_y M_s^2}{2})} \tag{5.3}$$

Here γ is the gyromagnetic ratio, A is the exchange interaction, M_S is the saturation magnetization, k is the wavelength of spin waves. In the ultra-thin film,

$$N_y \approx \frac{d}{d+\pi\sqrt{\frac{A}{K_U-\frac{\mu_0 M_s^2}{2}}}} \tag{5.4}$$

d is the thickness of the film and K_U is the PMA strength. Comparing our experimental observation and the calculated dispersion relation, the tendency is consistent but there is a discrepancy in the slope. It may originate from the nature of the domain walls or the integrated Co stripes. In Fe/Gd, domain walls are mainly Bloch-type but at the top and bottom surface, domain walls are tuned to N$\acute{e}$el-type. So the spin wave resonance frequencies are expected to be modified.

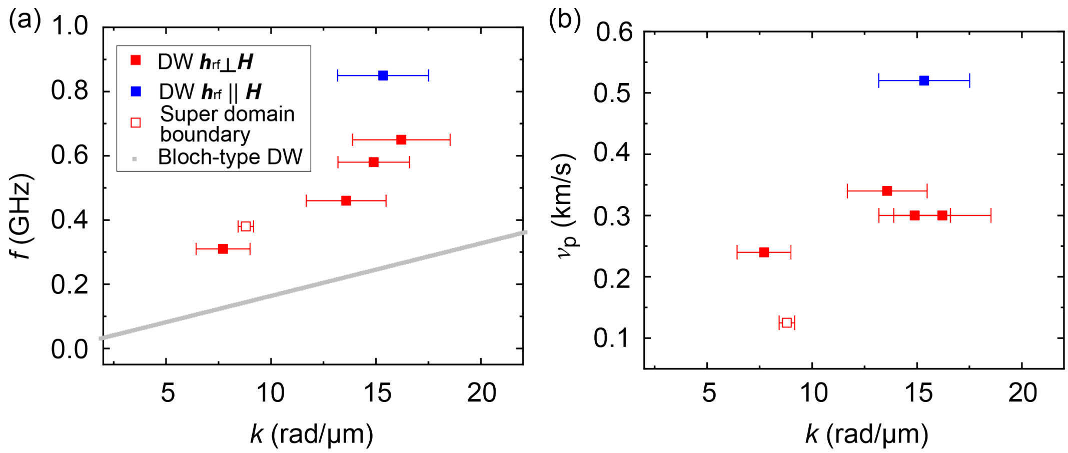

Figure 5.18 – **Dispersion relation and phase velocities of spin waves in domain walls.** Red squares are extracted from STXM measurements in domain walls where the dynamic component $\boldsymbol{h}_{\mathrm{rf}} \perp \boldsymbol{H}_{\perp}$. Blue squares are extracted from where the dynamic component $\boldsymbol{h}_{\mathrm{rf}} \parallel \boldsymbol{H}_{\perp}$. Hollow squares is extracted from the super-domain boundaries from the region 0.5 μm < x < 2 μm and y around 2.2 μm. Gray line is the calculated spin waves dispersion relation in Bloch-type domain wall using Eq. 5.3.

The spin waves phase velocities we obtained form SXTM data are in the same order with the reported value in domain walls in $Ni_81Fe_19/Ru/Co_40Fe_40B_20$ which is 0.317 km/s at 1.1 GHz and 0.307 km/s at 1.46 GHz [22] considering the doamin wall structure are also mixed from Bloch-type and N$\acute{e}$el-type. Higher phase velocities would be expected in Fe/Gd multilayers when the resonance will be excited above f = 1 GHz. Our experimental observations of the spin waves excited along extended and curved domain walls further prove the concept of reconfigurable spin wave guides in extended films with reasonable spin wave phase velocities.

5.4 Spin Dynamics of Skyrmions in Fe/Gd Multilayers

In the region of bare Fe/Gd multilayers with CPW integrated, single skyrmion and skyrmion pairs (Fig. 5.19) were observed. They were formed and remained stable close to the saturation field. According to the phase diagram reported in Ref. [155], they are skyrmions or antiskyrmions instead of type-II bubbles (as indicated in Fig. 1.4). The single skyrmion-A was stabilized in the gap between signal line and ground line in Fig. 5.19 (a) at $\mu_0 H_\perp$ = -5.5 mT. The width of skyrmion-A was w_A = 430 nm and its height was h_A = 460 nm. The normalized magnetization m_z is shown in Fig. 5.19 (b). Underneath the signal line a single skyrmion-B was found (Fig. 5.19 (c)) at $\mu_0 H_\perp$ = 5 mT. Sizes of this skyrmion were w_B = 430 nm and h_B = 410 nm. In the region of the 1D nanomagnet array underneath the signal line, a double skyrmion (skyrion in pair) was spotted as shown in Fig .5.19 (e) at $\mu_0 H_\perp$ = 19 mT. According to the transmission signals, they behaved as a merged skyrmion. The component m_z only had a change of 2π. Thus it had the skyrmion number of 1 which is identical to a single skyrmion. We label it as skyrmion-C. The width of this pair is w_C = 600 nm. The height at the center of the pair is h_C^{center} = 400 nm (at x = 320 nm). In the following calculation of spin waves wavelength excited in skyrmions, we approximate skyrmion-A and skyrmion-B to a circle structure with diameter averaging the width and height.

Skyrmion-A, B and pair C were stable at their position during the measurements when the transmitted microwave signals amounted to about -8 dbm. We were able to reproduce them after demagnetizing. Further individual skyrmions were erased with microwave current switched on or selectively moved by the X-ray irradiation. The following data were obtained on skyrmion A to C.

5.4.1 Spin Dynamics of Single Skyrmion

Skyrmion-A appeared in the gap at about 0.5 μm to the signal line edge. Here, the majority dynamic component $\boldsymbol{h}_{\text{rf}} \parallel \boldsymbol{H}_\perp$. Four dynamic modes were observed below 1 GHz. Snapshots of normalized dynamic signals of each mode are plotted in Fig. 5.20. Their detail motions are plotted in Appendix Fig. A.4 and A.5. They consist of different phase evolution such as breathing (BR), clockwise (CW) and counter clockwise (CCW) modes. Surprisingly, not only BR motion but also CW and CCW motions are excited which is in contrast with the report [51, 82].

Excitation at f = 0.38 GHz (Fig. 5.20 (a)): The dynamic mode can be separated into two parts: local BR and local CW motions. BR motion existed at the position of a tiny defect. This motion emitted a spin wave in CCW motion of wavelength λ = 363 nm. Its phase velocity is estimated to be v_g = 0.17 km/s.

Excitation at f = 0.46 GHz (Fig. 5.20 (b)): Here, the second order CW motion was observed. There are two anti-nodes along the skyrmion circumference. Wavelength and phase velocity are estimated to be λ = 363 nm and v_g = 0.18 km/s, respectively.

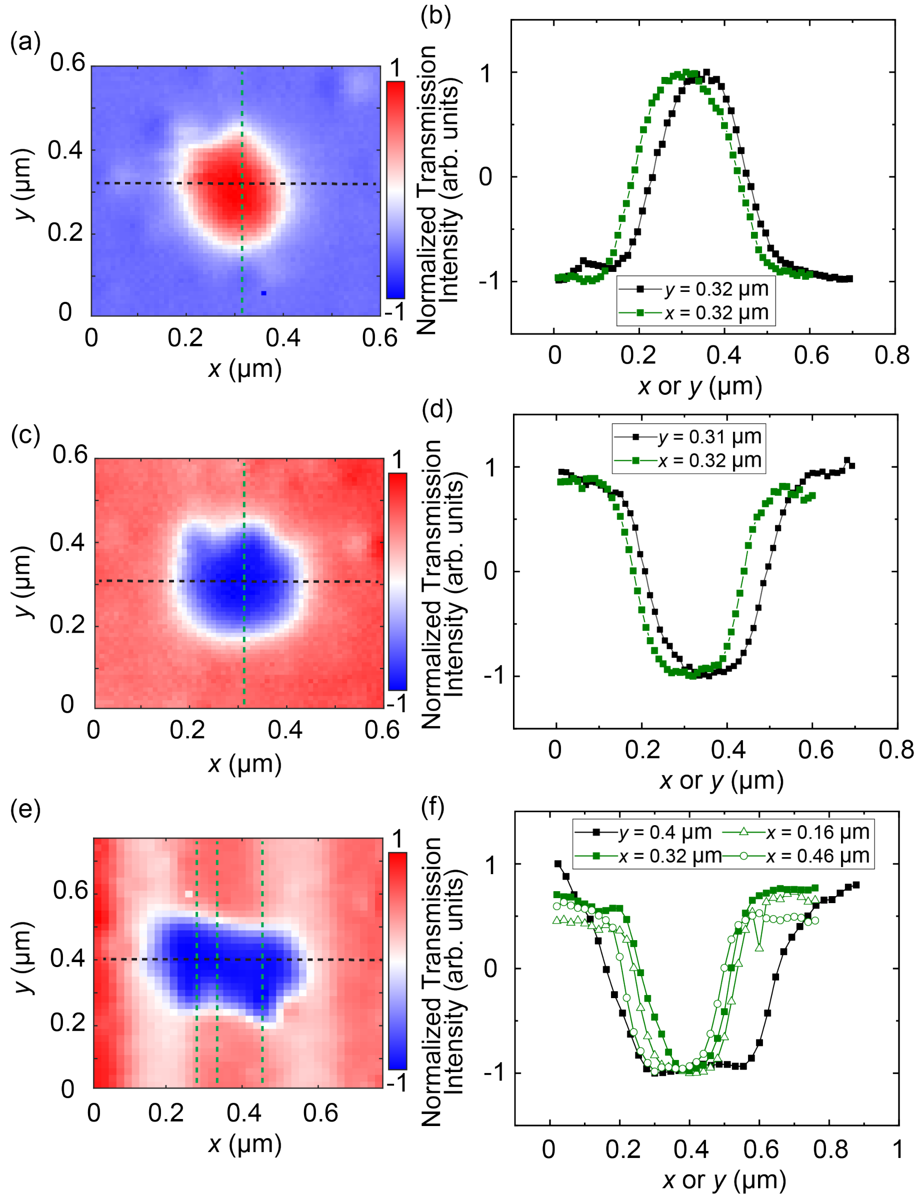

Figure 5.19 – **Static STXM image of skyrmions.** (a) and (b) $\mu_0 H_\perp$ = -5.5 mT. (c) and (d) $\mu_0 H_\perp$ = 5 mT. (e) and (f) $\mu_0 H_\perp$ = 19 mT. Color bar represents normalized X-ray transmission intensity. The line profiles in (b) (d) and (f) are corrected for the 30 degree sample tilting angle with respect to X-ray.

Excitation at f = 0.65 GHz (Fig. 5.20 (c)): A complex mode profile is observed. BR motion along two axes marked by dark straight arrows is mixed with CW rotation.

Excitation at f = 0.73 GHz (Fig. 5.20 (d)): The motion is similar to the complex one at f = 0.65 GHz. Further spin dynamic signals were noticed near the skyrmion following the indication of the gray arrows.

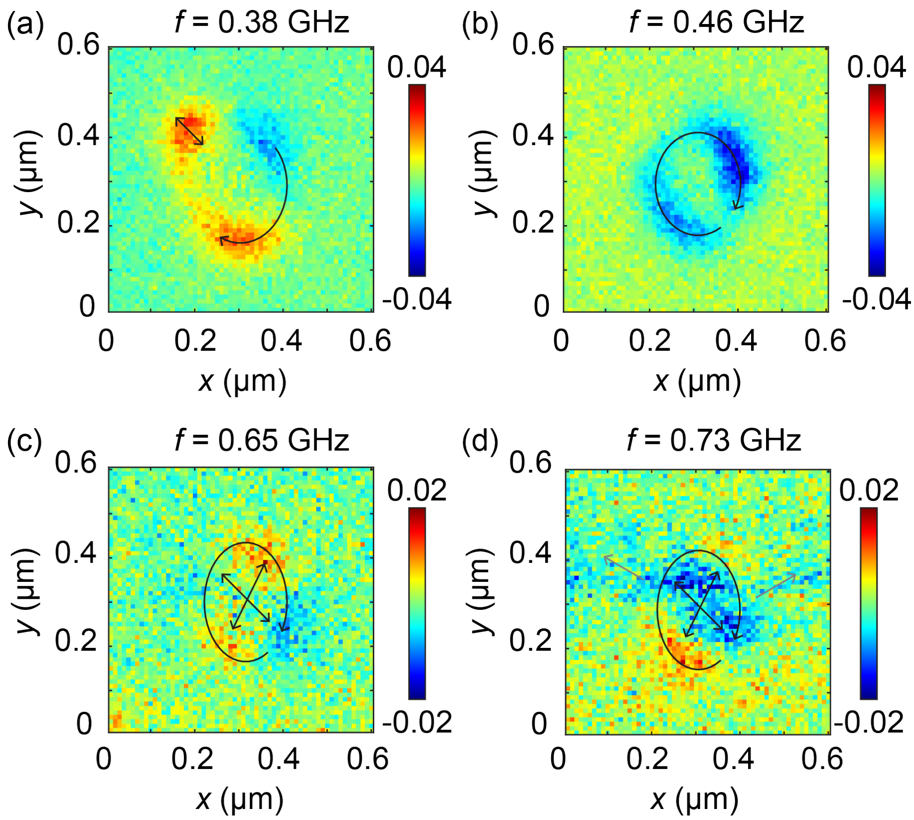

Figure 5.20 – **Spin-precessional motions of single skyrmion-A when $\boldsymbol{h}_{\mathrm{rf}} \parallel \boldsymbol{H}_{\perp}$.** Dynamic images with $\mu_0 H_{\perp}$ = -5.5 mT at (a) f = 0.38 GHz, (b) f = 0.46 GHz, (c) f = 0.65 GHz and (d) f = 0.73 GHz. Color bars represent the dynamic transmission signals normalized to the static signal. The black arrows indicate the phase evolution extracted form time-dependent data.

Skyrmion-B was located underneath the signal line at about 0.5 μm from the edge. The skyrmion core is opposite to skyrmion-A because the magnetic field was switched to the other direction $\mu_0 H_{\perp}$ = 5 mT. The main dynamic component for excitation was $\boldsymbol{h}_{\mathrm{rf}} \perp \boldsymbol{H}_{\perp}$. Four modes were observed (Fig. 5.21). Their detailed time-dependent motion can be found in Appendix Fig. A.6, A.7 and A.8. The four modes are categorized as follow.

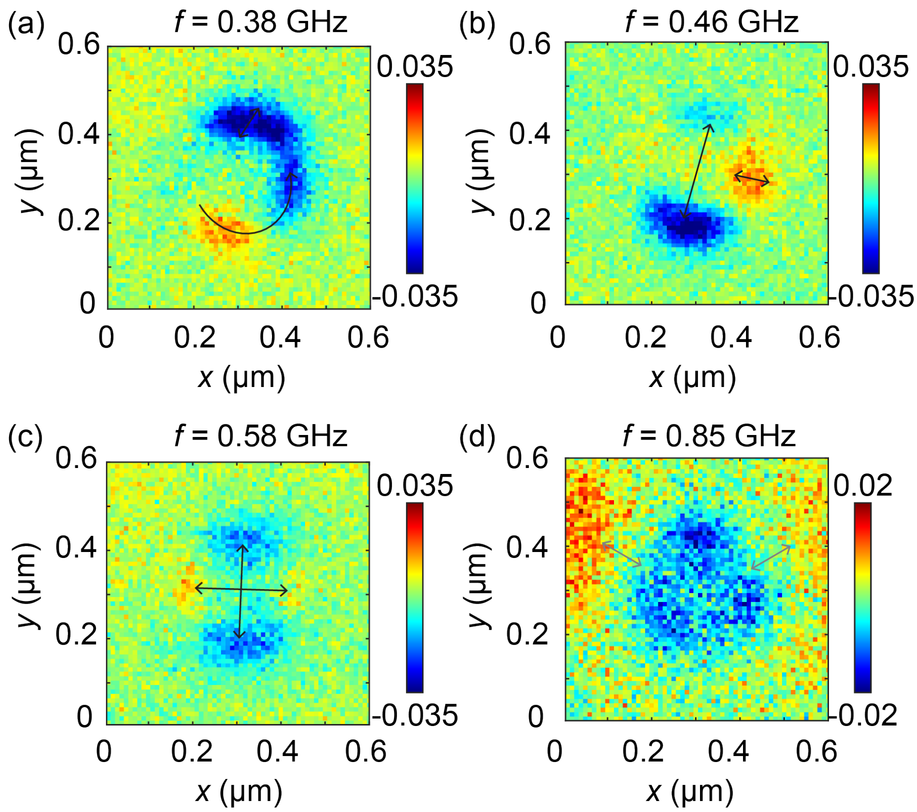

Figure 5.21 – **Spin-precessional motions of single skyrmion-B when $\boldsymbol{h}_{\text{rf}} \perp \boldsymbol{H}_{\perp}$.** Snapshots of skyrmion-B at $\mu_0 H_{\perp}$ = 5 mT excited at (a) f = 0.38 GHz, (b) f = 0.46 GHz, (c) f = 0.58 GHz and (d) f = 0.85 GHz. Color bars represent the dynamic transmission signals normalized to the static signal.

Excitation at f = 0.38 GHz (Fig. 5.21 (a): A combined local BR and local CCW motion are visible which is similar to skyrmion-A at the same frequency. But the sense of rotation of the spin waves is opposite to the skyrmion-A. We explain this by the opposite core magnetization direction (spin orientation π to -π to π instead of -π to π to -π). Spin waves are estimated to have wavelength λ = 273 nm and phase velocity v_g = 0.4 km/s.

Excitation at f = 0.46 GHz (Fig. 5.21 (b): BR motion is seen in two parts. One part is the BR motion along the axis around 15° tilted from the vertical axis. The other part is the local BR motion.

Excitation at f = 0.58 GHz (Fig. 5.21 (c): The excitation induced BR motions along two fixed axes. Those two axes are perpendicular to each other.

Excitation at f = 0.85 GHz (Fig. 5.21 (d): The motion is complex. There are two possible explanations: emission or scattering. If considering the emission model, skyrmion-B resonated in BR mode along all the circular directions and spin waves were emitted along the gray arrow. If considering the scattering mode, spin waves were excited near CPW but not limited to the skyrmion region. They excited the skyrmion BR motions and scattered from the skyrmion to the other directions along the gray arrows. Similar scattering processes were predicted on Bloch and Néel-type skyrmions [220, 221].

5.4.2 Spin Dynamics of the Skyrmion Pair

Two modes of skyrmion-C were observed below 1 GHz. Their snapshots are shown in Fig. 5.22 and Appendix Fig. A.9. Here $\boldsymbol{h}_{\mathrm{rf}} \perp \boldsymbol{H}_{\perp}$.

Excitation at $f = 0.33$ GHz (Fig. 5.22 (a): A local CW motion was emitted from the left bottom corner. Only half of the skyrmion was in resonance. The wavelength $\lambda = 239$ nm and the phase velocity was $v_g = 0.11$ km/s.

Excitation at $f = 0.59$ GHz (Fig. 5.22 (b): The motion can be described as butterfly flapping wings. It is constructed of BR motions with four fixed axes as indicated in Fig. 5.22 (b). BR motions along longer axes are in anti-phase with the motions in shorter axes.

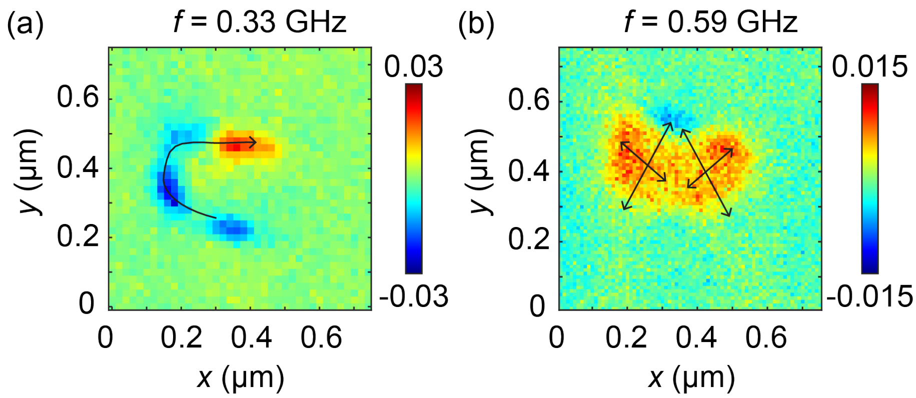

Figure 5.22 – **Spin-precessional motions of double skyrmion-C when $\boldsymbol{h}_{\mathrm{rf}} \perp \boldsymbol{H}_{\perp}$.** Snapshots of double skyrmion-C dynamic image with $\mu_0 H_{\perp} = 19$ mT at (a) $f = 0.33$ GHz and (b) $f = 0.59$ GHz. Color bars represent the dynamic transmission signals normalized to the static signal.

5.4.3 Discussion

In the following, we will compare the dynamic behaviors between dipolar skyrmion lattices (Fig. 1.13) and individual skyrmions. Despite the different frequencies of dynamics modes which should be related to the modification of material parameters due to hearing, both dipolar skyrmion lattice and individual dipolar skyrmion are experiencing rather complex motions combining breathing and rotation at the same time (Fig. 5.20). This is due to the complex skyrmion configurations which vary from Bloch-type skyrmion in middle layer to Néel-type skyrmion on the surfaces. When $\boldsymbol{h}_{\mathrm{rf}} \perp \boldsymbol{H}_z$, unlike the chiral magnets hosting Bloch-type skyrmions who can only resonance in CCW and CW modes[82], dipolar skyrmions can resonance in breathing motion. However when $\boldsymbol{h}_{\mathrm{rf}} \parallel \boldsymbol{H}_z$, there is only the breathing like motion obtained in dipolar skyrmion lattice. At the same time, rotational motion are noticed in individual dipolar skyrmions (Fig. 5.21). Higher order rotational motions (e.g. 2nd order) were seen only in individual skyrmions. Interestingly similar motions were predicted for Bloch-type skyrmion lattice in chiral magnet but those modes are not visible for CPW-based experiments [66].

5.5 Magnonic Grating Coupler Effect Generated by One-dimensional Co Nanostripe Arrays

The magnonic GC effect was observed in Fe/Gd multilayers integrated with 1D Co nanostripes whose periodicity amounted to $p = 450$ nm using all-electrical spin-wave spectroscopy. In Fig. 5.23, we display the spin wave spectroscopy of reflection signal S_{22} when an out-of-plane field $H_{\perp}$ was swept from 0 mT to 450 mT. Here we use the thru-configuration CPW design labeled as No. 5 in Table. 2.1.

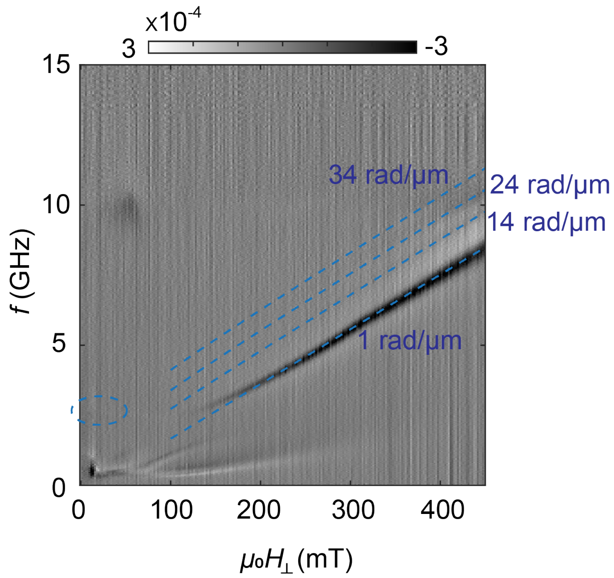

Figure 5.23 – **Spin wave spectroscopy on Fe/Gd multilayers with 1D Co nanomagnet array.** Reflection spectra of spin waves with 1D Co nanomagnet array with $p = 450$ nm. Here the color bar represents $\Delta S_{22}/\mu_0 \Delta H$. Dashed blue lines are field dependent spin wave branches with wavelength from 1 rad/μm to 34 rad/μm using the formalism of Kalinikos and Slavin for forward volume mode configuration [13]. Dashed blue circle highlights a resonance near 2.6 GHz.

In the S_{22} spectra, a strong mode is seen for $\mu_0 H_{\perp} \geq 120$ mT indicating the Fe/Gd multilayers entering the saturated state. There are three other weak modes at higher frequency. We plot the field dependent resonance branches of forward volume magnetostatic spin waves (FVMSWs) the formalism of Kalinikos and Slavin with wavevetors of $k = 1$ rad/μm, 14 rad/μm, 24 rad/μm and 34 rad/μm using the parameters from section 5.1.1. We find they are at the frequencies corresponding to the higher frequency modes. Those are the features of short-waved spin waves emitted from the GC made of Co nanostripes [166, 167]. The reciprocal lattice vector of the Co array is $G = 14$ rad/μm which agrees with the first GC mode. The other two modes reside at frequencies which correspond to slightly smaller wavevectors than the expected second order and third order of GC mode. Please note that this sample was fabricated on a Si_3N_4/Si substrate instead of the membrane windows. So the material parameters of Fe/Gd may differ from the characterized values in section 5.1.1. There are three modes below 2 GHz and they are assumed to be related to the domains. The number of resonance modes agrees with our reported observation using STXM (Fig. 5.17). The wide peak at about 10 GHz at 50 mT is the resonance mode from Co.

In the saturated state, the lowest wavelength we observed is 0.185 nm ($k = \frac{2\pi}{\lambda} = 34$ rad/μm) which is comparable to the dipolar skyrmion lattice size (Fig. 5.3) and smaller than the individual skyrmion size (Fig. 5.19). Thus it is very intriguing to explore this mode in the unsaturated state when the non-collinear structures are present. There is a mode at 2.6 GHz with very weak intensity (dashed circle in Fig. 5.23) and its appearance attracts our attention because it may originate from the GC mode in the unsaturated state. However the signal-to-noise ratio and sensitivity of the spin-wave spectroscopy is not enough for further exploration. Thus the STXM will be of special importance to resolve the GC mode in unsaturated states, and at the same time, to understand the role of domain lattices stabilized by Co nanomagnet arrays in exciting short-waved spin waves via a "built-in" grating coupler in Fe/Gd multilayers.

6 Conclusions and Outlook

In this thesis we have investigated the spin dynamics of non-collinear states in the chiral magnet Cu_2OSeO_3 (CSO) and amorphous Fe/Gd multilayers samples using broadband spin-wave spectroscopy, scanning micro-focus Brillouin light scattering (BLS), scanning transmission x-ray microscopy, magnetic force microscopy and micromagnetic simulation. In this chapter, we summarize the key results in the framework of this thesis in section 6.1. In section 6.2, we share the outlooks on our work and the future research topics based on our results.

6.1 Conclusions

In chapter 4, we discuss the helimagnons and spin dynamics of skyrmion lattices in the bulk chiral magnet CSO at cryogenic temperature. In the field polarized (FP) states induced with magnetic fields of different orientations, confined backward volume mode spin waves were observed in all-electrical spin-wave microscopy. Combined with the micromagnetic simulations, we find that confined backward volume spin wave modes consist not only of the dipolar spin wave mode with k defined by the sample boundaries, but also the exchange spin waves mode with k determined by the bulk DMI strength. We explored the role of DMI for confined mode and further focused on spin dynamics in non-collinear spin structures, namely helical, conical and skyrmion phases.

In the non-collinear states, in order to sort out the spin dynamics from different phases, we employed the micro-focus BLS with its scanning function in a cryostat which we integrated in the course of this thesis. Taking advantage of the scanning function and high sensitivity of BLS, we detected spin dynamics of conventional helical, conical and high temperature skyrmion phases found in CSO and other chiral magnets, as well as the special phases only found in CSO including the tilted conical phase and low temperature skyrmion phases when field $\boldsymbol{H}$ was applied along easy axis $\langle 001 \rangle$. Besides, we resolved the spin dynamics in the phase we interpret as the chiral soliton phase ($\boldsymbol{H}$ along $\langle 110 \rangle$) and elongated skyrmion lattice ($\boldsymbol{H}$ along $\langle 001 \rangle$). In the configuration of $\boldsymbol{H}$ along $\langle 001 \rangle$, we extended the temperature regime of the metastable skyrmion phases to low temperature via fast field cooling and laser illumination. We found out that in our experiments the green laser of BLS is essential for stabilizing the metastable phases. By comparing the Stokes and anti-Stokes signals, non-reciprocal characteristics were noticed for the -Q mode of tilted conical phase and breathing mode of the metastable skyrmion phases. The frequency difference of about 200 MHz was extracted from the non-reciprocal breathing modes between oppositely propagating magnons with $+\boldsymbol{k}$ and $-\boldsymbol{k}$ in the configuration of $\boldsymbol{H} \parallel$ k instead of backward volume spin wave. Furthermore, using the continuous-wave laser, we achieved the "brushing" of a 450 um-long track of a metastable phase that we interpreted as the elongated skyrmion lattice surrounded by conical and tilted conical phases. Our observations prove scanning BLS to be a efficient tool for exploring the one-to-one correspondence between non-collinear phases and their magnonic behaviors. The discovery of continuous-wave laser brushing skyrmion tracks offers a brand new approach for fabricating skyrmion devices and it is much easier to achieve compared with nano-fabrication or utilizing an ultra-fast laser.

In chapter 5, we reported the phase modification and spin dynamics in amorphous Fe/Gd multilayers with perpendicular magnetic anisotropy. The measurements were conducted by all-electrical spin-wave spectroscopy, magnetic force microscopy at room temperature and scanning x-ray transmission microscopy. By integrating the one-dimensional stripe arrays and two-dimensional disc arrays made of Cobalt, we modified the phase of the multilayers. Well-aligned stripe domains and square skyrmion lattices were formed. Assisted by micromagnetic simulations, we inferred the dipolar interaction to dominate the phase modification. In the dynamic measurements, using coplanar waveguides and microwave currents, we excited five spin waves modes in domain walls below 1 GHz. Four spin wave modes were excited with dynamic radio-frequency field $\boldsymbol{h}_{\mathrm{rf}} \perp \boldsymbol{H}$. Their wavevector increased with the frequency, which followed a consistent tendency of spin wave dispersion relations in Bloch-type domain wall. But the frequencies did not agree with the Block-type domain wall assumption and it may be related to the surface tilting of the spins from a Bloch-type to N$\acute{e}$el-type configuration. The shortest wavelength reached was 388 nm at f = 0.65 GHz. One more spin wave modes was excited with $\boldsymbol{h}_{\mathrm{rf}} \parallel \boldsymbol{H}$ at f = 0.85 GHz whose wavelength is λ = 409 nm. These modes propagated differently in the domain walls at different frequency. At f = 0.38 GHz, a magnon mode only existed only in the boundaries of multi-domains In single and double skyrmions, variable resonance modes including breathing and rotational motions were detected. The mode of shortest wavelength of λ = 239 nm was captured at 0.33 GHz in a double-skyrmion pair. At f = 0.85 GHz, we resolved the sign of spin wave scattering on skyrmions or spin wave emission. Our observations prove the nanomagnet arrays can be used to form skyrmion and domain lattices. The visualized dynamic resonances suggest domain walls and skyrmions as candidate for shrinking the wavelength of electromagnetic wave of meter and centimeters wavelength to spin waves of nanoscale wavelength. They can assist the design of miniaturized magnonic devices.

6.2 Outlook

In the following, we provide an outlook on the reported topics.

For the investigation of spin dynamics of bulk chiral magnet CSO at cryogenic temperature, theoretical models on spin dynamics in chiral soliton phase in CSO, and metastable skyrmion phases and phase X at low temperature considering cubic anisotropy are needed for a quantitative understanding of eigen-frequencies, dispersion relations, degree of polarization and non-reciprocity. Combining BLS with integrated CPWs and microwave irradiation, one could experimentally study the polarization of mode. Additional experiments on laser brushing of skyrmion tracks are needed to estimate the threshold of laser power for stabilizing and brushing the skyrmion phases, its laser wavelength dependence, possible anisotropy for brushing directions with respect to the field and crystallographic orientations, and whether there is a method to erase previously written tracks. Making use of the laser brushing, skyrmion tracks can be designed as intentionally seated mangon waveguide at specific frequencies (fulfilling the magnon dispersion relation in skyrmion phases). Furthermore, there are other skyrmion hosting materials such as the centrosymmetric magnets and Heusler alloys. The skyrmion lattices in the centrosymmetric magnets are extremely small down to the size of several nanometers [149, 150]. Considering that the spin dynamics are related to the size of the skyrmion lattices, they are of special interest for exploring the magnon band structures as magnonic crystals with smaller modulation period. Anti-skyrmions [152–155] also trigger further interest in resonant modes and magnon band structures because of their special non-trivial spin textures.

For the spin dynamics exploration on skyrmions and domain walls in amorphous Fe/Gd multilayers, we propose three directions. Firstly the spin dynamics of the two-dimensional skyrmion lattice induced by Co disc arrays would be interesting. It can reveal the difference between skyrmion lattices modes and single skyrmion dynamics experimentally. Secondly for the dynamic modes involving possible spin wave emission and scattering, a larger STXM imaging area would be important as a skyrmion further away from the CPW would be needed to avoid direct excitation of modes in the near field of a CPW. Thereby the scattering of propagating spin waves would be realized. Thirdly the CPW design need to be optimized for injecting higher power radio-frequency currents above $f = 1$ GHz. So that we can explore the magnonic grating coupler effects and resolve short-waved exchange spin waves modes in skyrmion phase. The domain lattices induced by Co structures can be also explored for the function of "built-in" grating couplers for generating exchange magnons.

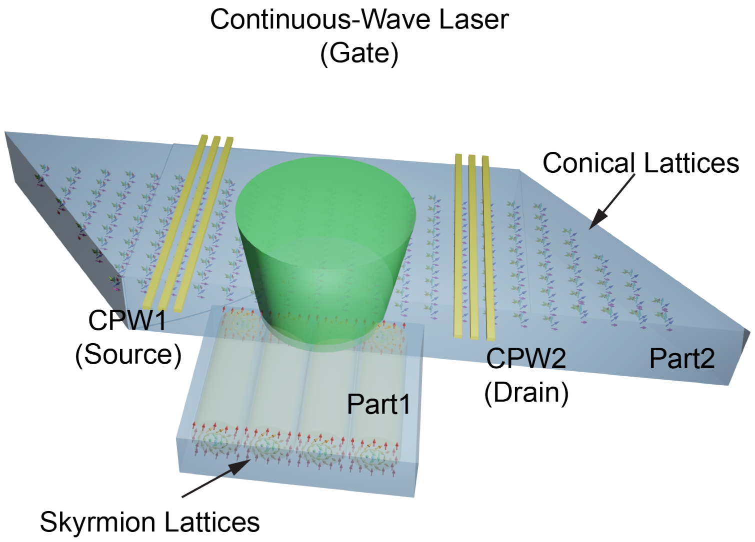

Figure 6.1 – **Sketch of a possible magnonic transistor based on skyrmion lattices.**

Thirdly, we suggest a possible magnon transistor design sketched in Fig. 6.1 functionalized as a mangnon switch. It consists of two parts of the same skyrmion hosting material with different shapes and thicknesses. Thereby demagnetization factors vary across the sample and thus might allow one to stabilize skyrmion phases in part1 and conical or tilted conical phases in part2 when a magnetic field H_0 is applied at the whole sample. CPW1 and CPW2 will be used for emission and detection of spin waves. They will take the function of "source" and "drain". A focused green laser is used for modifying the magnetic states in part2. It is the gate in this device.

The operation process of this transistor can be described as: (i) Reset the device with field H_R so part1 hosts skyrmion phases and part2 hosts conical or tilted conical phases. (ii) Inject radio-frequency signals in CPW1, only those frequencies satisfying the dispersion relation of magnons in conical phase will by transferred to CPW2. We label them as f_C. (iii) Switch on the laser, brushing the skyrmion phases into the region between source and drain and underneath CPWs. Now the dispersion relation were modified according to the skyrmion phases. Frequencies f_C are no longer allowed to pass. Only f_{SkL} are allowed to pass. (iv) Reset the device by applying field H_R to recover the function of f_C passing. f_{SkL} are no longer able to pass.

A An appendix

A.1 Flipped Lamella on Coplanar Waveguides with Grating Couplers

In order to explore the spin wave excitation and propagation in the low damping chiral magnet CSO, CPWs and nanomagnet arrays were integrated. We followed two strategies: flipping a thin lamella of CSO and placing it on top of the CPWs with grating arrays; fabricating the grating arrays and CPWs directly on top of the CSO bulk material. Both types of samples were achieved. Here we describe the process of the first strategy. The experiments are ongoing and results are not discussed in this thesis. We outline the developed recipe here.

SEM images are shown in Fig. A.1. CPWs made of Ti/Au were firstly fabricated on top of a SiO_2/Si substrate and then 1D Py nanostripe arrays were made on top of the CPW leads. Widths of the ground lines, gaps and signal lines were 2.1 μm, 1.6 μm and 1.7 μm, respectively. The center-to-center distance between two pairs of CPWs amounted to 10 μm. Widths of the nano-stripes were 120 nm and the periodicity was 270 nm. Both of those two procedures were conducted using ebeam-lithography (Fig. A.1 (a)). A CSO lamella was etched by FIB from a bulk CSO sample and flipped on top of the CPWs in the region with 1D grating arrays. The step-by-step process flow with recipe and details are stated below, followed by a schematic diagram in Fig. A.2.

I. CPW and marker fabrication by ebeam-lithography: The Si substrate was firstly cleaned by acetone and Isopropanol (IPA) and dried by blowing nitrogen gas. The Si substrate was pre-heated to 180°C for 300 s. Then a layer of 320-nm-thick EL9 was coated by 4000 rpm followed by a baking step performed at 180°C for 300 s. The second layer of ebeam resist 495 A2 was coated by 1700 rpm to make it 100 nm thick. It required another 300 s bake at 180°C. The structure was written by the EBPG5000ES system with 100 keV source, 100 nA beam current and 1200 μC/cm^2 dose. The patterns were written with in the substrate center without alignment procedure. The written pattern was immediately developed by MiBK:IPA 1:3 solution for 60 s after moving out of the vacuum environment of the ebeam chamber and cleaned by being placed in IPA for 1 min. 10-nm-thick Ti and 120-nm-thick Au were grown using the Leybold Optics LAB 600H machine. The sample was then placed in Remover 1165 solution for 2-3 days for lift-off processing. The cleaning procedure was conducted using IPA and DI water.

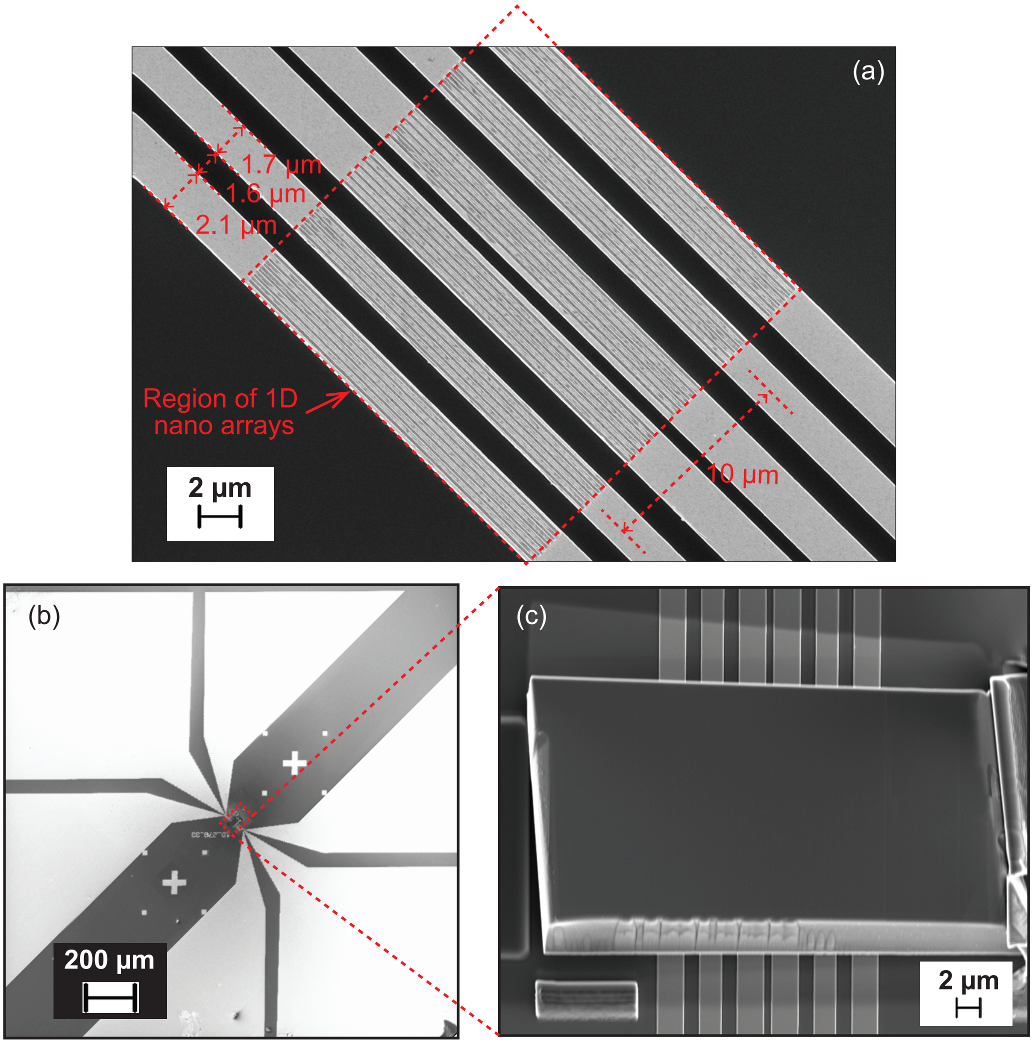

Figure A.1 – **SEM images of CSO samples flipped on CPW with grating arrays.** (a) SEM image of the region of 1D Py grating arrays on Au CPW. (b) SEM image of whole chip with flipped CSO lamella, 1D GC and CPW. The bright parts are the CPWs and the dark part is the SiO_2/Si substrate. (c) Zoomed-in SEM image of the flipped CSO lamella.

II. Grating coupler (GC) fabrication by ebeam-lithography: A similar procedure as the last step was performed but with different resists and a different ebeam writing setting. Here, after cleaning and pre-baking, we coated 180-nm-thick EL6 and 100-nm-thick 495 A2 with the spinning speed of 2500 rpm and 1700 rpm, respectively. 300 s of bake at 180 °C was needed after each coating. To write the 1D nanostructures, a dose of 600 $\mu C/cm^2$ was used with a 200 pA beam current. The same development procedure was applied as in the last step. Then

50-nm-thick Py was thermally evaporated using the Leybold Optics LAB 600H machine. One day long lift-off processing in Remover 1165 and cleaning with IPA and DI water followed.

III. Cutting the CSO lamella by focused ion beam technique: We cut the CSO lamella from a polished bulk sample with clearly identified crystallographic orientations. 50-nm-thick Pt layer was firstly sputtered by Pfeiffer SPIDER 600 in CMi as a conducting layer. FIB was performed with the FEI Nova 600 NanoLab machine at CMi and the Zeiss NVision 40 CrossBeam machine at CIME. A layer of 1-μm-thick Pt was firstly grown for surface protection. A standing lamella was etched using 30 kV ion source and variable ion current, from 27 nA to 700 pA. The final surface cleaning was conducted with 150 nA. Top, bottom and right edges were cut into 45 degree to avoid reflection of spin waves in the experiment. All the Pt material was removed from the top surface when the lamella was shaped to 45 degree. The dimensions of the lamella were about 25 μm × 15 μm × 2.5 μm.

IV. Flipping the CSO lamella on the CPWs with GCs: The CSO bulk sample was rotated 90 degree so the lamella was laying parallel to the SiO_2/Si substrate surface. The lamella was then picked by the micro-manipulator in the Zeiss NVision 40 CrossBeam chamber at CIME and placed on top of the region of the 1D GC but with a tiny tilting angle so that the 1D GCs were not damaged by the lamella. A carbon bar was used to fix the sample at the edge with 45 degree, as shown in Fig. A.1 (c).

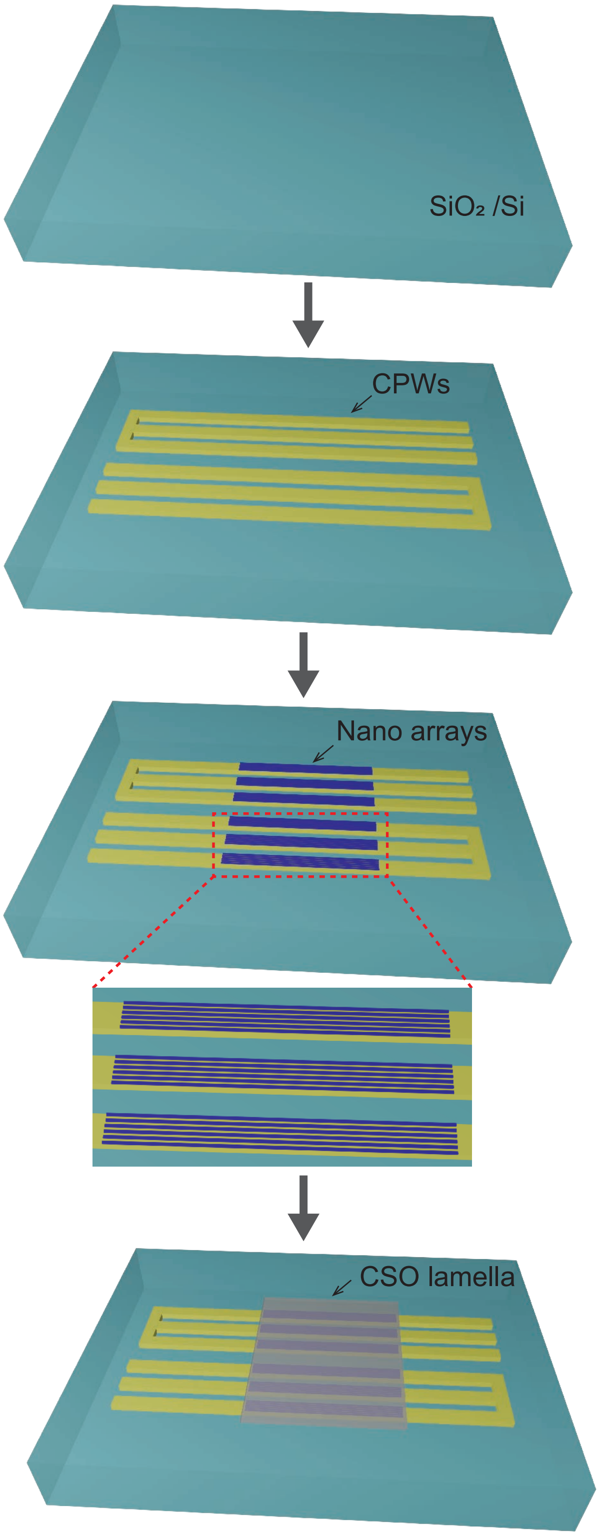

Figure A.2 – **Process flow of fabricating flipped CSO lamella on CPWs with GCs.**

A.2 Mumax3 Simulation Parameters

A.2.1 Confined Spin Waves in Bulk Chiral Magnets

Materials CSO bulk

Simulation cells: $N = 16\times512\times16$
Simulation cell size: $\Delta = 8\times4\times8$ nm^3
No PBC Saturation magnetization: $M_{\text{sat}} = 103$ kA/m
Exchange constant: $A_{\text{ex}} = 7\times10^{-13}$ J/m
Damping parameter: $\alpha = 0.0005$
Anisotropy strength: $K_{\text{C1}} = 0.6$ kJ/m^3
DMI constant: $D_{\text{bulk}} = 7.4\times10^{-5}$ J/m^2
Dynamic simulation duration: $T = 6$ ns
Simulation time step: $\delta t = 50$ ps

A.2.2 Interactions between Fe/Gd Multilayers and Co Arrays:

Material Fe/Gd multilayers

Simulation cells: $N = 256\times256\times40$
Simulations cells (for complete stripe): $N = 160\times1024\times40$
Simulation cell size: $\Delta = 1.4\times1.4\times2$ nm^3
PBC: (20,20,0) PBC (for complete stripe): (20,0,0) Saturation magnetization: $M_{\text{sat}} = 320$ kA/m
Exchange constant: $A_{\text{ex}} = 6\times10^{-12}$ J/m
Damping parameter: $\alpha = 0.01$
Anisotropy strength: $K_{\text{C1}} = 66$ kJ/m^3

Material Co

Simulation cells: $N = 256\times256\times10$
Simulations cells (for complete stripe): $N = 160\times1024\times10$
PBC: (20,20,0) PBC (for complete stripe): (20,0,0) Simulation cell size: $\Delta = 1.4\times1.4\times2$ nm^3
Saturation magnetization: $M_{\text{sat}} = 1400$ kA/m
Exchange constant: $A_{\text{ex}} = 1.4\times10^{-11}$ J/m
Damping parameter: $\alpha = 0.5$

A.3 Nonreciprocity in Dynamic Modes of Metastable Skyrmion Lattices

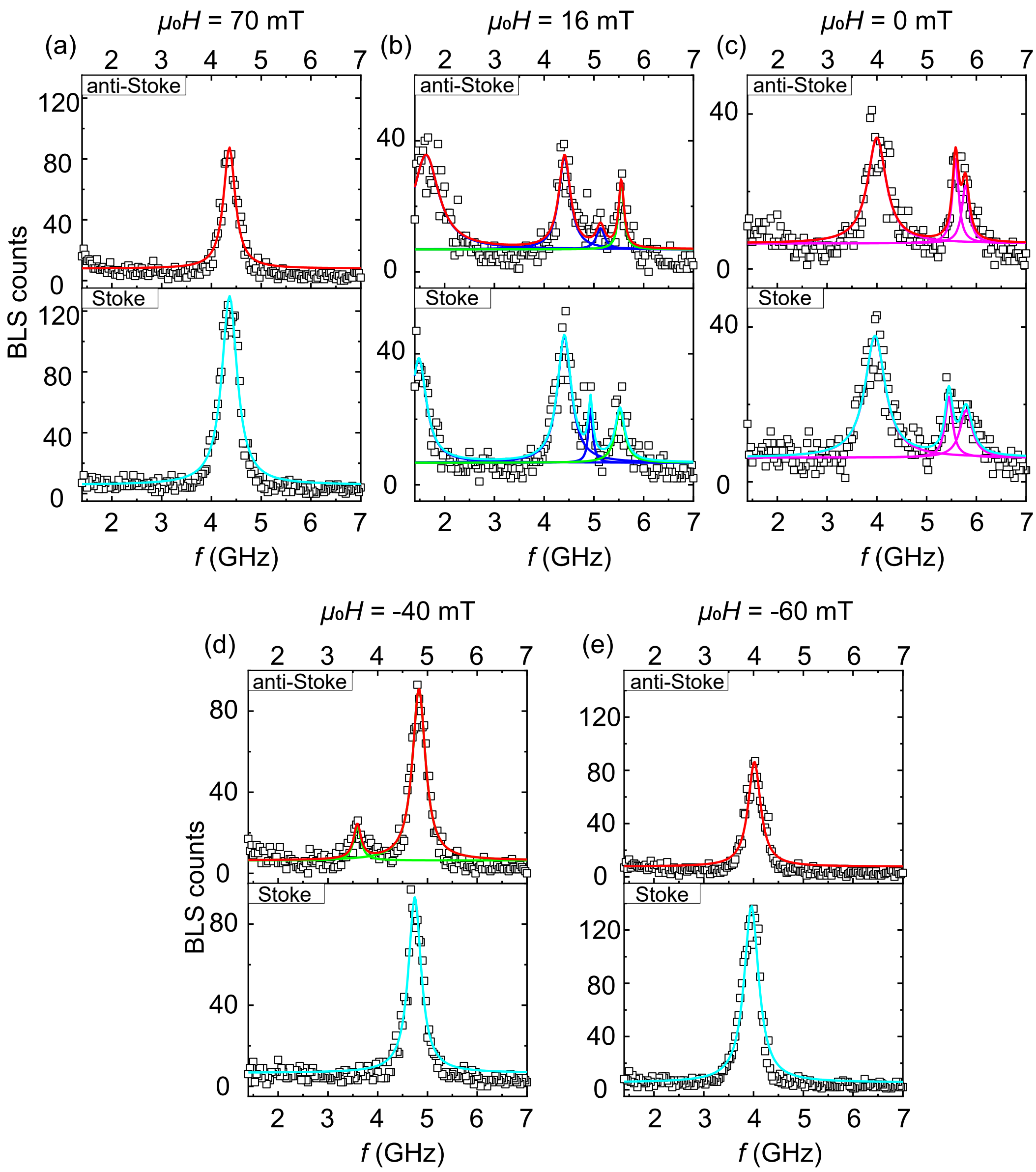

Figure A.3 – **Line plots of Stokes and Anti-Stokes BLS spectra with $\mu_0 H_{FC}$ = 16 mT.** Spectra are collected from (a) FP, (b) MT-h-SkL, (c) phase X, (d) conical and (e) FP states.

Table A.1 – Table of linewidth and area size of Anti-Stokes and Stokes peaks: FP and conical phases.

	Phase	FP 70 mT	FP -60 mT	Conical -40 mT	
	Mode			+Q	-Q
Linewidth (GHz)	Anti-Stokes	0.29±0.05	0.30±0.05	0.32±0.03	0.18±0.12
	Stokes	0.37±0.02	0.36±0.02	0.31±0.03	-
Area (arb. units)	Anti-Stokes	35.7±4.5	37.5±4.8	42.1±3.2	4.8±2.3
	Stokes	73.1±3.3	74.2±3.3	42.2±3.1	-

Table A.2 – Table of linewidth and area size of Anti-Stokes and Stokes peaks: MT-h-SkL phase.

	Phase	MT-h-SkL 16 mT			
	Mode	Mode (1) +Q	Mode (2) CW	Mode (3) BR	Mode (4) CCW
Linewidth (GHz)	Anti-Stokes	0.13±0.06	0.21±0.26	0.28±0.07	0.62±0.13
	Stokes	0.24±0.10	0.10±0.06	0.34±0.05	0.36±0.09
Area (arb. units)	Anti-Stokes	4.1±1.5	2.1±2.0	12.5±2.2	28.2±4.7
	Stokes	5.9±1.8	2.7±1.3	20.4±2.3	18.4±4.0

Table A.3 – Table of linewidth and area size of Anti-Stokes and Stokes peaks: phase X.

	Phase	Phase X 0 mT		
	Mode	X1	X2	X3
Linewidth (GHz)	Anti-Stokes	0.45±0.07	0.15±0.07	0.18±0.11
	Stokes	0.49±0.06	0.18±0.09	0.30±0.16
Area (arb. units)	Anti-Stokes	19.4±2.2	5.2±2.5	4.3±2.7
	Stokes	24.3±2.3	4.5±2.0	5.8±2.6

A.4 Snapshot of Skyrmion Dynamics in Fe/Gd Multilayers Resolved by STXM

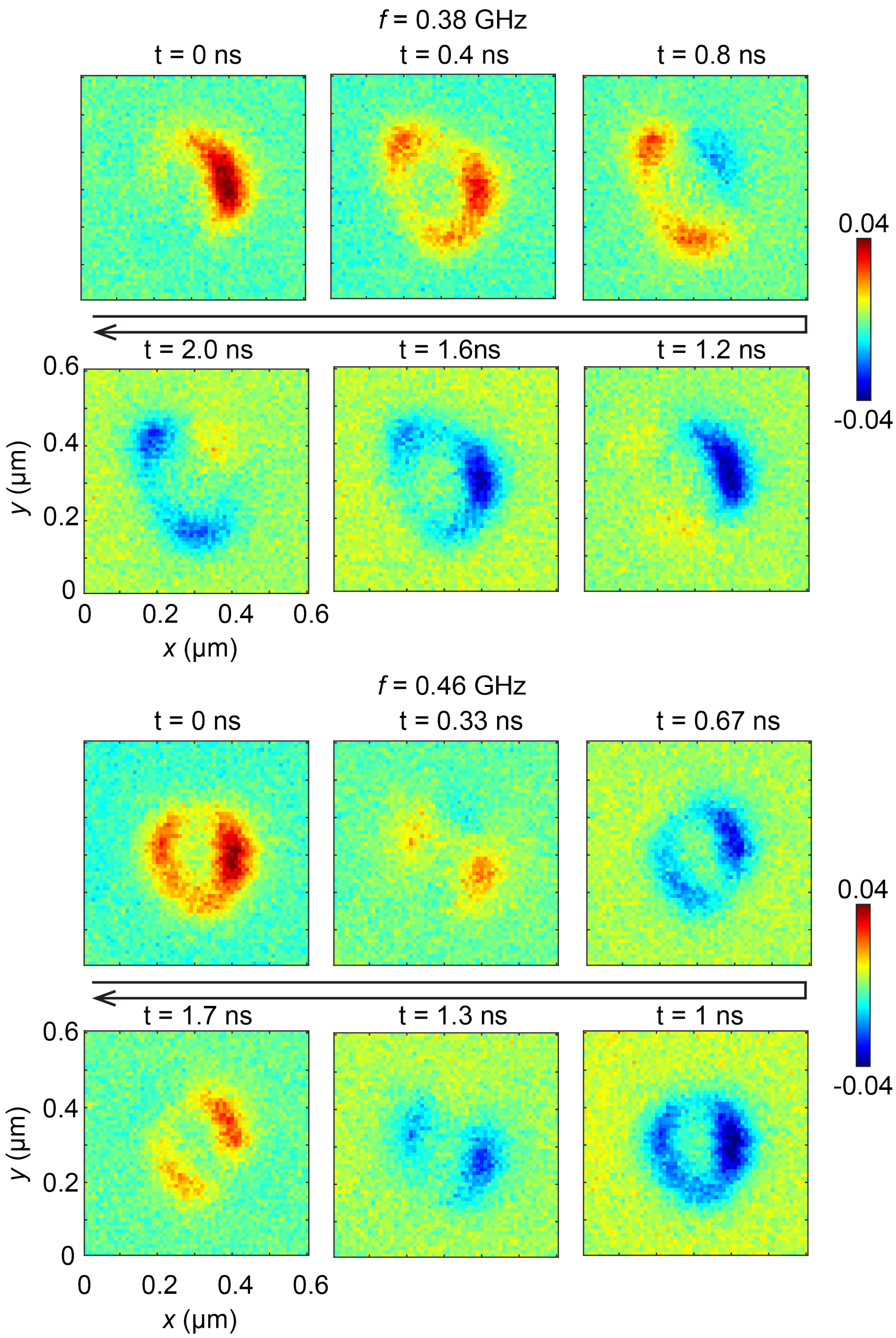

Figure A.4 – **Snapshot of Skyrmion-A Dynamics in Fe/Gd Multilayers Resolved by STXM.**

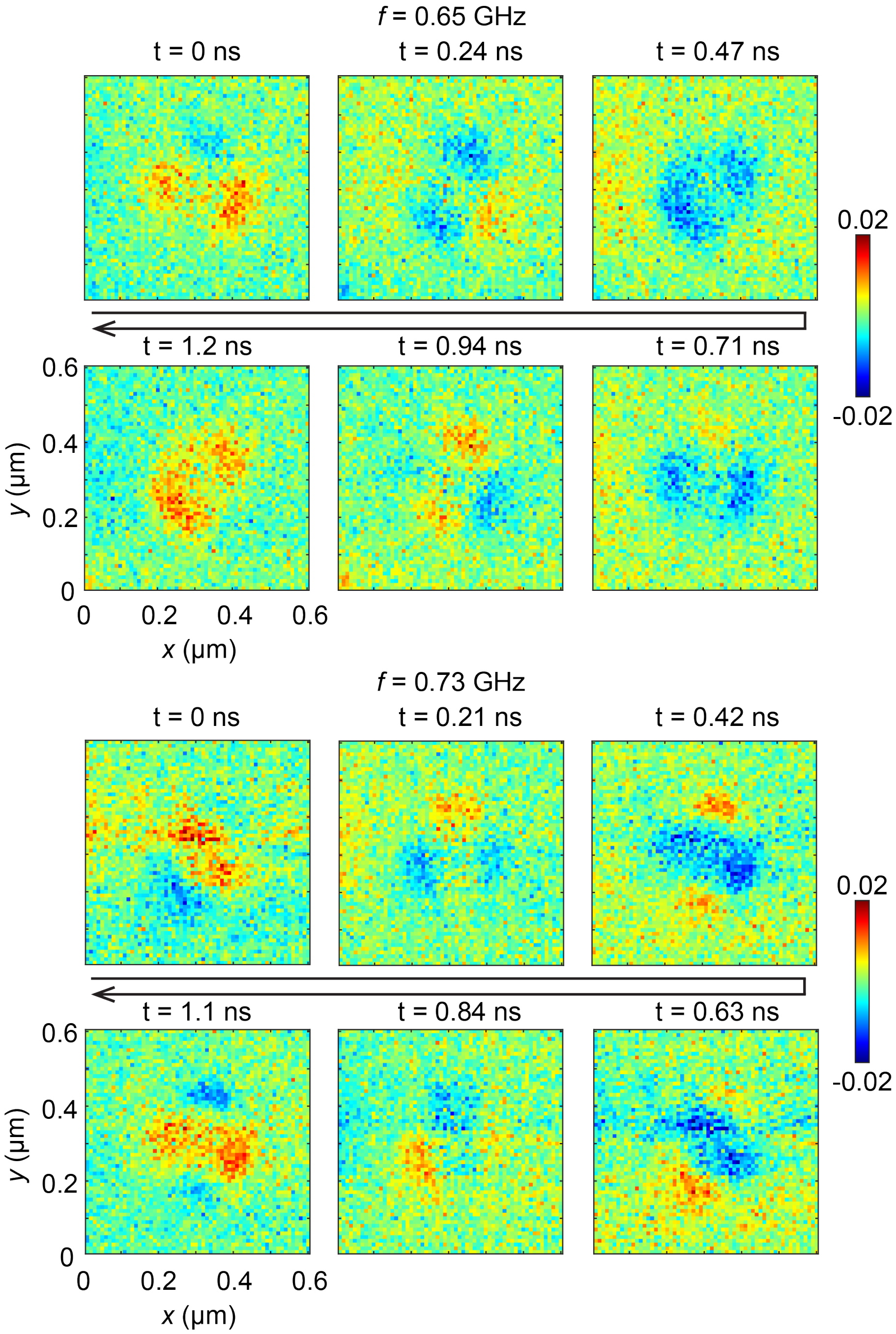

Figure A.5 – **Snapshot of Skyrmion-A Dynamics in Fe/Gd Multilayers Resolved by STXM.**

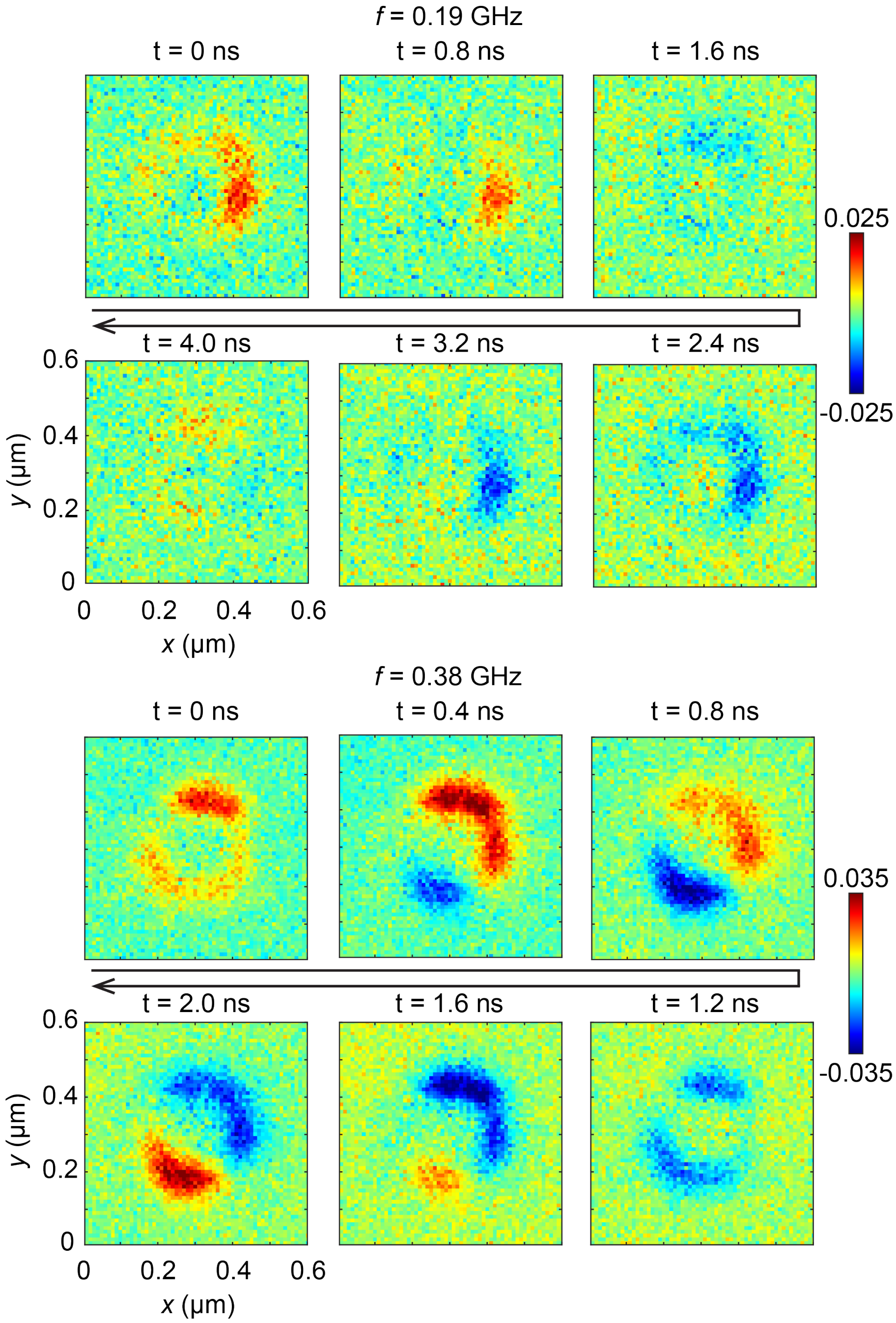

Figure A.6 – **Snapshot of Skyrmion-B Dynamics in Fe/Gd Multilayers Resolved by STXM.**

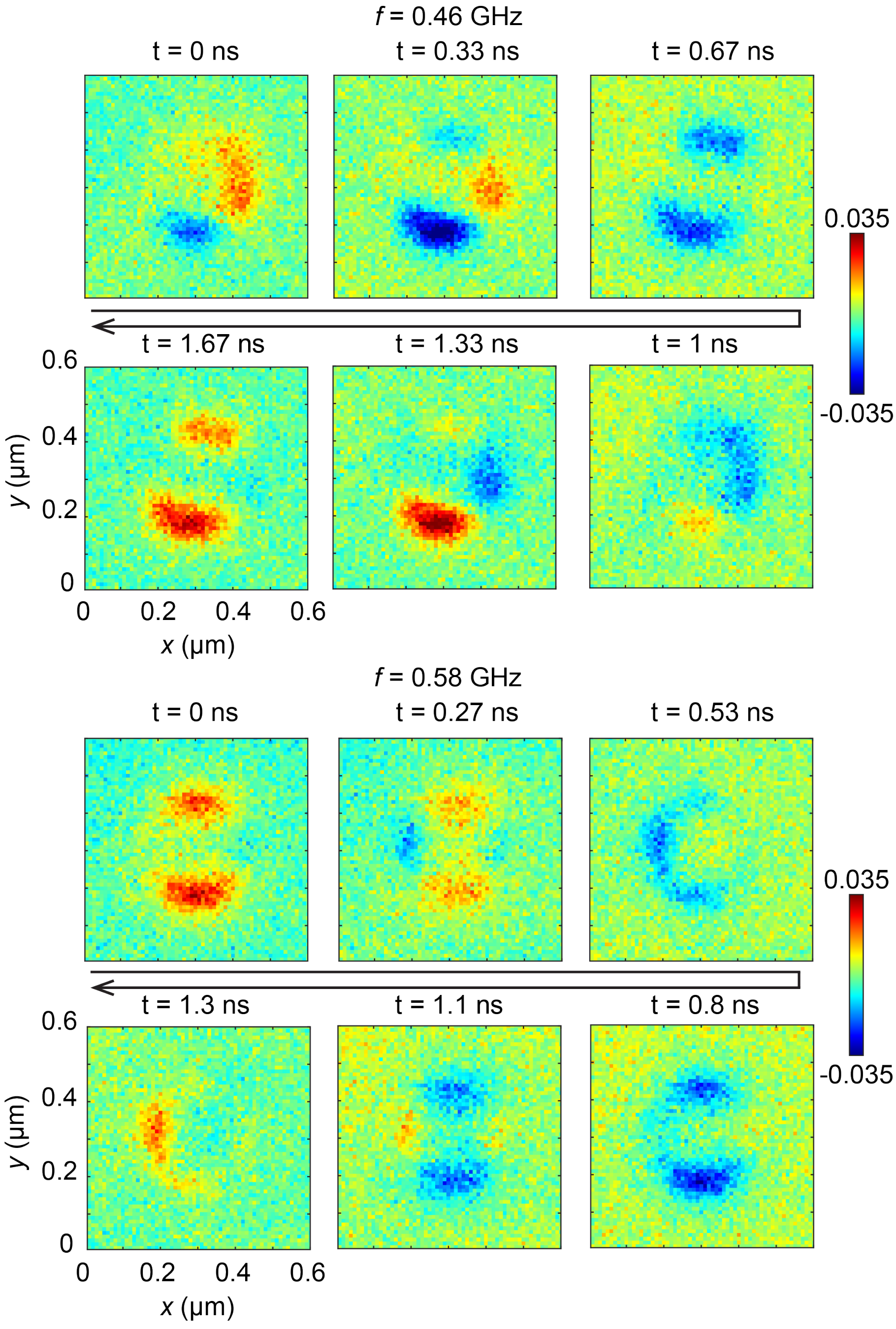

Figure A.7 – **Snapshot of Skyrmion-B Dynamics in Fe/Gd Multilayers Resolved by STXM.**

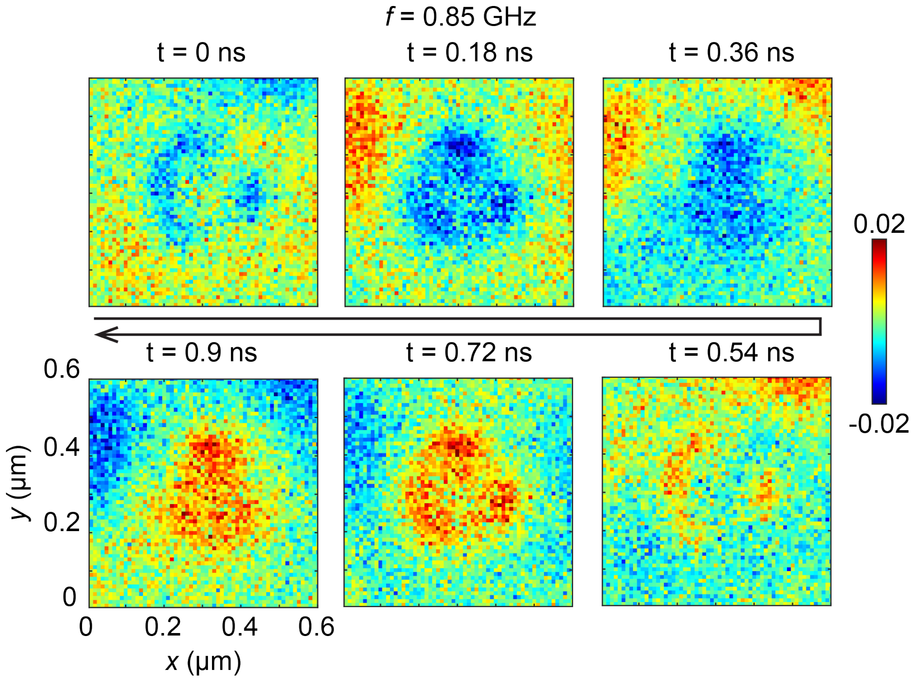

Figure A.8 – **Snapshot of Skyrmion-B Dynamics in Fe/Gd Multilayers Resolved by STXM.**

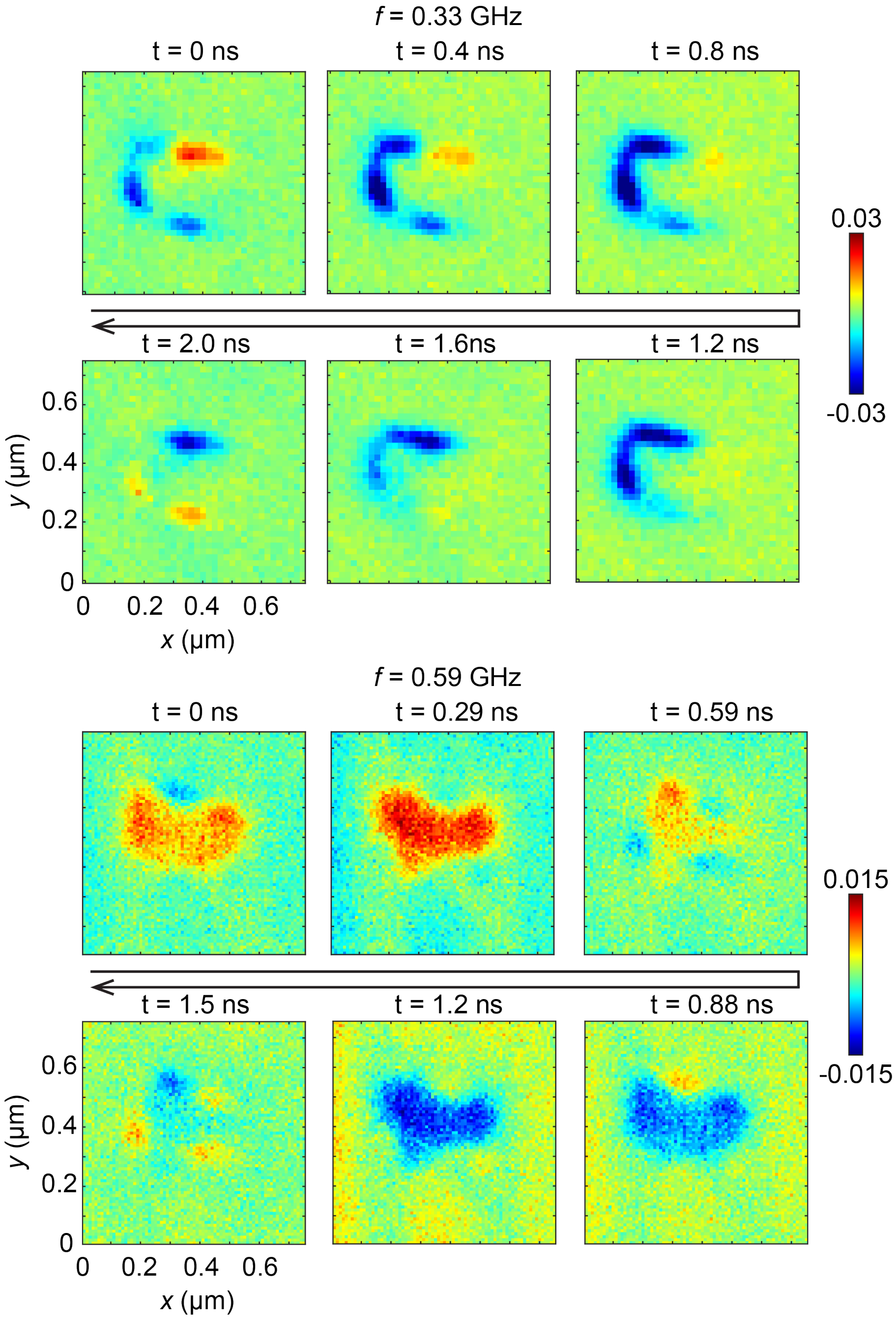

Figure A.9 – **Snapshot of Double Skyrmion-C Dynamics in Fe/Gd Multilayers Resolved by STXM.**

Bibliography

[1] Bird, H. Approaches to electronic miniaturization. *IEEE Trans. Components, Packag. Manuf. Technol. Part A* **18**, 274–278 (1995). URL http://ieeexplore.ieee.org/document/390303/.

[2] Chau, R., Doyle, B., Datta, S., Kavalieros, J. & Zhang, K. Integrated nanoelectronics for the future. *Nat. Mater.* **6**, 810–812 (2007). URL www.nature.com/naturematerialshttp://www.nature.com/articles/nmat2014.

[3] Coughlin, T. M. *Digital Storage in Consumer Electronics* (Spinger, 2008). URL https://linkinghub.elsevier.com/retrieve/pii/B9780750684651X50012.

[4] Miller, R. D. & Chandross, E. A. Introduction: Materials for Electronics. *Chem. Rev.* **110**, 1–2 (2010). URL https://pubs.acs.org/sharingguidelineshttps://pubs.acs.org/doi/10.1021/cr900384b.

[5] Mills, M. Hearing Aids and the History of Electronics Miniaturization. *IEEE Ann. Hist. Comput.* **33**, 24–45 (2011). URL http://ieeexplore.ieee.org/document/5771310/.

[6] Colinge, J. P. & Chandrakasan, A. *FinFETs and Other Multi-Gate Transistors* (Springer US, Boston, MA, 2008). URL http://link.springer.com/10.1007/978-0-387-71752-4.

[7] Kang, W., Huang, Y., Zhang, X., Zhou, Y. & Zhao, W. Skyrmion-Electronics: An Overview and Outlook. *Proc. IEEE* **104**, 2040–2061 (2016). URL https://ieeexplore.ieee.org/document/7544451/.

[8] Kostylev, M. P., Serga, A. A., Schneider, T., Leven, B. & Hillebrands, B. Spin-wave logical gates. *Appl. Phys. Lett.* **87**, 153501 (2005). URL http://aip.scitation.org/doi/10.1063/1.2089147.

[9] Khitun, A., Mingqiang Bao & Wang, K. Spin Wave Magnetic NanoFabric: A New Approach to Spin-Based Logic Circuitry. *IEEE Trans. Magn.* **44**, 2141–2152 (2008). URL http://ieeexplore.ieee.org/document/4604771/.

[10] Back, C. *et al.* The 2020 skyrmionics roadmap. *J. Phys. D. Appl. Phys.* **53**, 363001 (2020). URL https://doi.org/10.1088/1361-6463/ab8418https://iopscience.iop.org/article/10.1088/1361-6463/ab8418. 2001.00026.

[11] Serga, A. A., Chumak, A. V. & Hillebrands, B. YIG magnonics. *J. Phys. D. Appl. Phys.* **43**, 264002 (2010). URL https://iopscience.iop.org/article/10.1088/0022-3727/43/26/264002https://iopscience.iop.org/article/10.1088/0022-3727/43/26/264002/meta.

[12] Kruglyak, V. V., Demokritov, S. O. & Grundler, D. Magnonics. *J. Phys. D. Appl. Phys.* **43**, 260301 (2010). URL https://iopscience.iop.org/article/10.1088/0022-3727/43/26/260301.

[13] Kalinikos, B. A. & Slavin, A. N. Theory of dipole-exchange spin wave spectrum for ferromagnetic films with mixed exchange boundary conditions. *J. Phys. C Solid State Phys.* **19**, 7013–7033 (1986). URL https://iopscience.iop.org/article/10.1088/0022-3719/19/35/014.

[14] Mahmoud, A. *et al.* Introduction to spin wave computing. *J. Appl. Phys.* **128**, 161101 (2020). URL https://doi.org/10.1063/5.0019328http://aip.scitation.org/doi/10.1063/5.0019328. 2006.12905.

[15] Schneider, T. *et al.* Realization of spin-wave logic gates. *Appl. Phys. Lett.* **92**, 022505 (2008). URL https://doi.org/10.1063/1.2834714http://aip.scitation.org/doi/10.1063/1.2834714.

[16] Lee, K.-S. & Kim, S.-K. Conceptual design of spin wave logic gates based on a Mach–Zehnder-type spin wave interferometer for universal logic functions. *J. Appl. Phys.* **104**, 053909 (2008). URL http://aip.scitation.org/doi/10.1063/1.2975235.

[17] Klingler, S. *et al.* Design of a spin-wave majority gate employing mode selection. *Appl. Phys. Lett.* **105**, 152410 (2014). URL http://aip.scitation.org/doi/10.1063/1.4898042.

[18] Fischer, T. *et al.* Experimental prototype of a spin-wave majority gate. *Appl. Phys. Lett.* **110**, 152401 (2017). URL https://doi.org/10.1063/1.4979840http://aip.scitation.org/doi/10.1063/1.4979840.

[19] Wang, Q. *et al.* A magnonic directional coupler for integrated magnonic half-adders. *Nat. Electron.* **3**, 765–774 (2020). URL https://doi.org/10.1038/s41928-020-00485-6http://www.nature.com/articles/s41928-020-00485-6.

[20] Wagner, K. *et al.* Magnetic domain walls as reconfigurable spin-wave nanochannels. *Nat. Nanotechnol.* **11**, 432–436 (2016). URL www.nature.com/naturenanotechnologyhttp://www.nature.com/articles/nnano.2015.339.

[21] Albisetti, E. *et al.* Nanopatterning reconfigurable magnetic landscapes via thermally assisted scanning probe lithography. *Nat. Nanotechnol.* **11**, 545–551 (2016). URL www.nature.com/naturenanotechnologyhttp://www.nature.com/articles/nnano.2016.25.

[22] Sluka, V. *et al.* Emission and propagation of 1D and 2D spin waves with nanoscale wavelengths in anisotropic spin textures. *Nat. Nanotechnol.* **14**, 328–333 (2019). URL https://doi.org/10.1038/s41565-019-0383-4http://www.nature.com/articles/s41565-019-0383-4.

[23] Liu, C. *et al.* Current-controlled propagation of spin waves in antiparallel, coupled domains. *Nat. Nanotechnol.* **14**, 691–697 (2019). URL https://doi.org/10.1038/s41565-019-0429-7http://www.nature.com/articles/s41565-019-0429-7.

[24] Choudhury, S. *et al.* Voltage controlled on-demand magnonic nanochannels. *Sci. Adv.* **6**, eaba5457 (2020). URL http://advances.sciencemag.org/https://advances.sciencemag.org/lookup/doi/10.1126/sciadv.aba5457.

[25] Puszkarski, H. & Krawczyk, M. Magnonic Crystals — the Magnetic Counterpart of Photonic Crystals. *Solid State Phenom.* **94**, 125–134 (2003). URL www.scientific.net.https://www.scientific.net/SSP.94.125.

[26] Krawczyk, M. *et al.* Magnonic band structures in two-dimensional bi-component magnonic crystals with in-plane magnetization. *J. Phys. D. Appl. Phys.* **46**, 495003 (2013). URL https://iopscience.iop.org/article/10.1088/0022-3727/46/49/495003.

[27] Krawczyk, M. & Grundler, D. Review and prospects of magnonic crystals and devices with reprogrammable band structure. *J. Phys. Condens. Matter* **26**, 123202 (2014). URL https://iopscience.iop.org/article/10.1088/0953-8984/26/12/123202https://iopscience.iop.org/article/10.1088/0953-8984/26/12/123202/meta.

[28] Wang, Z. K. *et al.* Nanostructured Magnonic Crystals with Size-Tunable Bandgaps. *ACS Nano* **4**, 643–648 (2010). URL www.acsnano.orghttps://pubs.acs.org/doi/10.1021/nn901171u.

[29] Duerr, G., Thurner, K., Topp, J., Huber, R. & Grundler, D. Enhanced transmission through squeezed modes in a self-cladding magnonic waveguide. *Phys. Rev. Lett.* **108**, 227202 (2012). URL https://link.aps.org/doi/10.1103/PhysRevLett.108.227202.

[30] Tacchi, S. *et al.* Mode conversion from quantized to propagating spin waves in a rhombic antidot lattice supporting spin wave nanochannels. *Phys. Rev. B* **86**, 014417 (2012). URL https://link.aps.org/doi/10.1103/PhysRevB.86.014417.

[31] Semenova, E. K. & Berkov, D. V. Spin wave propagation through an antidot lattice and a concept of a tunable magnonic filter. *J. Appl. Phys.* **114**, 013905 (2013). URL http://aip.scitation.org/doi/10.1063/1.4812468.

[32] Kumar, D., Kłos, J. W., Krawczyk, M. & Barman, A. Magnonic band structure, complete bandgap, and collective spin wave excitation in nanoscale two-dimensional magnonic crystals. *J. Appl. Phys.* **115**, 043917 (2014). URL http://dx.doi.org/10.1063/1.4862911]http://aip.scitation.org/doi/10.1063/1.4862911.

[33] Qin, H., Both, G.-J., Hämäläinen, S. J., Yao, L. & van Dijken, S. Low-loss YIG-based magnonic crystals with large tunable bandgaps. *Nat. Commun.* **9**, 5445 (2018). URL https://doi.org/10.1038/s41467-018-07893-5http://www.nature.com/articles/s41467-018-07893-5.

[34] Mandal, R. *et al.* Effects of antidot shape on the spin wave spectra of two-dimensional Ni80Fe20 antidot lattices. *Appl. Phys. Lett.* **103**, 262410 (2013). URL https://doi.org/10.1063/1.4860959http://aip.scitation.org/doi/10.1063/1.4860959.

[35] Mandal, R., Barman, S., Saha, S., Otani, Y. & Barman, A. Tunable spin wave spectra in two-dimensional Ni 80 Fe 20 antidot lattices with varying lattice symmetry. *J. Appl. Phys.* **118**, 053910 (2015). URL http://aip.scitation.org/doi/10.1063/1.4928082.

[36] Mühlbauer, S. *et al.* Skyrmion lattice in a chiral magnet. *Science* **323**, 915–919 (2009). URL http://science.sciencemag.org/https://www.sciencemag.org/lookup/doi/10.1126/science.1166767.

[37] Yu, X. Z. *et al.* Real-space observation of a two-dimensional skyrmion crystal. *Nature* **465**, 901–904 (2010). URL http://www.nature.com/articles/nature09124.

[38] Yu, X. Z. *et al.* Near room-temperature formation of a skyrmion crystal in thin-films of the helimagnet FeGe. *Nat. Mater.* **10**, 106–109 (2011). URL www.nature.com/naturematerialshttp://www.nature.com/articles/nmat2916.

[39] Seki, S., Yu, X. Z., Ishiwata, S. & Tokura, Y. Observation of skyrmions in a multiferroic material. *Science* **336**, 198–201 (2012). URL http://science.sciencemag.org/https://www.sciencemag.org/lookup/doi/10.1126/science.1214143.

[40] Bauer, A. & Pfleiderer, C. Magnetic phase diagram of MnSi inferred from magnetization and ac susceptibility. *Phys. Rev. B - Condens. Matter Mater. Phys.* **85**, 214418 (2012). URL https://link.aps.org/doi/10.1103/PhysRevB.85.214418.

[41] Karube, K. *et al.* Robust metastable skyrmions and their triangular-square lattice structural transition in a high-temperature chiral magnet. *Nat. Mater.* **15**, 1237–1242 (2016). URL www.nature.com/naturematerialshttp://www.nature.com/articles/nmat4752.

[42] Milde, P. *et al.* Unwinding of a skyrmion lattice by magnetic monopoles. *Science* **340**, 1076–1080 (2013).

[43] Lancaster, T. *et al.* Transverse field muon-spin rotation signature of the skyrmion-lattice phase in Cu2OSeO3. *Phys. Rev. B - Condens. Matter Mater. Phys.* **91**, 224408 (2015). URL https://link.aps.org/doi/10.1103/PhysRevB.91.224408.

[44] Tokunaga, Y. *et al.* A new class of chiral materials hosting magnetic skyrmions beyond room temperature. *Nat. Commun.* **6**, 7638 (2015). URL www.nature.com/naturecommunicationshttp://www.nature.com/articles/ncomms8638.

[45] Sampaio, J., Cros, V., Rohart, S., Thiaville, A. & Fert, A. Nucleation, stability and current-induced motion of isolated magnetic skyrmions in nanostructures. *Nat. Nanotechnol.* **8**, 839–844 (2013). URL www.nature.com/naturenanotechnologyhttp://www.nature.com/articles/nnano.2013.210.

[46] Romming, N. *et al.* Writing and Deleting Single Magnetic Skyrmions. *Science* **341**, 636–639 (2013). URL http://science.sciencemag.org/https://www.sciencemag.org/lookup/doi/10.1126/science.1240573.

[47] Moreau-Luchaire, C. *et al.* Additive interfacial chiral interaction in multilayers for stabilization of small individual skyrmions at room temperature. *Nat. Nanotechnol.* **11**, 444–448 (2016). URL www.nature.com/naturenanotechnologyhttp://www.nature.com/articles/nnano.2015.313.

[48] Pollard, S. D. *et al.* Observation of stable Néel skyrmions in cobalt/palladium multilayers with Lorentz transmission electron microscopy. *Nat. Commun.* **8**, 14761 (2017). URL www.nature.com/naturecommunicationshttp://www.nature.com/articles/ncomms14761.

[49] Lee, J. C. T. *et al.* Synthesizing skyrmion bound pairs in Fe-Gd thin films. *Appl. Phys. Lett.* **109**, 022402 (2016). URL http://aip.scitation.org/doi/10.1063/1.4955462.

[50] Montoya, S. A. *et al.* Resonant properties of dipole skyrmions in amorphous Fe/Gd multilayers. *Phys. Rev. B* **95**, 224405 (2017). URL http://link.aps.org/doi/10.1103/PhysRevB.95.224405.

[51] Montoya, S. A. *et al.* Tailoring magnetic energies to form dipole skyrmions and skyrmion lattices. *Phys. Rev. B* **95**, 024415 (2017). URL https://link.aps.org/doi/10.1103/PhysRevB.95.024415.

[52] Montoya, S. A. *et al.* Spin-orbit torque induced dipole skyrmion motion at room temperature. *Phys. Rev. B* **98**, 104432 (2018). URL https://link.aps.org/doi/10.1103/PhysRevB.98.104432.

[53] Litzius, K. *et al.* Skyrmion Hall effect revealed by direct time-resolved X-ray microscopy. *Nat. Phys.* **13**, 170–175 (2017). URL www.nature.com/naturephysicshttp://www.nature.com/articles/nphys4000. 1608.07216.

[54] Chen, G. Skyrmion Hall effect. *Nat. Phys.* **13**, 112–113 (2017). URL www.nature.com/naturephysicshttp://www.nature.com/articles/nphys4030.

[55] Jiang, W. *et al.* Direct observation of the skyrmion Hall effect. *Nat. Phys.* **13**, 162–169 (2017). URL www.nature.com/naturephysicshttp://www.nature.com/articles/nphys3883. 1603.07393.

[56] Romming, N. *et al.* Writing and Deleting Single Magnetic Skyrmions. *Science* **341**, 636–639 (2013). URL http://science.sciencemag.org/https://www.sciencemag.org/lookup/doi/10.1126/science.1240573.

[57] Iwasaki, J., Mochizuki, M. & Nagaosa, N. Current-induced skyrmion dynamics in constricted geometries. *Nat. Nanotechnol.* **8**, 742–747 (2013). URL www.nature.com/naturenanotechnologyhttp://www.nature.com/articles/nnano.2013.176. 1310.1655.

[58] Jiang, W. *et al.* Blowing magnetic skyrmion bubbles. *Science* **349**, 283–286 (2015). URL http://science.sciencemag.org/https://www.sciencemag.org/lookup/doi/10.1126/science.aaa1442.

[59] Hrabec, A. *et al.* Current-induced skyrmion generation and dynamics in symmetric bilayers. *Nat. Commun.* **8**, 15765 (2017). URL www.nature.com/naturecommunicationshttp://www.nature.com/articles/ncomms15765. 1611.00647.

[60] Kiselev, N. S., Bogdanov, A. N., Schäfer, R. & Rößler, U. K. Chiral skyrmions in thin magnetic films: new objects for magnetic storage technologies? *J. Phys. D. Appl. Phys.* **44**, 392001 (2011). URL https://iopscience.iop.org/article/10.1088/0022-3727/44/39/392001https://iopscience.iop.org/article/10.1088/0022-3727/44/39/392001/meta. 1102.2726.

[61] Fert, A., Cros, V. & Sampaio, J. Skyrmions on the track. *Nat. Nanotechnol.* **8**, 152–156 (2013). URL http://arxiv.org/abs/1212.1101http://www.nature.com/articles/nnano.2013.29.

[62] Tomasello, R. *et al.* A strategy for the design of skyrmion racetrack memories. *Sci. Rep.* **4**, 6784 (2015). URL www.nature.com/scientificreportshttp://www.nature.com/articles/srep06784. 1409.6491.

[63] Zhang, X., Ezawa, M. & Zhou, Y. Magnetic skyrmion logic gates: conversion, duplication and merging of skyrmions. *Sci. Rep.* **5**, 9400 (2015). URL www.nature.com/scientificreportshttp://www.nature.com/articles/srep09400. 1410.3086.

[64] Zhang, X. *et al.* Skyrmion-skyrmion and skyrmion-edge repulsions in skyrmion-based racetrack memory. *Sci. Rep.* **5**, 7643 (2015). URL www.nature.com/scientificreportshttp://www.nature.com/articles/srep07643. 1403.7283.

[65] Fert, A., Reyren, N. & Cros, V. Magnetic skyrmions: advances in physics and potential applications. *Nat. Rev. Mater.* **2**, 17031 (2017). URL www.nature.com/natrevmatshttp://www.nature.com/articles/natrevmats201731.

[66] Garst, M., Waizner, J. & Grundler, D. Collective spin excitations of helices and magnetic skyrmions: Review and perspectives of magnonics in non-centrosymmetric magnets. *J. Phys. D. Appl. Phys.* **50**, 293002 (2017). URL https://doi.org/10.1088/1361-6463/aa7573http://stacks.iop.org/0022-3727/50/i=29/a=293002?key=crossref.20fc6ecb1a45d58744090fb9c4bf195b.

[67] Zhang, C. *et al.* Directional spin-wave propagation in the skyrmion chain. *J. Magn. Magn. Mater.* **490**, 165542 (2019). URL https://linkinghub.elsevier.com/retrieve/pii/S0304885319308558.

[68] Iwasaki, J., Beekman, A. J. & Nagaosa, N. Theory of magnon-skyrmion scattering in chiral magnets. *Phys. Rev. B* **89**, 064412 (2014). URL https://link.aps.org/doi/10.1103/PhysRevB.89.064412.

[69] Zhang, X. *et al.* Motion of skyrmions in nanowires driven by magnonic momentum-transfer forces. *New J. Phys.* **19**, 065001 (2017). URL https://doi.org/10.1088/1367-2630/aa6b70https://iopscience.iop.org/article/10.1088/1367-2630/aa6b70.

[70] Lan, J. & Xiao, J. Skew scattering and side jump of spin wave across magnetic texture. *arXiv* (2020). URL http://arxiv.org/abs/2010.04626. 2010.04626.

[71] Wang, Z. *et al.* Magnonic frequency comb through nonlinear magnon-skyrmion scattering. *arXiv* (2021). URL http://arxiv.org/abs/2102.02571. 2102.02571.

[72] Kataoka, M. Spin Waves in Systems with Long Period Helical Spin Density Waves Due to the Antisymmetric and Symmetric Exchange Interactions. *J. Phys. Soc. Japan* **56**, 3635–3647 (1987). URL https://journals.jps.jp/doi/pdf/10.1143/JPSJ.56.3635http://journals.jps.jp/doi/10.1143/JPSJ.56.3635.

[73] Cortés-Ortuño, D. & Landeros, P. Influence of the Dzyaloshinskii–Moriya interaction on the spin-wave spectra of thin films. *J. Phys. Condens. Matter* **25**, 156001 (2013). URL https://iopscience.iop.org/article/10.1088/0953-8984/25/15/156001.

[74] Moon, J.-H. *et al.* Spin-wave propagation in the presence of interfacial Dzyaloshinskii-Moriya interaction. *Phys. Rev. B* **88**, 184404 (2013). URL https://link.aps.org/doi/10.1103/PhysRevB.88.184404.

[75] Di, K. *et al.* Direct Observation of the Dzyaloshinskii-Moriya Interaction in a Pt/-Co/Ni Film. *Phys. Rev. Lett.* **114**, 047201 (2015). URL https://link.aps.org/doi/10.1103/PhysRevLett.114.047201.

[76] Di, K. *et al.* Asymmetric spin-wave dispersion due to Dzyaloshinskii-Moriya interaction in an ultrathin Pt/CoFeB film. *Appl. Phys. Lett.* **106**, 052403 (2015). URL https://doi.org/10.1063/1.4907173http://aip.scitation.org/doi/10.1063/1.4907173.

[77] Stashkevich, A. A. *et al.* Experimental study of spin-wave dispersion in Py/Pt film structures in the presence of an interface Dzyaloshinskii-Moriya interaction. *Phys. Rev. B* **91**, 214409 (2015). URL https://link.aps.org/doi/10.1103/PhysRevB.91.214409.

[78] Seki, S. *et al.* Magnetochiral nonreciprocity of volume spin wave propagation in chiral-lattice ferromagnets. *Phys. Rev. B* **93**, 235131 (2016). URL https://link.aps.org/doi/10.1103/PhysRevB.93.235131.

[79] Sato, T. J. *et al.* Magnon dispersion shift in the induced ferromagnetic phase of noncentrosymmetric MnSi. *Phys. Rev. B* **94**, 144420 (2016). URL https://link.aps.org/doi/10.1103/PhysRevB.94.144420.

[80] Schroeter, S. & Garst, M. Scattering of high-energy magnons off a magnetic skyrmion. *Low Temp. Phys.* **41**, 817–825 (2015). URL http://aip.scitation.org/doi/10.1063/1.4932356. 1504.02108.

[81] Stasinopoulos, I. *et al.* Low spin wave damping in the insulating chiral magnet Cu2OSeO3. *Appl. Phys. Lett.* **111**, 032408 (2017). URL https://doi.org/10.1063/1.4995240http://aip.scitation.org/doi/10.1063/1.4995240.

[82] Mochizuki, M. Spin-wave modes and their intense excitation effects in Skyrmion crystals. *Phys. Rev. Lett.* **108**, 017601 (2012). URL https://link.aps.org/doi/10.1103/PhysRevLett.108.017601.

[83] Onose, Y., Okamura, Y., Seki, S., Ishiwata, S. & Tokura, Y. Observation of magnetic excitations of skyrmion crystal in a helimagnetic insulator Cu2OSeO3. *Phys. Rev. Lett.* **109**, 037603 (2012). URL https://link.aps.org/doi/10.1103/PhysRevLett.109.037603.

[84] Okamura, Y. *et al.* Microwave magnetoelectric effect via skyrmion resonance modes in a helimagnetic multiferroic. *Nat. Commun.* **4**, 2391 (2013). URL www.nature.com/naturecommunicationshttp://www.nature.com/articles/ncomms3391.

[85] Ogawa, N., Seki, S. & Tokura, Y. Ultrafast optical excitation of magnetic skyrmions. *Sci. Rep.* **5**, 9552 (2015). URL www.nature.com/scientificreportshttp://www.nature.com/articles/srep09552.

[86] Weiler, M. *et al.* Helimagnon Resonances in an Intrinsic Chiral Magnonic Crystal. *Phys. Rev. Lett.* **119**, 237204 (2017). URL https://link.aps.org/doi/10.1103/PhysRevLett.119.237204.

[87] Aqeel, A. *et al.* Microwave Spectroscopy of the Low-Temperature Skyrmion State in Cu2OSeO3. *Phys. Rev. Lett.* **126**, 017202 (2021). URL https://link.aps.org/doi/10.1103/PhysRevLett.126.017202.

[88] Kugler, M. *et al.* Band Structure of Helimagnons in MnSi Resolved by Inelastic Neutron Scattering. *Phys. Rev. Lett.* **115**, 097203 (2015). URL https://link.aps.org/doi/10.1103/PhysRevLett.115.097203.

[89] Portnichenko, P. Y. *et al.* Magnon spectrum of the helimagnetic insulator Cu2OSeO3. *Nat. Commun.* **7**, 10725 (2016). URL www.nature.com/naturecommunicationshttp://www.nature.com/articles/ncomms10725.

[90] Weber, T. *et al.* Polarized inelastic neutron scattering of nonreciprocal spin waves in MnSi. *Phys. Rev. B* **100**, 060404 (2019). URL https://link.aps.org/doi/10.1103/PhysRevB.100.060404.

[91] Zhang, S. L. *et al.* Imaging and manipulation of skyrmion lattice domains in Cu2OSeO3. *Appl. Phys. Lett.* **109**, 192406 (2016). URL https://doi.org/10.1063/1.4967499http://aip.scitation.org/doi/10.1063/1.4967499.

[92] Zhang, S. L. *et al.* Multidomain Skyrmion Lattice State in Cu2OSeO3. *Nano Lett.* **16**, 3285–3291 (2016). URL https://pubs.acs.org/sharingguidelineshttps://pubs.acs.org/doi/10.1021/acs.nanolett.6b00845.

[93] Stasinopoulos, I. *et al.* Linearly polarized GHz magnetization dynamics of spin helix modes in the ferrimagnetic insulator Cu2OSeO3. *Sci. Rep.* **7**, 7037 (2017). URL www.nature.com/scientificreports/http://www.nature.com/articles/s41598-017-07020-2.

[94] Chacon, A. *et al.* Observation of two independent skyrmion phases in a chiral magnetic material. *Nat. Phys.* **14**, 936–941 (2018). URL http://www.nature.com/articles/s41567-018-0184-y.

[95] Okamura, Y. *et al.* Emergence and magnetic-field variation of chiral-soliton lattice and skyrmion lattice in the strained helimagnet Cu2OSeO3. *Phys. Rev. B* **96**, 174417 (2017). URL https://link.aps.org/doi/10.1103/PhysRevB.96.174417.

[96] A. G. Gurevich & G. A. Melkov. *Magnetization oscillations and waves, A. G. Gurevich, G. A. Melkov (1996).pdf* (CRC Press, Inc., 1996). URL https://www.routledge.com/Magnetization-Oscillations-and-Waves/Gurevich-Melkov/p/book/9780849394607.

[97] Coey, J. M. D. *Magnetism and Magnetic Materials*, vol. 9780521816 (Cambridge University Press, 2001). URL https://www.cambridge.org/core/books/magnetism-and-magnetic-materials/AD3557E2D4538CAA8488A8C1057313BChttps://www.cambridge.org/core/product/identifier/9780511845000/type/book.

[98] Dzyaloshinsky, I. A thermodynamic theory of “weak” ferromagnetism of antiferromagnetics. *J. Phys. Chem. Solids* **4**, 241–255 (1958). URL https://linkinghub.elsevier.com/retrieve/pii/0022369758900763.

[99] Moriya, T. Anisotropic Superexchange Interaction and Weak Ferromagnetism. *Phys. Rev.* **120**, 91–98 (1960). URL https://journals.aps.org/pr/abstract/10.1103/PhysRev.120.91https://link.aps.org/doi/10.1103/PhysRev.120.91.

[100] Hubert, A. & Schäfer, R. *Magnetic Domains* (Springer Berlin Heidelberg, Berlin, Heidelberg, 1998). URL http://link.springer.com/10.1007/978-3-540-85054-0.

[101] Cullity, B. D. & Graham, C. D. *Introduction to Magnetic Materials* (John Wiley and Sons, Inc., 2008). URL https://ieeexplore-ieee-org.ezproxy.lib.ucalgary.ca/book/6757880http://doi.wiley.com/10.1002/9780470386323.

[102] Aharoni A. *Introduction to the Theory of Ferromagnetism* (Oxford University Press, Oxford, United Kingdom, 2002), 2nd revise edn. URL https://global.oup.com/academic/product/introduction-to-the-theory-of-ferromagnetism-9780198508090.

[103] Ukleev, V. *et al.* Metastable solitonic states in the strained itinerant helimagnet FeGe. *Phys. Rev. B* **102**, 014416 (2020). URL https://link.aps.org/doi/10.1103/PhysRevB.102.014416.

[104] Nagaosa, N. & Tokura, Y. Topological properties and dynamics of magnetic skyrmions. *Nat. Nanotechnol.* **8**, 899–911 (2013). URL www.nature.com/naturenanotechnologyhttp://www.nature.com/articles/nnano.2013.243.

[105] Braun, H.-B. Topological effects in nanomagnetism: from superparamagnetism to chiral quantum solitons. *Adv. Phys.* **61**, 1–116 (2012). URL https://www.tandfonline.com/action/journalInformation?journalCode=tadp20http://dx.doi.org/10.1080/00018732.2012.663070http://www.tandfonline.comhttp://www.tandfonline.com/doi/abs/10.1080/00018732.2012.663070.

[106] Heinze, S. *et al.* Spontaneous atomic-scale magnetic skyrmion lattice in two dimensions. *Nat. Phys.* **7**, 713–718 (2011). URL www.nature.com/naturephysicshttp://www.nature.com/articles/nphys2045.

[107] Petrova, O. & Tchernyshyov, O. Spin waves in a skyrmion crystal. *Phys. Rev. B* **84**, 214433 (2011). URL https://link.aps.org/doi/10.1103/PhysRevB.84.214433.

[108] Schütte, C. & Garst, M. Magnon-skyrmion scattering in chiral magnets. *Phys. Rev. B* **90**, 094423 (2014). URL https://link.aps.org/doi/10.1103/PhysRevB.90.094423.

[109] Krawczyk, M. & Grundler, D. Review and prospects of magnonic crystals and devices with reprogrammable band structure. *J. Phys. Condens. Matter* **26**, 123202 (2014). URL https://iopscience.iop.org/article/10.1088/0953-8984/26/12/123202https://iopscience.iop.org/article/10.1088/0953-8984/26/12/123202/meta.

[110] Iwasaki, J., Beekman, A. J. & Nagaosa, N. Theory of magnon-skyrmion scattering in chiral magnets. *Phys. Rev. B* **89**, 064412 (2014). URL https://link.aps.org/doi/10.1103/PhysRevB.89.064412.

[111] Jonietz, F. *et al.* Spin Transfer Torques in MnSi at Ultralow Current Densities. *Science* **330**, 1648–1651 (2010). URL www.sciencemag.org/cgi/content/full/330/6011/1645/DC1https://www.sciencemag.org/lookup/doi/10.1126/science.1195709.

[112] Yu, X. *et al.* Skyrmion flow near room temperature in an ultralow current density. *Nat. Commun.* **3**, 988 (2012). URL www.nature.com/naturecommunicationshttp://www.nature.com/articles/ncomms1990.

[113] Romming, N. *et al.* Writing and Deleting Single Magnetic Skyrmions. *Science* **341**, 636–639 (2013). URL http://science.sciencemag.org/https://www.sciencemag.org/lookup/doi/10.1126/science.1240573.

[114] Iwasaki, J., Mochizuki, M. & Nagaosa, N. Current-induced skyrmion dynamics in constricted geometries. *Nat. Nanotechnol.* **8**, 742–747 (2013). URL www.nature.com/naturenanotechnologyhttp://www.nature.com/articles/nnano.2013.176. 1310.1655.

[115] Iwasaki, J., Mochizuki, M. & Nagaosa, N. Universal current-velocity relation of skyrmion motion in chiral magnets. *Nat. Commun.* **4**, 1463 (2013). URL www.nature.com/naturecommunicationshttp://www.nature.com/articles/ncomms2442.

[116] Jiang, W. *et al.* Blowing magnetic skyrmion bubbles. *Science* **349**, 283–286 (2015). URL http://science.sciencemag.org/https://www.sciencemag.org/lookup/doi/10.1126/science.aaa1442.

[117] Woo, S. *et al.* Observation of room-temperature magnetic skyrmions and their current-driven dynamics in ultrathin metallic ferromagnets. *Nat. Mater.* **15**, 501–506 (2016). URL www.nature.com/naturematerialshttp://www.nature.com/articles/nmat4593.

[118] Everschor-Sitte, K., Masell, J., Reeve, R. M. & Kläui, M. Perspective: Magnetic skyrmions—Overview of recent progress in an active research field. *J. Appl. Phys.* **124**, 240901 (2018). URL https://doi.org/10.1063/1.5048972http://aip.scitation.org/doi/10.1063/1.5048972.

[119] Huang, Y., Kang, W., Zhang, X., Zhou, Y. & Zhao, W. Magnetic skyrmion-based synaptic devices. *Nanotechnology* **28**, 08LT02 (2017). URL https://iopscience.iop.org/article/10.1088/1361-6528/aa5838https://iopscience.iop.org/article/10.1088/1361-6528/aa5838/meta.

[120] Song, K. M. *et al.* Skyrmion-based artificial synapses for neuromorphic computing. *Nat. Electron.* **3**, 148–155 (2020). URL https://doi.org/10.1038/s41928-020-0385-0http://www.nature.com/articles/s41928-020-0385-0.

[121] Qian, F. *et al.* New magnetic phase of the chiral skyrmion material Cu2OSeO3. *Sci. Adv.* **4**, eaat7323 (2018). URL http://advances.sciencemag.org/https://advances.sciencemag.org/lookup/doi/10.1126/sciadv.aat7323.

[122] Janson, O. *et al.* The quantum nature of skyrmions and half-skyrmions in Cu2OSeO3. *Nat. Commun.* **5**, 5376 (2014). URL www.nature.com/naturecommunicationshttp://www.nature.com/articles/ncomms6376.

[123] Kousaka, Y. *et al.* Chiral helimagnetism in T1/3NbS2 (T=Cr and Mn). *Nucl. Instruments Methods Phys. Res. Sect. A Accel. Spectrometers, Detect. Assoc. Equip.* **600**, 250–253 (2009). URL https://linkinghub.elsevier.com/retrieve/pii/S0168900208017208.

[124] Togawa, Y. *et al.* Chiral magnetic soliton lattice on a chiral helimagnet. *Phys. Rev. Lett.* **108**, 107202 (2012). URL https://link.aps.org/doi/10.1103/PhysRevLett.108.107202.

[125] Togawa, Y., Kousaka, Y., Inoue, K. & Kishine, J. I. Symmetry, structure, and dynamics of monoaxial chiral magnets. *J. Phys. Soc. Japan* **85**, 112001 (2016). URL http://doi.org/10.7566/JPSJ.85.112001http://journals.jps.jp/doi/10.7566/JPSJ.85.112001.

[126] Tsuruta, K. *et al.* Size dependence of discrete change in magnetization in single crystal of chiral magnet Cr1/3NbS2. *J. Appl. Phys.* **120**, 143901 (2016). URL https://doi.org/10.1063/1.4964427http://aip.scitation.org/doi/10.1063/1.4964427.

[127] Han, H. *et al.* Tricritical point and phase diagram based on critical scaling in the monoaxial chiral helimagnet Cr1/3NbS2. *Phys. Rev. B* **96**, 094439 (2017). URL https://link.aps.org/doi/10.1103/PhysRevB.96.094439.

[128] Yonemura, J. I. *et al.* Magnetic solitons and magnetic phase diagram of the hexagonal chiral crystal CrNb3S6 in oblique magnetic fields. *Phys. Rev. B* **96**, 184423 (2017). URL https://link.aps.org/doi/10.1103/PhysRevB.96.184423.

[129] Halder, M. *et al.* Thermodynamic evidence of a second skyrmion lattice phase and tilted conical phase in Cu2OSeO3. *Phys. Rev. B* **94**, 144429 (2018). URL https://link.aps.org/doi/10.1103/PhysRevB.98.144429.

[130] Bannenberg, L. J. *et al.* Multiple low-temperature skyrmionic states in a bulk chiral magnet. *npj Quantum Mater.* **4**, 11 (2019). URL https://doi.org/10.1038/s41535-019-0150-7http://www.nature.com/articles/s41535-019-0150-7.

[131] Okamura, Y., Kagawa, F., Seki, S. & Tokura, Y. Transition to and from the skyrmion lattice phase by electric fields in a magnetoelectric compound. *Nat. Commun.* **7**, 12669 (2016). URL www.nature.com/naturecommunicationshttp://www.nature.com/articles/ncomms12669.

[132] Nakajima, T. *et al.* Skyrmion lattice structural transition in MnSi. *Sci. Adv.* **3**, e1602562 (2017). URL http://advances.sciencemag.org/https://advances.sciencemag.org/lookup/doi/10.1126/sciadv.1602562.

[133] Yu, X. *et al.* Aggregation and collapse dynamics of skyrmions in a non-equilibrium state. *Nat. Phys.* **14**, 832–836 (2018). URL https://doi.org/10.1038/s41567-018-0155-3http://www.nature.com/articles/s41567-018-0155-3.

[134] Takagi, R. *et al.* Particle-size dependent structural transformation of skyrmion lattice. *Nat. Commun.* **11**, 5685 (2020). URL https://doi.org/10.1038/s41467-020-19480-8http://www.nature.com/articles/s41467-020-19480-8.

[135] Wilson, M. N. *et al.* Stability and metastability of skyrmions in thin lamellae of Cu2OSeO3. *arXiv* **2**, 013096 (2019). URL https://link.aps.org/doi/10.1103/PhysRevResearch.2.013096. 1909.07855.

[136] White, J. S. *et al.* Electric-Field-Driven Topological Phase Switching and Skyrmion-Lattice Metastability in Magnetoelectric Cu2OSeO3. *Phys. Rev. Appl.* **10**, 014021 (2018). URL https://link.aps.org/doi/10.1103/PhysRevApplied.10.014021. 1806.10330.

[137] Balasubramanian, B. *et al.* Chiral Magnetism and High-Temperature Skyrmions in B20-Ordered Co-Si. *Phys. Rev. Lett.* **124**, 057201 (2020). URL https://link.aps.org/doi/10.1103/PhysRevLett.124.057201.

[138] Adams, T., Garst, M., Bauer, A., Georgii, R. & Pfleiderer, C. Response of the Skyrmion Lattice in MnSi to Cubic Magnetocrystalline Anisotropies. *Phys. Rev. Lett.* **121**, 187205 (2018). URL https://link.aps.org/doi/10.1103/PhysRevLett.121.187205.

[139] Togawa, Y. *et al.* Magnetic soliton confinement and discretization effects arising from macroscopic coherence in a chiral spin soliton lattice. *Phys. Rev. B - Condens. Matter Mater. Phys.* **92**, 220412 (2015). URL https://link.aps.org/doi/10.1103/PhysRevB.92.220412.

[140] Pöllath, S. *et al.* Ferromagnetic Resonance with Magnetic Phase Selectivity by Means of Resonant Elastic X-Ray Scattering on a Chiral Magnet. *Phys. Rev. Lett.* **123**, 167201 (2019). URL https://link.aps.org/doi/10.1103/PhysRevLett.123.167201.

[141] Avci, C. O. *et al.* Interface-driven chiral magnetism and current-driven domain walls in insulating magnetic garnets. *Nat. Nanotechnol.* **14**, 561–566 (2019). URL https://doi.org/10.1038/s41565-019-0421-2http://www.nature.com/articles/s41565-019-0421-2.

[142] Shao, Q. *et al.* Topological Hall effect at above room temperature in heterostructures composed of a magnetic insulator and a heavy metal. *Nat. Electron.* **2**, 182–186 (2019). URL https://doi.org/10.1038/s41928-019-0246-xhttp://www.nature.com/articles/s41928-019-0246-x. 1904.07107.

[143] Caretta, L. *et al.* Interfacial Dzyaloshinskii-Moriya interaction arising from rare-earth orbital magnetism in insulating magnetic oxides. *Nat. Commun.* **11**, 1090 (2020). URL https://doi.org/10.1038/s41467-020-14924-7http://www.nature.com/articles/s41467-020-14924-7.

[144] Wang, H. *et al.* Chiral Spin-Wave Velocities Induced by All-Garnet Interfacial Dzyaloshinskii-Moriya Interaction in Ultrathin Yttrium Iron Garnet Films. *Phys. Rev. Lett.* **124**, 027203 (2020). URL https://link.aps.org/doi/10.1103/PhysRevLett.124.027203.

[145] Vansteenkiste, A. *et al.* The design and verification of MuMax3. *AIP Adv.* **4**, 107133 (2014). URL http://dx.doi.org/10.1063/1.4899186]http://aip.scitation.org/doi/10.1063/1.4899186. 1406.7635.

[146] Loudon, J. C. *et al.* Do Images of Biskyrmions Show Type-II Bubbles? *Adv. Mater.* **31**, 1806598 (2019). URL https://onlinelibrary.wiley.com/doi/abs/10.1002/adma.201806598.

[147] Wilhelm, H. *et al.* Precursor Phenomena at the Magnetic Ordering of the Cubic Helimagnet FeGe. *Phys. Rev. Lett.* **107**, 127203 (2011). URL https://link.aps.org/doi/10.1103/PhysRevLett.107.127203.

[148] Burn, D. M. *et al.* Field and temperature dependence of the skyrmion lattice phase in chiral magnet membranes. *Phys. Rev. B* **101**, 014446 (2020). URL https://link.aps.org/doi/10.1103/PhysRevB.101.014446.

[149] Hirschberger, M. *et al.* Skyrmion phase and competing magnetic orders on a breathing kagomé lattice. *Nat. Commun.* **10**, 5831 (2019). URL https://doi.org/10.1038/s41467-019-13675-4http://www.nature.com/articles/s41467-019-13675-4.

[150] Kurumaji, T. *et al.* Skyrmion lattice with a giant topological Hall effect in a frustrated triangular-lattice magnet. *Science* **365**, 914–918 (2019). URL http://science.sciencemag.org/https://www.sciencemag.org/lookup/doi/10.1126/science.aau0968. 1805.10719.

[151] Takagi, R. *et al.* Multiple- q noncollinear magnetism in an itinerant hexagonal magnet. *Sci. Adv.* **4**, eaau3402 (2018). URL http://advances.sciencemag.org/https://advances.sciencemag.org/lookup/doi/10.1126/sciadv.aau3402.

[152] Nayak, A. K. *et al.* Magnetic antiskyrmions above room temperature in tetragonal Heusler materials. *Nature* **548**, 561–566 (2017). URL https://www.nature.com/articles/nature23466http://www.nature.com/articles/nature23466.

[153] Saha, R. *et al.* Intrinsic stability of magnetic anti-skyrmions in the tetragonal inverse Heusler compound Mn1.4Pt0.9Pd0.1Sn. *Nat. Commun.* **10**, 5305 (2019). URL https://doi.org/10.1038/s41467-019-13323-xhttp://www.nature.com/articles/s41467-019-13323-x.

[154] Gao, S. *et al.* Fractional antiferromagnetic skyrmion lattice induced by anisotropic couplings. *Nature* **586**, 37–41 (2020). URL https://doi.org/10.1038/s41586-020-2716-8http://www.nature.com/articles/s41586-020-2716-8. 2009.11432.

[155] Heigl, M. *et al.* Dipolar-stabilized first and second-order antiskyrmions in ferrimagnetic multilayers. *arXiv* (2020). URL http://arxiv.org/abs/2010.06555. 2010.06555.

[156] Landau, L. & Lifshitz, E. On the theory of the dispersion of magnetic permeability in ferromagnetic bodies. In *Perspect. Theor. Phys.*, 51–65 (Elsevier, 1992). URL https://linkinghub.elsevier.com/retrieve/pii/B9780080363646500089.

[157] Gilbert, T. L. A phenomenological theory of damping in ferromagnetic materials. *IEEE Trans. Magn.* **40**, 3443–3449 (2004). URL https://ieeexplore.ieee.org/stamp/stamp.jsp?tp=&arnumber=1353448http://ieeexplore.ieee.org/document/1353448/.

[158] Polder, D. On the theory of ferromagnetic resonance. *Physica* **15**, 253–255 (1949). URL https://linkinghub.elsevier.com/retrieve/pii/0031891449900518.

[159] Yu, H. *et al.* High propagating velocity of spin waves and temperature dependent damping in a CoFeB thin film. *Appl. Phys. Lett.* **100**, 262412 (2012). URL http://dx.doi.org/10.1063/1.4731273http://aip.scitation.org/doi/10.1063/1.4731273.

[160] Kittel, C. On the Theory of Ferromagnetic Resonance Absorption. *Phys. Rev.* **73**, 155–161 (1948). URL https://link.aps.org/doi/10.1103/PhysRev.73.155.

[161] Kuświk, P., Głowiński, H., Coy, E., Dubowik, J. & Stobiecki, F. Perpendicularly magnetized Co 20 Fe 60 B 20 layer sandwiched between Au with low Gilbert damping. *J. Phys. Condens. Matter* **29**, 435803 (2017). URL https://doi.org/10.1088/1361-648X/aa834dhttps://iopscience.iop.org/article/10.1088/1361-648X/aa834d.

[162] Sandercock, J. R. & Wettling, W. Light scattering from surface and bulk thermal magnons in iron and nickel. *J. Appl. Phys.* **50**, 7784 (1979). URL https://doi.org/10.1063/1.326763http://scitation.aip.org/content/aip/journal/jap/50/B11/10.1063/1.326763.

[163] d'Allivy Kelly, O. *et al.* Inverse spin Hall effect in nanometer-thick yttrium iron garnet/Pt system. *Appl. Phys. Lett.* **103**, 082408 (2013). URL https://doi.org/10.1063/1.4819157http://aip.scitation.org/doi/10.1063/1.4819157.

[164] Yu, H. *et al.* Omnidirectional spin-wave nanograting coupler. *Nat. Commun.* **4**, 2702 (2013). URL www.nature.com/naturecommunicationshttp://www.nature.com/articles/ncomms3702.

[165] Yu, H. *et al.* Approaching soft X-ray wavelengths in nanomagnet-based microwave technology. *Nat. Commun.* **7**, 11255 (2016). URL www.nature.com/naturecommunicationshttp://www.nature.com/articles/ncomms11255.

[166] Liu, C. *et al.* Long-distance propagation of short-wavelength spin waves. *Nat. Commun.* **9**, 738 (2018). URL www.nature.com/naturecommunicationshttp://www.nature.com/articles/s41467-018-03199-8.

[167] Baumgaertl, K. *et al.* Nanoimaging of Ultrashort Magnon Emission by Ferromagnetic Grating Couplers at GHz Frequencies. *Nano Lett.* **20**, 7281–7286 (2020). URL https://dx.doi.org/10.1021/acs.nanolett.0c02645https://pubs.acs.org/doi/10.1021/acs.nanolett.0c02645.

[168] Weber, T. *et al.* Non-reciprocal magnons in non-centrosymmetric MnSi. *AIP Adv.* **8**, 101328 (2018). URL https://doi.org/10.1063/1.5041036http://aip.scitation.org/doi/10.1063/1.5041036.

[169] Seki, S. *et al.* Propagation dynamics of spin excitations along skyrmion strings. *Nat. Commun.* **11**, 256 (2020). URL https://doi.org/10.1038/s41467-019-14095-0http://www.nature.com/articles/s41467-019-14095-0.

[170] Schwarze, T. *et al.* Universal helimagnon and skyrmion excitations in metallic, semiconducting and insulating chiral magnets. *Nat. Mater.* **14**, 478–483 (2015). URL www.nature.com/naturematerials.

[171] Goncalves, F. J. *et al.* Collective resonant dynamics of the chiral spin soliton lattice in a monoaxial chiral magnetic crystal. *Phys. Rev. B* **95**, 104415 (2017). URL https://link.aps.org/doi/10.1103/PhysRevB.95.104415.

[172] Tokushuku, K., Kishine, J. I. & Ogata, M. Tunable spin dynamics in chiral soliton lattice. *J. Phys. Soc. Japan* **86**, 124701 (2017). URL https://doi.org/10.7566/JPSJ.86.124701http://journals.jps.jp/doi/10.7566/JPSJ.86.124701.

[173] Kishine, J. *et al.* Theory of standing spin waves in a finite-size chiral spin soliton lattice. *Phys. Rev. B* **100**, 024411 (2019). URL https://link.aps.org/doi/10.1103/PhysRevB.100.024411.

[174] Cardona, M. & Güntherodt, G. (eds.) *Light Scattering in Solids VII*, vol. 75 of *Topics in Applied Physics* (Springer Berlin Heidelberg, 2000). URL http://link.springer.com/10.1007/BFb0103383.

[175] Zhu, Y. (ed.) *Modern Techniques for Characterizing Magnetic Materials* (Springer-Verlag, New York, 2005). URL http://link.springer.com/10.1007/b101202.

[176] Sebastian, T., Schultheiss, K., Obry, B., Hillebrands, B. & Schultheiss, H. Micro-focused Brillouin light scattering: imaging spin waves at the nanoscale. *Front. Phys.* **3**, 35 (2015). URL http://journal.frontiersin.org/Article/10.3389/fphy.2015.00035/abstract.

[177] Wettling, W., Cottam, M. G. & Sandercock, J. R. The relation between one-magnon light scattering and the complex magneto-optic effects in YIG. *J. Phys. C Solid State Phys.* **8**, 211–228 (1975). URL https://iopscience.iop.org/article/10.1088/0022-3719/8/2/014.

[178] Grünberg, P. & Metawe, F. Light Scattering from Bulk and Surface Spin Waves in EuO. *Phys. Rev. Lett.* **39**, 1561–1565 (1977). URL https://link.aps.org/doi/10.1103/PhysRevLett.39.1561.

[179] Demokritov, S., Hillebrands, B. & Slavin, A. N. Brillouin light scattering studies of confined spin waves: linear and nonlinear confinement. *Phys. Rep.* **348**, 441–489 (2001). URL https://linkinghub.elsevier.com/retrieve/pii/S0370157300001162.

[180] Demokritov, S. & Demidov, V. Micro-Brillouin Light Scattering Spectroscopy of Magnetic Nanostructures. *IEEE Trans. Magn.* **44**, 6–12 (2008). URL https://ieeexplore.ieee.org/stamp/stamp.jsp?tp=&arnumber=4407581http://ieeexplore.ieee.org/document/4407581/.

[181] Sandweg, C. W. *et al.* Wide-range wavevector selectivity of magnon gases in Brillouin light scattering spectroscopy. *Rev. Sci. Instrum.* **81**, 073902 (2010). URL https://doi.org/10.1063/1.3454918http://aip.scitation.org/doi/10.1063/1.3454918.

[182] Ogawa, N. *et al.* Nonreciprocity of spin waves in the conical helix state. *Proc. Natl. Acad. Sci. U. S. A.* **118** (2021). URL https://www.pnas.org/lookup/suppl/.

[183] Stöhr, J. *et al.* Element-specific magnetic microscopy with circularly polarized X-rays (1993).

[184] Schneider, C. M. *et al.* Magnetic spectromicroscopy from Fe(100). *Appl. Phys. Lett.* **63**, 2432–2434 (1993). URL http://aip.scitation.org/doi/10.1063/1.110498.

[185] Stöhr, J., Padmore, H. A., Anders, S., Stammler, T. & Scheinfein, M. R. Principles of X-Ray Magnetic Dichroism Spectromicroscopy. *Surf. Rev. Lett.* **05**, 1297–1308 (1998). URL https://www.worldscientific.com/doi/abs/10.1142/S0218625X98001638.

[186] Stöhr, J. Exploring the microscopic origin of magnetic anisotropies with X-ray magnetic circular dichroism (XMCD) spectroscopy. *J. Magn. Magn. Mater.* **200**, 470–497 (1999). URL https://linkinghub.elsevier.com/retrieve/pii/S0304885399004072.

[187] Follath, R. *et al.* The X-ray microscopy beamline UE46-PGM2 at BESSY. In *AIP Conf. Proc.*, vol. 1234, 323–326 (2010). URL https://doi.org/10.1063/1.3463201http://aip.scitation.org/doi/abs/10.1063/1.3463201.

[188] Grimsditch, M., Malozemoff, A. & Brunsch, A. Standing spin waves observed by Brillouin scattering in amorphous metallic Fe80B20 films. *Phys. Rev. Lett.* **43**, 711–714 (1979). URL https://link.aps.org/doi/10.1103/PhysRevLett.43.711.

[189] Jorzick, J. *et al.* Brillouin light scattering from quantized spin waves in micron-size magnetic wires. *Phys. Rev. B* **60**, 15194–15200 (1999). URL https://link.aps.org/doi/10.1103/PhysRevB.60.15194.

[190] van Kampen, M. *et al.* All-Optical Probe of Coherent Spin Waves. *Phys. Rev. Lett.* **88**, 227201 (2002). URL https://link.aps.org/doi/10.1103/PhysRevLett.88.227201.

[191] Bayer, C. *et al.* Spin-wave excitations in finite rectangular elements of Ni80Fe20. *Phys. Rev. B - Condens. Matter Mater. Phys.* **72** (2005).

[192] Demidov, V. E., Hansen, U.-H. & Demokritov, S. O. Spin-Wave Eigenmodes of a Saturated Magnetic Square at Different Precession Angles. *Phys. Rev. Lett.* **98**, 157203 (2007). URL https://link.aps.org/doi/10.1103/PhysRevLett.98.157203.

[193] Demidov, V. E., Demokritov, S. O., Rott, K., Krzysteczko, P. & Reiss, G. Mode interference and periodic self-focusing of spin waves in permalloy microstripes. *Phys. Rev. B* **77**, 064406 (2008). URL https://link.aps.org/doi/10.1103/PhysRevB.77.064406.

[194] Mruczkiewicz, M. *et al.* Standing spin waves in magnonic crystals. *J. Appl. Phys.* **113**, 093908 (2013). URL https://doi.org/10.1063/1.4793085http://aip.scitation.org/doi/10.1063/1.4793085.

[195] An, T. *et al.* Unidirectional spin-wave heat conveyer. *Nat. Mater.* **12**, 549–553 (2013). URL www.nature.com/naturematerialshttp://www.nature.com/articles/nmat3628.

[196] Bozhko, D. A. *et al.* Unconventional spin currents in magnetic films. *Phys. Rev. Res.* **2**, 023324 (2020). URL https://link.aps.org/doi/10.1103/PhysRevResearch.2.023324.

[197] Garcia-Sanchez, F., Borys, P., Vansteenkiste, A., Kim, J. V. & Stamps, R. L. Nonreciprocal spin-wave channeling along textures driven by the Dzyaloshinskii-Moriya interaction. *Phys. Rev. B - Condens. Matter Mater. Phys.* **89**, 224408 (2014). URL https://link.aps.org/doi/10.1103/PhysRevB.89.224408. 1401.4439.

[198] Zingsem, B. W., Farle, M., Stamps, R. L. & Camley, R. E. Unusual nature of confined modes in a chiral system: Directional transport in standing waves. *Phys. Rev. B* **99**, 214429 (2019). URL https://link.aps.org/doi/10.1103/PhysRevB.99.214429.

[199] Josten, N. *et al.* Dynamic unidirectional anisotropy in cubic FeGe with antisymmetric spin-spin-coupling. *Sci. Rep.* **10**, 2861 (2020). URL http://www.nature.com/articles/s41598-020-59208-8. 1902.02665.

[200] Zhang, S. L. *et al.* Room-temperature helimagnetism in FeGe thin films. *Sci. Rep.* **7**, 1–10 (2017). URL http://dx.doi.org/10.1038/s41598-017-00201-z.

[201] Zhang, S. *et al.* Reciprocal space tomography of 3D skyrmion lattice order in a chiral magnet. *Proc. Natl. Acad. Sci.* **115**, 6386–6391 (2018). URL http://www.pnas.org/lookup/doi/10.1073/pnas.1803367115.

[202] Adams, T. *et al.* Long-wavelength helimagnetic order and skyrmion lattice phase in Cu2OSeO3. *Phys. Rev. Lett.* **108**, 237204 (2012). URL https://link.aps.org/doi/10.1103/PhysRevLett.108.237204.

[203] Ivković, I., Pajić, D., Ivek, T. & Berger, H. Two-step transition in a magnetoelectric ferrimagnet Cu2OSeO3. *Phys. Rev. B - Condens. Matter Mater. Phys.* **85**, 224402 (2012). URL https://link.aps.org/doi/10.1103/PhysRevB.85.224402.

[204] James, R. D. & Wuttig, M. Magnetostriction of martensite. *Philos. Mag. A* **77**, 1273–1299 (1998). URL https://www.tandfonline.com/action/journalInformation?journalCode=tphm20http://www.tandfonline.com/doi/abs/10.1080/01418619808214252.

[205] Yu, H. *et al.* Thermal spin torques in magnetic insulators. *Phys. Rev. B* **95**, 104432 (2017). URL https://link.aps.org/doi/10.1103/PhysRevB.95.104432.

[206] Versteeg, R. B. *et al.* Optically probed symmetry breaking in the chiral magnet Cu2OSeO3. *Phys. Rev. B* **94**, 094409 (2016). URL https://link.aps.org/doi/10.1103/PhysRevB.94.094409. 1605.01900.

[207] Huang, P. *et al.* In Situ Electric Field Skyrmion Creation in Magnetoelectric Cu2OSeO3. *Nano Lett.* **18**, 5167–5171 (2018). URL https://pubs.acs.org/sharingguidelineshttps://pubs.acs.org/doi/10.1021/acs.nanolett.8b02097. 1710.09200.

[208] Litzius, K. *et al.* The role of temperature and drive current in skyrmion dynamics. *Nat. Electron.* **3**, 30–36 (2020). URL https://doi.org/10.1038/s41928-019-0359-2http://www.nature.com/articles/s41928-019-0359-2.

[209] Yu, X. *et al.* Real-space observations of 60-nm skyrmion dynamics in an insulating magnet under low heat flow (2021). URL https://assets.researchsquare.com/files/rs-156692/v1_stamped.pdf.

[210] Lehmeyer, A. & Merten, L. Magnon-polaritons and magnetic reststrahlen-bands of uniaxial antiferromagnetic crystals. *J. Magn. Magn. Mater.* **50**, 32–38 (1985). URL https://linkinghub.elsevier.com/retrieve/pii/0304885385900836.

[211] Cao, Y., Yan, P., Huebl, H., Goennenwein, S. T. B. & Bauer, G. E. W. Exchange magnon-polaritons in microwave cavities. *Phys. Rev. B* **91**, 094423 (2015). URL https://link.aps.org/doi/10.1103/PhysRevB.91.094423.

[212] Klingler, S. *et al.* Spin waves in coupled YIG/Co heterostructures. *Phys. Rev. Lett.* **120**, 127201 (2018). URL https://link.aps.org/doi/10.1103/PhysRevLett.120.127201. 1712.02561.

[213] Chen, J. *et al.* Strong Interlayer Magnon-Magnon Coupling in Magnetic Metal-Insulator Hybrid Nanostructures. *Phys. Rev. Lett.* **120**, 217202 (2018). URL https://link.aps.org/doi/10.1103/PhysRevLett.120.217202.

[214] Qin, H., Hämäläinen, S. J. & van Dijken, S. Exchange-torque-induced excitation of perpendicular standing spin waves in nanometer-thick YIG films. *Sci. Rep.* **8**, 5755 (2018). URL www.nature.com/scientificreports/http://www.nature.com/articles/s41598-018-23933-y.

[215] Zhang, S. L. *et al.* Imaging and manipulation of skyrmion lattice domains in Cu2OSeO3. *Appl. Phys. Lett.* **109**, 192406 (2016). URL http://aip.scitation.org/doi/10.1063/1.4967499.

[216] Hamdi, M. & Mohseni, S. M. Temperature-induced coupled–decoupled transition in perpendicular pseudo spin valves. *J. Phys. D. Appl. Phys.* **50**, 115003 (2017). URL https://iopscience.iop.org/article/10.1088/1361-6463/aa5a72https://iopscience.iop.org/article/10.1088/1361-6463/aa5a72/meta.

[217] Kisielewski, M., Kisielewski, J., Sveklo, I., Wawro, A. & Maziewski, A. Micromagnetic Simulations of Magnetization Spatial Distribution in Ultrathin Cobalt Layers With Gradient Magnetic Anisotropy. *IEEE Trans. Magn.* **53**, 1–4 (2017). URL http://ieeexplore.ieee.org/document/7932946/.

[218] Hahn, M. B. Temperature in micromagnetism: cell size and scaling effects of the stochastic Landau–Lifshitz equation. *J. Phys. Commun.* **3**, 075009 (2019). URL https://doi.org/10.1088/2399-6528/ab31e6https://iopscience.iop.org/article/10.1088/2399-6528/ab31e6.

[219] Garcia-Sanchez, F. *et al.* Narrow Magnonic Waveguides Based on Domain Walls. *Phys. Rev. Lett.* **114**, 247206 (2015). URL https://link.aps.org/doi/10.1103/PhysRevLett.114.247206.

[220] Schütte, C. & Garst, M. Magnon-skyrmion scattering in chiral magnets. *Phys. Rev. B* **90**, 094423 (2014). URL https://link.aps.org/doi/10.1103/PhysRevB.90.094423.

[221] Zhang, X. *et al.* Motion of skyrmions in nanowires driven by magnonic momentum-transfer forces. *New J. Phys.* **19**, 065001 (2017). URL https://doi.org/10.1088/1367-2630/aa6b70https://iopscience.iop.org/article/10.1088/1367-2630/aa6b70.

Ms. Ping CHE

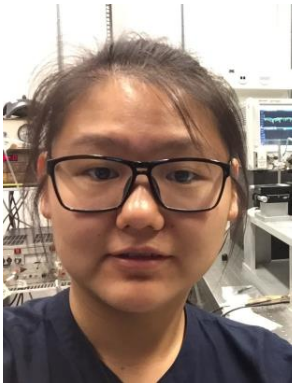

PhD student
Laboratory of Nanoscale Magnetic Materials and Magnonics (LMGN)
École Polytechnique Fédérale de Lausanne (EPFL)
Lausanne, Switzerland
Email: ping.che@epfl.ch

Education

10.2016-05.2021 PhD student, Doctoral Program in Physics, École Polytechnique Fédérale de Lausanne (EPFL), Lausanne, Switzerland

08.2015-08.2016 M. Sc., Applied Physics, Université Paris-Sud, Université Paris-Saclay, Paris, France

09.2010-07.2014 B. Eng., Electronic and Information Engineering, Beihang University (BUAA), Beijing, China

Research Experience

10.2016-05.2021 Doctoral Assistant supervised by Prof. Dirk Grundler, EPFL (CH)

- Exploration of spin dynamics in skyrmion hosting materials Cu_2OSeO_3 and FeGd multilayers, with integrated magnonic grating couplers (GCs) and coplanar waveguides (CPWs), by Brillouin light scattering (BLS), vector network analyzer (VNA) and X-ray transmission imaging.
- Exploration of short-waved spin wave excitations in insulating ferrimagnet yttrium ion garnet (YIG) films with magnonic GCs and magnetic CPWs by BLS and VNA.
- Establishment and optimization of the cryostat integrated with BLS platform.
- Device fabrication at nano-scale of bulk, thin films and membrane materials using: ebeam-lithography (EBL), photo-lithography, focus ion beam (FIB) etching, ion beam etching (IBE), inductively coupled plasma (ICP) etching, sputtering, thermal and magneto evaporation, lift-off techniques.
- Micromagnetic simulations of spin dynamics in skyrmion hosting materials using Mumax3.
- Supervising 3 master semester projects and co-supervising 2 master theses.

02.2016-08.2016 Master thesis student supervised by Prof. Jean-Philippe Ansermet, EPFL (CH)

- Investigating experimentally Magnetic Seebeck effect on propagating spin waves in YIG microstructures.

07.2014-08.2015 Research Assistant (full time) supervised by Prof. Haiming Yu, BUAA (CN)

- Spin caloritronic studies on magnetic nanostructures and Magnetic Seebeck effect.
- Excitation and detection of spin wave propagation in magnetic materials at gigahertz frequency with multiple-shape CPWs.

Publications

1. P. Che, I. Stasinopoulos, A. Mucchietto, J. Li, H. Berger, A. Bauer, C. Pfleiderer, and D. Grundler, "Confined dipole and exchange spin waves in single crystals of the chiral magnet Cu_2OSeO_3", *arXiv:*2104.06240 (2021).

2. A. KúkoĺIová, S. Escobar Steinvall, R.Paul, J.-B. Leran, P. Che, M. Hamdi, A. Mucchietto, D. Grundler, and A. Fontcuberta i Morral, "van der Waals Epitaxy of $Co_{10-x}Zn_{10-y}Mn_{x+y}$ Thin Films: Chemical Composition Engineering and Magnetic Properties", *J. Phys. Chem. C* acs.jpcc.1c00452 (2021).
3. P. Che*, K. Baumgaertl*, A. Kúkol'ová, C. Dubs, and D. Grundler, "Efficient wavelength conversion of exchange magnons below 100 nm by magnetic coplanar waveguides", *Nat. Commun.* **11**, 1445 (2020). (*equally contributed authors)
4. K. Baumgaertl, J. Gräfe, P. Che, A. Mucchietto, J. Förster, N. Träger, M. Bechtel, M. Weigand, G. Schütz, and D. Grundler. "Nanoimaging of ultrashort magnon emission by ferromagnetic grating couplers at GHz frequencies", *Nano Lett.* 20 (10), 7281-7286 (2020).
5. H. Wang, J. Chen, T. Liu, J. Zhang, K. Baumgaertl, C. Guo, Y. Li, C. Liu, P. Che, S. Tu, S. Liu, P. Gao, X. Han, D. Yu, M. Wu, D. Grundler, and H. Yu, "Chiral spin-wave velocities induced by all-garnet interfacial Dzyaloshinskii-Moriya interaction in ultrathin yttrium iron garnet films", *Phys. Rev. Lett.* **124**, 027203 (2020).
6. H. Yu, S. D. Brechet, P. Che, F. A. Vetro, M. Collet, S. Tu, Y. G. Zhang, Y. Zhang, T. Stueckler, L. Wang, H. Cui, D. Wang, C. Zhao, P. Bortolotti, A. Anane, J. P. Ansermet, and W. Zhao, "Thermal spin torques in magnetic insulators", *Phys. Rev. B* **95**, 104432 (2017).
7. P. Che, Y. Zhang, C. Liu, S. Tu, Z. Liao, D. Yu, F. A. Vetro, J. P. Ansermet, W. Zhao, L. Bi, and H. Yu, "Short-wavelength spin waves in yttrium iron garnet micro-channels on silicon", *IEEE Magn. Lett.* **7**, 1-4 (2016).

Manuscripts in Preparation

1. P. Che, *et al.* "Spin wave excitation of room-temperature dipole skyrmions in perpendicular magnetic anisotropy FeGd multilayers".
2. P. Che, *et al.* "Spin dynamics of the skyrmion and chiral soliton lattice in Cu_2OSeO_3 locally resolved by cryogenic Brillouin light scattering".

Proposals

2019-2020 "Exploration of short-waved magnons interacting with dipolar skyrmion lattices and chiral domain arrays" proposal submitted to Bessy II (Proposer). Accepted and funded.

2017-2018 Summer school "New Trends in Chiral Magnetism" proposal submitted to EuroTech Alliances (Proposer). Accepted and funded.

Conference Talks

06.2021 (Accepted) Contributed talk "X-ray transmission imaging of dipole skyrmion dynamics" on SolSky-Mag, San Sebastian (Gipuzkoa), Spain.

04.2021 Contributed talk "Spin Dynamics of Skyrmion Lattices in a Chiral Magnet Resolved by Micro-Focus Brillouin Light Scattering", Intermag, online.

11.2020 Contributed Talk "Spin Dynamics of Skymion and Chiral Soliton Lattices in Cu_2OSeO_3 Locally Resolved by Scanning Brillouin Light Scattering", MMM, online.

08.2019 Contributed talk "Bulk magnon modes in Cu_2OSeO_3 detected by Brillouin light scattering microscopy at tow temperature" on Joint Annual Meeting of SPS and ÖPG, Zurich, Switzerland.

07.2019 Contributed talk "Broadband emission and detection of magnons from hybrid magnetic waveguides down to 100 nm wavelength" on Magnonics conference, Carovigno, Italy. (Student Grant winner)

09.2018 Poster "Discretized spin waves in single crystals of the chiral magnet Cu_2OSeO_3" on Joint European Magnetic Symposia (JEMS) Conference, Mainz, Germany.

08.2018 Poster "Discretized spin waves in single crystals of the chiral magnet Cu_2OSeO_3" on Swiss Workshop on Materials with Novel Electronic Properties (MaNEP), Les Diablerets, Switzerland.

08.2017 Poster "Broadband spin-wave spectroscopy performed on single crystals of the insulating chiral magnet Cu_2OSeO_3", Joint Annual Meeting of SPS and ÖPG, Genève, Switzerland.

Memberships and Services

22nd-24th, July, 2019 **Organizer (together with Prof. Dirk Grundler)**

Workshop "Micromagnetic simulation on skyrmion hosting materials" on EPFL campus.

20th-24th, August, 2018 **Chair of the organization committee**

EuroTech Summer School "New Trends in Chiral Magnetism" jointly organized by EPFL, TU/e, DTU and TUM (https://ntcm2018.epfl.ch/) on EPFL campus.

Language Skills

Chinese (native), English (C1), French (A2/B1).

Ce document a été imprimé au Centre d’impression EPFL,
imprimerie climatiquement neutre, certifiée myClimate.